“In like manner the loadstone has its poles, by nature north and south, being definite and determined points set in the stone, the primary boundaries of motions and effects, the limits and governors of the many actions and powers.”

- William Gilbert, *De Magnete* (1600)

UNIVERSITY
OF TWENTE.

Shaping Magnetics in Surgical Robotics – Michiel Richter

Shaping Magnetics in Surgical Robotics

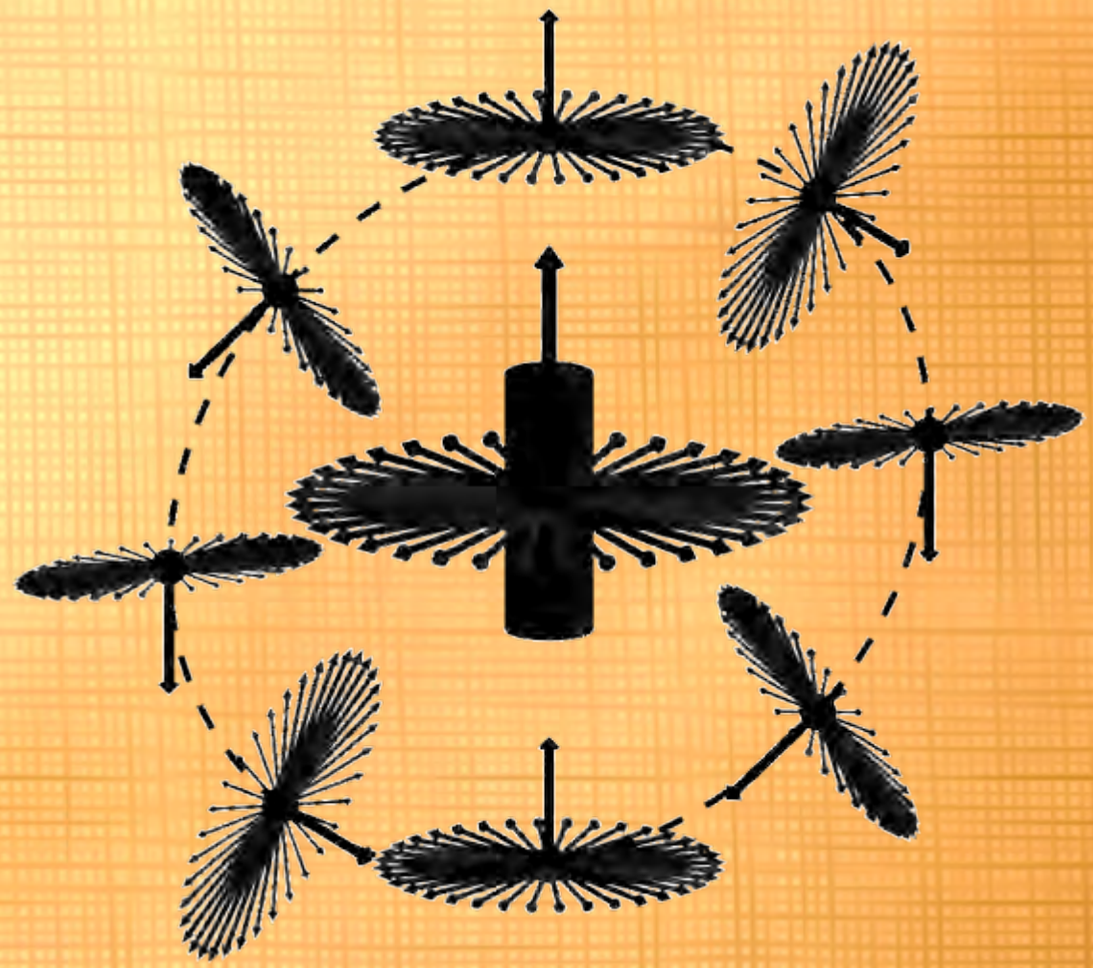

A Dissertation on Continuum Robots

Michiel Richter

Shaping Magnetics in Surgical Robotics

– A Dissertation on Continuum Robots –

Michiel Richter

This dissertation has been approved by:

Promotor:
prof.dr. Sarthak Misra

Co-promotor:
dr. V. Kalpathy Venkiteswaran

Cover design: NAME
Lay-out: NAME
Printed by: NAME
ISBN (print): NUMBER
ISBN (digital): NUMBER
DOI: NUMBER

DISSERTATION

to obtain
the degree of doctor at the University of Twente,
on the authority of the rector magnificus,
prof.dr.ir A. Veldkamp,
on account of the decision of the Doctorate Board,
to be publicly defended
on Wednesday 2 July 2025 at 14.45 hours

by

Michiel Richter

born on the 27th of April, 1994
in Hardenberg, The Netherlands

Graduation Committee:

Chair / secretary:	
prof.dr.ir. H.F.J.M. Koopman	*University of Twente*
Promoter:	
prof.dr. S. Misra	*University of Twente,* *University of Groningen,* *University Medical Center Groningen*
Co-promotor:	
dr. V. Kalpathy Venkiteswaran	*University of Twente*
Committee Members:	
prof.dr.ir N.J.J. Verdonschot	*University of Twente*
prof.dr.ir D.M. Brouwer	*University of Twente*
prof.dr. E.C.J. Consten	*Meander Medisch Centrum,* *University Medical Center Groningen*
prof.dr J.-P. de Vries	*University Medical Center Groningen*
dr. D. Makarov	*Helmholtz-Zentrum Dresden-Rossendorf e.V.*
dr. A. Sadeghi	*University of Twente*

This work is part of the research project **MAESTRO** funded by the European Research Council (ERC) under the European Union's Horizon 2020 Research and Innovation Programma, grant number 866494.

MAESTRO

Funded by
the European Union

European Research Council

Established by the European Commission

To my loving parents,
and my dear fiancé, Jessica

Dutch Summary

Medische continuum robots, zoals stuurbare voerdraden, katheters en endoscopen, zijn flexibele structuren. Sinds de opkomst van minimaal invasieve chirurgie worden ze alomtegenwoordig gebruikt voor verschillende diagnostische en therapeutische toepassingen. Traditioneel worden deze apparaten handmatig bestuurd door een opererend arts.

De afgelopen decennia is onderzoek gedaan naar magnetisch aangestuurde continuumrobots. Vergeleken met andere aansturingstechnieken – mechanisch, fluïdisch – biedt magnetisme een uniek voordeel. Namelijk, krachten en koppels kunnen direct worden uitgeoefend op een magnetisch uiteinde van een continuumrobot via een extern opgewekt magnetisch veld.

Hoewel onderzoek naar magnetische aansturing zich in het verleden vaak heeft gericht op het geleiden van endovasculaire voerdraden en het navigeren van pulmonale of gastro-intestinale endoscopen, is de praktische klinische implementatie vooralsnog beperkt succesvol gebleken. Dit kan hypothetisch worden toegeschreven aan een combinatie van uitdagingen, zoals kosten, de fysieke omvang van magnetische robotinfrastructuur (machines die magneetvelden opwekken), afhankelijkheid van complementaire medische systemen (zoals beeldvormingstechnologieën) of functionele overlap met eenvoudigere en gebruiksvriendelijkere alternatieven.

Dit proefschrift heeft als doel de functionaliteit en praktische toepasbaarheid van magnetische continuumrobots (MCR's) uit te breiden. **Deel I** richt zich op modellering en regeltechniek van MCR's. In **Hoofdstuk 2** worden extra aansturingspunten – magnetisch responsieve lichaamssegmenten – geïntroduceerd aan MCR's, als uitbreiding op MCR's die traditioneel enkel één magneet aan hun uiteinde dragen. Een quasi-statisch simulatiemodel wordt geformuleerd om de vervorming van MCR's onder gegenereerde magnetische velden te voorspellen. Dit model ondersteunt de onderling onafhankelijke aansturing van de MCRs aansturingspunten naar voorgeschreven richtingen. Hierdoor kunnen vormveranderende MCR's functioneren als kleinschalige continuumrobotarmen voor medische toepassingen.

Als uitbreiding op vormverandering behandelt **Hoofdstuk 3** de veilige geleiding van (mogelijk) gevaarlijke chirurgische instrumenten met MCR's. Door gebruik te maken van slimme materialen met variabele stijfheid wordt een selectief vormvergrendelende MCR ontwikkeld. Hierdoor kan de vorm dynamisch worden geconfigureerd met magnetische velden. Het eerder genoemde simulatiemodel wordt uitgebreid om rekening te houden met variabele stijfheid. Dit model wordt toegepast op open-lus en simulatiegebaseerde magnetische configuratie van de vorm van de MCR. Deze benadering wordt gebruikt een (biopsie)naald naar verschillende doelen binnen een driedimensionale(3D) robotische werkruimte te geleiden.

Deel II introduceert nieuwe ontwerpen voor MCR's in de context van interne magnetische interacties. Afwijkend van traditionele ontwerpen met geëxtrudeerde 2D-vormen, zoals cilinders of balken, onderzoekt **Hoofdstuk 4** een specifiek 3D-ontwerp voor MCR's, bedoeld om inherent lokale magnetische interacties tussen lichaamssegmenten (gunstig) te benutten. Een spiraalvormig ontwerp gemaakt van een magnetisch polymeer wordt voorgesteld. Magnetische krachten tussen de spiraalwindingen zijn bedoeld om de algehele buigflexibiliteit te verbeteren. Het ontwerp wordt geoptimaliseerd om de bestuurbaarheid door externe magnetische velden te verbeteren voor endovasculaire navigatie.

Hoofdstuk 5 presenteert een alternatief voor extern aangestuurde MCR's door ze te integreren met lokale bronnen van magnetische velden. Hier worden modellen van het lokale magnetische veld gebruikt om niet-uniforme magnetisatieprofielen voor de MCR's te berekenen, waardoor taak-specifieke bewegingen (zoals trekken) van de robot mogelijk worden. Daarnaast wordt aangetoond hoe deze machines aan een andere continuumrobot kunnen worden bevestigd als functionele componenten. Deze vooruitgang op het gebied van magnetische zachte machines kan nieuwe chirurgische continuumrobots inspireren met gelokaliseerde machines voor bijvoorbeeld gerichte medicijnafgifte.

Deel III verschuift het onderzoek van functionaliteit naar de praktische toepasbaarheid van MCR's in de context van magnetische lokalisatie binnen het menselijk lichaam. In vergelijking met conventionele beeldgebaseerde

lokalisatie bieden MCRs de unieke mogelijkheid tot magnetische lokalisatie – het reconstrueren van zijn positie – op basis van metingen van zijn magnetische veld buiten het lichaam. **Hoofdstuk 6** toont aan dat door het magnetische veld te interpreteren dat wordt geproduceerd door een draaiende magnetisch dipool met loodrechte magnetisatie- en rotatieassen, de 3D-positie en rotatieas kunnen worden gereconstrueerd ten opzichte van slechts één veldsensor. Als verlengstuk wordt aangetoond dat deze informatie kan worden gebruikt om gerichte veldgeneratie voor MCR-actuatie te ondersteunen.

Deel IV formuleert algemene conclusies en bespreekt richtingen en overwegingen voor toekomstig onderzoek in de context van magnetische continuumrobots.

English Summary

Medical continuum robots, such as actuable guidewires, catheters, and endoscopes, are flexible structures. They became omnipresent in numerous diagnostic and therapeutic applications since the advent of minimally invasive procedures. Traditionally, these devices are steered manually by a clinician considering, as well as through the internal transmission of mechanical forces.

The past few decades introduced research on magnetically actuated continuum robots. Compared to other methods of actuation–mechanical, fluidic–magnetics offer a distinct advantage. Forces and torques can be directly applied to the magnetic tip of a continuum robot via an external magnetic field. This is particularly advantageous for steering the tip of long, slender devices.

Although research on magnetic actuation focused on guiding endovascular wires and navigating pulmonary or gastrointestinal endoscopes, its practical clinical implementation has seen limited success. This is hypothetically due to a combination of challenges, related to costs, the physical footprint of magnetic robotic infrastructure, reliance on complementary medical systems (particularly imaging technologies), or functional overlap with simpler, more user-friendly alternatives.

This dissertation aims to expand the functionality and practicality of magnetic continuum robots (MCRs). **Part I** focuses on modeling and control of MCRs. In **Chapter 2**, additional actuation points—magnetically responsive body segments—are introduced to MCRs, extending beyond the traditional non-magnetic wires or tubes equipped with a permanent magnet at the distal tip. A quasi-static continuum mechanics model is developed to simulate the deformation of MCRs under applied magnetic fields. The model informs the closed-loop multi-point orientation control of an MCR's actuation points. This allows shape deforming MCRs to function as small-scale continuum robotic arms for medical applications.

As an extension of shape deformation, **Chapter 3** addresses the safe guidance of hazardous surgical tools using MCRs. By using smart materials with variable stiffness, a selectively shape-locking MCR is developed, allowing its shape to be dynamically configured using magnetic fields. The continuum mechanics model is expanded to account for variable stiffness and pre-curvature, and applied to open-loop, model-based magnetic configuration of the MCR's shape. This approach is used to demonstrate the guidance of a (biopsy) needle to various targets within a three-dimensional (3D) robotic workspace.

Part II introduces new designs for MCRs in the context of internal magnetic interactions, and model-based design optimization. Stepping away from traditional designs comprising extruded 2D shapes, such as cylinders or beams, **Chapter 4** explores a 3D design specific for MCRs that is intended to beneficially utilize inherent local magnetic interactions between body segments. A helical design of a magnetic soft polymer is proposed whose inherent magnetic forces between helical windings is purposed to improve the structural bending flexibility. The design is optimized as to improve steerability by external magnetic fields for endovascular navigation.

Chapter 5 presents an alternative to externally actuated MCRs by integrating them with local field sources. Here, models of the local magnetic field are used to compute nonuniform magnetization profiles for the MCRs, enabling task-specific–pulling or gripping–motion of its body. Additionally, we demonstrate attaching these machines onto another continuum device as functional components. This progress on magnetic soft machines could inspire new surgical continuum robots with localized magnetic soft machines for, e.g., targeted drug delivery.

Part III shifts research from functionality towards practicality of MCRs in the context of magnetic incorporeal (in the body) localization. Compared to conventional image-based localization, unique to MCRs is the possibility for magnetic localization–reconstructing pose information based on extracorporeal measurements of its magnetic field. **Chapter 6** demonstrates that by interpreting the magnetic field produced by a rotating magnetic dipole with perpendicular magnetization and rotation axes, its 3D position and rotation axis can be reconstructed relative to just one field sensor. It is

shown that this information can be used to inform targeted field generation for MCR actuation.

Part IV draws overall conclusions and considers directions and considerations for future works in the context of magnetic continuum robots.

Contents

1

Introduction

This dissertation comprises a collection of peer-reviewed research articles that explore the design, fabrication, control, modeling, and localization of small-scale (electro)magnetic robots for minimally invasive surgery. It begins with a brief introduction to the origins of magnetism in medicine, the early use of magnets in surgical applications, the evolution of modern magneto-surgical systems, and the current research challenges in the field.

1.1 Origin of magnetism in medicine

The discovery of applications of magnetism in medicine has occurred synchronously with major scientific breakthroughs in human history that span millennia. Synchronous with written and archeological evidence of iron smelting in Anatolia (modern-Turkey) around 1200 B.C., the first effects of magnetism were reported [1]. Smelted iron was observed to attract to naturally occurring iron oxide magnetized by lightning strikes, found in ancient Greece, Egypt, China, and Mesoamerica [2]. These naturally occuring magnets came to be known as lodestone or magnetite, whose name as the story goes originates from a Greek shepherd (Magnes) who found that iron nails in his shoes stuck to the ore, or from the Greek county of Magnesia where magnetite was found [3].

During the centuries that followed up until the end of the middle ages, fantastical medical properties were assigned to magnets, among which: curing arthritis and gout, drawing poison from wounds, or curing baldness when a

Figure 1.1: (Left) The Hirschberger electromagnet, ca 1883, attached to a chemical battery; used to remove metallic objects from the eye [6]. (Right) Dr. Otto Haab and his large electromagnet activated with a foot pedal. Published in Scientific American, ca 1911 [7].

magnet was worn or placed in the mouth [4]. In parallel, in 1289 A.D., the first treatise on magnetized needles was published that documented magnetic properties how they are still taught in schools today: magnetic forces act at a distance on magnetic materials, equal poles repel, opposite poles attract [5].

Rudimentary attraction between magnets (or magnets and magnetic materials) was coined to remove (pull) foreign metallic objects from the body. These objects could be lodged iron arrow tips, swallowed needles, or iron particles embedded in the eye (a consequence of lack of safety glasses during the industrial revolution) [8]. These magnets were, as we call them now, permanent magnets, but would be considered weak magnets by today's standards. Therefore, these magnets had to be of considerable size to have a meaningful effect.

In the nineteenth century, the discovery of electromagnetism [9] and the invention of the electromagnet [10], led to the first medical electromagnets for ophthalmic use, see Fig. 1.1 [6], [11]. Also during this period, discovery of the law of electrostatics (force between stationary electrically charged particles) [12], the force between current-carrying wires [13], the conceptualization of "*lines of force*" (now known as magnetic field lines) [14], the principle of inexistence of magnetic monopoles [15], and the discovery of linearity between created magnetic field strength and electric current [16], ultimately led to the summary of all preceding work and synthesis of four fundamental differential equations today known as Maxwell's equations that unified electricity and magnetism [17]. These equations still form the foundation of magnetic actuation methods used in modern magnetic surgical robots [18]

1.2 Advent of magnetic surgical robotics

In 1962, the development of superconducting electromagnets [25] led to an upgrade of previous (resistive) electromagnets [23] and magnetic resonance imaging systems [26], significantly increasing the reachable field strength. Almost synchronously, new permanent magnets were discovered made of somarium-cobalt (SmCo) [27] and, later, neodymium-iron-boron (NdFeB) [20], that provided up to fifty times more resistance to demagnetization compared to previously standard aluminium-nickel-cobalt magnets, and which were up to six times more powerful in terms of magnetic strength (Fig. 1.2A). These powerful permanent magnets became part of the first millimeter-sized magnetically guided devices for vascular exploration and treatment, by integration with existing tools (wires or tubes) and guidance with electromagnets around 1970 (Fig. 1.2B) [19], [24], [28].

Superconducting electromagnets became part of the first magnetic manipulation system, proposed for neurosurgical stereotaxis (Fig. 1.2C-D) [29]. This system was shortly thereafter used in one of the first papers that investigated computer controlled model-based control of a magnetic seed in 1996 [30], tested in an animal study for catheter manipulation in 2000 [31], and tested for endocardial mapping and radiofrequency ablation in 2002 [32]. Nevertheless, practical limitations were apparent: a small workspace and a large system, expensive liquid-helium-based cryogenic cooling, and difficult integration with medical imaging systems [33].

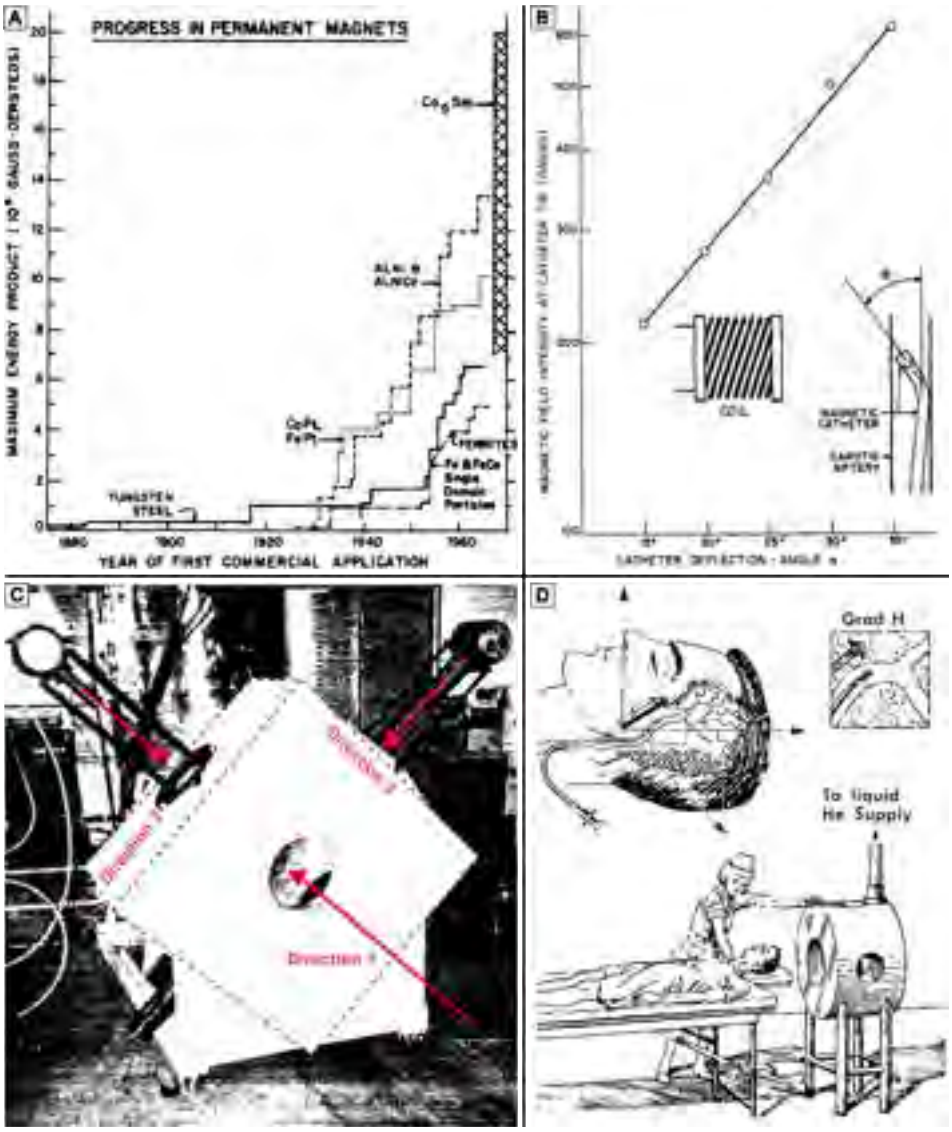

Figure 1.2: (**A**) Progress in strength of permanent magnets [19]. Current-day magnets are even stronger [20]. (**B**) These strong magnets were attached to wires and tubes to make the first magnetic robots steerable by an external electromagnet coil, ca. 1969 [21]. (**C**) One of the first prototype multiple-superconducting coils magnetic manipulation systems for neurosurgical stereotaxis (mass: 1300 kg), ca. 1992 [22]. (**D**) Concept of magnetic neurosurgical stereotaxis; a field gradient–grad H–pulls a wire through cerebral vasculature, ca. 1969 [23], [24].

Continued development on magnetic manipulation moved away from superconducting coils towards permanent magnets, and from neurosurgical stereotaxis to cardiac ablation [34]–[37]. By that time, the company that developed the system, founded in 1990, chose to keep its original name: *Stereotaxis Inc.* The company went public in 2004 and can still be found on the New York Stock Exchange today.

1.3 Research continues

The stage was set for a surge in research activity on magnetic surgical robots: physical principles underlying magnetic manipulation were well understood, strong (electro)magnets were commercially available, advances in computing power and simulation software allowed for more detailed models and increasing control frequency, and a clinic-ready system had been developed that could serve as a comparative 'gold standard'.

Research institutions started in-house development of magnetic manipulation systems comprising electromagnets, permanent magnets, or a combination thereof [38]–[40]. Some attempts were made to also valorize these early systems, that were intended to steer magnet-tipped conventional medical instruments [41], [42]; these efforts were discontinued at the pre-commercialization stage [43]. Nevertheless, some of these machines were predecessors of improved systems that are now implemented or investigated for clinical use (Fig. 1.3) [44]–[46].

Availability of research oriented magnetic manipulation systems enabled further investigation related to design, fabrication, modeling, and control of a range of magnetically responsive robots. Furthermore, 3D tracking and shape reconstruction of magnetic robots was further investigated by integrating manipulation systems with medical imaging technology, or developing novel sensorized robots, to achieve new closed-loop position and orientation control of magnetic robots. Among these robots were traditional elongate devices (wires, tubes, endoscopes), but also novel micro-sized mechanisms such as soft flagellar robots.

The field of soft robotics (the term "soft" applies to the body of the robot,

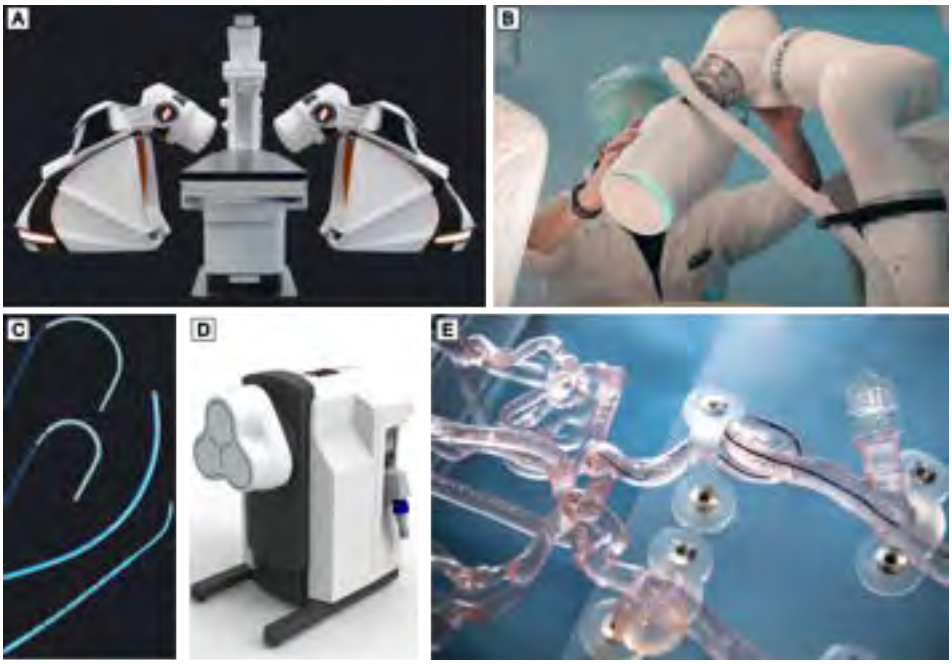

Figure 1.3: Examples of magnetic manipulation infrastructure in the commercialization stage. (**A**) Stereotaxis GenesisX magnetic navigation system based on a pair of large permanent magnets to the side of a patient bed [47]. (**B**) Flux One magnetic navigation system based on an electromagnet-mounted robot arm [48]. (**C**) Stereotaxis Map-iT magnetic catheters for cardiac ablation [49]. (**D**) MagnebotiX Navion magnetic navigation system based on a triangular arrangement of three electromagnets [50]. (**E**) Nanoflex Robotics magnetic guidewire for endovascular interventions [51].

being made of compliant polymers such as silicone) gained a surge in popularity around 2015 [52]. In parallel, researchers started experimenting with mixing powdered NdFeB and polymers to create "shape-programmable magnetic soft matter", which introduced a new design parameter: magnetization profile [53], [54]. Magnetic soft robots could now be made with simple two-dimensional (2D) geometry, but with elaborate 3D nonuniform magnetization (or polarity). These robots could exhibit complex motion in an applied magnetic field [55]. Also, magnetic powder-doped polymers became compliant alternatives to rigid magnets [56], with additional possibilities to be injection molded or 3D-printed into intricate shapes.

At this point it may be apparent that the design space of magnetic manipulation systems and magnetically responsive robots is large and continuously expanding. These systems and robots all differ in shape, material, motion, magnetic properties, or intended application. Therefore, properly defining what a robot is (and is not) is important.

1.4 Nomenclature

In this subsection, naming conventions are given to describe different types of magnetic surgical robots. The presented naming conventions consider mechanical and magnetic properties. This list is not exhaustive, but gives a foundation on categorizing different types of robots relevant to this dissertation:

- **Robot** – A mechanical body that performs a (pre-)programmed task by converting supplied energy into motion.
- **Magnetic Robot** – A robot that converts magnetic potential energy into motion.

Here, it may be relevant to briefly elaborate on the concept of magnetic potential energy and the workings of a magnetic robot. Such a robot carries a magnet, which can be described in terms of its strength/magnetic moment ($\boldsymbol{m}$) and position ($\boldsymbol{p}$). When inside a magnetic field ($\boldsymbol{b}(\boldsymbol{p})$), the magnet has a magnetic potential energy ($U = -\boldsymbol{m} \cdot \boldsymbol{b}(\boldsymbol{p})$). This magnet experiences a torque ($\boldsymbol{\tau} = \boldsymbol{m} \times \boldsymbol{b}(\boldsymbol{p})$) in the direction that minimizes U. Also, the magnet experiences a force ($\boldsymbol{f} = -\nabla U$), where ∇ is the gradi-

ent operator. Therefore, a magnetic dipole has some potential energy in a magnetic field, and experiences a torque and force. This combination of torque and force on a body is also called a wrench. A magnetically-induced wrench can be used to induce motion of a mechanical body to perform a task: a magnetic robot.

Although multiple types of magnetism exist, common to magnetic surgical robots are electromagnets [57] and ferromagnets [58]. The latter can be categorized as hard/permanent or soft magnets. These types differ in terms of resistance to demagnetization. Hard magnets retain magnetic polarity (south-north) even upon removal of an applied magnetic field; soft magnets lose their magnetic polarity.

- **Hard Magnetic Robot** – A magnetic robot carrying hard/permanent magnets that experience a wrench in a magnetic field.
- **Soft Magnetic Robot** – A magnetic robot carrying soft magnets that magnetizes and experience a wrench in a magnetic field.
- **Electromagnetic Robot** – A magnetic robot with electrically conductive components that generates a magnetic moment upon electrical activation, and experiences a wrench in a magnetic field.

Additional to magnetic properties of robots, are structural properties. These properties often determine the functionality, performance, and application of robots. This may be used to denote different types robots made of soft or rigid materials, or that move via bending or joints.

- **Soft Robot** – A robot made of soft materials (silicones, rubbers, polymers). For surgical robots, "soft" may be unofficially interpreted as materials with elastic modulus less than 100 MPa.
- **Articulated Robot** – A robot made of a series of rigid links connected and moved by rotary joints. Also called "serial robot" or "rigid-link robot".
- **Continuum Robot** – A robot made of a continuous, flexible body that moves by bending, stretching, and twisting.

Combining the nomenclatures for robot structure and magnetization leads

to descriptions of types of magnetic robots.

- **Hard Magnetic Soft Continuum Robot** – A continuum robot made of soft materials with embedded hard magnetic particles.

Finally, magnetic robots move in response to an applied magnetic field. A common approach to steering magnetic robots is via manipulating the magnetic fields they are exposed to. These fields are generated by field sources–permanent magnets, electromagnets–which are collected to form systems responsible for manipulating magnetic fields required for actuation of magnetic robots.

- **Magnetic Manipulation System** – A collection of magnetic field sources capable of manipulating a magnetic field inside its workspace.
- **Magnetic Actuation** – The process of actuating/steering a magnetic robot by manipulating the applied magnetic field.

As noted previously, this non-exhaustive nomenclature represents general guidelines for naming of magnetic surgical robotic infrastructure of certain type. As an extension, combinations of robot types are possible. For example, a continuum robot may be part soft and part rigid, and have magnetic particles embedded continuously throughout its body or have hard magnets at discrete locations. Furthermore, the nomenclature could be extended with information on shape (helical), motion (rolling), or fabrication (printing). Sometimes synonymous words are used, such as "continuum manipulator" instead of "continuum robot". Also, names of tools may be used instead, such as "magnetic guidewire" or "magnetic catheter", which are also (usually) continuum robots.

1.5 Challenges and research questions

This dissertation considers the class of ***hard magnetic continuum robots***. Although seemingly specific, this category holds a considerable design space for robots: soft/rigid/hybrid, shape/geometry, magnets or embedded particles, uniform or nonuniform magnetic polarity, or stationary or dynamic magnetic moment.

Magnetic continuum robots are part of a long history in progress of continuum robots, from rigid to flexible structures, from metallic to soft bodies, and from passive to active (magnetic) materials [59]. Despite the rapid developments in the past two decades, much research is still being done on further advancing magnetic continuum robots regarding modeling and control, design, and localization methods [60].

1.5.1 Modeling and control

Mathematical models of magnetic continuum robots can simulate their deformation in response to applied magnetic fields [61]. Unique to these robots is that deformation in nonuniform magnetic fields changes their magnetic potential energy. As a result, their deformation response is highly nonlinear with respect to the magnetic fields generated by manipulation systems.

To steer magnetic continuum robots, representative (quasi-)static or dynamic models are integrated with control algorithms that also account for the manipulation system's field generation. These algorithms generally involve locally linearizing the robots' deformation response to the reconfiguration of the manipulation system and its associated field.

This model-based control approach has used to show position control of magnet-tipped devices using models with varying levels of abstraction [62], [63].However, these examples are limited to a single actuation point (the tip magnet), limiting the robots to simple first-order shapes (e.g., J-shaped configurations). This restricts the robots' reachable workspace, especially when compared to articulated robots with multiple joints and degrees of freedom. By incorporating additional magnets along the length of a continuum robot, it becomes possible to achieve more complex, higher-order shapes (e.g., S-shaped configurations).

Achieving higher-order shapes of continuum robots within a manipulation system's workspace presents several challenges. First, the magnetic continuum robot is intrinsically coupled to the manipulation system through the generated magnetic field. Adjusting the manipulation system reconfigures the field throughout the workspace, altering the magnetic potential energy at every actuation point along the robot. Second, geometrically

precise models have high computational cost, with further increases as the continuum robot's structure becomes more complex. Third, manipulation systems and magnetic continuum robots vary in design, requiring a control method that is adaptable to different implementations of magnetic surgical robotic infrastructure.

These challenges form the basis of the first research question (RQ):

RQ.1

How to model multi-magnet continuum robots, as well as formulate a general control method for achieving higher-order shapes of these robots in the workspace of manipulation systems?

The shape of a magnetic continuum robot is such that its magnetic and elastic potential energy are in equilibrium. However, when these robots are used for coaxial/nested guidance of surgical tools, the combined structure's elasticity changes. Consequently, maintaining the desired shape of the nested robot and tool requires an adjustment in the generated magnetic potential energy.

Therefore, models of continuum robots must be extended to account for elasticity of guided tools. Although possible from a modeling perspective [64], a major physical drawback is applying the necessary field for the required magnetic potential energy.

A potential solutions is the use of smart materials such as temperature-controlled variable stiffness polymers. These polymers shift transition between low- and high-stiffness states. This property has been used to dynamically reinforce a robot's rigidity, resisting deformation during tool guidance and preventing the need for stronger magnetic fields [65]–[67].

Nevertheless, extending mathematical models of magnetic continuum robots with shape-locking capability and nested tools, as well as integration in a algorithm for magnetic- and temperature-controlled shape configuration for tool guidance, is an unexplored topic. Therefore, the second RQ is:

RQ.2

How to extend geometrically exact models of magnetic continuum robots to include variable stiffness and guidance of nested tools, as well as formulate a control method for tool guidance?

1.5.2 Magnetic design

Generally, magnetic continuum robots have shapes that can be described as extruded 2D shapes such as cylinders and beams [60]. For these robots, the primary magnetic interaction occurs between the robot body and the applied magnetic field [68].

Rare examples exist where the passive field generated by the robot's body is used to apply a wrench onto itself [69]. Here, two magnetic spheres were interconnected by flexible rod. It was reported that the dipole-dipole interactions between the spheres produced a restoring torque that opposed bending in an applied magnetic field when the spheres were positioned too close to each other. Although this principle of "local magnetic interactions" was observed, it was neither quantified nor investigated.

It appears that to date, the underlying principles governing local magnetic interactions are unexplored. Therefore, the question remains if modified designs of magnetic continuum robots can somehow beneficially utilize local magnetic interactions. Accordingly, the third RQ is:

RQ.3

How can magnetic continuum robots be designed to beneficially utilize local dipole interactions?

Regardless of design, magnetic continuum robots have traditionally been actuated by magnetic fields generated through magnetic manipulation systems. These systems comprise field sources positioned at a distance from a robot. At a distance, they generally produce uniform fields with constant direction and strength across the robot [40]. This simplifies the design of a robot's magnetization profile, as their deformation is governed solely by

an alignment of its magnetization vectors with the applied field [70].

An extension to physically detached continuum robots and electromagnetic field sources, are those that are physically attached [71]. Here, the nonuniform field from electromagnets exert both torque and force on the robot. These forces have been used to induce simple linear push/pull motion on robots with unidirectional magnetization [72]. This interaction between physically attached field sources and continuum robots could be called an "active local magnetic interaction".

Achieving more complex shape deformation of continuum robots by active magnetic interactions would require more sophisticated magnetization profiles. Considering a field of constant shape, the magnetization profile is the governing factor that determines the magnetic potential energy of the robot in the field. This phenomenon has not yet been explored, and results in the fourth RQ is:

RQ.4

How to shape magnetization profiles of continuum robots to achieve pre-programmed shape deformation in locally generated nonuniform fields?

1.5.3 Intracorporeal localization

Despite the design possibilities for manipulation systems and continuum robots, examples of magnetically-assisted surgery are rare in clinical practice, limited to the Stereotaxis system [73]. One reason, and a key challenge, is the need for intracorporeal localization of manipulators–finding the position and orientation of a manipulator in the body–necessary for targeted generation of actuation fields. One investigated solution is to integrate manipulation systems with medical imaging systems. However, this approach creates a direct functional dependency and requires communication between both systems. This can be challenging, especially when the systems are produced by different manufacturers. Another solution is sensorization (optical, strain) of devices for shape reconstruction, which complicates their design by requiring additional integrated hardware [74].

A new approach to pose reconstruction involve magnetic localization methods, which rely on detecting magnetic fields to reconstruct the relative pose of the field source. One method uses the static field generated by stationary permanent magnets within the body, but its accuracy is affected by Earth's static background field [75]. Another method uses field sensors embedded in continuum robots to measure dynamic fields produced by manipulation systems [76]. While this approach allows for filtering of Earth's field, it requires additional electronic hardware within the robot, which limits its potential for miniaturization.

In both approaches, as well as in the previously presented research questions, continuum robots are assumed to generate static magnetic fields. A novel approach to overcome the aforementioned limitations could involve designing continuum robots capable of generating dynamic fields. This would facilitate intracorporeal localization through external sensing, and leads to the formulation of the fifth and final RQ:

RQ.5

How to achieve intracorporeal localization of magnetic continuum robots by interpreting their inherent field externally?

1.6 Thesis Outline

Each research question (RQ) corresponds to a chapter in this dissertation. Each chapter represents a scientific publication/manuscript in a peer-reviewed journal. The chapters are divided among three parts, (I) modeling and control, (II) design, and (III) localization.

In **Part I**, the geometrically exact Cosserat rod theory–a continuum mechanics representation of one-dimensional slender structures–is used to formulate quasi-static models of magnetic continuum robots, applied in nonlinear control algorithms. **Chapter 2** (RQ.1) extends Cosserat rod models with distributed magnetically responsive components, enabling the modeling of magnetic continuum robots carrying multiple magnets. Also, this chapter introduces a multipole expansion model to simulate magnetic fields and create a virtual representation of a magnetic manipulation system.

These models are integrated into a closed-loop control algorithm with stereo vision-based feedback, demonstrating iterative reconfiguration of the manipulation system to shape the field and achieve independent orientation control of the robot's distributed magnets. **Chapter 3** (RQ.2) further advances the Cosserat rod model to include nested guidance of other continuum devices and variable stiffness shape-locking capability. Modeling of nested guidance is inspired from concentric tube robots, while shape-locking is achieved by introducing variable (pre-)curvature vectors within the model.

In **Part II**, the Cosserat rod model for magnetic continuum robots and the multipole expansion model for magnetic field sources are applied to the design of robots with a focus on local magnetic interactions. **Chapter 4** (RQ.3) introduces a novel geometric design of soft/rigid hybrid continuum robots, modeling dipole-dipole torques and forces to quantify the effects of passive local magnetic interactions on its mechanical response to external fields. **Chapter 5** (RQ.4) investigates shaping magnetization profiles for soft continuum robots in nonuniform fields generated by surface-attached electromagnetic sources. Multipole expansion models simulate these fields to optimize magnetization vectors and generate torques and forces in desired directions of motion.

In **Part III**, clinical considerations for magnetic continuum robots are addressed. **Chapter 6** (RQ.5) investigates intracorporeal localization by interpreting the robot's magnetic field. We show that this approach enables configuring magnetic manipulation systems for actuation, reducing previous reliance on medical imaging for 3D localization.

Concluding, **Part IV** presents the main findings of the doctoral research and offers insights for future studies.

1.7 Scientific Output

All the research studies that constitute this doctoral thesis have been supported by the funds from the European Research Council (ERC) under the European Union's Horizon 2020 Research and Innovation Programme (Grant agreement #866494–Project MAESTRO).

All the studies presented in this thesis have been performed with the experimental setups at the ***Surgical Robotics Laboratory (SRL)***, in the Department of Biomechanical Engineering of the University of Twente, Enschede, the Netherlands.

1.7.1 International peer-reviewed journal articles

The studies and chapters presented in this doctoral thesis have been a part of the following articles that have been published or are under review in the following international peer-reviewed journals:

- **M. Richter**, V. K. Venkiteswaran, and S. Misra, "Multi-point orientation control of discretely-magnetized continuum manipulators," *IEEE Robotics and Automation Letters*, vol. 6, no. 2, pp. 3607–3614, 2021.

- **M. Richter**, M. Kaya, J. Sikorski, L. Abelmann, V. K. Venkiteswaran, and S. Misra, "Magnetic soft helical manipulators with local dipole interactions for flexibility and forces," *Soft Robotics*, vol. 10, no. 3, pp. 647–659, 2023.

- **M. Richter**, J. Sikorski, P. Makushko, Y. Zabila, V. K. Venkiteswaran, D. Makarov, and S. Misra, "Locally addressable energy efficient actuation of magnetic soft actuator array systems," *Advanced Science*, vol. 10, no. 24, pp. 2302077, 2023.

- **M. Richter**, V. K. Venkiteswaran, and S. Misra, "Concentric tube-inspired magnetic reconfiguration of variable stiffness catheters for needle guidance," *IEEE Robotics and Automation Letters*, vol. 8, no. 10, pp. 6555–6562, 2023.

- **M. Richter**, L. Masjosthusmann, P. Makushko, V. K. Venkiteswaran, D. Makarov, and S. Misra, "Magnetic localization and manipulation of locking synchronous motors," *Communications Engineering*, 2025. [Submitted, under review]

1.7.2 Co-authored peer-reviewed journal articles

- J. J. Huaroto, **M. Richter**, M. Malafaia, J. Kim, C.-S. Kim, J.-O. Park, J. Sikorski, and S. Misra, "Magneed–needle-shaped electromagnets for localized actuation within compact workspaces," *IEEE Robotics and Automation Letters*, vol. 8, no. 6, pp. 3908–3915, 2023.

- L. Masjosthusmann, **M. Richter**, P. Makushko, D. Makarov, and S. Misra, "Miniaturized variable stiffness gripper locally actuated by magnetic fields," *Advanced Intelligent Systems*, vol. 6, no. 9, pp. 2400037, 2024.

- F. De Tommasi, **M. Richter**, L. D'Alvia, M. Carassiti, E. Palermo, Z. Del Prete, E. Schena, S. Misra, and V. K. Venkiteswaran, "Multi-sensing system based on fiber bragg grating technology in variable stiffness catheter for temperature and force measurements," *2024 IEEE International Symposium on Medical Measurements and Applications (MeMeA)*, 2024.

1.7.3 International peer-reviewed conferences

- **M. Richter**, V. K. Venkiteswaran, and S. Misra, "Multi-point orientation control of discretely-magnetized continuum manipulators," *2021 IEEE International Conference on Robotics and Automation (ICRA)*, 2021. [Finalist for best conference paper award on Mechanisms and Design]

1.7.4 Invited journal articles

- **M. Richter**, V. K. Venkiteswaran, J.-P. de Vries, and S. Misra, "APOLLO: advanced magnetic probes for minimally invasive endovascular interventions," *European Heart Journal*, vol. 45, no. 29, pp. 2589–2591, 2024.

I

Shaping Fields, Bending Robots

Preface

Magnetic continuum manipulators deform through direct application of forces and torques (wrench) by external magnetic fields, rather than internal propagation of wrenches in fluidic or mechanical designs. This property has made magnetic manipulation a prominent choice for actuating the distal end of elongate devices like wires and tubes in cardiovascular interventions. However, their control is complex, requiring an understanding of how reconfiguring a magnetic manipulation system ***shapes*** the field and its spatial derivatives, which determine the applied wrench on a magnet, that in turn ***bends*** the elastic body of the continuum manipulator. This calls for accurate models of the manipulation system and continuum manipulator, and integration thereof to a control algorithm.

Chapter 2 introduces the first iteration of a multipole expansion model, which accurately describes the magnetic field and its spatial derivatives for both electromagnetic and permanent magnetic sources. This field model is used to construct a virtual representation of a physical magnetic manipulation system. The chapter also explores the implementation of a continuum mechanics-based rod model for predicting the deformation of continuum manipulators containing multiple permanent magnets. These models are integrated into a closed-loop control algorithm, utilizing shape feedback from a stereo vision setup. The chapter ends with an experimental demonstration of independent orientation control of two magnets integrated in a continuum robot, within the workspace of the manipulation system.

Chapter 3 extends the rod model to multiple concentric continuum devices. Furthermore, the passive elastic body of the continuum manipulator is replaced with an active variable stiffness polymer that enables locking its shape post-deformation. The chapter explores model-based magnetic reconfiguration of a shape-locking guiding catheter designed for safe endovascular needle guidance. This chapter also introduces a new concept of modeling a magnetic guiding catheter and needle as a concentric-tube robot pair, as well as model-based magnetically-assisted shape configuration of variable stiffness catheters using external magnetic fields.

2

Multi-point Orientation Control of Discretely-Magnetized Continuum Manipulators

Note: *The following chapter is adapted from the article "Multi-point orientation control of discretely-magnetized continuum manipulators" by* ***M.Richter****, V. Kalpathy Venkiteswaran, and S. Misra, published in "IEEE Robotics and Automation Letters", vol. 6, pp. 3607-3614, April 2021. The chapter has been reformatted in terms of figures and tables to fit this doctoral thesis. No changes to the technical contents of this peer-reviewed manuscript have been made.*

Authors' Contributions: *MR and VKV conceived the project and managed the research. MR fabricated the magnetic continuum manipulator, formulated the control algorithm, and implemented models of the manipulator and manipulation system. MR compiled figures and videos with support by VKV and SM. Finally, MR and VKV wrote the manuscript with contributions from SM. VKV and SM supervised this project.*

Funding Information: *This work is supported by the European Research Council (ERC) under the European Union's Horizon 2020 Research and Innovation programme under Grant 866494 project – MAESTRO.*

Abstract

In the past decade, remote actuation through magnetic fields has been used for position and orientation control of continuum manipulators (CMs) with a single magnet at the distal tip. By leveraging multiple points of actuation along the length of the CM it is possible to achieve increasingly complex shapes, which could be of interest in complex navigation tasks, for example, in minimally invasive surgery. In this study we present an approach for multi-point orientation control of discretely magnetized CMs. The approach is demonstrated with a manipulator that contains two permanent magnets, which are each actuated inside a non-homogeneous magnetic field. We formulate an accurate field model that conforms to Maxwell's equations and apply this to the available actuation system. Furthermore, Cosserat rod theory is used to model the manipulator deformation under external wrenches, and is utilized to numerically compute a Jacobian necessary to calculate the actuation inputs. During experiments, a stereo vision setup is used for manipulator shape feedback. Target orientations are manually provided as input to show independent orientation control of the two permanent magnets. Additionally, simulations with an extended virtual clone of the electromagnetic system are performed to show the capability of achieving more complex manipulator shapes. In both scenarios, it is observed that the algorithm is able to independently control the orientation of two interconnected magnets in a non-uniform magnetic field.

2.1 Introduction

Continuum manipulators (CMs) are continuously deformable elastic structures. Compared to traditional rigid link robots, CMs have infinite degrees of freedom (DOFs) which allows them to deform at any point along their length. This property makes CMs dexterous, enabling them to navigate through constricted spaces and cluttered environments [59]. The challenge lies in steering and navigation of CMs, as actuation at multiple points along the CM also requires actuators at those points. However, actuators attached to the body of the CM increase its size, which is disadvantageous in confined workspaces [77]. Magnetic actuation provides the potential for miniaturization by moving the actuation system outside the confined environment [78].

Magnetized CMs can be discretely or continuously magnetized. Discretely magnetized CMs contain rigid magnetic, and flexible non-magnetic material. The rigid magnetic material can be divided into actively magnetized electromagnets[79], or permanent magnets [80]. Alternatively, continuously magnetized CMs consist of magnetic composite polymers [56]. These can be used to fabricate specialized magnetization profiles for target applications [54], [81]. The magnetized CMs deform due to a magnetic wrench, exerted on their magnetic regions by a magnetic field. A theoretical minimum of seven magnetic degrees of freedom is required for wrench control. However, these systems may suffer from magnet orientation-dependent singularities. By instead providing eight magnetic degrees of freedom such singularities are avoided [82].

In literature, different configurations of magnetic actuation systems have been designed based on application requirements. Such systems employ stationary electromagnets [38], [83], mobile electromagnets [62], [84], or mobile permanent magnets [80], as sources of the magnetic field. The mobile actuation systems have the advantage of an open and typically larger workspace than stationary systems, while requiring smaller external magnets [85]. Precise magnetic field information from each field source is required for actuation. Previously used approaches model the magnetic field either using an arbitrary function and fit unknown coefficients with least squares optimization [84], [86], or use a first-order dipole approximation [80]. The former approach does not typically enforce constraints on the spatial gradients of the magnetic field, and the latter ignores higher order field effects that are more prominent closer to the field source [87]. A recently used approach, that solves the aforementioned disadvantages, is to express the magnetic field as the gradient of a scalar potential (scalar harmonic function), and use measurement-informed least squares optimization to fit unknown coefficients [88].

A mathematical model of the manipulator is used to compute its deformation under exerted magnetic torques and forces, which result from the interaction with an external magnetic field. These models generally have a trade-off between accuracy and computational efficiency [77], [89]. In our work, Cosserat rod theory is used to model the CM. Cosserat rod theory gives an exact solution to the statics of the CM, while additionally

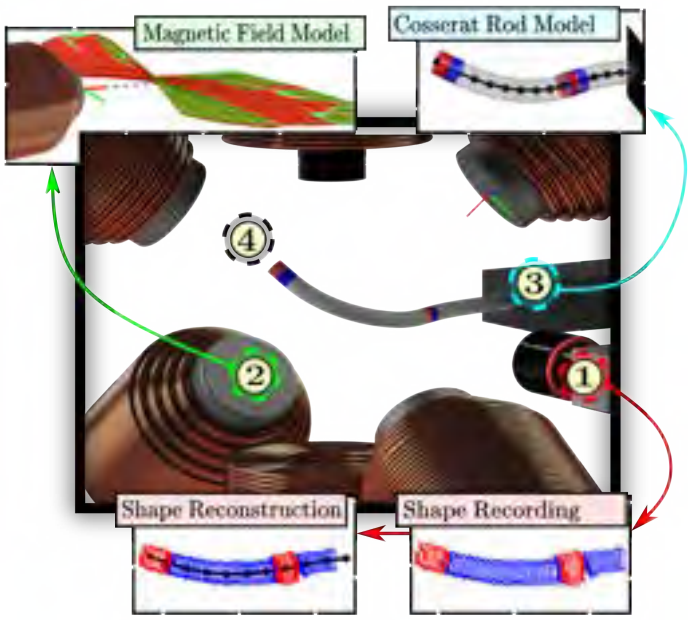

Figure 2.1: In this study we use BigMag, an array of 6 mobile electromagnetic coils [84], to perform closed-loop orientation control of two permanent magnets carried by a continuum manipulator (CM). ① Shape reconstruction of the CM is performed with a stereo vision setup. ② A model of the magnetic field then predicts exerted magnetic wrenches on the CM. ③ With Cosserat rod theory a quasi-static forward model of the CM is produced. ④ This model is used to predict changes in magnet orientations, due to changes in the currents and positions of the electromagnets, in order to actuate the CM.

accommodating variations in the stiffness, body loading, and cross-section geometry of a CM [63], [90].

Rigid-link and Cosserat rod models have recently been used for position control of a CM with a single magnet at its distal tip [63], [91]. In addition, unidirectional steering within a uniform magnetic field has been shown with permanent magnets integrated into the distal tip of a CM [42], [92]. Through the actuation of a CM at the distal tip, it is only possible to achieve first-order shapes of the CM body. By introducing multiple actuation points (magnets) along the length of the manipulator, it is possible

to achieve higher order shapes, which is of interest in complex navigation tasks during minimally invasive surgery. Compared to existing works, the effect of magnetic forces (field gradients) cannot be neglected when multiple independently controlled magnets are in close proximity. It should be noted that manipulating the field at one magnet inherently changes the field at other magnets carried by the CM. Furthermore, actuation of one magnet inherently actuates the magnets in close proximity. The control algorithm should therefore be able to predict and compensate for this interdependence.

In this study we show closed-loop orientation control of two magnets along a discretely magnetized CM (Fig. 2.1). The magnet orientations are independently controlled by exerting necessary magnetic torques and forces through manipulating the external non-homogeneous magnetic field generated by BigMag, an array of six mobile electromagnetic coils [84]. We formulate a magnetic field model that conforms to Maxwell's equations to accurately predict magnetically exerted wrenches on the CM. A stereo vision setup records the actuation workspace and is used for shape reconstruction of the CM. Cosserat rod theory is applied to construct a forward model of the CM to predict changes in the CM shape due to variations in the external magnetic field. In addition, BigMag is extended with eight additional electromagnets in simulation to improve achievable fields at the workspace edge to show that the control algorithm is able to achieve complex geometries of the CM. All the above-mentioned steps are detailed in the following sections, followed by discussion and conclusions.

2.2 Theory

In this section, the model used for analysis of the continuum manipulator is described, followed by the formulation of a Cartesian multipole expansion of a scalar potential for accurate, measurement-informed fitting of a magnetic field and magnetic field gradient map.

2.2.1 Cosserat rod model

Consider a CM attached proximally to a rigid base and free-floating at the distal tip (Fig. 2.2). The CM carries two permanent magnets: one at an

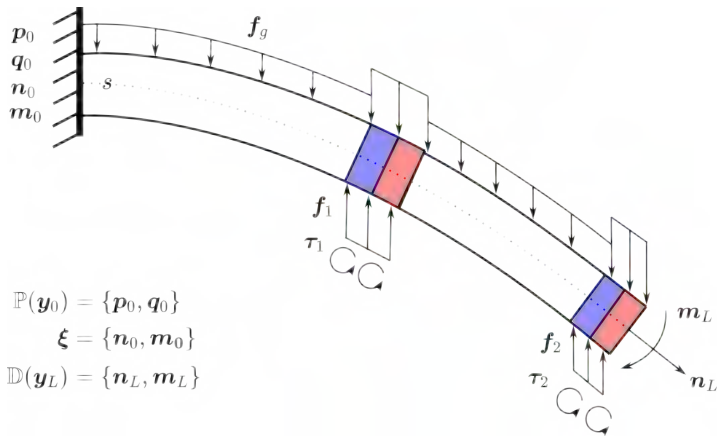

Figure 2.2: Proximally fixed, and distally free-floating, discretely magnetized continuum manipulator (CM), characterized by a centerline parameter ($s \in [0, L]$), subject to distributed magnetic forces ($\boldsymbol{f}_m(s)$) and torques ($\boldsymbol{\tau}_m(s)$, $m = 1, 2$), and gravitational forces ($\boldsymbol{f}_g(s)$). Material cross-sections along s are characterized by a position ($\boldsymbol{p}(s)$), orientation quaternion ($\boldsymbol{q}(s)$), internal force ($\boldsymbol{n}(s)$), and internal moment ($\boldsymbol{m}(s)$); collected in state parameter vector ($\boldsymbol{y}(s)$). Known proximal and distal boundary conditions are denoted as $\mathbb{P}(\boldsymbol{y}_0)$ and $\mathbb{D}(\boldsymbol{y}_L)$, respectively. Unknown proximal states are collected in an optimization vector ($\boldsymbol{\xi}$).

intermediate position along the body and one at the distal tip. The magnets experience a magnetic force and torque within an external magnetic field, causing the CM to deform. Gravity also acts on the CM. To control the shape of a magnetized CM, we need to predict the (change in) shape of the CM when loaded by magnetic forces and torques. For this we use a Cosserat rod model of the CM.

In Cosserat rod theory the body of the manipulator is characterized by centerline parameter $s \in [0, L]$, where $L \in \mathbb{R}^+$ represents the manipulator length. In addition, a set of material state parameters $\boldsymbol{y}(s)$, relative to a global reference frame, are assigned to cross-sections along the centerline of the manipulator,

$$\boldsymbol{y}(s) = \begin{bmatrix} \boldsymbol{p}(s)^T & \boldsymbol{q}(s)^T & \boldsymbol{n}(s)^T & \boldsymbol{m}(s)^T \end{bmatrix}^T \in \mathbb{R}^{13}, \tag{2.1}$$

where $\boldsymbol{p} \in \mathbb{R}^3$ denotes the Cartesian position, $\boldsymbol{q} = (q_r, \boldsymbol{q}_i) \in \mathbb{H}$ the orientation quaternion (where $q_r \in \mathbb{R}$ and $\boldsymbol{q}_i \in \mathbb{R}^3$ are the real and imaginary

components, respectively [93]), $\boldsymbol{n} \in \mathbb{R}^3$ the internal force, and $\boldsymbol{m} \in \mathbb{R}^3$ the internal bending moment [94].

The state parameters evolve along s according to the Cosserat rod ordinary differential equations (ODEs):

$$\begin{aligned} \boldsymbol{p}' &= \boldsymbol{R}(\boldsymbol{q})\boldsymbol{v}, & \boldsymbol{v} &= \boldsymbol{K}_s^{-1}\boldsymbol{R}(\boldsymbol{q})^T\boldsymbol{n} + \hat{\boldsymbol{v}} \\ \boldsymbol{q}' &= \frac{1}{2}\begin{bmatrix} -\boldsymbol{q}_i^T \\ q_r\boldsymbol{I}_3 - [\boldsymbol{q}_i]_\times \end{bmatrix}\boldsymbol{R}(\boldsymbol{q})\boldsymbol{u}, & \boldsymbol{u} &= \boldsymbol{K}_b^{-1}\boldsymbol{R}(\boldsymbol{q})^T\boldsymbol{m} + \hat{\boldsymbol{u}} \\ \boldsymbol{n}' &= -\boldsymbol{f} \\ \boldsymbol{m}' &= -\boldsymbol{p}' \times \boldsymbol{n} - \boldsymbol{\tau}, \end{aligned} \tag{2.2}$$

where the explicit dependence on s is omitted for brevity, $\boldsymbol{I}_3 \in \mathbb{R}^{3\times3}$ is an identity matrix, and $[\cdot]_\times : \mathbb{R}^3 \to \mathbb{R}^{3\times3}$ represents a mapping to a skew-symmetric matrix [63]. We use the notation $\partial_s\boldsymbol{p} \equiv \boldsymbol{p}'$ to denote the partial derivative of the state parameter with respect to s. In addition, $\boldsymbol{R}(\boldsymbol{q}) \in \mathrm{SO}(3)$ is given by

$$\boldsymbol{R}(\boldsymbol{q}) = q_r^2\boldsymbol{I}_3 + \boldsymbol{q}_i\boldsymbol{q}_i{}^T + 2q_r[\boldsymbol{q}_i]_\times + [\boldsymbol{q}_i]_\times^2. \tag{2.3}$$

The set of thirteen coupled nonlinear ODEs in (2.2) relate external forces $\boldsymbol{f}(s) \in \mathbb{R}^3$ and torques $\boldsymbol{\tau}(s) \in \mathbb{R}^3$ to changes in internal forces and moments. The internal forces and torques determine the material strain $\boldsymbol{v}(s) \in \mathbb{R}^3$ and bending $\boldsymbol{u}(s) \in \mathbb{R}^3$, which determine the pose of the material frame[94]. The values of $\hat{\boldsymbol{v}}$ and $\hat{\boldsymbol{u}}$ represent the intrinsic material strain and curvature of the CM in its undeformed reference state, taken as $\hat{\boldsymbol{v}} = [0, 0, 1]^T$ and $\hat{\boldsymbol{u}} = [0, 0, 0]^T$, and $\boldsymbol{K}_s, \boldsymbol{K}_b \in \mathbb{R}^{3\times3}$ are diagonal shear/extension and bending/torsion stiffness matrices, respectively [90].

Figure 2.2 shows a discretely magnetized continuum manipulator, consisting of alternating flexible non-magnetic, and rigid magnetic, material attached proximally, at $\boldsymbol{y}_0 \equiv \boldsymbol{y}(s = 0)$, to a rigid base. The manipulator body is subject to a distributed gravitational force $\boldsymbol{f}_g \in \mathbb{R}^3$, and the magnets experience a distributed wrench $\boldsymbol{w}_m = [\boldsymbol{f}_m^T, \boldsymbol{\tau}_m^T]^T$ when placed in a magnetic field, where m represents the magnet index.

The manipulator statics is solved as a boundary value problem (BVP), which contains information about the shape of the CM. Let $\mathbb{P}(\boldsymbol{y}_0)$ be the set of constant proximal boundary conditions and $\mathbb{D}(\boldsymbol{y}_L)$ the set of constant distal boundary conditions, which, assuming no load on the distal tip, are given by

$$\begin{aligned} \mathbb{P}(\boldsymbol{y}_0) &= \begin{bmatrix} \boldsymbol{p}_0^T & \boldsymbol{q}_0^T \end{bmatrix}^T \in \mathbb{R}^7, \\ \mathbb{D}(\boldsymbol{y}_L) &= \begin{bmatrix} \boldsymbol{n}_L^T & \boldsymbol{m}_L^T \end{bmatrix}^T = \begin{bmatrix} \boldsymbol{0}^T & \boldsymbol{0}^T \end{bmatrix}^T \in \mathbb{R}^6. \end{aligned} \tag{2.4}$$

Then, a vector of unknown proximal state parameters is defined ($\boldsymbol{\xi} = [\boldsymbol{n}_0^T, \boldsymbol{m}_0^T]^T \in \mathbb{R}^6$) and optimized to satisfy the distal boundary condition $\mathbb{D}(\boldsymbol{y}_L)$. We solve the BVP with forward integration using an explicit Runge-Kutta fourth order method, and convex optimization with Levenberg-Marquardt [95]. This approach requires discretization of the manipulator centerline.

To fully capture the material transition between flexible and rigid material during forward integration, it is necessary to separately discretize each occurring flexible and rigid section into $N_f \in \mathbb{N}$ and $N_r \in \mathbb{N}$ subsections. Given $M \in \mathbb{N}$ recurring sections, there will exist $N = M\,(N_f + N_r) + 1$ material points along s (Fig. 2.2). Forward integration from $\boldsymbol{y}_0$ then gives material state parameters of the CM (2.1) at each discretized point along the manipulator centerline–the shape solution:

$$\boldsymbol{Y}(\boldsymbol{\xi}) = \begin{bmatrix} \boldsymbol{y}_0 & \boldsymbol{y}_1 & \dots & \boldsymbol{y}_N \end{bmatrix} \in \mathbb{R}^{13\times N}, \tag{2.5}$$

The distal boundary condition and shape solution are compared to formulate a residual vector ($\boldsymbol{r} = \mathbb{D}(\boldsymbol{y}_L) - \mathbb{D}(\boldsymbol{y}_N)$). A shape solution $\boldsymbol{Y}(\boldsymbol{\xi})$ is accepted if $\boldsymbol{r}(\boldsymbol{\xi})$ is below an arbitrarily chosen error threshold. Otherwise, $\boldsymbol{\xi}$ is updated with Levenberg-Marquardt.

2.2.2 Magnetic field map

The magnetic wrench experienced by the CM (Fig. 2.2) depends on the external magnetic field generated by the magnetic actuation system. Accurate estimation of magnetic forces and torques follows from the quality of

the model that describes the actuation magnetic field. Each actuator magnet represents a source of a magnetic field ($\boldsymbol{B}(\boldsymbol{p}, I) \in \mathbb{R}^3$) with associated spatial field gradients ($\boldsymbol{B}_\nabla(\boldsymbol{p}, I) \in \mathbb{R}^{3\times3}$), where $I \in \mathbb{R}$ denotes the current through an electromagnet. For electromagnets operating outside their saturation region, i.e. where their generated field is linear with current, a unit-current field ($\boldsymbol{\beta}(\boldsymbol{p}) \in \mathbb{R}^3$) and gradient ($\boldsymbol{\beta}_\nabla(\boldsymbol{p}) \in \mathbb{R}^{3\times3}$) model can be formulated and used to linearly describe the field at different operating currents. In the paragraphs below we present a model for the magnetic field that conforms to Maxwell's equations and that can be applied to individual azimuthally symmetric field sources (e.g. solenoids).

In a current-free workspace, the field is both divergence- and curl-free, which allows expressing the field as the gradient of a scalar potential,

$$\boldsymbol{B}(\boldsymbol{p}, I) = \nabla\Psi(\boldsymbol{p}) \cdot I, \tag{2.6}$$

where $\Psi(\boldsymbol{p})$ is a nonlinear scalar function in the position vector $\boldsymbol{p}$ [18]. Consider an orthonormal body coordinate frame attached to the face of an azimuthally symmetric electromagnet, where $\hat{\boldsymbol{x}}$ is the zenith direction of the electromagnet. Then it can be shown that it is possible to describe the generated magnetic field with a scalar potential given by

$$\Psi(\boldsymbol{p}) = \sum_{k=1}^{P} \Psi_k(\boldsymbol{p}) \cdot a_k, \qquad \Psi_k(\boldsymbol{p}) = \frac{\partial^k}{\partial x^k}\left(\frac{1}{\|\boldsymbol{p}\|}\right), \tag{2.7}$$

where $k > 0$ to exclude the monopole term, $P \in \mathbb{N}$ denotes the number of poles in the multipole expansion, and a_k are unknown coefficients. The derivation of Eqn. 2.7 has been omitted for brevity.

The unknown coefficients (a_k) are obtained by measurement-informed linear least squares. The measurement setup, measurement equipment specifications, and measurements are described in, and taken from, [84]. Measurements ($\boldsymbol{B}(\boldsymbol{p}_{ij}, I_f)$) were performed at locations ($\boldsymbol{p}_{ij} = [x_i, y_j, 0]^T$) in a grid in front of the electromagnet, where $i = 1, 2, \ldots, m$ and $j = 1, 2, \ldots, n$, at a fitting current ($I_f = 4A$). The scalar coefficients (a_k) are subsequently

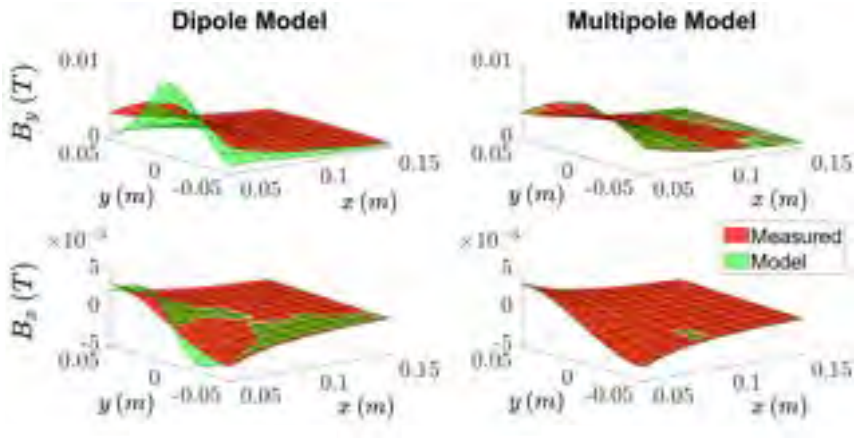

Figure 2.3: Surface plots of the x- and y-components of the magnetic field (B_x and B_y) obtained from measurements (red) and model (green) of the magnetic fields on a grid in the xy-plane in front of of an air-cored electromagnet of BigMag, comparing a least-squares fit of the point dipole model (left column, $P = 1$) to our multipole field model (right column, $P = 6$).

computed from

$$\begin{bmatrix} \nabla\Psi_1(\boldsymbol{p}_{11}) & \dots & \nabla\Psi_P(\boldsymbol{p}_{11}) \\ & \vdots & \\ \nabla\Psi_1(\boldsymbol{p}_{mn}) & \dots & \nabla\Psi_P(\boldsymbol{p}_{mn}) \end{bmatrix}^{\dagger} \begin{bmatrix} \boldsymbol{B}(\boldsymbol{p}_{11}, I_f) \\ \vdots \\ \boldsymbol{B}(\boldsymbol{p}_{mn}, I_f) \end{bmatrix} = \begin{bmatrix} a_1 \\ \vdots \\ a_P \end{bmatrix}, \tag{2.8}$$

where $[\cdot]^{\dagger}$ denotes the Moore-Penrose pseudoinverse. The unit-current field and gradient map are thereafter given by

$$\boldsymbol{\beta}(\boldsymbol{p}) = \frac{\nabla\Psi(\boldsymbol{p})}{I_f}, \quad \boldsymbol{\beta}_{\nabla}(\boldsymbol{p}) = \begin{bmatrix} \frac{\partial\boldsymbol{\beta}(\boldsymbol{p})}{\partial x} & \frac{\partial\boldsymbol{\beta}(\boldsymbol{p})}{\partial y} & \frac{\partial\boldsymbol{\beta}(\boldsymbol{p})}{\partial z} \end{bmatrix}. \tag{2.9}$$

The above described fitting procedure is applied to the six mobile electromagnets inside BigMag (the actuation system utilized in this paper) such that the magnetic field within the workspace can be accurately computed given the electromagnet currents and positions.

A visual comparison between a linear least squares (LLSQ) fit of a point dipole model and the multipole model, for an air-cored electromagnet of BigMag, is given in Fig. 2.3. The norm of the root-mean-square error for the dipole fit is 1.18 mT, and for the multipole model 0.16 mT, for measurements with a resolution of 0.1 mT.

2.2.3 Orientation control

In this section we present the control scheme used for multi-point orientation control of a discretely magnetized continuum manipulator. Consider the experimental setup represented by Fig. 2.1. The CM is suspended horizontally within the workspace, visualized using a stereo vision setup [91], and actuated with a magnetic field generated by $N_I \in \mathbb{R}^+$ electromagnets with currents $\left(\boldsymbol{I} \in \mathbb{R}^{N_I}\right)$ and $N_\theta \in \mathbb{R}^+$ pose parameters $\left(\boldsymbol{\theta} \in \mathbb{R}^{N_\theta}\right)$ [84]. First we measure the CM magnet poses with stereo vision. Second, the measured poses and actuation parameters $\{\boldsymbol{I}, \boldsymbol{\theta}\}$ are used to compute magnetic wrenches acting on the CM. Third, an orientation Jacobian is computed that maps incremental changes in $\{\boldsymbol{I}, \boldsymbol{\theta}\}$ to changes in CM magnet orientations. Finally, the CM magnets are steered towards a desired orientation by updating the actuation parameters $\{\boldsymbol{I}, \boldsymbol{\theta}\}$.

The control scheme (Fig. 2.4) is divided into four blocks (A-D), which are discussed in the subsections below. Axis-angle and quaternion representations for CM magnet orientations are used interchangeably.

2.2.4 Magnet pose sensing

The stereo vision setup and shape reconstruction algorithm records the CM as a 3D point cloud and fits a 3D polynomial ($\boldsymbol{P}(s)$) from the CM proximal base to the distal tip [91]. From $\boldsymbol{P}(s)$ we obtain measured magnet positions $\left(\boldsymbol{p}_m \in \mathbb{R}^3\right)$ and orientations ($\boldsymbol{q}_m \in \mathbb{H}$), with knowledge of the magnet centerline positions ($s_m \in [0, L]$), as follows

$$\begin{aligned} &\boldsymbol{p}_m = \boldsymbol{P}(s_m), \qquad && \boldsymbol{p}'_m = \left(\boldsymbol{P}(s_m + \delta s) - \boldsymbol{P}(s_m)\right)/\delta s, \\ &\begin{matrix} \phi_m = \cos^{-1}\left(\hat{\boldsymbol{z}} \cdot \hat{\boldsymbol{p}}'_m\right) \\ \boldsymbol{k}_m = \widehat{[\hat{\boldsymbol{z}} \times \hat{\boldsymbol{p}}'_m]} \end{matrix}, && \Rightarrow \boldsymbol{q}_m = \begin{bmatrix} \cos\left(\frac{\phi_m}{2}\right) \\ \boldsymbol{k}_m \sin\left(\frac{\phi_m}{2}\right) \end{bmatrix}, \end{aligned} \tag{2.10}$$

where $\hat{\boldsymbol{z}}$ is the unit global vertical axis superimposed on the magnet center of mass used as a reference for the CM magnet angle of rotation ($\phi_m \in \mathbb{R}$) and axis of rotation $\left(\boldsymbol{k}_m \in \mathbb{R}^3\right)$, and $\boldsymbol{p}'_m$ is the axial direction of the CM at magnet m. The inherent sign ambiguity of the axis-angle representation is solved by choosing the $\boldsymbol{k}_m$ of least angular distance from an arbitrary desired axis of rotation $\left(\boldsymbol{k}^d_m\right)$. The magnetic dipole moments $\left(\boldsymbol{\mu}_m \in \mathbb{R}^3\right)$ are known relative to, and therefore found from, $\boldsymbol{q}_m$.

2.2.5 Magnetic wrench

The magnetic wrench $\left(\boldsymbol{w}_m \in \mathbb{R}^6\right)$ exerted on $M \in \mathbb{N}$ CM magnets $(m = 1, \ldots, M)$ is computed from knowledge of the actuation parameters $\{\boldsymbol{I}, \boldsymbol{\theta}\}$ and magnet poses $\{\boldsymbol{p}_m, \boldsymbol{q}_m\}$. We compute a current-to-wrench map $(\boldsymbol{T})$, which is composed of a current-to-field map $\left(\boldsymbol{T}_\beta(\boldsymbol{p}_m, \boldsymbol{\theta}) : \mathbb{R}^{N_I} \to \mathbb{R}^{8M}\right)$ and field-to-wrench map $\left(\boldsymbol{T}_\mu(\boldsymbol{q}_m) : \mathbb{R}^{8M} \to \mathbb{R}^{6M}\right)$, defined at the center of mass of the magnets.

To compute $\boldsymbol{T}_\beta(\boldsymbol{p}_m, \boldsymbol{\theta})$, we first map the unit-current field map of each electromagnet (section 2.2.2) to a global representation. Let $\{\mathcal{G}\}$ and $\{\mathcal{C}_j\}$ represent the global reference frame and body frame of an electromagnetic coil $(j = 1, \ldots, N_I)$, such that

$$\begin{aligned} {}^{\mathcal{G}}_{\mathcal{C}_j}\boldsymbol{\beta}(\boldsymbol{p}_m, \boldsymbol{\theta}) &= {}^{\mathcal{G}}_{\mathcal{C}_j}R(\boldsymbol{\theta})\,{}^{\mathcal{C}_j}\boldsymbol{\beta}\left({}^{\mathcal{C}_j}\boldsymbol{p}_m\right), \\ {}^{\mathcal{G}}_{\mathcal{C}_j}\boldsymbol{\beta}_\nabla(\boldsymbol{p}_m, \boldsymbol{\theta}) &= {}^{\mathcal{G}}_{\mathcal{C}_j}R(\boldsymbol{\theta})\,{}^{\mathcal{C}_j}\boldsymbol{\beta}_\nabla\left({}^{\mathcal{C}_j}\boldsymbol{p}_m\right){}^{\mathcal{G}}_{\mathcal{C}_j}R(\boldsymbol{\theta})^T. \end{aligned} \tag{2.11}$$

In addition, we define a map $\mathbb{G}(\boldsymbol{\beta}_\nabla) : \mathbb{R}^{3\times3} \to \mathbb{R}^5$ that returns a vector of the five linearly independent spatial gradient components of the field [83]. The current-to-field map for a single CM magnet at position $\boldsymbol{p}_m$ is subsequently defined as

$$\boldsymbol{T}_\beta(\boldsymbol{p}_m, \boldsymbol{\theta}) = \begin{bmatrix} {}^{\mathcal{G}}_{\mathcal{C}_1}\boldsymbol{\beta} & \cdots & {}^{\mathcal{G}}_{\mathcal{C}_{N_I}}\boldsymbol{\beta} \\ \mathbb{G}\left({}^{\mathcal{G}}_{\mathcal{C}_1}\boldsymbol{\beta}_\nabla\right) & \cdots & \mathbb{G}\left({}^{\mathcal{G}}_{\mathcal{C}_{N_I}}\boldsymbol{\beta}_\nabla\right) \end{bmatrix}. \tag{2.12}$$

To compute $\boldsymbol{T}_\mu(\boldsymbol{q}_m)$, first consider the expression for the magnetic wrench

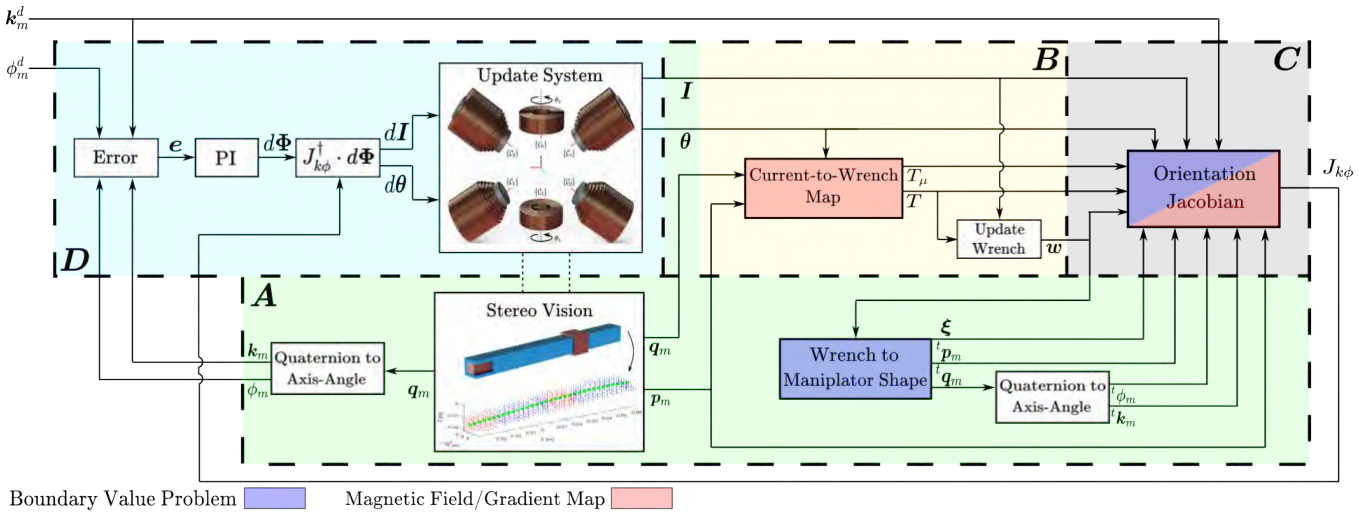

Figure 2.4: Orientation control diagram. ($\boldsymbol{A}$) A stereo vision setup records a 3D point cloud of the continuum manipulator (CM) that holds information about the measured magnet poses $\{\boldsymbol{p}_m, \boldsymbol{q}_m\}$. Knowledge of the magnetic wrench ($\boldsymbol{w}$) acting on the magnets is used to solve the CM statics (shape) with a Cosserat rod model, which holds information about theoretical magnet poses $\{{}^t\boldsymbol{p}_m, {}^t\boldsymbol{q}_m\}$. ($\boldsymbol{B}$) Measured magnet poses and electromagnet currents and positions $\{\boldsymbol{I}, \boldsymbol{\theta}\}$ of the system are used to compute the magnetic wrench. ($\boldsymbol{C}$) An orientation Jacobian ($\boldsymbol{J}_{k\phi}$) is computed (algorithm 1) that maps incremental changes in $\{\boldsymbol{I}, \boldsymbol{\theta}\}$ to changes in magnet orientations. ($\boldsymbol{D}$) The orientation Jacobian and error between desired and measured magnet orientation are used to update $\{\boldsymbol{I}, \boldsymbol{\theta}\}$.

($\boldsymbol{w}_m$) on a magnetic dipole within an external magnetic field,

$$\boldsymbol{w}_m = \begin{bmatrix} \boldsymbol{\tau}_m \\ \boldsymbol{f}_m \end{bmatrix} = \begin{bmatrix} \boldsymbol{\mu}_m(\boldsymbol{q}_m) \times \boldsymbol{B}(\boldsymbol{p}_m, \boldsymbol{I}, \boldsymbol{\theta}) \\ \nabla\big(\boldsymbol{\mu}_m(\boldsymbol{q}_m) \cdot \boldsymbol{B}(\boldsymbol{p}_m, \boldsymbol{I}, \boldsymbol{\theta})\big) \end{bmatrix}. \tag{2.13}$$

This expression is written to a matrix-vector multiplication that yields the field-to-wrench map,

$$\boldsymbol{T}_\mu(\boldsymbol{q}_m) = \begin{bmatrix} \big[\boldsymbol{\mu}_m(\boldsymbol{q}_m)\big]_\times & 0 \\ 0 & \mathbb{M}\big(\boldsymbol{\mu}_m(\boldsymbol{q}_m)\big) \end{bmatrix}, \tag{2.14}$$

where $[\cdot]_\times : \mathbb{R}^3 \to \mathbb{R}^{3\times3}$ represents a map to a skew-symmetric matrix, and $\mathbb{M}(\boldsymbol{\mu}) : \mathbb{R}^3 \to \mathbb{R}^{3\times5}$ maps the independent spatial field gradients to forces on the dipole [83],

$$\mathbb{M}(\boldsymbol{\mu}) = \begin{bmatrix} \mu_x & \mu_y & \mu_z & 0 & 0 \\ 0 & \mu_x & 0 & \mu_y & \mu_z \\ -\mu_z & 0 & \mu_x & -\mu_z & \mu_y \end{bmatrix}. \tag{2.15}$$

Then, current-to-field and field-to-wrench maps can be multiplied to map currents ($\boldsymbol{I}$) in the system to magnetic wrenches on the CM magnets,

$$\begin{aligned} \boldsymbol{w}_m &= \boldsymbol{T}_\mu(\boldsymbol{q}_m)\boldsymbol{T}_\beta(\boldsymbol{p}_m, \boldsymbol{\theta})\boldsymbol{I} \\ &= \boldsymbol{T}(\boldsymbol{p}_m, \boldsymbol{q}_m, \boldsymbol{\theta})\boldsymbol{I}. \end{aligned} \tag{2.16}$$

Finally, for M CM magnets ($m = 1, \ldots, M$), we then obtain a vector of wrenches $\big(\boldsymbol{w} = [\boldsymbol{w}_1^T, \boldsymbol{w}_2^T, \ldots, \boldsymbol{w}_M^T]^T\big)$. Given the magnetic wrenches on the magnets, we can solve the CM statics as a boundary value problem (BVP) and obtain the theoretical shape (Eqn. 2.5). This shape solution contains the theoretical magnet poses $\{{}^t\boldsymbol{p}_m, {}^t\boldsymbol{q}_m\}$, which are required to compute the orientation Jacobian.

2.2.6 Orientation Jacobian

The orientation Jacobian maps incremental changes in actuation parameters to changes in magnet orientations. Let $N_A = N_I + N_\theta$ represent the number of actuation parameters. Then the orientation Jacobian $\big(\boldsymbol{J}_{k\phi} \in \mathbb{R}^{2M\times N_A}\big)$ is numerically computed by solving N_A BVPs (section 2.2.1), each concerning a virtually incremented actuation parameter, a resulting new virtual

wrench on the CM, and a following virtual manipulator response predicted from the Cosserat rod model. An informed guess for the optimization vector $\left(\boldsymbol{\xi}^i\right)$ is provided before solving each BVP (Fig. 2.2).

Algorithm 1 presents the procedure of computing $\boldsymbol{J}_{k\phi}$, where we simulate open loop control cycles. First, one actuation parameter is incremented and the change in exerted magnetic wrench ($d\boldsymbol{w}$) computed. Third, an informed guess, given by

$$\boldsymbol{\xi}^i\left(\boldsymbol{\xi}, d\boldsymbol{w}, \boldsymbol{p}_m\right) = \boldsymbol{\xi} + \sum_{m=1}^{M} \begin{bmatrix} d\boldsymbol{f}_m \\ d\boldsymbol{\tau}_m + (\boldsymbol{p}_m - \boldsymbol{p}_0) \times d\boldsymbol{f}_m \end{bmatrix}, \tag{2.17}$$

is formulated as an initial solution to the BVP, with $\boldsymbol{p}_0$ the CM base position (Fig. 2.2). The CM statics are subsequently solved as a BVP to obtain the shape solution $\left(\boldsymbol{Y}(\boldsymbol{\xi}^i)\right)$. Fourth, the new theoretical magnet poses $\{{}^t\bar{\boldsymbol{k}}_m, {}^t\bar{\phi}_m\}$ are taken from the shape solution. Finally, the linear approximation of the change in CM magnet orientation due to a change in electromagnet current ($dI_j,\ j = 1, \ldots, N_I$) is defined as

$$\begin{aligned} \frac{d\left(\boldsymbol{k}_m^d \cdot \boldsymbol{k}_m\right)}{dI_j} &= \frac{\boldsymbol{k}_m^d \cdot \left({}^t\bar{\boldsymbol{k}}_m - {}^t\boldsymbol{k}_m\right)}{dI_j}, \\ \frac{d\phi_m}{dI_j} &= \frac{{}^t\bar{\phi}_m - {}^t\phi_m}{dI_j}, \end{aligned} \tag{2.18}$$

and similarly for a change in electromagnet pose ($d\theta_l,\ l = 1, \ldots, N_\theta$); $\boldsymbol{k}_m^d$ denotes the desired axis of rotation of the CM magnet. The steps are repeated for all N_A actuation parameters. The orientation Jacobian is then, for $M = 2$ CM magnets, constructed as

$$\boldsymbol{J}_{k\phi} = \begin{bmatrix} \frac{d\left(\boldsymbol{k}_1^d \cdot \boldsymbol{k}_1\right)}{dI_1} & \cdots & \frac{d\left(\boldsymbol{k}_1^d \cdot \boldsymbol{k}_1\right)}{dI_{N_I}} & \frac{d\left(\boldsymbol{k}_1^d \cdot \boldsymbol{k}_1\right)}{d\theta_1} & \cdots \\ \frac{d\phi_1}{dI_1} & \cdots & \frac{d\phi_1}{dI_{N_I}} & \frac{d\phi_1}{d\theta_1} & \cdots \\ \frac{d\left(\boldsymbol{k}_2^d \cdot \boldsymbol{k}_2\right)}{dI_1} & \cdots & \frac{d\left(\boldsymbol{k}_2^d \cdot \boldsymbol{k}_2\right)}{dI_{N_I}} & \frac{d\left(\boldsymbol{k}_2^d \cdot \boldsymbol{k}_2\right)}{d\theta_1} & \cdots \\ \frac{d\phi_2}{dI_1} & \cdots & \frac{d\phi_2}{dI_{N_I}} & \frac{d\phi_2}{d\theta_1} & \cdots \end{bmatrix}. \tag{2.19}$$

The orientation Jacobian ($\boldsymbol{J}_{k\phi}$) represents a linear map from increments in actuation parameters to changes in magnet orientation, and is used to update the actuation parameters.

Algorithm 1: Computation of the Orientation Jacobian

Input : · Magnet pose info $\boldsymbol{p}_m, {}^t\boldsymbol{p}_m, \{{}^t\boldsymbol{k}_m, {}^t\phi_m\}$
· Cosserat model base state parameters $\boldsymbol{\xi}$
· Current- and Field-to-Wrench maps $\boldsymbol{T}, \boldsymbol{T}_\mu$
· Magnetic wrench $\boldsymbol{w}$
· Actuation parameters $\boldsymbol{I}, \boldsymbol{\theta}$
· Desired magnet axes of rotation $\boldsymbol{k}_m^d$

Output: Orientation Jacobian, $\boldsymbol{J}_{k\phi}$

$dI, d\theta \in \mathbb{R}^+$
/* Current to Orientation Change */
for $j \leftarrow 1$ **to** N_I **do**
  $\boldsymbol{I}_j = \boldsymbol{I}_j + dI$
  $\bar{\boldsymbol{w}} = \boldsymbol{T}\boldsymbol{I}$ // New wrench
  $d\boldsymbol{w} = \bar{\boldsymbol{w}} - \boldsymbol{w}$ // Change in wrench
  Compute informed guess $\boldsymbol{\xi}^i\,(\boldsymbol{\xi}, d\boldsymbol{w}, \boldsymbol{p}_m)$
  Solve manipulator shape $\boldsymbol{Y}(\bar{\boldsymbol{w}}, \boldsymbol{\xi}^i)$ // BVP (2.5)
  Get new magnet poses $\{{}^t\bar{\boldsymbol{p}}_m, {}^t\bar{\boldsymbol{k}}_m, {}^t\bar{\phi}_m\} \leftarrow \boldsymbol{Y}$
  Fill column of $\boldsymbol{J}_{k\phi}$
  $\boldsymbol{I}_j = \boldsymbol{I}_j - dI$
end for
/* Position to Orientation Change */
for $l \leftarrow 1$ **to** N_θ **do**
  $\boldsymbol{\theta}_l = \boldsymbol{\theta}_l + d\theta$
  Recompute $\boldsymbol{T}_\beta(\boldsymbol{p}_m, \boldsymbol{\theta})$ and $\boldsymbol{T} = \boldsymbol{T}_\mu \boldsymbol{T}_\beta$ // (2.12)
  $\bar{\boldsymbol{w}} = T\boldsymbol{I}$ // New wrench
  ⋮
  $\boldsymbol{\theta}_l = \boldsymbol{\theta}_l - d\theta$
end for
return $\boldsymbol{J}_{k\phi}$

2.2.7 Updating actuation parameters

The actuation parameters $\{\boldsymbol{I}, \boldsymbol{\theta}\}$ are updated to decrease the error $(\boldsymbol{e}_m)$ between given desired magnet orientation $\{\boldsymbol{k}_m^d, \phi_m^d\}$ and measured orientation $\{\boldsymbol{k}_m, \phi_m\}$, which is computed as

$$\boldsymbol{e}_m = \begin{bmatrix} 1 - \boldsymbol{k}_m^d \cdot \boldsymbol{k}_m \\ \phi_m^d - \phi_m \end{bmatrix} \Rightarrow \boldsymbol{e} = \begin{bmatrix} \boldsymbol{e}_1 \\ \boldsymbol{e}_2 \end{bmatrix}. \tag{2.20}$$

The error $(\boldsymbol{e})$ is given to a proportional-integral (PI) controller to compute an orientation step $(d\boldsymbol{\Phi})$. Then the actuation parameters are updated according to

$$\begin{bmatrix} d\boldsymbol{I}^T, & d\boldsymbol{\theta}^T \end{bmatrix}^T = \boldsymbol{J}_{k\phi}^{\dagger} \cdot d\boldsymbol{\Phi}. \tag{2.21}$$

The Moore-Penrose pseudoinverse of $\boldsymbol{J}_{k\phi}$ is computed through singular value decomposition as $\boldsymbol{J}_{k\phi}^{\dagger} = VS^{\dagger}U^T$, where S is a diagonal matrix of singular values $(\sigma_i > \sigma_{i+1})$. To improve numerical stability we select singular values according to

$$S_{ii} = \begin{cases} \sigma_i & \text{If } \sigma_1/\sigma_i \leq 10^5 \\ 0 & \text{If } \sigma_1/\sigma_i > 10^5 \end{cases}. \tag{2.22}$$

When an angular error term in $\boldsymbol{e}$ reduces below an arbitrary threshold, its respective integrated term in the PI controller is set to zero. The proportional and integral coefficients of the PI controller are determined through trial and error.

2.3 Experiments and simulation

The experiments and simulations in this section aim to show that it is possible to achieve convergence of multiple magnets to desired orientations by generating a non-homogeneous magnetic field. First, experimental validation of planar steering is described, followed by simulated results of 3D steering. The actuation of the CM, in the experiment and simulation, can be seen in the supplementary video.

2.3.1 Experiment

The experimental setup is represented by Fig. 2.1. The CM consists of subsections of flexible polyurethane rubber (PMC-770, Smooth-On Inc., USA) and rigid neodymium (NdFeB) magnets. Dipole moments ($\boldsymbol{\mu}_m$) and dimensions are shown in Fig. 2.5. The magnetic actuation system, BigMag, consists of six electromagnets oriented towards the center of a spherical workspace of diameter 11 cm (Fig. 2.5, $N_I = 6$, $N_\theta = 2$). The workspace is recorded using two Dalsa Genie Nano RGB cameras (Teledyne Dalsa, Waterloo, ON, Canada). The control system is implemented in C++14 on a computer running a Linux Ubuntu 14.04.01 OS with an Intel Xeon E5 CPU, NVidia Quadro K4200 GPU, and 32 GB RAM [91].

Experiments were performed in 2D where the CM is suspended in plane with the actuator electromagnets $\left(\boldsymbol{k}_m^d = \boldsymbol{k}_m = \hat{\boldsymbol{y}}\right)$. Figure 2.5 provides side views of time-evolved shapes of the CM during the experiment. The measured magnet angles of rotation (AoR, ϕ_m) are defined relative to the global $\hat{\boldsymbol{z}}$ ($t = 320$ s, blue arrow). Steps in desired AoR are provided manually during the experiment, keeping electromagnet currents within the limits of ± 8 A. The AoR are shown against the elapsed time.

The step size in current (dI) and position ($d\theta$) to compute the orientation Jacobian ($\boldsymbol{J}_{k\phi}$) were determined as 0.2 A and 2 °, respectively, based on trial and error. The computation time for $\boldsymbol{J}_{k\phi}$ was 158 ± 64 ms and 165 ± 53 ms with and without the informed guess (Eqn. 2.17), respectively.

2.3.2 Simulation

Fig. 2.6 shows side, top, and isometric views of the CM's shape during simulation with iteration number $\mathrm{i} \in \mathbb{N}$. The magnetic field is generated with a virtual clone of BigMag extended with additional electromagnets ($N_I = 14$, $N_\theta = 2$). A unique non-homogeneous field is generated at the center of mass of each magnet to simultaneously steer the theoretical AoR $\left({}^t\phi_m\right)$ of the magnets to their respective target AoR $\left(\phi_m^d\right)$. In addition, the theoretical axes of rotation $\left({}^t\boldsymbol{k}_m\right)$ of the magnets are steered towards their respective target $\left(\boldsymbol{k}_m^d\right)$ to minimize the angular distance ($\angle$Axis) between them. The computation time required to compute the orientation Jacobian with and without providing an informed guess is 260 ± 41 ms and $420 \pm$

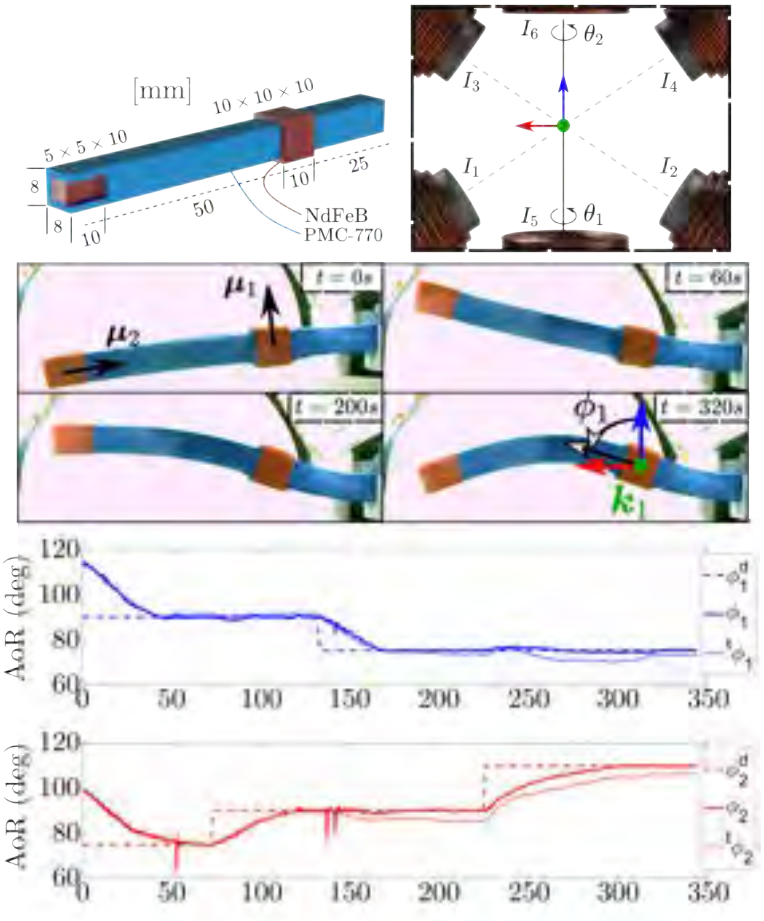

Figure 2.5: Model of the continuum manipulator (CM) consisting of flexible polyurethane rubber (PMC-770) and rigid neodymium magnets (NdFeB), with dimensions given in millimeters. The magnet dipole moments, $\boldsymbol{\mu}_m$, are shown at $t = 0$s. Magnet angles of rotation (AoR) are measured relative to the global $\hat{\boldsymbol{z}}$ axis, superimposed on the magnet center, shown at $t = 320$s. The CM is actuated inside the workspace of BigMag in plane with six electromagnets [84]. Side views of time-evolved shapes of the continuum manipulator are shown and desired, ϕ_m^d, measured ϕ_m, and predicted, ${}^t\phi_m$, AoR are plot for magnet 1 (blue) and 2 (red) in degrees against time t.

16 ms, respectively.

2.4 Discussion

The closed-loop response of the magnet orientations (Fig. 2.5) shows the control algorithm can achieve accurate independent multi-point orientation control in 2D. Compared to other works, the magnetic forces cannot be ignored due to the non-homogeneity of the actuation field and the close proximity of the magnets; Fig. 2.7 shows the deflection of the CM for the experiment in Sec. 2.3.1 calculated with the Cosserat rod model, both with and without magnetic forces. It is noticeable that the calculated shape of the manipulator when the magnetic forces are ignored is significantly different from when they are included. Additionally, it was also necessary to formulate and apply an accurate magnetic field model to the electromagnets in BigMag, and use a Cosserat rod model to simulate movement of the CM in a non-homogeneous magnetic field. The accuracy of the models determine the accuracy of the terms in the orientation Jacobian used for control.

The experiments that showed independent orientation control of two magnets were limited to 2D because of the available actuation DOFs. The minimum bounds on the necessary magnetic DOFs is three per magnet for orientation control, considering magnetic forces negligible. However, because the effect of forces is pronounced for magnets in close proximity, more than three magnetic actuation DOFs per magnet are required. Since the magnetic forces are dependent on five field gradient terms, the maximum additional actuation DOFs per magnet is five. Thus, for singularity-free wrench control a total of eight magnetic DOFs per magnet are required, as proven by Petruska and Nelson [82]. Therefore we limited our experiments to the planar case and performed a 3D simulation with the maximum bound of sixteen DOFs for two magnets. In practice fewer may be required since the solution of the magnetic wrench is not unique. Furthermore, such large multi-coil systems have a limited workspace and are infeasible in practice. These systems are would ideally be replaced by a system with dedicated (electro)magnets for each CM magnet, attached as end-effectors to multi-DOF robot arms [62]. In this case the terms in the orientation Jacobian ($\boldsymbol{J}_{k\phi}$) would be replaced according to the available DOFs: (electro)magnet poses and currents. In addition, with an application-specific

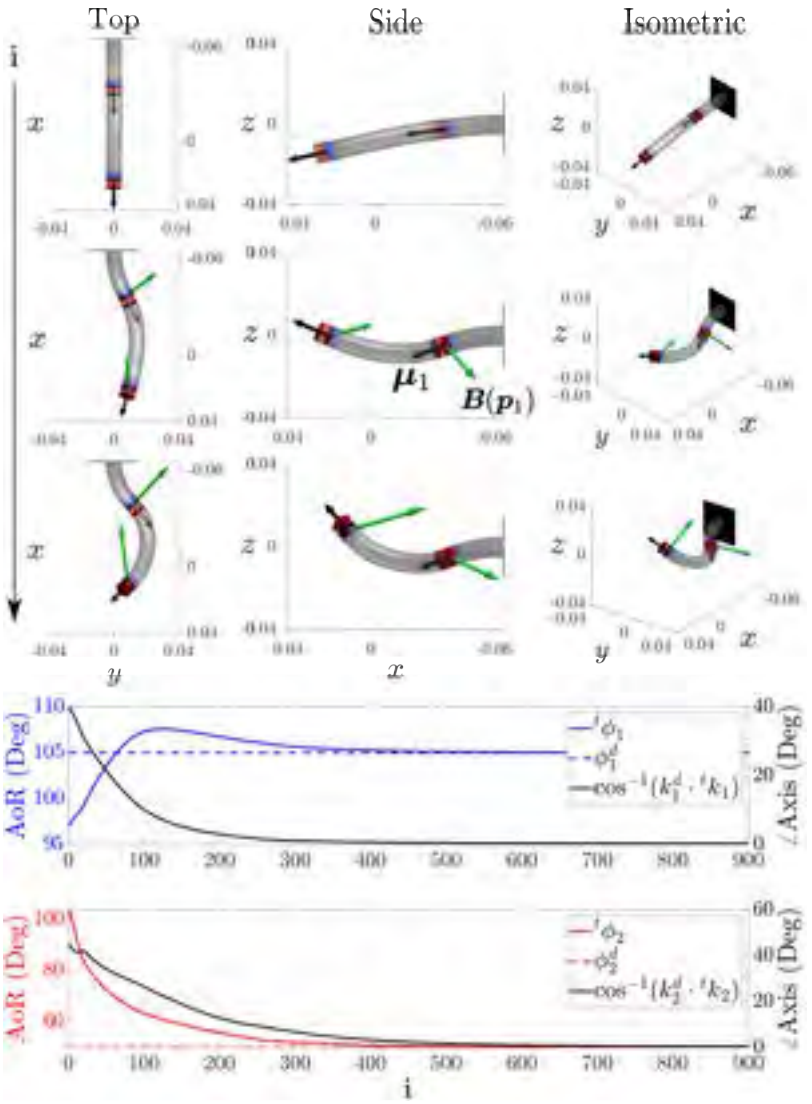

Figure 2.6: Top, side, and isometric views of CM shapes at starting, intermediate, and final iteration numbers (i) with dimensions shown in meters. Trajectories of the theoretical magnet angles of rotation (AoR, ${}^t\phi_m$), for the proximal and distal magnet, are given in blue and red, respectively. Also, the trajectories of the angular distances between the theoretical and desired axes of rotation (∠Axis) are shown.

acutation system, it would be possible to utilize the null-space of $\boldsymbol{J}_{k\phi}$ to accomplish a secondary task, such as increasing the static equilibrium stability of the CM [63].

The time required for CM shape reconstruction and computing $\boldsymbol{J}_{k\phi}$ (approximately the same) limited the achievable control frequency to 2Hz, which is less than desired for closed-loop control. Full shape reconstruction of a CM is in practice infeasible with stereo vision or ultrasound due to time constraints and because torsion cannot be reliably measured. For this reason, other sensing modalities such as fiber Bragg gratings should be considered [96]. Furthermore, the computational efficiency for constructing $\boldsymbol{J}_{k\phi}$ can be significantly improved because the necessary (independent) boundary value problems (BVPs) were solved in series rather than in parallel. With parallel computing the necessary computation time could be reduced to that of a single constituent BVP, which took on average 20ms. With the improved guess (Eqn. 2.17) we did not observe an increase in control frequency during closed-loop experiments, whereas in open-loop simulation the informed guess improved the computation time. This is because both the feedback and the forward model are calculated using the Cosserat rod model. However, when stereo vision is used for closed-loop control, the CM shape feedback diverges from the forward model.

Finally, the formulated magnetic field (gradient) model has shown able to accurately describe the generated magnetic field of an azimuthally symmetric field source. Because the model conforms to Maxwell's equations for fields in a current-free workspace, it can also be applied to accurately estimate the spatial gradients of the field. Compared to previous works, this provides the ability to utilize magnetically exerted forces in addition to torques for closed-loop control of magnetized CMs.

2.5 Conclusions and Future Work

In this paper, an approach for closed-loop multi-point orientation control of discretely magnetized CMs is presented. The effect of magnetic forces must be considered and the novel magnetic field model was able to accurately describe the magnetic field and field gradients required for computing the exerted magnetic torques and forces. In addition, the employed quasi-static

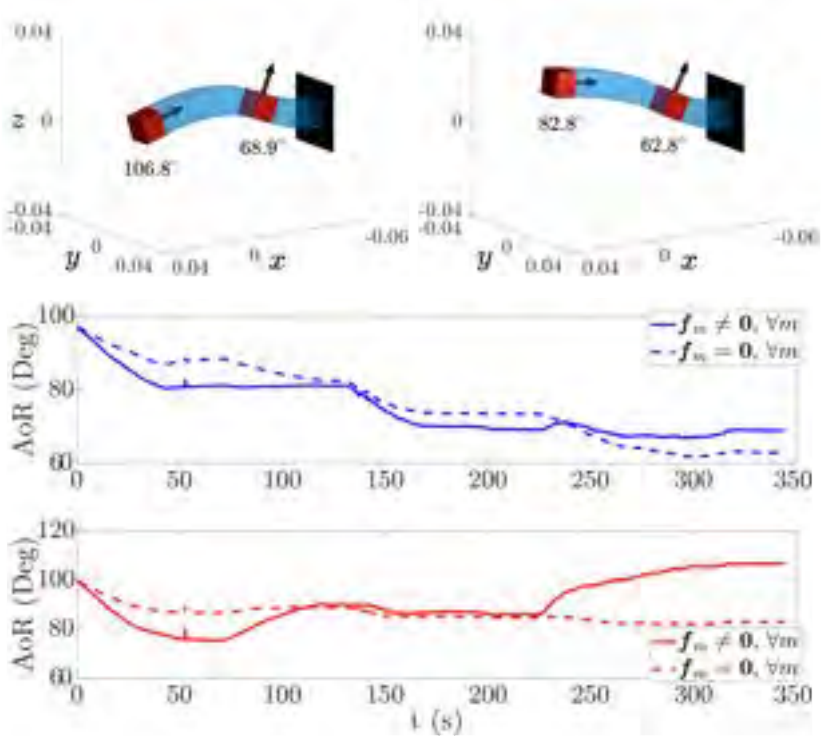

Figure 2.7: A comparison between the theoretical shape of the CM, including and excluding magnetic forces ($\boldsymbol{f}_m$). At the top is the shape of the CM with (left) and without (right) magnetic forces at $t = 320s$ in Fig. 2.5; dimensions are shown in meters. The trajectories of the theoretical angles of rotation (AoR, ${}^t\phi_m$) for the proximal and distal magnet are shown in blue and red, respectively.

Cosserat rod model of the CM was able to predict the magnet orientation changes in a varying non-homogeneous magnetic field. Both the field and Cosserat rod models were applied to construct a numerically-computed orientation Jacobian to linearize changes in actuation parameters to changes in magnet orientations. In the end, the presented control strategy has shown able to achieve accurate independent orientation control of two permanent magnets in 2D inside BigMag, and in 3D simulation using an extended virtual clone of BigMag. However, the computational cost of shape reconstruction and the Jacobian limited the control frequency to 2Hz.

Future work will focus on implementing parallel computing and we hypothesize that this will lead to a significant increase in the achievable control frequency. Futhermore, since the presented magnetic field map is accurate in describing the spatial gradients of the magnetic field, we would like to apply it to magnetic force-based manipulation tasks.

3

Concentric Tube-inspired Magnetic Reconfiguration of Variable Stiffness Catheters for Needle Guidance

Note: *The following chapter is adapted from the article "Concentric tube-inspired magnetic reconfiguration of variable stiffness catheters for needle guidance" by* ***M. Richter****, V. Kalpathy Venkiteswaran, and S. Misra, published in "IEEE Robotics and Automation Letters", vol. 8, pp. 6555-6562, August 2023. The chapter has been reformatted in terms of figures and tables to fit this doctoral thesis. No changes to the technical contents of this peer-reviewed manuscript have been made.*

Authors' Contributions: *MR conceived the project and managed the research. MR fabricated the magnetic continuum manipulator, formulated the control algorithm, and implemented models of the manipulator and manipulation system. MR compiled figures and videos with support by VKV and SM. Finally, MR wrote the manuscript with contributions from VKV and SM. VKV and SM supervised this project.*

Funding Information: *This work was supported by the European Research Council (ERC) under the European Union's Horizon 2020 Research and Innovation programme under Grant 866494 project – MAESTRO.*

Abstract

Guiding catheters assist in delivering hazardous equipment such as needles through non-solid mediums like cavities and vasculature. Traditionally, metallic needles are passed through metallic guiding catheters, which are limited to linear paths or require anatomy-specific designs. Recently, variable stiffness active guiding catheters (AGCs) made of shape memory polymers have been developed. These AGCs can adapt to anatomy and guide equipment in their rubber and glass phases, respectively. However, passing needles can cause deflection of the AGC and misalignment with the target. To address this, magnetic configuration of AGCs based on concentric-tube models is proposed to compensate for needle-induced AGC deflection. Experiments demonstrate shape configuration of AGCs using magnetic fields computed pre-experimentally, followed by needle guidance to three different targets. The results show AGC deflection of up to 69° and needle-induced backward deflection up to 39°, with a maximum target misalignment of 4°.

3.1 Introduction

Guiding catheters provide enclosed pathways for access by surgical instruments to target sites [97]. For example, flexible polymer-based catheters guide balloons and stents for endovascular interventions [98]. Also, rigid metallic catheters guide needles along linear paths [99], whereas nested precurved metallic catheters can guide needles along curved paths [100], [101]. In the latter case, an anatomy-specific design is required to ensure safe extension in the body [102].

Recently, variable stiffness active guiding catheters (AGCs) have been developed that hold potential for enabling configurable curved needle pathways [66], [67]. Specifically, AGCs made from shape memory polymers exhibit a temperature-dependent shift in elastic modulus around a glass-transition temperature, between the rubber (flexible) and glass (stiff) phase of the polymer [103]. Although the elastic modulus of a shape memory polymer ranges between a few MPa to GPa [67], common needle materials such as nitinol or stainless steel have an elastic modulus on the order of tens to hundreds of GPA [104]. Consequently, AGCs and needles may

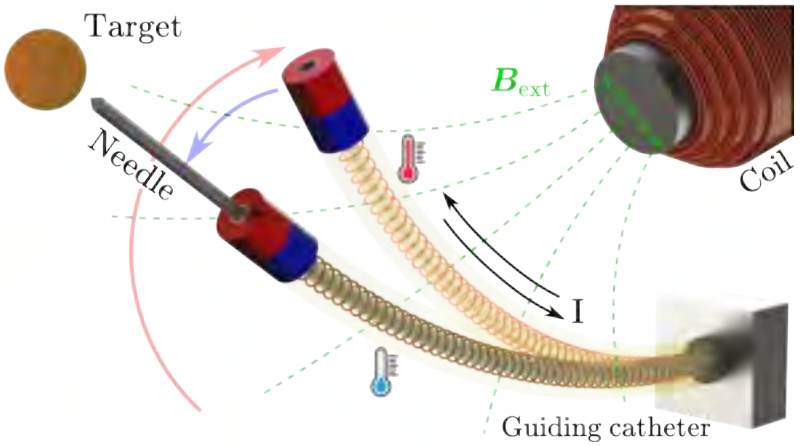

Figure 3.1: An active guiding catheter (AGC) and needle with similar flexur rigidity are arranged concentrically. Initially, the AGC is heated using current (I) to increase flexibility. Then, an external magnetic field ($\boldsymbol{B}_{\text{ext}}$) is used to magnetically deflect the AGC. Next, the AGC is cooled to fix its shape and achieve a new pre-curvature. Finally, the needle is inserted through the AGC, causing the AGC to deform and align with the target.

have a similar bending stiffness and act as a balanced-stiffness concentric-tube robot (CTR) [102].

Balanced-stiffness CTRs are defined as a collection of nested rods with similar bending stiffnesses, different pre-curvatures, and the ability to rotate and translate relative to each other [64]. These CTRs can be modeled with Cosserat rod theory [105], which accommodates variations in pre-curvature, material properties, cross-sectional geometry, and external loading between rods [63], [106]. Within Cosserat rod theory, the shapes of unloaded and loaded rods are described by pre-curvature and curvature vectors, respectively [95].

An AGC has two states: flexible and stiff, associated with the rubber- and glass-phase of the shape memory polymer, respectively. In the rubber phase, the curvature can be easily changed using external actuation [103]. After transitioning to the stiff state, the curvature can be shape-locked to become the glass-phase AGC pre-curvature. Through modeling, the glass-

phase pre-curvature can be configured to compensate for any additional deflection due to a passing needle.

Magnetically-assisted reconfiguration of an AGC removes the need for internal actuation (e.g., tendons), which permits integration of heating and cooling mechanisms [107], [108]. The addition of a magnetic dipole makes the AGC susceptible to deformation by a magnetic wrench, exerted by an external magnetic field [103]. Magnetic fields are generated by either permanent- or electromagnet-based actuation systems, which are able to manipulate the fields to exert prescribed wrenches on dipoles in their actuation workspace [68].

To the authors' knowledge, the use of AGCs for needle guidance, their modeling as balanced-stiffness concentric-tube robots, and their magnetically-assisted reconfiguration in order to compensate for needle-induced backward deflection, shown in Fig. 3.1, have not yet been explored. This study applies a concentric-tube model based on Cosserat rod theory for shape configuration of a shape memory polymer-based AGC, using magnetic fields from an electromagnetic actuation systems. Experiments show that the AGC shape can compensate for needle-induced backward deflections and guide the needle to various targets in the actuation workspace.

3.2 Theory

In this section, a summary of the static modeling theory for Cosserat rods is presented, but comprehensively reported in [95], [109]. This is followed by the application of Cosserat rod theory in modeling concentric-tube robots [110]. Thereafter, computation of curvature vectors of deformed rods is discussed based on arc-parameterization of their centerline curve and Frenet-Serret reference frames.

3.2.1 Cosserat rods

Consider a rod with a known length (l). The rod is characterized by a centerline parameter ($s \in [0, l]$), which defines a set of material states $\{\boldsymbol{p}(s),\ \boldsymbol{q}(s),\ \boldsymbol{n}(s),\ \boldsymbol{m}(s)\}$, where $\boldsymbol{p}(s) \in \mathbb{R}^3$ is the centerline curve, $\boldsymbol{q}(s) \in \mathbb{H}$ an orientation quaternion, $\boldsymbol{n}(s) \in \mathbb{R}^3$ the internal force, and $\boldsymbol{m}(s) \in \mathbb{R}^3$ the

internal moment [90]. Arc-derivatives of the material states ($\{\dot{\boldsymbol{p}}(s), \dot{\boldsymbol{q}}(s), \dot{\boldsymbol{n}}(s), \dot{\boldsymbol{m}}(s)\}$) determine their propagation along s, where $\dot{*}(s) = \partial *(s)/\partial s$.

Arc-derivatives of material states are ordinary differential equations (ODEs) that depend on external distributed forces and moments $\{\boldsymbol{f}(s), \boldsymbol{\tau}(s)\}$ to determine the magnitude of rod deformation [90]. The problem of calculating the deformed rod shape can be formulated as a boundary value problem (BVP) [95]. Generally, the solution process involves discretizing the rod centerline (s) into a discrete number of segments ($D \in \mathbb{Z}^+$) with length $\Delta s := l/D$ [111]. Proximal boundary conditions may include pose, whereas distal boundary conditions include loading. Solving the BVP provides a shape solution,

$$\boldsymbol{Y} = \begin{bmatrix} \boldsymbol{y}(0) & \boldsymbol{y}(\Delta s) & \dots & \boldsymbol{y}(D\Delta s) \end{bmatrix} \in \mathbb{R}^{13\times(D+1)}, \tag{3.1}$$

including material states at discrete points along the centerline, where $\boldsymbol{y}(s) = \langle \boldsymbol{p}(s), \boldsymbol{q}(s), \boldsymbol{n}(s), \boldsymbol{m}(s) \rangle \in \mathbb{R}^{13}$ and $\langle * \rangle$ represents a vectorization operation to a column vector.

3.2.2 Concentric-tube robots

Combining nested rods with different pre-curvatures constitutes a concentric-tube robot (CTR). For ease of representation, consider $i \in \{1, 2\}$ rods ($i = 1$ represents the outer rod) and assume that $l_1 \geq l_2$. The objective is to compute the deformed centerline curve of the outer rod (which is the same as all inner rods). That is, compute $\{\boldsymbol{p}_1(s), \boldsymbol{q}_1(s)\}$, as a result of the passing inner rod ($i = 2$), where $\boldsymbol{q}_i(s) = \langle \mathrm{Re}(q_i), \mathrm{Im}(\boldsymbol{q}_i) \rangle \in \mathbb{H}$ ($\mathrm{Re}(q_i) \in \mathbb{R}, \mathrm{Im}(\boldsymbol{q}_i) \in \mathbb{R}^3$) is an orientation quaternion.

Each (cylindrical) rod in a CTR has an elastic modulus (E_i), shear modulus (G_i), second moment of area ($I_i = I_{x,i} = I_{y,i}$), polar moment of area ($J_i = 2I_i$), and bending stiffness matrix ($\boldsymbol{K}_i = \mathrm{diag}(E_iI_i, E_iI_i, G_iJ_i)$, assuming rotational symmetry of the rod cross-sections. Then, deformation of the CTR is determined by the sum of internal forces and moments in each rod:

$$\boldsymbol{n}(s) = \textstyle\sum_{i=1}^{N} \boldsymbol{n}_i, \quad \boldsymbol{m}(s) = \sum_{i=1}^{N} \boldsymbol{m}_i, \quad N = 2. \tag{3.2}$$

The two-rod CTR material state vector is defined as [110]

$$\boldsymbol{y}(s) = \langle \boldsymbol{p}_1 \quad \boldsymbol{q}_1 \quad \boldsymbol{n} \quad \boldsymbol{m}^b_{\mathrm{xy}} \quad m^b_{1,\mathrm{z}} \quad m^b_{2,\mathrm{z}} \quad \theta_2 \rangle, \tag{3.3}$$

where $\boldsymbol{m}^b_{\mathrm{xy}} \in \mathbb{R}^2$ denotes the xy-component of $\boldsymbol{m}$ expressed in the body frame of tube $i = 1$, $m^b_{i,\mathrm{z}} \in \mathbb{R}$ is the z-component of $\boldsymbol{m}_i$ expressed in the body frame of tube i, and $\theta_2 \in \mathbb{R}$ is the rotation of body frame 2 with respect to body frame 1 about the common z-axis.

Deformation of a CTR as a result of relative configurations of concentric-tubes can again be solved as a BVP [110], with the ODEs being summarized in figure 3.2.

3.2.3 Arc-parameterized (pre-)curvature

Cosserat rod-inspired models map the reference (unloaded) configuration of rods to a deformed (loaded) configuration. The (un)loaded rod configuration is described by a pre-curvature vector ($\boldsymbol{u}^*(s)$) and curvature vector ($\boldsymbol{u}(s)$), respectively. Characteristic for shape-lockable rods such as AGCs is that the deformed state can be assigned as a new reference configuration after shape locking, i.e. $\boldsymbol{u}^*(s) \leftarrow \boldsymbol{u}(s)$. Therefore, it is required to be able to formulate $\boldsymbol{u}(s)$ from the shape solution of the associated BVP, equation (3.1).

The (pre-)curvature vectors are obtained from continuous vector functions in the arc-centerline parameter (s), which can be computed from the continuous centerline curve ($\boldsymbol{p}(s)$). However, the shape solution only provides $\boldsymbol{p}(d\Delta s) \leftarrow \boldsymbol{Y}$, $d \in \{1, 2, ..., D\}$ at discrete points along the centerline, equation (3.1). Forming a continuous function in s from discrete points is referred to as arc-parameterization.

Arc-parameterized position

Given known positions ($\boldsymbol{p}(d\Delta s)$) at discrete centerline points, a ζ-order 3D polynomial ($\boldsymbol{p}(s) \in \mathbb{R}^3$, $\zeta \in \mathbb{Z}^+$) can be fit [91]. Fitting $\boldsymbol{p}(s)$ can be achieved with linear least squares, giving the arc-parameterized centerline

$$\dot{\boldsymbol{p}}_1(s) = \boldsymbol{R}(\boldsymbol{q}_1)\boldsymbol{v} \tag{3.4a}$$

$$\dot{\boldsymbol{q}}_1(s) = 0.5 \begin{bmatrix} -\mathrm{Im}(\boldsymbol{q}_1)^{\mathrm{T}} \\ \mathrm{Re}(\boldsymbol{q}_1)\mathcal{I}_3 - [\mathrm{Im}(\boldsymbol{q}_1)]_\times \end{bmatrix} \boldsymbol{R}(\boldsymbol{q}_1)\boldsymbol{u}_1 \tag{3.4b}$$

$$\dot{\boldsymbol{n}}(s) = -\textstyle\sum_{i=1}^{N} \boldsymbol{f}_i^b \tag{3.4c}$$

$$\dot{\boldsymbol{m}}_{xy}^b(s) = \{[\boldsymbol{u}_1]_\times \boldsymbol{m}^b - [\hat{\boldsymbol{z}}]_\times \boldsymbol{R}(\boldsymbol{q}_1)^{\mathrm{T}} \boldsymbol{n}\}_{\mathrm{xy}} \tag{3.4d}$$

$$\dot{m}_{i,z}^b(s) = -\hat{\boldsymbol{z}}^{\mathrm{T}} [\boldsymbol{u}_i]_\times \boldsymbol{m}_i^b \tag{3.4e}$$

$$\dot{\theta}_i(s) = u_{i,z} - u_{1,z} \tag{3.4f}$$

$$\boldsymbol{u}_{1,xy}(s) = \frac{\boldsymbol{m}_{xy}^b + \sum_{i=1}^{N} E_i I_i \boldsymbol{R}_z(\theta_i)\boldsymbol{u}_{i,xy}^*}{\sum_{i=1}^{N} E_i I_i} \tag{3.5a}$$

$$u_{i,z}(s) = (m_{i,z}^b + G_i J_i u_{i,z}^*)/(G_i J_i) \tag{3.5b}$$

$$\boldsymbol{u}_i(s) = \boldsymbol{R}_z(\theta_i)\boldsymbol{u}_1 + \dot{\theta}_i \hat{\boldsymbol{z}} \tag{3.5c}$$

$$\boldsymbol{m}_i^b(s) = \boldsymbol{K}_i(\boldsymbol{u}_i - \boldsymbol{u}_i^*) \tag{3.5d}$$

$$\boldsymbol{m}^b(s) = \textstyle\sum_{i=1}^{N} \boldsymbol{R}_z(\theta_i)\boldsymbol{m}_i^b \tag{3.5e}$$

Figure 3.2: Static Cosserat rod ordinary differential equations (ODE) for concentric-tube robots [110]. Definitions: centerline parameter (s), position ($\boldsymbol{p} \in \mathbb{R}^3$), orientation quaternion ($\boldsymbol{q} \in \mathbb{H}$), internal force ($\boldsymbol{n} \in \mathbb{R}^3$), internal moment ($\boldsymbol{m} \in \mathbb{R}^3$), relative base rotation ($\theta \in \mathbb{R}$), external force ($\boldsymbol{f}_i^b \in \mathbb{R}^3$), strain vector ($\boldsymbol{v} \in \mathbb{R}^3$), curvature vector ($\boldsymbol{u}_i \in \mathbb{R}^3$), pre-curvature vector ($\boldsymbol{u}_i^* \in \mathbb{R}^3$), elastic modulus ($E_i \in \mathbb{R}$), shear modulus ($G_i \in \mathbb{R}$), second moment of area ($I_i \in \mathbb{R}$), polar moment of area ($J_i \in \mathbb{R}$), and bending stiffness matrix ($\boldsymbol{K}_i \in \mathbb{R}^{3\times3}$), for $i \in \{1, ..., N\}$ nested rods. Notations: $*_i^b$ represents a variable of rod i in the reference (body) frame of rod 1, $\hat{*}$ a unit-vector, $[*]_\times : \mathbb{R}^3 \to \mathbb{R}^{3\times3}$ a mapping to a skew symmetric matrix, and $\dot{*} := \partial * / \partial s$. Explicit dependence on (s) by the variables on the right-hand side in equations (2a)-(2f) and (3a)-(3e) has been omitted for readability.

curve of the form

$$\begin{bmatrix} \boldsymbol{c}_\zeta \\ \vdots \\ \boldsymbol{c}_1 \end{bmatrix} = \begin{bmatrix} (1\Delta s)^\zeta \mathcal{I}_3 & \dots & (1\Delta s)\mathcal{I}_3 \\ \vdots & \ddots & \vdots \\ (D\Delta s)^\zeta \mathcal{I}_3 & \dots & (D\Delta s)\mathcal{I}_3 \end{bmatrix}^\dagger \begin{bmatrix} \boldsymbol{p}(1\Delta s) - \boldsymbol{p}(0) \\ \vdots \\ \boldsymbol{p}(D\Delta s) - \boldsymbol{p}(0) \end{bmatrix},$$

$$\boldsymbol{p}(s) = \boldsymbol{c}_\zeta s^\zeta + \ldots + \boldsymbol{c}_1 s + \boldsymbol{p}(0), \tag{3.6}$$

where $\boldsymbol{c}_\zeta \in \mathbb{R}^3$ and $[*]^\dagger$ represents the Moore-Penrose pseudoinverse. The centerline curve is subsequently used within Frenet-Serret formulas to define arc-parameterized orthonormal reference frames.

3

Arc-parameterized orientation

Frenet-Serret frames provide closed-form equations to formulate orthonormal reference frames ($\boldsymbol{R}(s) \in \mathrm{SO}(3)$) using a tangent ($\boldsymbol{t}(s)$), principal normal ($\boldsymbol{r}(s)$), and binormal ($\boldsymbol{b}(s)$) unit vector:

$$\boldsymbol{t}(s) = \frac{\dot{\boldsymbol{p}}}{\|\dot{\boldsymbol{p}}\|},\ \boldsymbol{r}(s) = \frac{\dot{\boldsymbol{p}}\times\ddot{\boldsymbol{p}}}{\|\dot{\boldsymbol{p}}\times\ddot{\boldsymbol{p}}\|} \times \boldsymbol{t},\ \boldsymbol{b}(s) = \frac{\dot{\boldsymbol{p}}\times\ddot{\boldsymbol{p}}}{\|\dot{\boldsymbol{p}}\times\ddot{\boldsymbol{p}}\|}. \tag{3.7}$$

The principal normal has been denoted as $\boldsymbol{r}(s)$ instead of the more common $\boldsymbol{n}(s)$, to not confuse with the notation for internal force in Cosserat rod theory [112].

The tangent and normal vectors describe the rod bending plane, while the binormal vector represents the rotation axis. Arc-derivatives of the Frenet-Serret frame axes are given by

$$\frac{\partial \boldsymbol{t}}{\partial s} = \kappa \boldsymbol{r}, \quad \frac{\partial \boldsymbol{r}}{\partial s} = -\kappa \boldsymbol{t} + \tau \boldsymbol{b}, \quad \frac{\partial \boldsymbol{b}}{\partial s} = -\tau \boldsymbol{r}, \tag{3.8}$$

where $\kappa(s)$ and $\tau(s)$ represent the curvature and torsion of $\boldsymbol{p}(s)$, defined as

$$\kappa(s) = \frac{\|\dot{\boldsymbol{p}}\times\ddot{\boldsymbol{p}}\|}{\|\dot{\boldsymbol{p}}\|^3}, \quad \tau(s) = \frac{(\dot{\boldsymbol{p}}\times\ddot{\boldsymbol{p}})\cdot\dddot{\boldsymbol{p}}}{\|\dot{\boldsymbol{p}}\times\ddot{\boldsymbol{p}}\|^2}. \tag{3.9}$$

Notably, $\tau(s)$ sets the minimum order of $\boldsymbol{p(s)}$ to three. Then, the arc-parameterized Frenet-Serret frame and its derivative are defined as:

$$\boldsymbol{R}(s) = \begin{bmatrix} \boldsymbol{r}, & \boldsymbol{b}, & \boldsymbol{t} \end{bmatrix}, \quad \dot{\boldsymbol{R}}(s) = \begin{bmatrix} \dot{\boldsymbol{r}}, & \dot{\boldsymbol{b}}, & \dot{\boldsymbol{t}} \end{bmatrix}, \tag{3.10}$$

where $\dot{\boldsymbol{r}} := \partial \boldsymbol{r}/\partial s$; similarly for $\dot{\boldsymbol{b}}$ and $\dot{\boldsymbol{t}}$. The reference frames and its arc-derivatives are required to compute the rod curvature vector.

Arc-parameterized curvature

The curvature vector ($\boldsymbol{u}(s) \in \mathbb{R}^3$) describes how the Frenet-Serret frame ($\boldsymbol{R}(s)$) changes along the centerline parameter (s). Given $\boldsymbol{R}(s)$ and $\dot{\boldsymbol{R}}(s)$, the curvature vector is computed as

$$\boldsymbol{u}(s) = \left(\boldsymbol{R}(s)^{\mathrm{T}} \dot{\boldsymbol{R}}(s)\right)^{\vee}, \tag{3.11}$$

where $[*]^{\vee} : \mathbb{R}^{3\times3} \rightarrow \mathbb{R}^3$ extracts the three-dimensional vector ($\boldsymbol{u}(s)$) from the skew-symmetric matrix [113]. This arc-parameterized curvature vector can be assigned to a Cosserat rod as a new pre-curvature vector ($\boldsymbol{u}^*(s) \leftarrow \boldsymbol{u}(s)$), setting the deformed shape as the updated reference configuration. We note that, when a pre-curvature ($\boldsymbol{u}^*(s)$) is assigned to a Cosserat rod, then $\boldsymbol{R}(s=0)$ should be used as a proximal boundary condition for orientation ($\boldsymbol{q}(0) \leftarrow \boldsymbol{R}(0)$).

3.3 Methods

In this section, a simulation framework is presented that is used to magnetically configure the AGC shape in order to guide a needle towards a target position, shown in Fig. 3.3(A)-(C). The concentric arrangement of the AGC and needle is considered as a balanced-stiffness CTR.

The following nomenclature is used to interchangeably denote the Cosserat rod model and physical AGC (rod 1) in rubber (flexible) and glass (stiff) phase, needle (rod 2), and AGC-needle CTR: unloaded flexible AGC ($\mathcal{C}^*_{1,\mathrm{f}}$); loaded flexible AGC ($\mathcal{C}_{1,\mathrm{f}}$); loaded and stiffened AGC ($\mathcal{C}_{1,\mathrm{s}}$), needle ($\mathcal{C}_2$); and AGC-needle CTR ($\mathcal{C}_{12,\mathrm{s}} \leftarrow (\mathcal{C}_{1,\mathrm{s}}, \mathcal{C}_2)$).

The pre-curvatures of $\mathcal{C}^*_{1,\mathrm{f}}$ and $\mathcal{C}_2$ are considered constant ($\boldsymbol{u}^*_{1,\mathrm{f}}(s) = \boldsymbol{u}^*_2(s) = \langle 0,0,0 \rangle$). Further, the pre-curvature of $\mathcal{C}_{1,\mathrm{s}}$ is variable and equal to the curvature of $\mathcal{C}_{1,\mathrm{f}}$ at the point of stiffening ($\boldsymbol{u}^*_{1,\mathrm{s}} \leftarrow \boldsymbol{u}_{1,\mathrm{f}}$). Finally, $\mathcal{C}_{12,\mathrm{s}}$ depends on the pre-curvatures of $\mathcal{C}_{1,\mathrm{s}}$ and $\mathcal{C}_2$. Herein, reconfiguration of $\boldsymbol{u}^*_{1,\mathrm{s}}$ is achieved by exerting a magnetic torque ($\boldsymbol{\tau}_{\mathrm{mag}}$) on $\mathcal{C}^*_{1,\mathrm{f}}$.

First, the simulation framework is presented that is used to compute required magnetic torques on the AGC tip for shape reconfiguration. Second,

a method for generating the associated magnetic field with an electromagnetic actuation system is discussed. Finally, the fabrication of the AGC and its stiffness characterization is described.

3.3.1 Simulation framework

The simulation framework considers the AGC and needle as Cosserat rods, and their concentric configuration as a balanced-stiffness CTR. The deformation of a rod by external magnetic loading, or internal loading by relative translation of rods in a CTR, is solved as a BVP.

Boundary value problem

Herein, each BVP considers the AGC to have a constant length (l_1) and needle to have a variable length ($l_2 \in [0, l_1]$), shown in Fig. 3.3(D). Each rod is subjected to a distributed gravitational force ($\boldsymbol{f}^b_{i,\mathrm{g}}(s)$, expressed in the local AGC body frame.
For the proximal boundary condition, the AGC is fixed at the base ($s = 0$) with invariant position ($\boldsymbol{p}_1(0)$) and orientation ($\boldsymbol{q}_1(0)$). In addition, because the needle is straight, any axial rotation with respect to the AGC (θ_2) is considered inconsequential to the CTR shape and therefore set to zero. Internal forces and moments are unknown and grouped in a proximal optimization vector ($\boldsymbol{\xi}(0) = \langle \boldsymbol{n}(0), \boldsymbol{m}^b_{\mathrm{xy}}(0), m^b_{1,\mathrm{z}}(0), m^b_{2,\mathrm{z}}(0) \rangle$).

The intermediate boundary condition ($s = l_2$) concerns the axial internal moment ($m^b_{2,\mathrm{z}}(l_2)$) at the needle tip. Because the needle is considered unloaded within the AGC, $m^b_{2,\mathrm{z}}(l_2)$ is assigned a zero value.

For the distal boundary condition, the AGC tip ($s = l_1$) experiences a point gravitational force ($\boldsymbol{f}^b_{\mathrm{g}}(l_1) \in \mathbb{R}^3$) and magnetic torque ($\boldsymbol{\tau}^b_{\mathrm{mag}} \in \mathbb{R}^3$) due to an external magnetic field ($\boldsymbol{B}_{\mathrm{ext}} \in \mathbb{R}^3$), providing a boundary condition for internal force ($\boldsymbol{n}(l_1)$) and moment ($\boldsymbol{m}^b_1(l_1)$), respectively.

Solving a BVP is achieved as follows. Starting from the proximal state vector ($\boldsymbol{y}(0) = \boldsymbol{y}(\boldsymbol{p}_1(0), \boldsymbol{q}(0), \theta_2, \boldsymbol{\xi})$), equation (3.3), the state parameters are forward integrated using the static Cosserat rod ODEs, equations (4a)-(5e), using a fourth-order Runge-Kutta method. Thereafter, the errors between the intermediate and distal boundary conditions and the associated

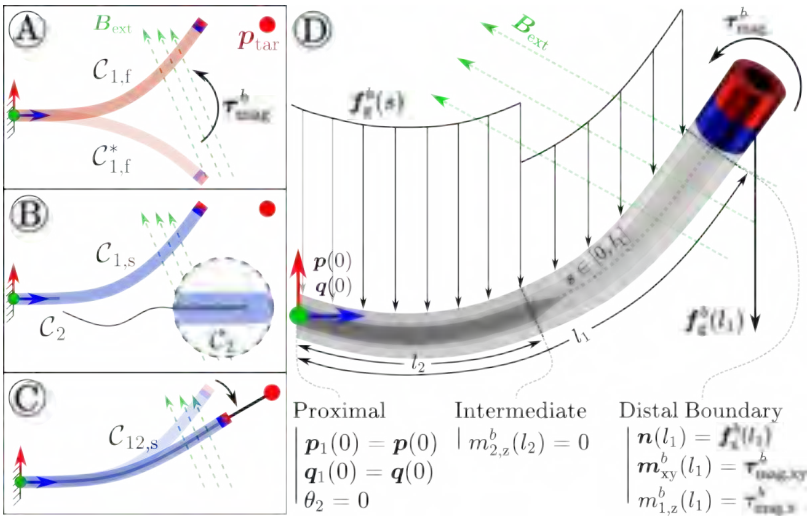

Figure 3.3: Schematic representation of the simulation framework and Cosserat rod-inspired modeling of rod deflection under external loads. (A) Over-deflection of an AGC in the flexible rubber phase from its undeformed ($\mathcal{C}^*_{1,\mathrm{f}}$) to deformed ($\mathcal{C}_{1,\mathrm{f}}$) state towards a target position ($\boldsymbol{p}_{\mathrm{tar}}$) by a magnetic torque ($\boldsymbol{\tau}^b_{\mathrm{mag}}$) exerted by an external field ($\boldsymbol{B}_{\mathrm{ext}}$). (B) Cooling of the AGC towards the stiff glass phase for shape locking ($\mathcal{C}_{1,\mathrm{s}} \leftarrow \mathcal{C}_{1,\mathrm{f}}$). Introduction of needle ($\mathcal{C}_2$). (C) Passing of needle induces deformation of $\mathcal{C}_{1,\mathrm{s}}$, representing a balanced-stiffness concentric-tube robot (CTR). The CTR ($\mathcal{C}_{12,\mathrm{s}} \leftarrow (\mathcal{C}_{1,\mathrm{s}}, \mathcal{C}_2)$) aligns with the target position. (D) Boundary value problem representation for computing AGC deformation as a result of external loading or needle passing. AGC (length l_1) with centerline parameter ($s \in [0, l_1]$), base position $\boldsymbol{p}(s=0)$ and orientation $\boldsymbol{q}(0)$, distributed ($\boldsymbol{f}^b_{\mathrm{g}}(s)$) and point tip ($\boldsymbol{f}^b_{\mathrm{g}}(l_1)$) gravitational force, and magnetic torque ($\boldsymbol{\tau}^b_{\mathrm{mag}}$). Needle (length $l_2 \in [0, l_1]$) having relative base rotation (θ_2) with respect to the AGC, and tip axial moment ($m^b_{2,\mathrm{z}}$).

integrated state parameters are used to update the proximal optimization vector ($\boldsymbol{\xi}(0)$) using Levenberg-Marquardt convex optimization [111].

AGC shape configuration

The simulation framework for finding the required magnetic torque ($\boldsymbol{\tau}^b_{\text{mag}}$) for shape configuration of the AGC, is schematically represented in Fig. 3.4(A1)-(A3). The algorithm attempts to find the required $\boldsymbol{\tau}^b_{\text{mag}}$ on $\mathcal{C}^*_{1,\text{f}}$, such that stiffening of $\mathcal{C}_{1,\text{f}}$ to $\mathcal{C}_{1,\text{s}}$ and subsequent passing of $\mathcal{C}_2$, minimizes the angular targeting error (α) between $\mathcal{C}_{12,\text{s}}$ and a target position ($\boldsymbol{p}_{\text{tar}}$).

Within the local AGC body frame, the magnetic torque is only considered about the xy-axes as its magnet is axially-magnetized. Thus, the problem of computing the error-minimizing torque is formulated as

$$\boldsymbol{\tau}^b_{\text{mag,xy}} \leftarrow \underset{\boldsymbol{\tau}^b_{\text{mag,xy}}}{\arg\min}\ \alpha. \tag{3.12}$$

The process of computing $\boldsymbol{\tau}^b_{\text{mag,xy}}$ involves an interative numerical optimization routine, shown in 3.4(B). Given a guess for $\boldsymbol{\tau}^b_{\text{mag}} = \langle \boldsymbol{\tau}^b_{\text{mag,xy}}, 0 \rangle$ which represents a distal boundary condition for all BVPs within an interation, the deflection of $\mathcal{C}^*_{1,\text{f}}$ to $\mathcal{C}_{1,\text{f}}$ is computed as a BVP, providing a discretized shape solution $\boldsymbol{Y}_{1,\text{f}}$, equation 3.1.

Discrete centerline positions ($\boldsymbol{p}_{1,\text{f}}(d\Delta s) \leftarrow \boldsymbol{Y}_{1,\text{f}}$), are used to compute an arc-parameterized centerline curve ($\boldsymbol{p}_{1,\text{f}}(s)$), Frenet-Serret frames ($\boldsymbol{R}(s)$), and curvature vector ($\boldsymbol{u}_{1,\text{f}}(s)$), equations (3.6)-(3.11). The curvature vector is then assigned as a pre-curvature vector to $\mathcal{C}_{1,\text{s}}$ ($\boldsymbol{u}^*_{1,\text{s}}(s) = \boldsymbol{u}_{1,\text{f}}(s)$).

Thereafter, $\mathcal{C}_{1,\text{s}}$ and $\mathcal{C}_2$ are combined to form $\mathcal{C}_{12,\text{s}}$, representing the CTR with a stiffened AGC and fully inserted needle ($l_2 = l_1$). The CTR shape is again solved as a BVP, providing a shape solution ($\boldsymbol{Y}_{12,\text{s}}$) and associated centerline curve ($\boldsymbol{p}_{12,\text{s}}(s)$). The CTR tip position and direction ($\{\boldsymbol{p}_{12}(l_1), \hat{\boldsymbol{p}}_{12}(l_1)\}$), as well as known target position ($\boldsymbol{p}_{\text{tar}}$), are used to

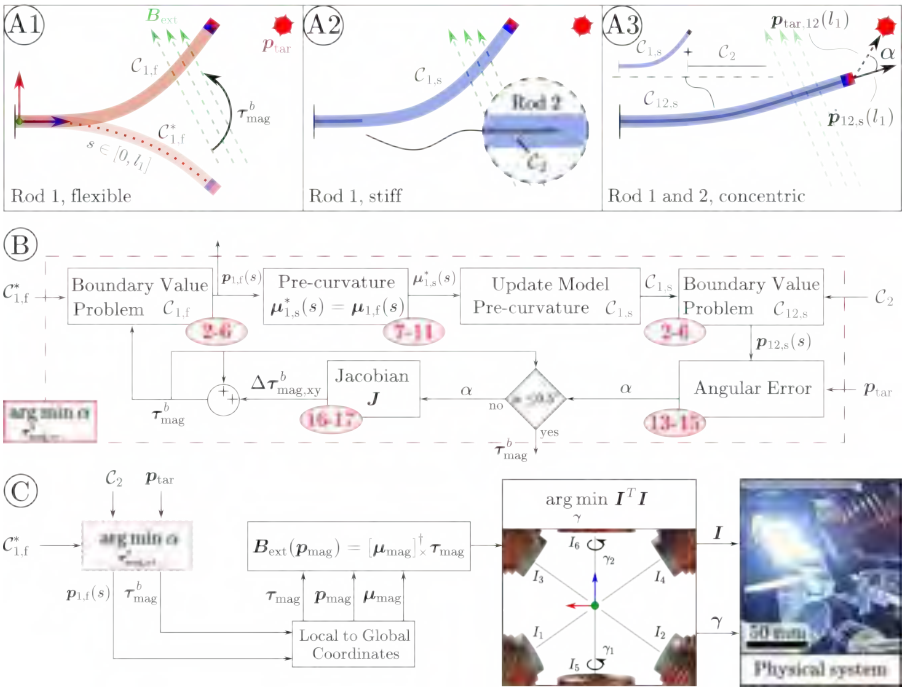

Figure 3.4: Simulation framework. (A1) Unloaded rubber-phase active guiding catheter (AGC, $\mathcal{C}^*_{1,\mathrm{f}}$) with length ($l_1$) and centerline parameter (s) is deflected ($\mathcal{C}_{1,\mathrm{f}}$) by a magnetic torque ($\boldsymbol{\tau}^b_{\mathrm{mag}}$) from an external field ($\boldsymbol{B}_{\mathrm{ext}}$) towards a target position ($\boldsymbol{p}_{\mathrm{tar}}$). (A2) The AGC cools down and stiffens ($\mathcal{C}_{1,\mathrm{s}}$), assuming a new pre-curvature. A needle ($\mathcal{C}_2$) is introduced. (A3) The insertion of the needle causes $\mathcal{C}_{1,\mathrm{s}}$ to deflect backward, resulting in a concentric configuration ($\mathcal{C}_{12,\mathrm{s}}$). The distal tip of $\mathcal{C}_{12,\mathrm{s}}$ has an axial direction vector ($\dot{\boldsymbol{p}}_{12,\mathrm{s}}$) and tip-target vector ($\boldsymbol{p}_{\mathrm{tar},12}$), with an angular error (α). (B) A numerical optimization algorithm minimizes α by computing the appropriate $\boldsymbol{\tau}^b_{\mathrm{mag}}$. In each iteration, $\boldsymbol{\tau}^b_{\mathrm{mag}}$ is updated, resulting in a new centerline polynomial ($\boldsymbol{p}_{1,\mathrm{f}}(s)$) for $\mathcal{C}_{1,\mathrm{f}}$. The associated curvature vector ($\boldsymbol{u}_{1,\mathrm{f}}(s)$) assigned as the pre-curvature vector ($\boldsymbol{u}^*_{1,\mathrm{s}}(s)$) for $\mathcal{C}_{1,\mathrm{s}}$. Then, concentric shape ($\mathcal{C}_{12,\mathrm{s}}$) is solved, and the distal position ($\boldsymbol{p}_{12,\mathrm{s}}(l_1)$) and axial direction vector ($\dot{\boldsymbol{p}}_{12,\mathrm{s}}(l_1)$) are obtained. These values are used to compute α, determining whether $\boldsymbol{\tau}^b_{\mathrm{mag}}$ is updated or accepted as a solution. Associated equation numbers (3.x) are shown in the red ellipsoids. (C) The solution for $\boldsymbol{\tau}^b_{\mathrm{mag}}$ and AGC centerline polynomial $\boldsymbol{p}_{1,\mathrm{f}}(s)$ are transformed to global reference coordinates of the actuation workspace. These values are used to compute tip-magnet position ($\boldsymbol{p}_{\mathrm{mag}}$), dipole moment ($\boldsymbol{\mu}_{\mathrm{mag}}$), and required field ($\boldsymbol{B}_{\mathrm{ext}}$). The field is generated by an electromagnetic actuation system utilizing six mobile coils [84].

compute the targeting error,

$$\hat{\boldsymbol{p}}_{12,\mathrm{s}}(l_1) = \widehat{\boldsymbol{p}_{12,\mathrm{s}}(l_1) - \boldsymbol{p}_{12,\mathrm{s}}(l_1\text{-}\Delta s)}, \tag{3.13}$$

$$\hat{\boldsymbol{p}}_{\mathrm{tar},12}(l_1)) = \widehat{\boldsymbol{p}_{\mathrm{tar}} - \boldsymbol{p}_{12,\mathrm{s}}(l_1)}, \tag{3.14}$$

$$\alpha = \cos^{-1}\Big(\hat{\boldsymbol{p}}_{12,\mathrm{s}}(l_1) \cdot \hat{\boldsymbol{p}}_{\mathrm{tar},12}(l_1)\Big), \tag{3.15}$$

where $\hat{*}$ denotes a unit-vector. If α falls below a threshold, the solution for $\boldsymbol{\tau}^b_{\mathrm{mag}}$ is accepted. Otherwise $\boldsymbol{\tau}^b_{\mathrm{mag}}$ is updated.

In order to update $\boldsymbol{\tau}^b_{\mathrm{mag}}$, a Jacobian matrix ($\boldsymbol{J}$) is computed that relates increments in torque ($\delta\boldsymbol{\tau}^b_{\mathrm{mag,xy}}$) to changes in targeting error ($\delta\alpha$). Given the targeting angular error for some torque ($\alpha(\boldsymbol{\tau}^b_{\mathrm{mag,xy}})$), and the error for an incremented torque ($\alpha(\boldsymbol{\tau}^b_{\mathrm{mag,xy}} + d\boldsymbol{\tau}^b_{\mathrm{mag,xy}})$), the Jacobian is defined as

$$\boldsymbol{J} = \Big(\alpha(\boldsymbol{\tau}^b_{\mathrm{mag,xy}} + d\boldsymbol{\tau}^b_{\mathrm{mag,xy}}) - \alpha(\boldsymbol{\tau}^b_{\mathrm{mag,xy}})\Big) \;/\; (d\boldsymbol{\tau}^b_{\mathrm{mag,xy}})^{\mathrm{T}}, \tag{3.16}$$

Then, the torque step is computed as

$$\Delta\boldsymbol{\tau}^b_{\mathrm{mag,xy}} = -\left(\boldsymbol{J}^{\mathrm{T}}\boldsymbol{J} + \lambda\mathcal{I}_2\right)^{-1}\boldsymbol{J}^{\mathrm{T}}\alpha, \tag{3.17}$$

where $\lambda \in \mathbb{R}^+$ is a damping factor.

3.3.2 Magnetic actuation

A transformation ${}^a\boldsymbol{H}_b = ({}^a\boldsymbol{R}_b, {}^a\boldsymbol{p}_b) \in \mathrm{SE}(3)$ is defined that maps the local AGC body frame to a reference actuation frame. Then, the torque represented in the actuation frame is given by $\boldsymbol{\tau}_{\mathrm{mag}} = {}^a\boldsymbol{R}_b\boldsymbol{\tau}^b_{\mathrm{mag}}$. An external magnetic field ($\boldsymbol{B}_{\mathrm{ext}}$) exerts the desired $\boldsymbol{\tau}_{\mathrm{mag}}$ on the AGC tip magnet.

The magnetic torque ($\boldsymbol{\tau}_{\mathrm{mag}}$) and force ($\boldsymbol{f}_{\mathrm{mag}}$) exerted by $\boldsymbol{B}_{\mathrm{ext}}$ on a dipole ($\boldsymbol{\mu}_{\mathrm{mag}}$) at position ($\boldsymbol{p}_{\mathrm{mag}}$), is given by

$$\boldsymbol{\tau}_{\mathrm{mag}} = [\boldsymbol{\mu}_{\mathrm{mag}}]_{\times}\boldsymbol{B}_{\mathrm{ext}}(\boldsymbol{p}_{\mathrm{mag}}) \tag{3.18}$$

$$\boldsymbol{f}_{\mathrm{mag}} = \nabla\boldsymbol{B}_{\mathrm{ext}}(\boldsymbol{p}_{\mathrm{mag}})\boldsymbol{\mu}_{\mathrm{mag}}, \tag{3.19}$$

where $\nabla = \langle\partial/\partial x, \partial/\partial y, \partial/\partial z\rangle$ is the gradient function, $\boldsymbol{p}_{\mathrm{mag}} = {}^a\boldsymbol{R}_b\boldsymbol{p}_{1,\mathrm{f}}(l_1) + {}^a\boldsymbol{p}_b$ is obtained from the last computed BVP shape solution, and $\boldsymbol{\mu}_{\mathrm{mag}} =$

${}^a\boldsymbol{R}_b\hat{\boldsymbol{p}}_{1,\mathrm{f}}(l_1)\mu_{\mathrm{mag}}$, with $\hat{\boldsymbol{p}}_{1,\mathrm{f}}(l_1)$ computed similarly to equation 3.13 and μ_{mag} the dipole moment magnitude of the AGC tip magnet.

The simulation framework discussed above assumes uniformity of the magnetic field (*i.e.* $\boldsymbol{f}_{\mathrm{mag}} = \langle 0,0,0\rangle$) such that $\boldsymbol{\tau}_{\mathrm{mag}}$ is a unique solution for a desired AGC shape. Therefore, $\boldsymbol{B}_{\mathrm{ext}}$ can be found from equation (3.18). Herein, $\boldsymbol{B}_{\mathrm{ext}}$ is generated by a magnetic actuation system comprising six mobile coils with actuation parameters including angular positions ($\boldsymbol{\gamma} \in \mathbb{R}^2$) and currents ($\boldsymbol{I} \in \mathbb{R}^C$, $C = 6$), shown in Fig. 3.4(C) [84]. Each coil ($c \in \{1,\ldots,C\}$) contributes magnetic fields and gradients

$$\boldsymbol{B}_{\mathrm{ext},c}(\boldsymbol{\gamma}, I_c, \boldsymbol{p}_{\mathrm{mag}}) = \beta_{\mathrm{ext},c}(\boldsymbol{\gamma}, \boldsymbol{p}_{\mathrm{mag}})I_c, \tag{3.20}$$

$$\nabla\boldsymbol{B}_{\mathrm{ext},c}(\boldsymbol{\gamma}, I_c, \boldsymbol{p}_{\mathrm{mag}}) = \nabla\beta_{\mathrm{ext},c}(\boldsymbol{\gamma}, \boldsymbol{p}_{\mathrm{mag}})I_c, \tag{3.21}$$

where $\beta_{\mathrm{ext},c} \in \mathbb{R}^3$ and $\nabla\beta_{\mathrm{ext},c} \in \mathbb{R}^{3\times3}$ are coil-specific unit-current field vector and gradient matrix functions, respectively [111]. Then, the torque and force on a dipole within the actuation workspace is given by

$$\begin{aligned}\boldsymbol{\tau}_{\mathrm{mag}} &= \sum_{c=1}^{C} \underbrace{[\boldsymbol{\mu}_{\mathrm{mag}}]_\times \boldsymbol{\beta}_{\mathrm{ext},c}(\boldsymbol{\gamma}, \boldsymbol{p}_{\mathrm{mag}})}_{\boldsymbol{\tau}_{\mathrm{mag},c}} I_c \\ &= \begin{bmatrix}\boldsymbol{\tau}_{\mathrm{mag},1} & \ldots & \boldsymbol{\tau}_{\mathrm{mag},C}\end{bmatrix} \boldsymbol{I} = \boldsymbol{T}_{\mathrm{mag}}\boldsymbol{I},\end{aligned} \tag{3.22}$$

$$\begin{aligned}\boldsymbol{f}_{\mathrm{mag}} &= \sum_{c=1}^{C} \underbrace{\nabla\beta_{\mathrm{ext},c}(\boldsymbol{\gamma}, \boldsymbol{p}_{\mathrm{mag}})\boldsymbol{\mu}_{\mathrm{mag}}}_{\boldsymbol{f}_{\mathrm{mag},c}} I_c \\ &= \begin{bmatrix}\boldsymbol{f}_{\mathrm{mag},1} & \ldots & \boldsymbol{f}_{\mathrm{mag},C}\end{bmatrix} \boldsymbol{I} = \boldsymbol{F}_{\mathrm{mag}}\boldsymbol{I}.\end{aligned} \tag{3.23}$$

Because $\boldsymbol{\tau}_{\mathrm{mag}}$ and $\boldsymbol{f}_{\mathrm{mag}}$ are nonlinear in $\boldsymbol{\gamma}$, computing the coil current-minimizing positions is formulated as a numerical optimization problem

$$\arg\min_{\boldsymbol{\gamma}}(\boldsymbol{I}^{\mathrm{T}}\boldsymbol{I}), \quad \text{s.t. } |I_c| \leq 8 \text{ A}, \forall I_c \in \boldsymbol{I}, \tag{3.24}$$

where for each $\boldsymbol{\gamma}$, $\boldsymbol{I}$ is found from linear least squares

$$\boldsymbol{I} = \begin{bmatrix}\boldsymbol{T}_{\mathrm{mag}} \\ \boldsymbol{F}_{\mathrm{mag}}\end{bmatrix}^{\dagger} \begin{bmatrix}\boldsymbol{\tau}_{\mathrm{mag}} \\ \boldsymbol{f}_{\mathrm{mag}}\end{bmatrix}. \tag{3.25}$$

Finally, the computed solution of $\{\boldsymbol{I}, \boldsymbol{\gamma}\}$ is passed on to the physical magnetic actuation system, shown in Fig. 3.4(C), resulting in actuation of the AGC.

3.3.3 Fabrication and stiffness characterization

The AGC (ID: 1.2 mm, OD: 4 mm, L: 45 mm) consists of a PTFE tube (ID: 1.2 mm, OD: 1.4 mm, L: 45 mm), copper heating coil (0.2 mm wire diameter), and shape memory polymer (MP3510, SMPTechnologies, Japan) with a glass transition temperature of 35 °C, glass phase at ≤20 °C, and rubber phase at ≥60 °C [103]. Fabrication of the AGC was performed within a cylindrical silicone mold (SORTA-Clear 40, Smooth-On Inc., USA). Firstly, copper wire is wound around the tube, seven axially-magnetized ring magnets (N48, ID: 1.5 mm, OD: 4 mm, L: 1 mm, Neomagnete, Germany) slid over the end, and the tube is placed centrally within the mold. Secondly, the shape memory polymer is injected into the mold from a dual cartridge (50 ml 1:1 Dual Cartridge B-System, Adhesive Dispensing Ltd., UK) with a static mixer nozzle (MBH04-12D, Adhesive Dispensing Ltd., UK). Thirdly, the AGC is vulcanized at 70°C for 2 h and removed from the mold. In addition to the AGC, the needle is a straight stainless-steel cylinder (OD: 1 mm, L: 200 mm).

Stiffness characterization

The elastic moduli of the AGC in both rubber ($E_{1,\mathrm{f}}$) and glass phase ($E_{1,\mathrm{s}}$) at heated (60 °C) and room (25 °C) temperature, respectively, are required by the previously described Cosserat rod models in order to determine the curvatures of $\mathcal{C}_{1,\mathrm{f}}$ and $\mathcal{C}_{1,\mathrm{s}}$, after actuation or passing of $\mathcal{C}_2$, respectively. By considering the AGC as a tip-loaded cantilever beam, the elastic moduli are measured experimentally, Fig. 3.5(A)-(D), from the flexural modulus of elasticity [114]

$$E = mgl^2/2I\phi, \tag{3.26}$$

where m is the load mass, $g = 9.81\,\mathrm{m/s^2}$, $I = \pi(r_\mathrm{o}^4 - r_\mathrm{i}^4)/4$ the second moment of area of the AGC where r_o and r_i are the outer and inner radius, and ϕ the deflection angle. Based on the measurements, $E_{1,\mathrm{f}} \approx 7\,\mathrm{MPa}$ and $E_{1,\mathrm{s}} \approx 0.5\,\mathrm{GPa}$, which is consistent with literature for the mentioned

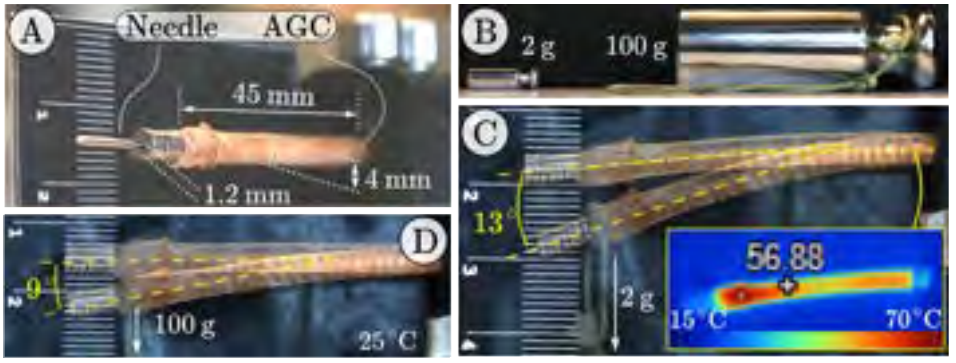

Figure 3.5: Stiffness characterization of the active guiding catheter (AGC). (A) Setup with a horizontally suspended AGC. (B) Weights that are hung on the AGC tip to induce deflection. (C) AGC in the glass phase at 25 °C room temperature with a deflection angle of $\phi = 9°$ due to a 100 g weight. (D) AGC in the rubber phase at an elevated temperature approaching 60 °C with a deflection angle of $\phi = 13°$ due to a 2 g weight.

temperatures [67], [103]. Additionally, the needle is assigned the elastic modulus of stainless steel ($E_2 = 193$ GPa).

3.4 Results

During experiments, the aim is for the simulation framework to inform magnetically-assisted AGC reconfiguration such that a needle is guided towards different targets.

Figure 3.6 presents the experimental setup, including the horizontally-suspended unactuated AGC ($\mathcal{C}^*_{1,\mathrm{f}}$, length $l_1 = 45$ mm) and three targets (5 mm diameter) within the workspace of the magnetic actuation system. The tip of $\mathcal{C}^*_{1,\mathrm{f}}$ is located at $\langle -5, 0, 0 \rangle$ mm, target 1 at $\langle 50, -2, 27 \rangle$ mm, target 2 at $\langle 46, -32, 7 \rangle$ mm, and target 3 at $\langle 34, 35, -30 \rangle$ mm, with respect to the center of the actuation workspace.

Each target corresponds to a separate experiment conducted at 25 °C room temperature, shown in Fig. 3.6(T1)-(T3). First, the simulation framework computes $\boldsymbol{\tau}_{\mathrm{mag}}$ and associated magnetic field. Then, the actuation system

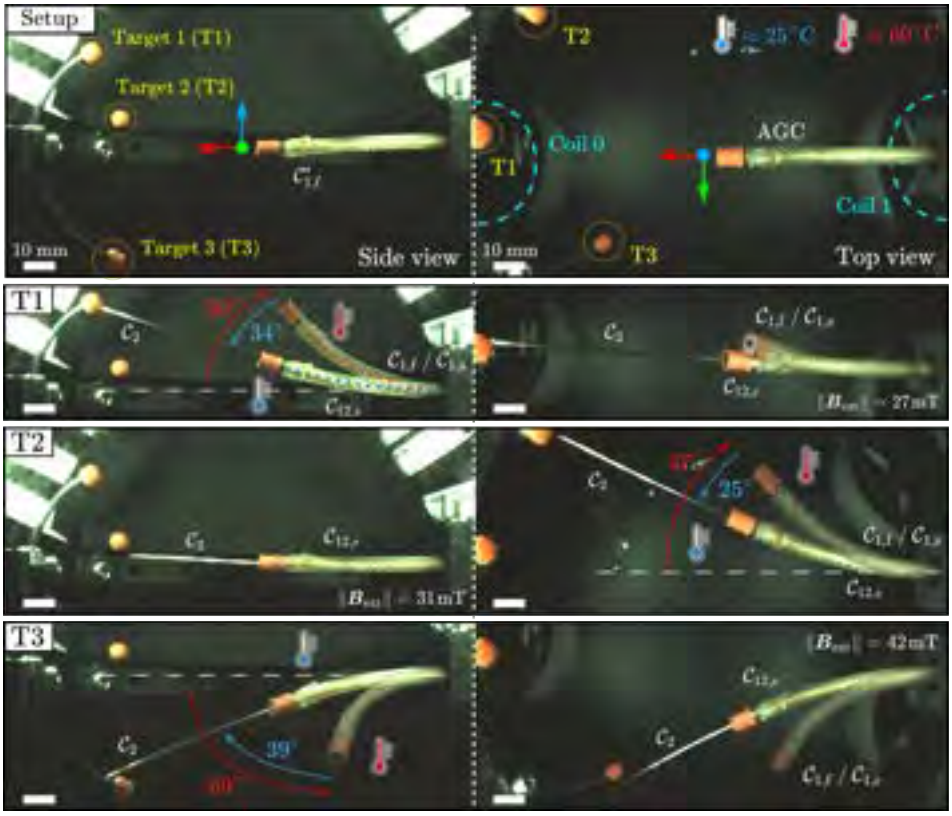

Figure 3.6: Experimental results. The setup shows the horizontally suspended active guiding catheter (AGC) in its undeformed state ($\mathcal{C}^*_{1,\mathrm{f}}$), targets 1-3 (T1-T3), and two coils of the magnetic actuation system [84]. Each experiment is performed as follows. First, the AGC is heated (flexible) and magnetically deflected ($\mathcal{C}_{1,\mathrm{f}}$). Second, the AGC is passively cooled (stiffened) during 120 sec, locking its shape ($\mathcal{C}_{1,\mathrm{s}}$). Third, a needle ($\mathcal{C}_2$) is passed through the AGC, giving a concentric configuration ($\mathcal{C}_{12,\mathrm{s}}$) in elastic equilibrium and aligned with a target. *Scale bar: 10 mm.*

is adjusted to the specified configuration and the AGC heated above 60 °C with a current of 2 A for 60 sec, resulting in the deflection of $\mathcal{C}^*_{1,\mathrm{f}}$ to $\mathcal{C}_{1,\mathrm{f}}$. Thereafter, $\mathcal{C}_{1,\mathrm{f}}$ is passively cooled for 120 sec to room temperature, causing the AGC to assume a fixed shape ($\mathcal{C}_{1,\mathrm{s}}$). Finally, $\mathcal{C}_2$ is inserted through $\mathcal{C}_{1,\mathrm{s}}$.

The volumes of $\mathcal{C}_{1,\mathrm{s}}$ and $\mathcal{C}_{12,\mathrm{s}}$ are segmented into voxels using stereo vision, as depicted in Fig. 3.7(A1)-(A2). An iterative reconstruction algorithm is then employed to obtain discrete centerline points from the voxels. These points are used to fit a 3D centerline polynomial, equation (3.6) [91].

Figure 3.7(B1) shows the centerline polynomials of $\mathcal{C}_{1,\mathrm{s}}$ obtained from the simulation framework ($\boldsymbol{p}_{1,\mathrm{s}}(s)$) and voxel-based reconstruction ($\bar{\boldsymbol{p}}_{1,\mathrm{s}}(s)$). Figure 3.6(B2) presents the angular difference between the axial directions of the centerline curves ($\angle\boldsymbol{p}_{1,\mathrm{s}}, \bar{\boldsymbol{p}}_{1,\mathrm{s}}$) and between the axial directions of the centerline curves and the suspending x-axis of the AGC ($\hat{\boldsymbol{x}}$). Similarly, figure 3.7(C1), centerline polynomials of $\mathcal{C}_{12,\mathrm{s}}$ are obtained from the simulation framework ($\boldsymbol{p}_{12,\mathrm{s}}(s)$) and voxel-based reconstruction ($\bar{\boldsymbol{p}}_{12,\mathrm{s}}(s)$), along with tangent lines aligned with their tip directions, i.e. tangent to $\boldsymbol{p}_{12,\mathrm{s}}(l_1)$ and $\bar{\boldsymbol{p}}_{12,\mathrm{s}}(l_1)$. Figure 3.7(C2) indicates the angular difference between the axial directions of the centerline curves ($\angle\boldsymbol{p}_{12,\mathrm{s}}, \bar{\boldsymbol{p}}_{12,\mathrm{s}}$) and the axial directions of the centerline curves and the suspending x-axis of the AGC.

The simulated backward deflection, that is $\angle(\boldsymbol{p}_{1,\mathrm{s}}(l_1), \hat{\boldsymbol{x}})$ to $\angle(\boldsymbol{p}_{12,\mathrm{s}}(l_1), \hat{\boldsymbol{x}})$, for target 1 was 30° (48° to 18°), for target 2 it was 35° (58° to 24°), and for target 3 it was 49° (83° to 34°). Comparatively, the measured backward deflection, that is $\angle(\bar{\boldsymbol{p}}_{1,\mathrm{s}}(l_1), \hat{\boldsymbol{x}})$ to $(\angle\bar{\boldsymbol{p}}_{12,\mathrm{s}}(l_1), \hat{\boldsymbol{x}})$, for target 1 was 34° (50° to 16°), for target 2 it was 25° (47° to 22°), and for target 3 it was 39° (69° to 30°). The shortest distances between the target and needle (represented by the tangent lines to $\bar{\boldsymbol{p}}_{12,\mathrm{s}}(l_1)$) are 2.3 mm, 7.1 mm, and 7.7 mm.

Therefore, the difference between $\angle(\boldsymbol{p}_{1,\mathrm{s}}(l_1), \hat{\boldsymbol{x}})$ and $\angle(\bar{\boldsymbol{p}}_{1,\mathrm{s}}(l_1), \hat{\boldsymbol{x}})$ of the AGC for target 1 was 2° (48° and 50°), for target 2 it was 11° (58° and 47°), and for target 3 it was 14° (83° and 69°). In addition, the difference between $\angle(\boldsymbol{p}_{12,\mathrm{s}}(l_1), \hat{\boldsymbol{x}})$ and $\angle(\bar{\boldsymbol{p}}_{12,\mathrm{s}}(l_1), \hat{\boldsymbol{x}})$ of the CTR for target 1 was 2° (18° and 16°), for target 2 it was 2° (24° and 22°), and for target 3 it was 4° (34° and 30°).

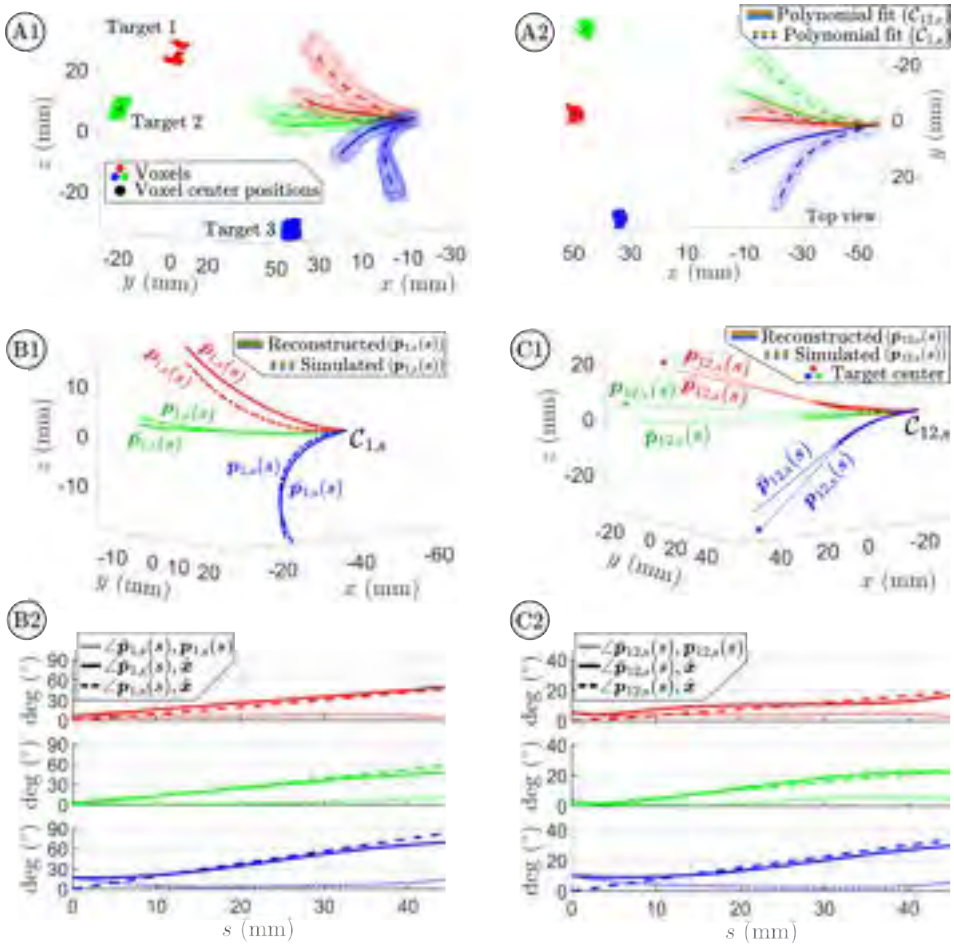

Figure 3.7: Results analysis. (A1) - (A2) Segmented voxels of targets, deflected AGC ($\mathcal{C}_{1,s}$), and AGC-needle ($\mathcal{C}_{12,s}$) with reconstructed centerline curves, equation (3.6). (B1) Polynomial centerline curves of $\mathcal{C}_{1,s}$: desired simulated curve ($\boldsymbol{p}_{1,s}(s)$) and reconstructed curve ($\bar{\boldsymbol{p}}_{1,s}(s)$). The curves vary with the centerline parameter ($s \in [0, l_1]$, $l_1 = 45$ mm the AGC length). (B2) For $\mathcal{C}_{1,s}$, the angular deflection of the centerline curves with respect to the suspending x-axis of the AGC, and angular error between the centerline curves, along s. (C1) Centerline curves of $\mathcal{C}_{12,s}$ with tangent lines to $\boldsymbol{p}_{12,s}(l_1)$ and $\bar{\boldsymbol{p}}_{12,s}(l_1)$. (C2) For $\mathcal{C}_{12,s}$, the angular deflection of the centerline curves with respect to the suspending x-axis of the AGC, and angular error between the centerline curves, along s.

Video recordings of the experiments are provided in the supplementary material. Additionally, the MATLAB implementation of the simulation framework is available online at `https://github.com/MichielRichter/Active_Guiding_Catheters`.

3.5 Discussion

The results demonstrate the simulation framework's ability to predict the backward deflection of $\mathcal{C}_{1,\mathrm{s}}$ to $\mathcal{C}_{12,\mathrm{s}}$ and provide information on the required magnetic torque for achieving $\mathcal{C}_{1,\mathrm{s}}$ from $\mathcal{C}^*_{1,\mathrm{f}}$. Needle targeting errors are associated with model inaccuracies regarding, e.g., elastic modulus, moment of area, magnetic field and gradient maps. Additionally, the magnetic torque was calculated for $\mathcal{C}^*_{1,\mathrm{f}}$ but the field generated for $\mathcal{C}_{1,\mathrm{f}}$. Because the torque on a dipole changes with its rotation in a field, the field should ideally move to match the AGC deflection. For moving fields the robustness of the actuation should be considered [63].

Closed-loop control can compensate for model inaccuracies [111]. However, the simulation framework's convergence time for computing the required magnetic torque reaches several minutes, which is infeasible for closed-loop control. Potential solutions for achieving future closed-loop control of balanced-stiffness AGCs and needles are discussed below.

Firstly, computation time can be reduced by making informed predictions on the required deflection of $\mathcal{C}_{1,\mathrm{s}}$ to reach a desired deflection of $\mathcal{C}_{12,\mathrm{s}}$. We observe that the measured (and simulated) backward deflection angles for each target correlates to the bending stiffness (EI) ratio of the rods. In this work, the EI-ratio ($E_2I_2/E_{1,\mathrm{s}}I_1$) between the needle and AGC is 1.57. Comparatively, the ratio of the measured deflection of $\mathcal{C}_{1,\mathrm{s}}$ $(50°, 47°, 69°)$ to the backward deflection $(34°, 25°, 39°)$ was 1.47, 1.88, and 1.77, respectively for each target. Therefore, a prediction of required $\mathcal{C}_{1,\mathrm{s}}$ deflection could be made based on the EI-ratio with a straight $\mathcal{C}_2$ as

$$\angle\mathcal{C}_{12,\mathrm{s}}, \mathcal{C}^*_{1,\mathrm{f}} \approx \angle\mathcal{C}_{1,\mathrm{s}}, \mathcal{C}^*_{1,\mathrm{f}} - \frac{\angle\mathcal{C}_{1,\mathrm{s}}, \mathcal{C}^*_{1,\mathrm{f}}}{1 + (E_{1,\mathrm{s}}I_1/(E_2, I_2))}. \tag{3.27}$$

Secondly, we observed that $\mathcal{C}_{12,\mathrm{s}}$ can be further steered over small angles ($\approx 1°$) by a field of 35 mT (supplementary video). The bending susceptibility of the CTR to the external field appears greater towards the reference configuration of the rod with the highest bending stiffness.

Thirdly, retracting the needle from $\mathcal{C}_{12,\mathrm{s}}$ allows for a new AGC stiffness transition and reconfiguration. Although the active heating and passive cooling method used in this study takes a few minutes, is impractical, and allows the AGC to slightly deviate from the initially-deflected shape during cooling (supplementary video), previous studies have shown that actively heated and cooled AGCs can achieve stiffness transition in less than 10 sec [107]. Active heating and cooling enables stiffness control. The temperature of $\mathcal{C}_{1,\mathrm{s}}$ can be regulated in the glass-transition region, whereby the backward deflection of $\mathcal{C}_{12,\mathrm{s}}$ by $\mathcal{C}_2$ becomes controllable.

Fourthly, alternative modeling approaches, such as constant-curvature models [115], [116], can improve computation time at the expense of accuracy. Additionally, the torque-optimization step can be replaced with human-in-the-loop control of the magnetic field. This approach involves imaging-based reconstruction of the AGC and predicting needle-induced deformation. In this case, one BVP is required, as opposed to solving six BVPs per iteration step as shown in Fig. 3.4(B). Three-dimensional reconstruction of the AGC can be achieved using various medical imaging modalities [117], such as a rotating C-arm fluoroscopy system [118], [119]. Finally, when a target is surrounded by a solid medium, it is possible to use steerable needles [120], [121].

Regarding applicability of the presented work, the outer diameter of the AGC (4 mm) is relatively large compared to metallic needle-guiding endovascular catheters [99], but chosen based on the commercial availability of the ring-shaped permanent magnets. However, the results may be generalized to combinations of needles and AGCs with similar EI-ratio. For example, an EI-ratio similar to the one in this study (1.57) can be achieved with a combination of a 22-gauge (0.7 mm) superelastic nitinol needle ($E = 50$ GPa) and an AGC with equal inner diameter, 1.7 mm outer diameter, and elastic modulus of 1 GPa (herein the AGC elastic modulus (0.5 GPA) is lower than commonly reported values [67], [103]).

Such dimensions are suitable for endovascular applications such as transjugular liver biopsy [99]. However, a smaller EI-ratio is preferable as the configuration of $\mathcal{C}_{12,\mathrm{s}}$ will be dominated by $\mathcal{C}_{1,\mathrm{s}}$ rather than $\mathcal{C}_2$, which facilitates larger possible deflection angles [64].

A reduction in EI-ratio may be achieved by using more flexible needles, but which may limit propagation through tissue as needle buckling becomes of concern [104].. Alternatively, the elastic modulus of the AGC can be increased. An AGC with an $E_{1,\mathrm{s}}$ of 4.1 GPa has been reported with the addition of metallic filler particles, which inherently results in an increase in $E_{1,\mathrm{f}}$ [67]. Because $E_{1,\mathrm{f}}$ affects the required magnetic field to deflect $\mathcal{C}^*_{1,\mathrm{f}}$ to $\mathcal{C}_{1,\mathrm{f}}/\mathcal{C}_{1,\mathrm{s}}$ and $E_{1,\mathrm{s}}$ affects the induced deflection by $\mathcal{C}_2$, the primary limiting factor for the application of AGCs in needle guidance is the glass stiffness.

Finally, the shape memory polymer that was used to make the AGC has a rubber-phase temperature of 60 °C [103]. However, the permitted surface temperature for endovascular applications is limited to 41 °C [107]. Therefore, the outer surface of the AGC should be insulated or be made of a shape memory polymer with a lower transition temperature.

3.6 Conclusion

Shape memory polymer-based AGCs and straight metallic needles behave as balanced-stiffness CTRs. Magnetic reconfiguration of AGCs enables compensating for needle elasticity. Cosserat rod models can predict the required AGC shape, such that needle-induced backward deflection aligns the CTR with a target position. Increasing bending stiffness of the AGC compared to the needle will reduce the magnitude of needle-induced backward deflection, potentially reducing computational cost of the model.

The convergence time of the simulation framework is infeasible for closed-loop control. Human-in-the-loop control instead of the torque-optimization may reduce the number of required BVPs to solve. Also, informed predictions on the required AGC shape can be made based on the bending stiffness ratio between the AGC and needle. Further, active heating and cooling enables stiffness control of the AGC, which can be used in combination with the needle elasticity to induce relaxation and further deflection of the CTR.

Future work can address closed-loop control and miniaturization of the AGC to clinically-relevant dimensions.

II

It's by Design

Preface

In this part we consider two important design parameters of magnetic continuum manipulators: geometry and magnetization. Geometrically, common shapes of manipulators can be described as extruded 2D cross-section, such as rectangles or circles, that result in elongate block- or cylinder-shaped designs, such as those in chapter 2 and 3, respectively. The magnetization profile of manipulators–the north-pole direction along the manipulator's length–determines the mechanical response to an applied magnetic field. This field is usually assumed to be a uniform "far field", generated by a manipulation system positioned at a relatively large distance from the manipulator. Far fields are often considered to span a wide workspace, challenging independent actuation of manipulators in close proximity.

Alternatively, the concept of locally generated and confined "near fields" is less common. In this dissertation, near fields describe the interaction between closely positioned (electro)magnets. For example, near fields can be passively generated by one segment of a manipulator to act on another segment, or be actively generated by a manipulation system directly attached to the manipulator. The hypothesis, then, is that ***it's by design*** of the geometric and magnetic properties of manipulators, that near fields can complement far fields.

Chapter 4 introduces a new 3D geometric design for continuum manipulators, based on segments of helix-shaped magnetic soft polymer composite. These helices have a uniform axial magnetization, allowing the near field generated by each winding to interact with neighboring windings. As segments bend in a far field, the distance between windings decreases, amplifying the inter-winding forces. The distributed near field in multiple segments acts to improve its bending response to far fields.

Chapter 5 presents a new paradigm for magnetic soft machines that consist of surface-attached flexible planar electromagnetic coils and a continuum manipulators. Here, we propose shaping the 3D magnetization profile based on the nonhomogeneous near field on the coil's surface. A range of proximally arranged machines are demonstrated, capable of independent activation, as well as lifting, tilting, pulling, or grasping objects in close proximity.

4

Magnetic Soft Helical Manipulators with Local Dipole Interactions for Flexibility and Forces

Note: *The following chapter is adapted from the article "Magnetic soft helical manipulators with local dipole interactions for flexibility and forces" by* ***M. Richter****, M. Kaya, J. Sikorski, L. Abelmann, V. Kalpathy Venkiteswaran, and S. Misra, published in "Soft Robotics", vol. 10, no. 3, pp. 647-659, June 2023. The chapter has been reformatted in terms of figures and tables to fit this doctoral thesis. No changes to the technical contents of this peer-reviewed manuscript have been made.*

Authors' Contributions: *MR conceived the project and managed the research. MR and MK fabricated the magnetic polymer composite helices. MR formulated models, and performed simulations and experiments. LA aided in magnetizing the helices. MR compiled figures and videos with support by JS, VKV, and SM. Also, MR, MK, JS, LA, VKV, and SM participated in discussions on the selection of demonstrations. Finally, MR wrote the manuscript with contributions from all authors. SM supervised this project.*

Funding Information: *This research has received funding from the European Research Council (ERC) under the European Union's Horizon 2020 Research and Innovation programme (Grant Agreement #866494 - project MAESTRO).*

Abstract

Magnetic continuum manipulators (MCMs) are a class of continuum robots that can be actuated without direct contact by an external magnetic field. MCMs operating in confined workspaces, such as those targeting medical applications, require flexible magnetic structures that contain combinations of magnetic components and polymers to navigate long and tortuous paths. In cylindrical MCM designs, a significant trade-off exists between magnetic moment and bending flexibility as the ratio between length and diameter decreases. In this study, we propose a new MCM design framework that enables increasing diameter without compromising on flexibility and magnetic moment. Magnetic soft composite helices constitute bending regions of the MCM and are separated by permanent ring magnets. Local dipole interactions between the permanent magnets can reduce bending stiffness, depending on their size and spacing. For the particular segment geometry presented herein, the local dipole interactions result in a 31 % increase in angular deflection of composite helices inside an external magnetic field, compared to helices without local interactions. Also, we demonstrate fabrication, maneuverability, and example applications of a multi-segment MCM in a phantom of the abdominal aorta, such as passing contrast dye and guidewires.

4.1 Introduction

Continuum manipulators (CMs) rely on deformation of their elastic structure for motion and task execution [59]. CMs have found applications in medicine with varying methods of actuation, such as mechanical, fluidic, and magnetic [43], [77]. For example, pre-curved concentric tubes have been proposed for transnasal surgery [122], tendon-driven catheters for cardiac steering [123], [124], and hydraulically- and pneumatically-actuated CMs for endoscopy [125], [126]. A drawback of aforementioned CMs is the need for on-board actuators such as cables and fluidic circuitry. More recently magnetic actuation has been explored for contactless actuation of magnetic CMs (MCMs) during cardiovascular navigation [56], [127]–[130], cardiac ablation [66], [73], subretinal injections [131], atherectomy [132], capsule drug delivery [133], shaping variable stiffness guiding sheaths [67], and endoscopy [134]–[136].

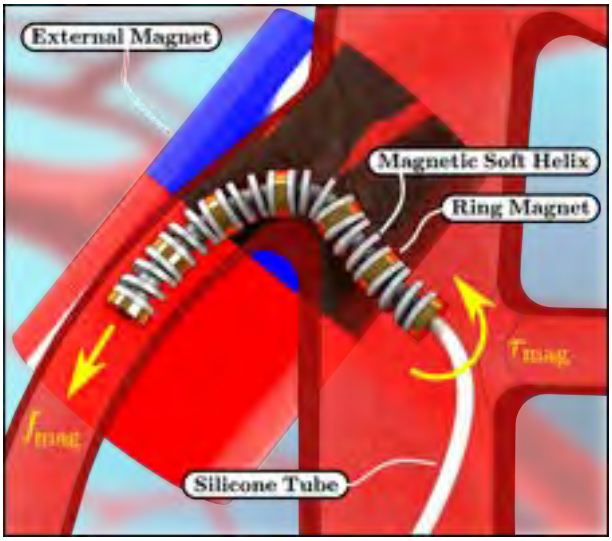

Figure 4.1: Multi-segmented magnetic continuum manipulator (MCM); a series arrangement of ring magnets and magnetic soft helices assembled on a hollow silicone tube backbone. The helical design provides an inherent flexibility that readily deflects in response to magnetic torque ($\boldsymbol{\tau}_{\text{mag}}$). The structural magnetic moment allows pulling by a magnetic force ($\boldsymbol{f}_{\text{mag}}$). The actuating field is generated by an external magnet.

MCM actuation relies on interaction with an external magnetic field [137], and are suitable for traversing tortuous paths [92]. However, the required field is important to consider for medical applications. The space inside an operating room constrains the size of a magnetic actuation system [73], [85], and the required field depends on MCM design and application.

Previous designs of MCMs use rigid permanent magnet(s) [42], [66], [92], [138] or magnetic polymer composite (MPC) [56], [139], integrated at the tip of CMs. MPC consists of magnetic micro-particles suspended in an elastomer base. The volume fraction of magnetic particles as well as their magnetization profile can be predefined to achieve pre-programmed behaviour of MPC robots [58], [140], [141]. As such, a wide range of motion may be achieved in an external magnetic field [54], [70], [81]. Although the material used in MCMs can vary, most designs have a slender cylindrical geometry and use either rigid magnets or MPC. For slender designs, i.e. where the MCM length is significantly bigger than the diameter, magnetic volume and moment decreases. Reducing magnetic moment decreases the magnitude of exerted magnetic forces and torques. The gained flexibility inherent to a slender design compensates for the reduction in torque [56], [92], [131], but at the cost of reduction in actuation force [62], [66].

Material properties that affect magnetic moment are (average) magnetization and volume. For cylindrical MCMs, magnetic moment and bending stiffness scale with the second and fourth power of radius, respectively. Magnetization scales linearly with magnetic volume fraction, but at an exponential cost in bending stiffness. [56] Therefore, bending stiffness increases at higher rate than magnetic moment with diameter. Stiffness can be partially compensated by interaction between internal magnets, i.e. local dipole interactions, which cause forces and torques exerted between segments of the MCM to affect its elasticity. [69] To the authors' best knowledge, using dipole interactions in MCMs to directly reduce bending stiffness as well as indirectly increasing magnetic moment has not yet been explored.

We present an MCM design to enable increasing diameter without compromising on bending flexibility, magnetic moment, and thereby magnetic pulling forces. The proposed design combines MPC single-helices with intermittent permanent ring magnets, assembled over a flexible tube (Fig. 4.1). We investigate the local dipole interaction effect on promoting or opposing deflection of segments. We fabricate an MCM with the proposed design and quantify exerted magnetic forces by an external permanent magnet. Finally, we demonstrate maneuverability of the MCM inside a phantom of the abdominal aorta and use the central channel of the tube to show example applications, such as contrast dye injection and guidewire delivery.

Herein the MCM segment design is presented, followed by a general outline on Cosserat rod modeling of segments. We implement the model, choose geometrical properties of MPC helices based on simulations and workspace-constraints, and present fabrication of segments and a multi-segment MCM. This is followed by measuring the dipole interaction effect on the deflection response of segments in an external magnetic field. Maneuverability and example applications of the MCM design are demonstrated in a silicone phantom of the abdominal aorta. The presented theory and experiments provide design principles for devices based on assemblies of MPC and permanent magnets.

4.2 Theory

We present theory on segment design. Additionally, a Cosserat rod model is discussed to simulate deflection response of segments in external fields.

4.2.1 Segment design

A segment comprises two ring magnets and an MPC helix shaped as a cored closed and ground compression spring (Fig. 4.2A). Ring magnets have predetermined length (L_{mag}). The helix contains a suspension of praseodymium-iron-boron microparticles (PrFeB) and polydimethylsiloxane (PDMS), has a length (L), radius (R), cylinder outer radius (r_{oc}), cylinder inner radius (r_{ic}), and number of windings (W). A helix boundary deflection angle (Θ) is assigned (Fig. 4.2B), giving a maximum deflection angle ($\theta = \Theta/W$) for each winding (Fig. 4.2D).

Dependent design variables of the helix are winding width ($w = R - r_{\mathrm{oc}}$), height (h), and pitch ($p = R\theta$). The height necessary to achieve a desired L can be derived from the helix outer upper boundary curve,

$$\boldsymbol{u}(\beta) = \begin{bmatrix} x_{\mathrm{u}}(\beta) \\ y_{\mathrm{u}}(\beta) \\ z_{\mathrm{u}}(\beta) \end{bmatrix} = \begin{bmatrix} R\cos(\beta) \\ R\sin(\beta) \\ \frac{\beta}{2\pi}(h+p)+h \end{bmatrix}, \tag{4.1}$$

where $\beta \in [0, 2\pi W + \phi]$ denotes the revolution angle with $\phi \in [0, 2\pi)$. The value of ϕ is chosen to achieve axially symmetric bending flexibility of the helix. We choose ϕ such that $w = z_u(\phi) - h$, because the ground ends have height (h). Rearranging to solve for ϕ gives

$$\phi = \frac{h}{h+p} 2\pi. \tag{4.2}$$

Since $z_{\mathrm{u}}(\beta_{\max}) = L$ ($\beta_{\max} = 2\pi W + \phi$) we can derive from Eqn. 4.1 that

$$h = \frac{L - Wp}{2 + W}. \tag{4.3}$$

Given a segment design, we define a relative magnetic moment ($\mu_{\mathrm{rel}} \in [0, 1]$) of an MCM as the ratio between magnetic moment of the MCM and a

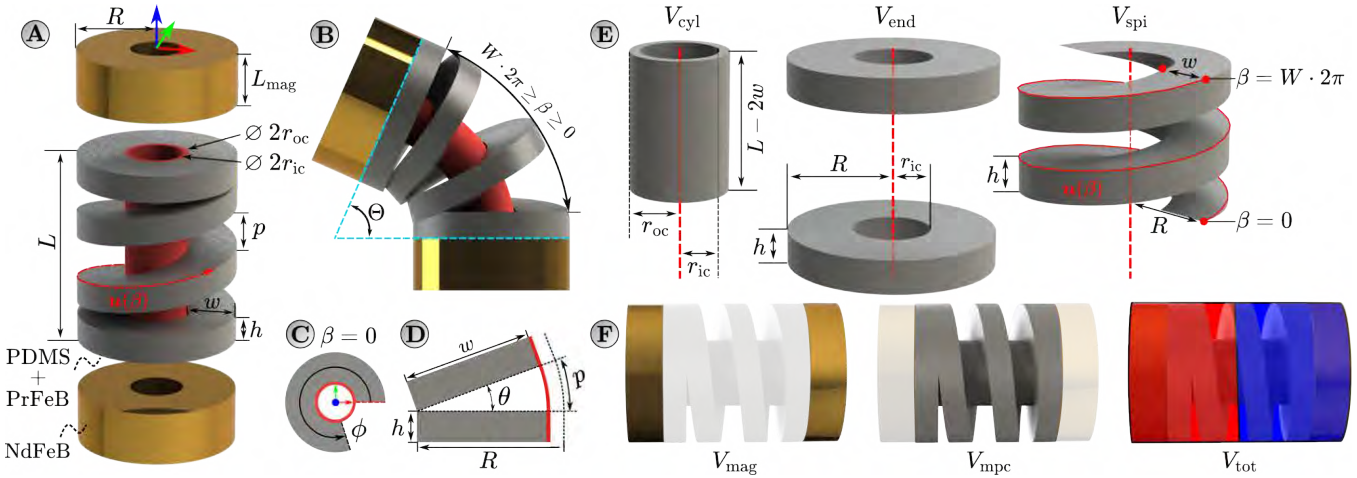

Figure 4.2: Design of a magnetic segment. (A) Segments are made from magnetic polymer composite (MPC) and neodymium-iron-boron (NdFeB) ring magnets. MPC contains a suspension of polydimethylsiloxane (PDMS) and praseodymium-iron-boron (PrFeB) microparticles. The MPC is shaped as a closed and ground compression spring (gray) with a core cylinder (red). The spring/helix has an outer upper boundary curve ($\boldsymbol{u}(\beta)$) and has windings ($W \in \mathbb{Z}^+$) with a width (w), height (h), and pitch (p). The core cylinder has an outer radius (r_{oc}), inner radius (r_{ic}), and a length (L). (B) Segment bending is limited to a boundary deflection angle (Θ). The helical part of the spring is described by revolution angle (β). (C) Transverse cross-section of the helix. The core cylinder is shown with the red circle. MPC surrounds the cylinder with a sector angle (ϕ). (D) Single pitch bending. With each pitch the helix can bend with $\theta = \Theta/W$ before adjacent windings touch. (E) Subvolumes of the MPC helix: the core cylinder (V_{cyl}), end disks (V_{end}), and spiral (V_{spi}). Subvolumes are used to compute total MPC volume. (F) Subvolumes of a segment: ring magnets (V_{mag}) and MPC helix (V_{mpc}). Combined volume is compared to total occupied volume (V_{tot}). Total occupied volume represents that of a reference solid cylindrical magnet with equal dimensions.

reference solid cylindrical magnet of equal length, diameter, and remanence of materials. The value μ_{rel} is dimensionless and describes the achievable magnetic moment of a segment/MCM design, and is calculated from the relative absolute (V_{rel}) and magnetic (M_{rel}) volume:

$$V_{\text{rel}} = \frac{(S+1)V_{\text{mag}} + SV_{\text{mpc}}}{V_{\text{tot}}(S)}, \tag{4.4}$$

$$M_{\text{rel}} = \frac{(S+1)V_{\text{mag}} + S\Phi V_{\text{mpc}}}{V_{\text{tot}}(S)}, \tag{4.5}$$

$$\mu_{\text{rel}} = M_{\text{rel}} V_{\text{rel}}, \tag{4.6}$$

where $S \in \mathbb{Z}^+$ is the number of segments in an MCM, $V_{\text{mag}} = \pi(R^2 - r_{\text{ic}}^2)L_{\text{mag}}$ denotes ring magnet volume, V_{mpc} the MPC helix volume, $\Phi \in [0, 1]$ the volume fraction of PrFeB microparticles, and $V_{\text{tot}}(S) = \pi R^2(SL + (S+1)L_{\text{mag}})$ the reference magnet volume (Fig. 4.2F). The MPC helix volume (V_{mpc}) is computed from three smaller volumes (Fig. 4.2E): core cylinder (V_{cyl}), closed and ground ends (V_{end}), and spiral (V_{spi}),

$$V_{\text{mpc}} = V_{\text{cyl}} + V_{\text{end}} + V_{\text{spi}}, \tag{4.7}$$

as follows:

$$\begin{aligned} V_{\text{cyl}} &= \pi(r_{\text{oc}}^2 - r_{\text{ic}}^2)(L - 2h) \\ V_{\text{end}} &= 2\pi(R^2 - r_{\text{ic}}^2)h, \\ V_{\text{spi}} &= 2\frac{wh}{\phi}\int_0^{\phi} \beta\sqrt{R^2 + \dot{z}_{\text{u}}^2}\,\mathrm{d}\beta + \\ &\qquad wh\int_{\phi}^{2\pi W - \phi} \sqrt{R^2 + \dot{z}_{\text{u}}^2}\,\mathrm{d}\beta, \end{aligned} \tag{4.8}$$

where $\dot{z}_{\text{u}} = \partial z_{\text{u}}/\partial\beta$.

4.2.2 Cosserat rod model

A Cosserat rod model is a continuum mechanics model used to compute statics and dynamics of CMs, comprehensively reported in the works by Till *et al.* [95] and Edelmann *et al.* [63] Magnetic segments are characterized by a centerline parameter ($s \in [0, L + 2L_{\text{mag}}]$) and discretized into N subsegments (Fig. 4.3A) of length (Δs_n) to obtain $N + 1$ centerline points

$(s_0, s_1, \ldots, s_N)$. Each centerline point has associated material states: position $\left(\boldsymbol{p}_n \in \mathbb{R}^3\right)$, orientation quaternion $\left(\boldsymbol{q}_n = (q_r, \boldsymbol{q}_i) \in \mathbb{H},\ q_r \in \mathbb{R},\ \boldsymbol{q}_i \in \mathbb{R}^3\right)$, internal force $\left(\boldsymbol{n}_n \in \mathbb{R}^3\right)$, and internal moment $\left(\boldsymbol{m}_n \in \mathbb{R}^3\right)$. The evolution of material states from s_{n-1} to s_n depends on a set ordinary partial differential equations [63]. Change in pose between subsegments is determined by shear/extension and bending/torsion stiffness matrices $(\boldsymbol{K}_{\text{se}}, \boldsymbol{K}_{\text{bt}} \in \mathbb{R}^{3\times3})$, as well as distributed external magnetic forces and torques $(\boldsymbol{f}_{\text{mag}}, \boldsymbol{\tau}_{\text{mag}} \in \mathbb{R}^3)$, also called magnetic wrench.

Herein we extend existing static Cosserat rod models to account for non-homogeneity of magnetic fields and gradients across the cross-sectional area of subsegments (Fig. 4.3A). The magnetic field $(\boldsymbol{B}(\boldsymbol{p}) \in \mathbb{R}^3)$ is composed of a homogeneous external field $(\boldsymbol{B}_{\text{ext}} \in \mathbb{R}^3)$ and non-homogeneous ring magnet field $(\boldsymbol{B}_{\text{ring}}(\boldsymbol{p}) \in \mathbb{R}^3)$,

$$\boldsymbol{B}\left(\boldsymbol{p}\right) = \boldsymbol{B}_{\text{ext}} + \boldsymbol{B}_{\text{ring}}\left(\boldsymbol{p}\right). \tag{4.9}$$

The total magnetic wrench on a subsegment is computed as the sum of distributed wrenches. Given a subsegment with pose $(\boldsymbol{p}_n, \boldsymbol{q}_n)$, we discretize its cross-sectional area into smaller sector areas $(\Delta A_{n,o})$ with volumes $(\Delta V_{n,o} = \Delta A_{n,o}\Delta s_n \in \{\Delta V_{n,1}, \ldots, \Delta V_{n,O}\})$. Each sector area has its own pose $(\boldsymbol{p}_{n,o}, \boldsymbol{q}_n)$, where $\boldsymbol{p}_{n,o} = \boldsymbol{p}_n + \boldsymbol{R}(\boldsymbol{q}_n)\boldsymbol{p}_o$, with $\boldsymbol{R}(\boldsymbol{q}_n) \in \mathrm{SO}(3)$ a rotation matrix associated with orientation quaternion $(\boldsymbol{q}_n)$ and $\boldsymbol{p}_o$ the xy-position in the center of $\Delta A_{n,o}$, respectively (Fig. 4.3C). Then the wrench is computed as

$$\begin{aligned}
\boldsymbol{f}_{\text{mag}}(\boldsymbol{p}_n, \boldsymbol{q}_n) &= \sum_{o=1}^{O} \underbrace{\nabla\left(\frac{\partial \boldsymbol{\mu}(\boldsymbol{q}_n)}{\partial V} \cdot \boldsymbol{B}\left(\boldsymbol{p}_{n,o}\right)\right)}_{\boldsymbol{f}_{\text{mag}}(\boldsymbol{p}_{n,o}, \boldsymbol{q}_n)} \Delta V_{n,o}, \\
\boldsymbol{\tau}_{\text{mag}}(\boldsymbol{p}_n, \boldsymbol{q}_n) &= \sum_{o=1}^{O} \left(\frac{\partial \boldsymbol{\mu}(\boldsymbol{q}_n)}{\partial V} \times \boldsymbol{B}\left(\boldsymbol{p}_{n,o}\right)\right) \Delta V_{n,o} \\
&\quad + (\boldsymbol{p}_{n,o} - \boldsymbol{p}_n) \times \boldsymbol{f}_{\text{mag}}(\boldsymbol{p}_{n,o}, \boldsymbol{q}_n),
\end{aligned} \tag{4.10}$$

with $\boldsymbol{\mu}(\boldsymbol{q}_n)$ the magnetic dipole moment of the subsegment with partial

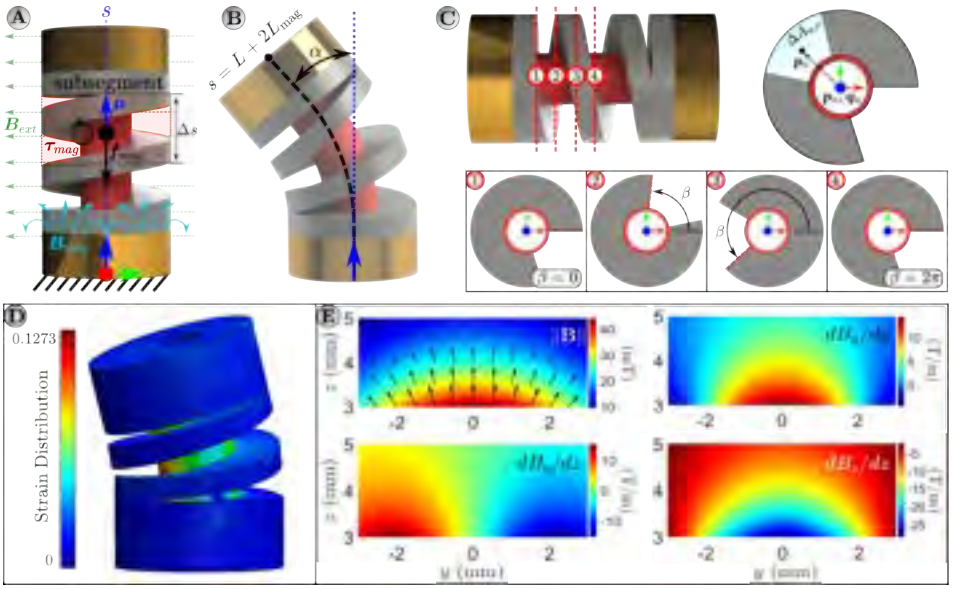

Figure 4.3: Modeling of magnetic segments with Cosserat rods. (A) A segment with centerline parameter ($s \in [0, L + 2L_{\text{ring}}]$) is discretized into subsegments of length (Δs_n), with $n \in [0, 1, \ldots, N]$. Each subsegment has a dipole moment ($\boldsymbol{\mu}$) and experiences a magnetic torque ($\boldsymbol{\tau}_{\text{mag}}$) and force ($\boldsymbol{f}_{\text{mag}}$). The magnetic torques and forces are due to a homogeneous external magnetic field ($\boldsymbol{B}_{\text{ext}}$) and non-homogeneous magnetic field from the base ring magnet ($\boldsymbol{B}_{\text{ring}}$). Both base and tip ring magnets have the same geometry and magnetic moment. (B) The segment responds to the magnetic field with tip deflection (α). (C) Cross sections (1-4) along the centerline show a rotating pattern as a function of the revolution angle (β). In order to compute magnetic forces and torque acting on the n^{th} subsegment, the cross-sectional area is divided in discrete parts (ΔA_o), $o \in [0, 1, \ldots, O]$, with a center position ($\boldsymbol{p}_o$) defined relative to the subsegment centerline pose ($\boldsymbol{p}_n, \boldsymbol{q}_n$). (D) Strain distribution of segments during deflection. (E) FEM estimates of the magnetic field ($\boldsymbol{B}_{\text{ring}}$) in the yz-plane generated by the proximal ring magnet with outer diameter 4 mm, inner diameter 1.5 mm, and length 1 mm. The field magnitude and non-zero gradients are shown between 3 mm and 5 mm. Field directions are represented by black arrows. The fields and gradients are responsible for local dipole interactions with the segment tip ring magnet.

derivative

$$\frac{\partial \boldsymbol{\mu}(\boldsymbol{q}_n)}{\partial V} = \frac{\Phi B_r}{\mu_0} \boldsymbol{R}(\boldsymbol{q}_n)\hat{\boldsymbol{e}}_3, \tag{4.11}$$

where μ_0 is the vacuum permeability, Φ the magnetic particle volume fraction, and B_r the magnetic particle residual flux density. The sector-shaped cross-sections (Fig. 4.3C) exhibit a rotating pattern along s by a revolution angle (β). Defining $s_\beta \in [0, L-2h]$ that starts on the level of $\beta = 0$ (Fig. 4.2E), the corresponding revolution angle can be found as $\beta = 2\pi W s_\beta/(L-2h)$.

The magnetic wrench causes deflection (α) of magnetic segments (Fig. 4.3B). Magnitude of deformation is determined by shear/extension and bending/torsion stiffness matrices ($\boldsymbol{K}_{\text{se}}, \boldsymbol{K}_{\text{bt}}$) along the segment, defined as

$$\boldsymbol{K}_{\text{se}} = \begin{pmatrix} G_n & 0 & 0 \\ 0 & G_n & 0 \\ 0 & 0 & E_n \end{pmatrix} A_n, \ \boldsymbol{K}_{\text{bt}} = \begin{pmatrix} E_n & E_n & 0 \\ E_n & E_n & 0 \\ 0 & 0 & G_n \end{pmatrix} \boldsymbol{J}_n, \tag{4.12}$$

where G_n and E_n are the material shear and elastic moduli, A_n is the cross-section area, and $\boldsymbol{J}_n \in \mathbb{R}^{3\times 3}$ is a rotational inertia matrix [95]. The rotational inertia matrix is defined as

$$\boldsymbol{J}_n = \begin{pmatrix} I_{xx} & I_{xy} & 0 \\ I_{yx} & I_{yy} & 0 \\ 0 & 0 & I_{zz} \end{pmatrix}. \tag{4.13}$$

For MPC helices we consider only the end disks and the core cylinder, i.e. we do not account for the spiral in computing the cross-sectional area or area moment of inertia for a cross-section, because the majority of strain during bending is concentrated in the core cylinder (Fig. 4.3D). For the core cylinder $I_{xx} = I_{yy} = \pi(r_{\text{oc}}^4 - r_{\text{ic}}^4)/4$, $I_{zz} = I_{xx} + I_{yy}$, and $I_{xy} = I_{yx} = 0$. For end disks and ring magnets $I_{xx} = I_{yy} = \pi(R^4 - r_{\text{ic}}^4)/4$, $I_{zz} = I_{xx} + I_{yy}$, and $I_{xy} = I_{yx} = 0$. Given the rotational inertia matrix as well as the distributed magnetic wrench, the segment statics can be solved as a boundary value problem [95].

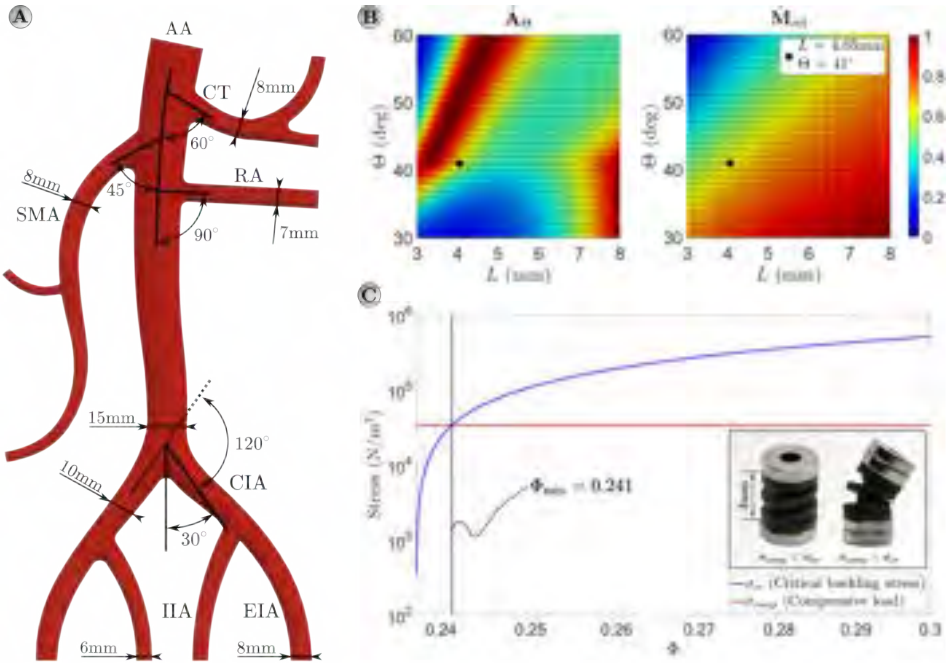

Figure 4.4: Model-based design of magnetic segments. (A) A planar diagram of the abdominal aorta (AA) with major branches: celiac trunk (CT), superior mesenteric artery (SMA), renal arteries (RA). The aortic bifurcation gives rise to the common iliac arteries (CIA), leading to the internal iliac arteries (IIA) and external iliac arteries (EIA). Given vessel diameters and branching angles are within the ranges reported in literature. Design constraints are imposed on segments based on anatomical geometry. (B) Normalized simulation results of segment deflection ($\alpha(L_i, \Theta_j)$) and relative magnetic moment ($\mu_{\text{rel}}(L_i, \Theta_j)$), according to Eqns. 4.17 ($\hat{\boldsymbol{A}}_\Theta$) and 4.18 ($\hat{\boldsymbol{M}}_{\text{rel}}$). Results are shown for combinations $L_i, \Theta_j \in \mathbb{S}$ (Eqn. 4.16). The color bar applies to both plots. (C) Normalized sum of simulation results is chosen as a cost function to decide on helix length (L) and boundary deflection (Θ). A photograph of a final segment is shown with annotated dimensions. A complete list of dimensions and material properties is given in Table 4.1.

Quantity	Symbol	Value
Magnetic Polymer Composite Helices		
Helix length	L	4 mm
Boundary deflection	Θ	40 °
Helix radius	R	2 mm
Windings	W	2
Cylinder outer radius	r_{oc}	0.95 mm
Cylinder inner radius	r_{ic}	0.75 mm
PDMS shore hardness	H	33
PDMS Poisson's ratio	ν	0.40
Volume fraction	Φ	0.25
PrFeB remanence	B_{r}	1 T
Ring Magnets		
Magnet length	L_{mag}	1 mm
Magnet outer radius	R	2 mm
Magnet inner radius	R	0.75 mm
NdFeB remanence	B_{r}	1.35 T

Table 4.1: Segment design parameters as used in this article. Definitions are shown in Figure 4.2A. Remanence of neodymium-iron-boron (NdFeB) and praseodymium-iron-boron (PrFeB) and material properties of polydimethylsiloxane (PDMS) are listed as used for simulations.

4.3 Methods

The Cosserat rod model is used to simulate deflection of magnetic segments by an external homogeneous magnetic field. Simulation results and design constraints are used to choose design parameters of segments. An MCM is assembled as a series of segments. Experiments are performed to validate the model, investigate the effect of local dipole interactions on segment flexibility, quantify forces on the MCM by an external permanent magnet, and demonstrate maneuverability of the MCM using magnetic wrenches exerted by the external permanent magnet.

4.3.1 Model-based segment design

In simulations, segments are considered fixed at the base and free at the tip (Fig. 4.3A). The previously described Cosserat rod model is implemented in MATLAB 2020B (MathWorks, Natick, MA, USA). Segments are simulated without a backbone. A perpendicular external uniform magnetic field ($\|\boldsymbol{B}_{\mathrm{ext}}\| = 20$ mT) is applied together with a non-uniform local field ($\boldsymbol{B}_{\mathrm{ring}}$) from the base ring magnet (Fig. 4.3A). Segment tip angular

deflection (α) as a result of the magnetic wrench is computed (Fig. 4.3B). The ring magnet field is estimated from a finite element model (FEM) in COMSOL 5.6 (COMSOL, Burlington, VT, USA), shown in Figure 4.3E. We estimate the magnetic field at positions ($\boldsymbol{p}$) in the yz-plane above the ring magnet and fit a model to obtain an analytical description of the estimated field and gradients, representing the 3D field due to the axial symmetry of the ring magnet field [111].

Commercially available ring magnets are used (OD: 4 mm. ID: 1.5 mm), which constrains segment design accordingly. Material properties of ring magnets and MPC helices are listed in Table 4.1. The MPC consist of PDMS with predefined Shore A hardness ($H = 33$) and magnetic volume fraction ($\Phi = 0.25$). The PDMS elastic modulus and MPC shear modulus are determined by Gent's relation [142] and a Mooney-model [56], [143], respectively,

$$E_{\text{pdms}} = \frac{0.0981(56 + 7.66H) \cdot 10^6}{0.137505(254 - 2.54H)} \tag{4.14}$$

$$G_{\text{mpc}} = \frac{E_{\text{pdms}}}{2(1+\nu)} \exp\left(\frac{2.5\Phi}{1 - 1.35\Phi}\right), \tag{4.15}$$

with constant Poisson ratio ($\nu = 0.40$).

Segment design variables are helix length (L) and boundary deflection angle (Θ), which determine relative magnetic moment (μ_{rel}) and deflection response (α) inside an external magnetic field. A range of helix lengths ($L_i \in \{L_1, \ldots, L_I\}$) and deflections ($\Theta_j \in \{\Theta_1, \ldots, \Theta_J\}$) are considered. To demonstrate workspace-constrained segment design, we choose a phantom of the adult human abdominal aorta as the MCM navigation environment due to confinement, tortuosity, and path length (Fig. 4.4A). We impose that a multi-segment MCM should be able to bend 120 ° within 15 mm for maneuverability and define a set of valid combinations as

$$\mathbb{S} = \left\{ L_i, \Theta_j \;\middle|\; \frac{120}{\Theta_j} L_i + \left\lfloor \frac{120}{\Theta_j} \right\rfloor L_{\text{mag}} \leq 15 \right\}. \tag{4.16}$$

Branching angles and vessel diameters of the phantom are within dimensions reported in literature [144]–[149]. To match fabrication constraints as

well as ensure structural integrity of MPC helices we set a minimum winding height ($h \geq 0.6$ mm) and height-to-pitch ratio ($h/p \geq 0.9$). Angular deflection ($\alpha(L_i, \Theta_j)$) is computed from segment tip orientation ($\boldsymbol{q}_N$) obtained from the BVP solution [111]. Relative magnetic moment $\mu_{\text{rel}}(L_i, \Theta_j)$ is computed with Eqn. 4.4.

From simulations we obtain matrices $\boldsymbol{A} \in \mathbb{R}^{I \times J}$ and $\boldsymbol{M}_{\text{rel}} \in \mathbb{R}^{I \times J}$ with components $\alpha(L_i, \Theta_j)$ and $\mu_{\text{rel}}(L_i, \Theta_j)$. Our aim is that $\alpha(L_i, \Theta_j) \rightarrow \Theta_j$ within the applied external field ($\|\boldsymbol{B}_{\text{ext}}\| = 20$ mT). We define an absolute deflection mismatch $\tilde{A}_{ij} = \mid \alpha(L_i, \Theta_j) - \Theta_j \mid$, giving $\tilde{\boldsymbol{A}} \in \mathbb{R}^{I \times J}$ that is normalized to give highest weight to combinations $\{L_i, \Theta_j\}$ that provide $\alpha(L_i, \Theta_j) \rightarrow \Theta_j$,

$$\hat{\boldsymbol{A}}_{\Theta} = \frac{\mid \tilde{\boldsymbol{A}} - \max\left(\tilde{\boldsymbol{A}}\right) \mid}{\max\left(\mid \tilde{\boldsymbol{A}} - \max \tilde{\boldsymbol{A}} \mid\right)}. \tag{4.17}$$

Additionally, to increase the weight of high compared to low $\mu_{\text{rel}}(L_i, \Theta_j) \in \boldsymbol{M}_{\text{rel}}$, we normalize all values in $\boldsymbol{M}_{\text{rel}}$ according to:

$$\hat{\boldsymbol{M}}_{\text{rel}} = \frac{\boldsymbol{M}_{\text{rel}} - \min\left(\boldsymbol{M}_{\text{rel}}\right)}{\max\left(\boldsymbol{M}_{\text{rel}}\right) - \min\left(\boldsymbol{M}_{\text{rel}}\right)}. \tag{4.18}$$

Values in $\hat{\boldsymbol{A}}_{\Theta}$ and $\hat{\boldsymbol{M}}_{\text{rel}}$ for $L_i, \Theta_j \in \mathbb{S}$ are shown in Figure 4.4B. The combination $L = 4$ mm and $\Theta = 40\ ^{\circ}$ is chosen based on a cost function ($\hat{\boldsymbol{A}}_{\Theta} + \hat{\boldsymbol{M}}_{\text{rel}}$). The relative magnetic moment of the MCM (μ_{rel}) for multiple segments ($S \in \mathbb{Z}^{+}$) is shown in Figure 4.5, for designs with an open and closed core cylinder, and helices without magnetic particles.

4.3.2 Fabrication

MPC consists of a base elastomer material with a suspension of ferromagnetic particles. We choose polydimethylsiloxane (PDMS, Sylgard 184 silicone elastomer, Farnell, UK) of its low elastic modulus and biocompatibility [92], [150]. The secondary MPC ingredient is praseodymium microparticles (PrFeB) with an average diameter of 5 µm (MQFP-16-7-11277, Magnequench GmbH, Germany). PrFeB was chosen based on availability and can be interchanged with NdFeB for a higher remanent magnetization. The

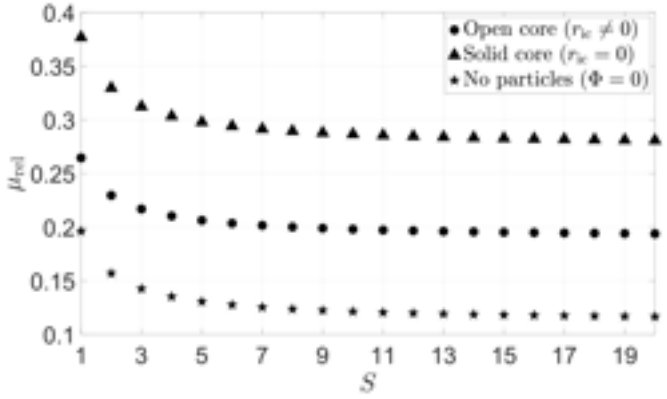

Figure 4.5: Relative magnetic moment (μ_{rel}) of an MCM with $S \in \mathbb{Z}^+$ segments. The values of μ_{rel} are specific to CMs made from segments with design variables as listed in Table 4.1. Values are shown for three cases: segments with open ($r_{\text{ic}} = 0$) and closed ($r_{\text{ic}} \neq 0$) central core cylinders, and segments without magnetic particles ($\Phi = 0$). The presented MCM ($S = 9$) has a relative magnetic moment of 0.2.

PDMS is mixed at base:curing agent ratio of 10:1, PrFeB added at a volumetric ratio (Φ) of 0.25, and the suspension degassed in a vacuum chamber.

A mold and center rods are printed (Form-2, Clear resin, Formlabs, USA) and baked at 120 °C for 1 h to prevent PDMS curing inhibition [151]. The mold is treated with release spray (Ease Release 200, Smooth-On Inc., USA) prior to MPC injection. The molding process is shown in Figure 4.6A-B. First, rods are placed in the molds, forcing injected MPC along the helical path. Second, rods are removed and the mold further filled with MPC. Third, rods are reintroduced and the MPC vulcanized at 90 °C for 1 h. Finally, the molds are placed inside a uniform magnetic field of 2 T, generated by an electromagnet (GMW 3474-140, GMW, Redwood City, California), to axially magnetize the MPC helices.

The multi-segment MCM (Fig. 4.6C-D) is assembled by sliding MPC helices and N48 NdFeB ring magnets (ID: 1.5 mm, OD: 4 mm, $L_{\text{mag}} = 1$ mm (Neomagnete, Berlin, Germany)) over a silicone tube (ID: 0.5 mm, OD: 1.5 mm, Advanced Fluid Solutions, UK). The faces of ring magnets and helices are

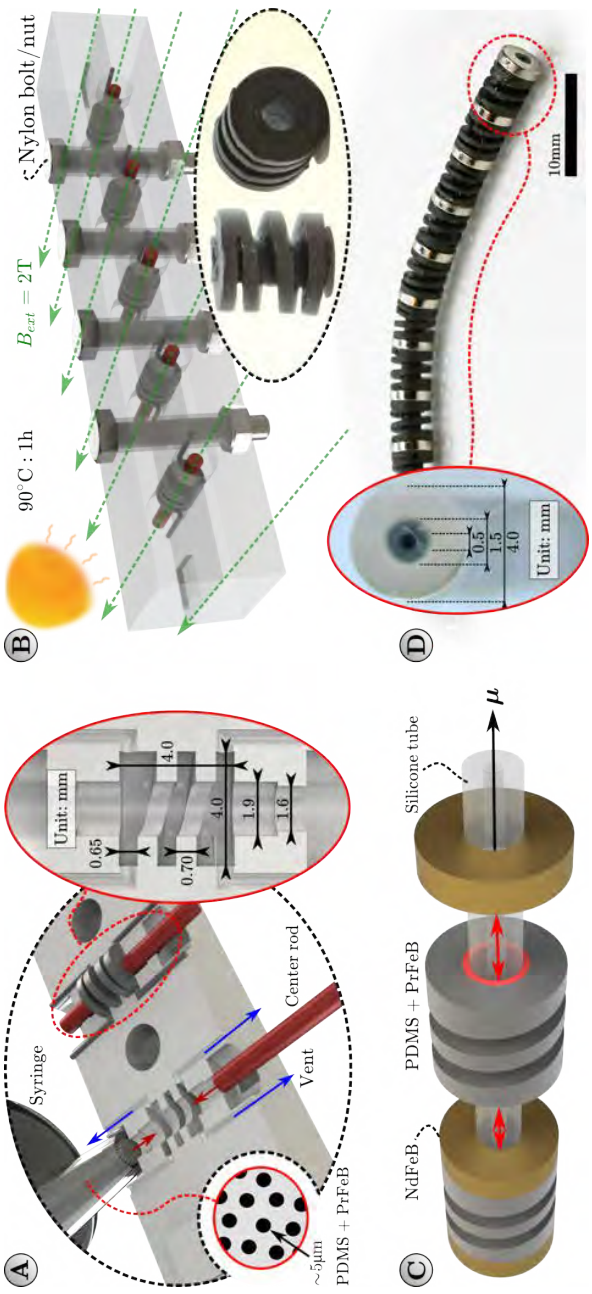

Figure 4.6: Fabrication process of segments and the MCM. (A) Injection molding. A magnetic polymer composite (MPC) mixture of polydimethylsiloxane (PDMS) and praseodymium-iron-boron (PrFeB) microparticles is injected in a mold fabricated by means of stereolithography. The segment open central channel is obtained by placing a center rod (shown in red) to occupy the center of the mold. (B) The MPC inside the molds is heat cured and magnetized inside a 2 T uniform external field. The center rods are subsequently pulled out to get the final MPC helices. (C) Assembly of the multi-segment MCM. Permanent ring magnets and MPC helices are slid over a silicone tube and fixed in place with Loctite 401. The red circle indicates the core cylinder of the MPC helix, which is part of the bulk helical structure and is made of the same material. (D) Final assembled multi-segment MCM. Zoomed in frontal image of the MCM tip with 4 mm diameter, showing the silicone tube backbone (OD: 1.5 mm) with open central lumen (ID: 0.5 mm).

further adhered using Loctite 401.

4.3.3 Local dipole interactions and flexibility

To validate the Cosserat rod model and demonstrate the effect of local dipole interactions, we consider angular deflection of three different segments: helix, helix with a tip magnet, and helix with a base and tip magnet (Fig. 4.7A). The same helix is used to avoid variations between samples. Segments are suspended horizontally in the workspace of an electromagnetic actuation system [84].

A perpendicularly oriented magnetic field is applied to deflect the segments. The workspace is recorded with two Dalsa Genie Nano RGB cameras (Teledyne Dalsa, Waterloo, ON, Canada). Tip deflection is computed with a previously reported shape reconstruction algorithm [91], [111]. Additionally, flexibility is demonstrated by comparing deflection of a three-segment MCM to that of an MPC-cylinder. The MPC-cylinder is made as a solid cylinder with $\Phi = 0.2$ to match the relative magnetic moment of the MCM (Fig. 4.5).

Magnetic forces on the multi-segment MCM (Fig. 4.6D) are quantified using the setup shown in Figure 4.7C. The MCM is fixed in a rigid non-magnetic holder and attached to a three-axis force sensor (K3D40, ME-Meßsysteme GmbH, Henningsdorf, Germany). A cylindrical magnet (composed of 2 magnets: N45, 45 mm diameter, 30 mm length) is moved with a robotic arm in parallel over the MCM and an MPC-cylinder with equal length, diameter, and magnetic moment, from a distance of 40 mm.

To analyze the local dipole interactions between multiple ring magnets in an MCM, we simulate interaction between 2-5 ring magnets at various relative angles. Bending torques on the tip magnet due to the collective field and field gradients of preceding magnets are computed.

4.3.4 Phantom navigation

Maneuverability of the multi-segment MCM is demonstrated inside a silicone vascular phantom using magnetic wrenches exerted by an external permanent magnet. The phantom is fabricated with silicone rubber (40 Shore A hardness, Siliconesandmore, The Netherlands) with a removable

ABS scaffold [152]. The phantom represents the abdominal aorta and its major branches. We lubricate the phantom with silicone oil to reduce friction. Pulsatile flow is mimicked with a peristaltic pump (ISM 404, Ismatec, Wertheim, Germany) and an emulsion of water and red food dye. Two example demonstrations are performed: flow-off and flow-on. With flow-off, delivery of a contrast dye simulant through the MCM backbone, as well as passing a guidewire in vessel bifurcations is shown. For the demonstration with the guidewire (OD: 0.89 mm, Terumo Europe), the silicone tube backbone is replaced with a PTFE backbone (ID: 1.4 mm, OD: 1.48 mm, Zeus Inc.). During flow-on, the pulsatile flow of the pump is set to 2.7 L/min, which is within the physiological range found in the abdominal aorta [153].

4.4 Results

Experiments are performed to demonstrate the effect of local dipole interactions on bending flexibility of magnetic segments. Flexibility of the helical design is compared to an MPC-cylinder with similar length, diameter, and magnetic moment. Forces on the MCM exerted by an external permanent magnet are quantified for demonstration of MCM maneuverability. Finally, maneuverability of the MCM is shown using magnetic wrenches exerted by an external magnet.

4.4.1 Local dipole interactions

Influence of local dipole interactions between ring magnets on the bending response of magnetic segments is demonstrated by measuring tip angular deflection (α) for three different segments: MPC helix (red), helix and tip magnet (green), and helix with tip and base magnet (blue), shown in Figure 4.7A. Helices are designed to bend a maximum of $\Theta = 40$ °. For each field magnitude ($\|\boldsymbol{B}_{\text{ext}}\| \in [0, 30]$ mT) we reconstruct the segment tip deflection 12 times. [111] For the segment shown in Figure 4.7A, the addition of the base magnet reduces the required external field magnitude on average by 31 % for similar deflection angle, in the range of 5-25 mT.

Cosserat model predictions of helix deflection with a tip and base magnet (dashed blue), and with only a tip magnet (dashed green), follow the measured deflections during the transient response (Fig. 4.7A). However,

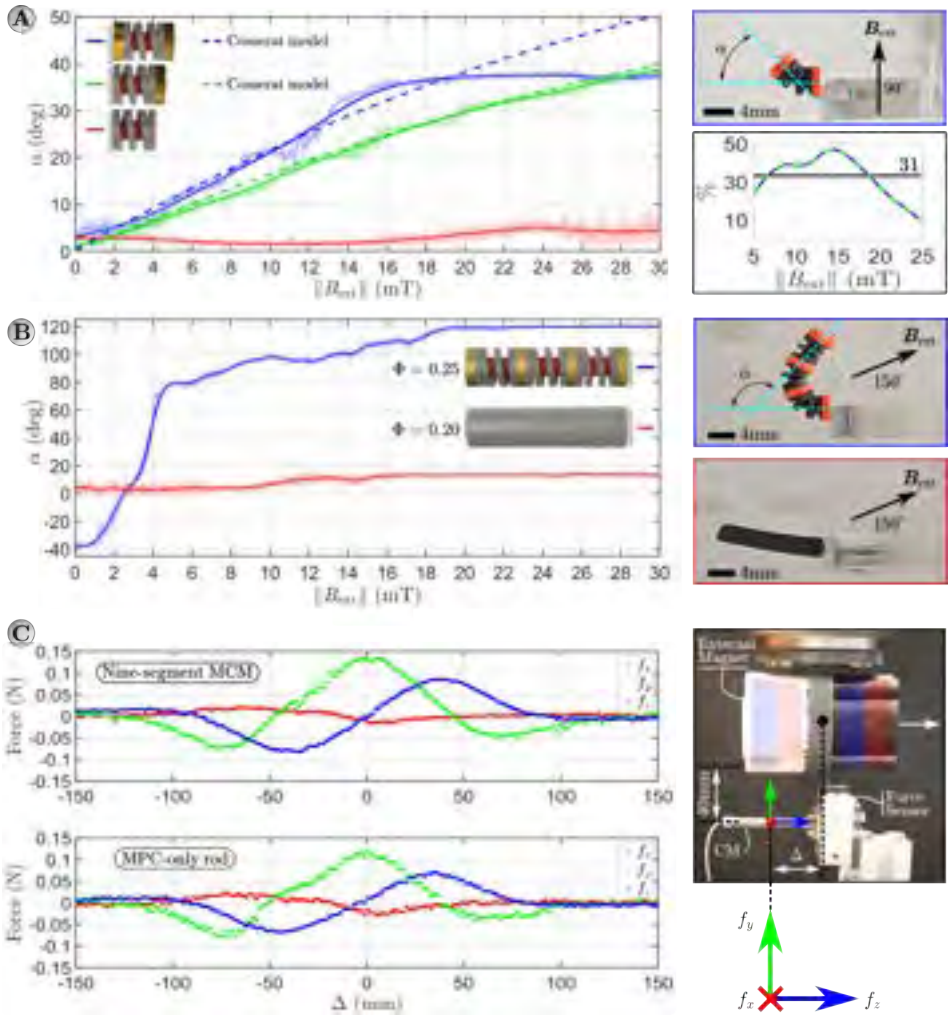

Figure 4.7: Results showing local dipole interactions, flexibility, and exerted forces with external magnetic field and field gradients. (A) Angular deflection (α) of an MPC helix (red), MPC helix with tip magnet (green), and MPC helix with tip and base magnet (blue). Mean measured (dotted, 12 measurements), standard deviation (shaded), best fit (solid), and model prediction (dashed) are shown. The blue best fit shows 31 % increased tip deflection compared to green best fit. (B) Angular deflection of a three-segment MCM and MPC-cylinder with equal dimensions and relative magnetic moment. (C) Magnetic forces exerted on a nine-segment MCM and an MPC-cylinder ($\Phi = 0.2$) of similar dimensions and relative magnetic moment. An external magnet at a distance of 40 mm is moved in parallel over the MCM and rod. Measurements are shown for relative displacements (Δ).

physical bending limitations imposed by Θ are not captured by the model. Therefore, the model may be inaccurate in modeling deflection response of multiple connected segments. Model and experimental results suggest that Cosserat rods can be used to predict the effect of local dipole interactions on the deflection response of single-segments. Model versatility allows changing parameters such as magnetic particle concentration, helix and ring magnet dimensions, backbone, as well as magnetization direction, depending on the intended application. The model is available online at `https://github.com/MichielRichter/Magnetic-Soft-Helical-Manipulators`.

Trade-off between magnetic moment and bending flexibility is demonstrated with deflection of a three-segment MCM and MPC-cylinder of similar length, diameter, and magnetic moment (Fig. 4.7B). The three-segment MCM and MPC-cylinder deflect on average 119° and 16° within 20 mT, respectively. The three-segment MCM has a relative magnetic moment (μ_{rel}) of 0.2, which is the same as the MPC rod ($\Phi = 0.2$). We note that a volume fraction of 0.2 for MPC rods has been reported optimal for bending. [56] We observe an unequal amount of bending by segments as each preceding segment experiences additional torques from subsequent segments. This can be addressed by providing different magnetic volume fractions (Φ) to the helices [70].

Magnetic forces on the multi-segment MCM are quantified and compared to an MPC-cylinder (0.2 volume fraction) of similar length, diameter, and magnetic moment, using the setup shown in Figure 4.7C. Forces are exerted by an external magnet composed of two cylindrical NdFeB magnets (45 mm diameter, 30 mm height, N45, Supermagnete), separated by 10 mm. The external magnet is moved in parallel over the MCMs at a 40 mm distance. Magnetic field gradients are responsible for exerted forces (dB_z/dz) and range from 0.7-1 T/m, at a field of 20-30 mT, which can be generated by reported electromagnet and permanent magnet based manipulation systems. [39], [130], [154], [155] Axial force (f_z), attractive force (f_y), and lateral force (f_x) on the MCMs are shown for offsets (Δ) between the centers of mass of the MCMs and magnet. Measured forces are similar in magnitude, indicating a similar magnetic moment of MCMs. Maximum axial force is 0.09 N. We observe nonzero f_x, which is attributed to misalignment of the axial directions of the permanent magnet and MCM. Also,

we observe a non-symmetric force profile for f_y and f_z around $\Delta = 0$, which is due to the 10 mm gap between the two cylindrical magnets that make up the permanent magnet.

Finally, the collective contribution of multiple ring magnets on local dipole interactions is analyzed in simulation for up to five consecutive ring magnets. Ring magnets have relative deflections (1-40°), representing various magnitudes of MCM retroflexion (Fig. 4.8). Ring magnets are represented in the yz-plane. Bending torques due to collective ring magnet fields ($\tau_{x,B}$) and field gradients (τ_{x,B_∇}) on the tip magnet are shown in red, and their sum shown in blue. These local gradients act to increase deflection, while local fields act to oppose. Deflection increases as long as the influence of the collective gradient is dominant compared to the collective field. For a set of two ring magnets used in our work, separated by $L = 4$mm, we observe that the torque due to both field and gradient follows τ_{x,B_∇}. However, increasing the number of magnets shifts the exerted torque towards $\tau_{x,B}$. Decreasing distance between magnets can prevent $\tau_{x,B}$ becoming dominant, as gradients increase faster than fields with decreasing magnet-magnet distance.

4.4.2 Phantom navigation

MCM maneuverability is shown in a phantom representing the human adult abdominal aorta and compared to an MPC-cylinder (0.2 volume fraction). The external magnet (Fig. 4.7C) is manually moved beneath the phantom (Fig. 4.9A) at a 30-40 mm distance. The phantom trajectory includes bifurcations with angles up to 135°. The MCM (Fig. 4.9B) takes on J- and S-shaped forms where the MPC-rod is unable to.

Additionally, to show application of the backbone, the MCM is steered from the left common iliac to the superior mesenteric artery where a contrast dye simulant (water with red dye) is released (Fig. 4.9C, Supplementary Video S1). The simulant is injected with a syringe through the free-hanging backbone from outside the phantom. Then, with the peristaltic pump turned on (flow of 2.7 L/min) the MCM is navigated through the phantom (total path length >50 cm) within 1 min (Fig. 4.9D). Additionally, the backbone may be used as a guiding sheath for, e.g., guidewires to reach distal

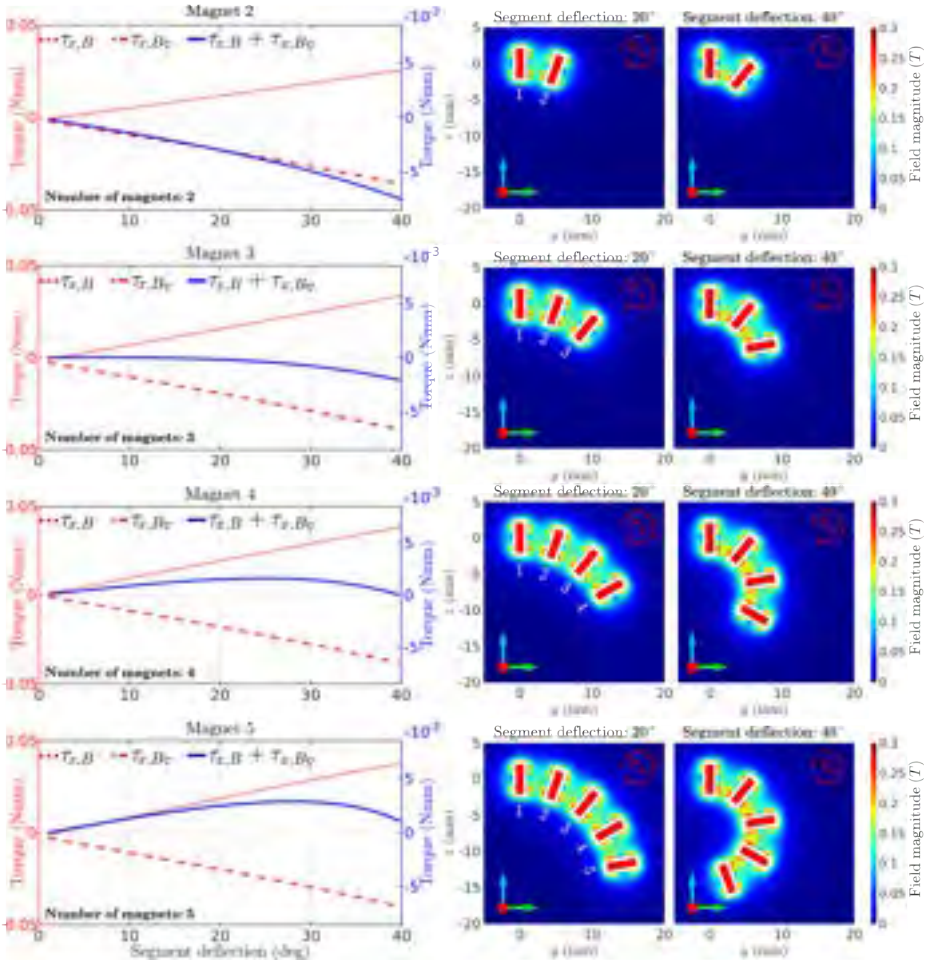

Figure 4.8: Simulation analysis of torques exerted on the tip magnet by collective fields ($\tau_{x,B}$) and field gradients (τ_{x,B_∇}) of preceding magnets. Shown for sets of 2-5 magnets at relative deflections of 1-40°. Left column shows bending torques. Middle column shows positions of ring magnets with relative deflections of 20°. Right column shows positions of ring magnets with relative deflections of 40°. Values are specific to MCM design parameters given in Table 4.1. Magnetic fields from MPC helices are not included.

vessel bifurcations (Fig. 4.9E, Supplementary Video S2). In the future, actuation can be improved by teleoperation of robotically-moved external magnets [155]. Additionally, imaging may be performed with, e.g., C-arm fluoroscopy [128].

During actuation, we initially experienced significant friction between the MCM and phantom. The friction coefficient between silicone surfaces has been reported to be on the order of 1, while that between catheters and porcine vasculature to be between 0.02 and 0.04 [156], [157]. To reduce the friction between the MCM and phantom, we lubricated the phantom with silicone oil. We did not experience hydrodynamic drag forces during navigation, but note that the viscosity of blood in the abdominal aorta may be five times higher than water [158]. Also, at a flow of 2.7 L/min the pump revolutions per minute is higher compared to the beats per minute of a heart at rest. Further, the phantom does not mimic material properties of human blood vessels. In reality, movement through vessels may deform them and possible damaging effects on vessel walls remains to be investigated.

Demonstrations are performed in a 2D phantom. One of the factors that need to be considered for 3D navigation is MCM weight. The presented nine-segment MCM design has a mass of 2.25 g and weight 0.022 N, which can be lifted using the external magnetic field gradients used in this work. Also, insertion into vasculature requires an introducer sheath, which will be a source of friction but could be combined with manual or robotic insertion. Finally, we chose to perform MCM demonstrations in a vascular phantom as it allowed workspace-specific MCM design due to the confinement, nonlinear paths, and sharp turns. We note that this decision is theoretically and design motivated, rather than for a specific application. Therefore, the design principles presented herein may be translated to other medical and non-medical environments.

4.5 Conclusions

We propose a new design for MCMs that combines permanent magnets and MPC and enables increasing diameter without compromising on flexibility and magnetic moment. The condensed hard magnetic particles inside the

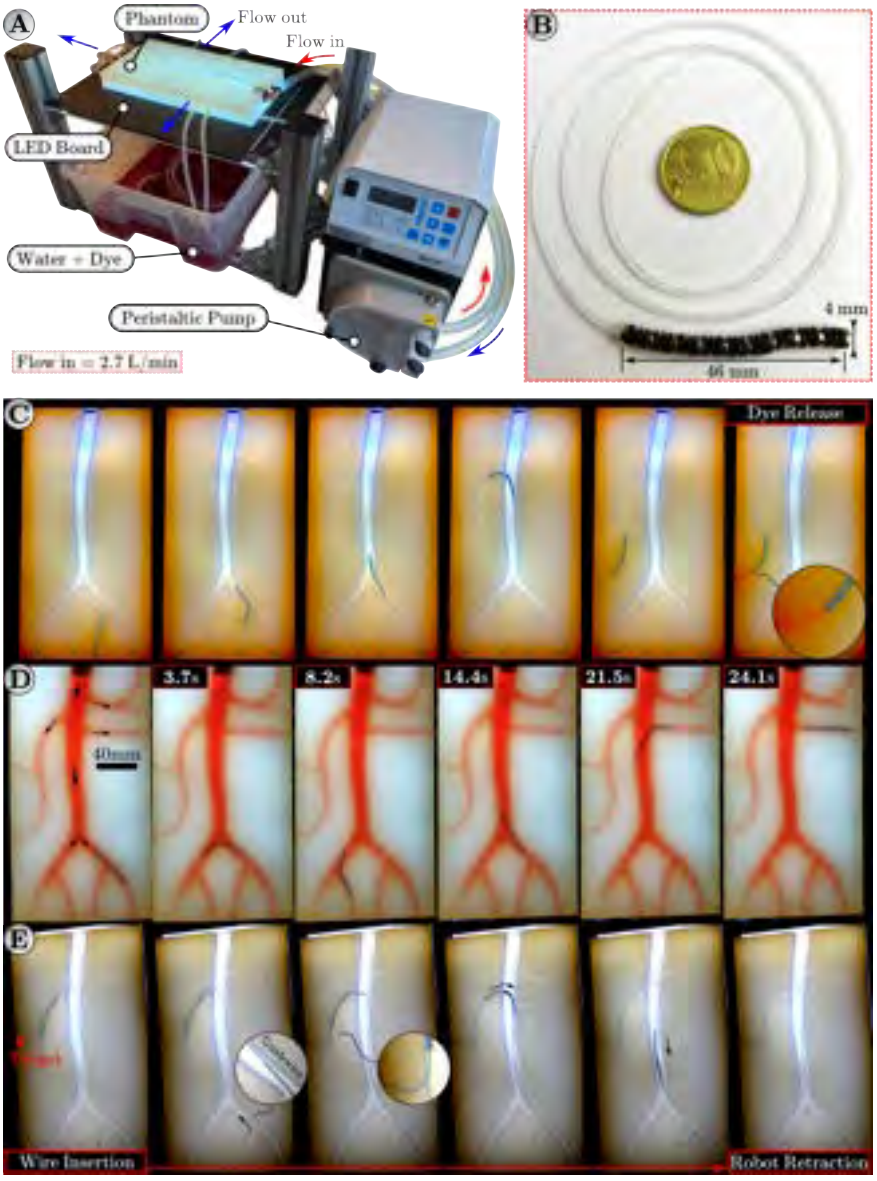

Figure 4.9: Navigation experiments. (A) 2D silicone phantom on an LED board, connected to a peristaltic pump. (B) Assembled 9-segment MCM: 10 ring magnets and 9 MPC helices. (C) MCM maneuvered with a hand-held magnet at 30-40mm; dye simulant released at tip. (D) MCM maneuvered with pump on (2.7L/min); flow direction and MCM positions shown. (E) PTFE backbone replaces silicone tube to pass a guidewire; MCM retracted after delivery

MCM enables utilizing magnetic force for actuation. Compared to MPC-cylinders, the proposed design uses MPC-helices and increases magnetic volume fraction, adds intermittent permanent magnets, and utilizes local dipole interactions between magnets to compensate for additional MPC stiffness. Local dipole interactions between magnets can oppose or promote deflection, depending on dominance of local fields or gradients in exerting bending torques, respectively.

Cosserat rod models can incorporate local dipole interaction effects on segment deflection. The versatility of the model allows changing segment dimensions, magnetic properties, and backbone, depending on intended application. A limitation of the model is that physical bending constraints of segments are not considered. Furthermore, bending torques from collective local fields can increase faster than the local gradients and may become dominant in opposing deflection. Consequently, simulated local dipole interactions within single-segments can not be generalized to multiple connected segments.

In experiments we achieved a 31 % increased tip deflection in single-segments with local dipole interactions compared to those without. Magnetic forces on the order of 0.09 N at external field gradients of 0.7 T/min were able to navigate the MCM through a silicone phantom (length >50 cm) within 1 min. Although comparisons with MPC-cylinders were made regarding maneuverability, the MCM fabrication process is more involved and relatively difficult to apply to submillimeter scales.

In the future, application-specific optimization of the proposed design for both tethered and untethered applications can be studied. While the dipole interaction effect for a particular configuration has been presented, addressing this for other scenarios warrants further investigation. Finally, combining the MCM with backbones made of smart materials, such as thermoset shape memory polymers, may be investigated further.

5

Locally addressable energy efficient actuation of magnetic soft actuator array systems

Note: *The following chapter is adapted from the article "Locally addressable energy efficient actuation of magnetic soft actuator array systems" by* ***M. Richter****, J. Sikorski*, P. Makushko, Y. Zabila, V. Kalpathy Venkiteswaran, D. Makarov, and S. Misra, published in "Advanced Science", vol. 10, no. 24, pp. 2302077, June 2023. The chapter has been reformatted in terms of figures to fit this doctoral thesis. No changes to the technical contents of this peer-reviewed manuscript have been made.*

Authors' Contributions: *MR and JS conceived the project and managed the research. MR fabricated the magnetic composite sheets. JS fabricated the magnetic effectors, and performed and recorded experiments. PM and YZ designed and fabricated planar electromagnetic coils. MR provided the magnetic near-field model. PM performed SEM and VSM characterization of the magnetic composites. PM carried out magnetic stray field imaging and analysis with support by YZ and DM. Additionally, PM and DM fabricated the planar electromagnetic coils and performed SEM measurements on composite sheets. MR compiled figures and videos with support by JS, VKV, PM, DM, and SM. Also, MR, JS, PM, VKV, DM, and SM participated in discussions on the selection of demonstrators and development of the concept of using near-fields for actuation of magnetic soft robots. Finally, MR and JS wrote the manuscript with contributions from all authors. DM and SM supervised this project.*

Funding Information: This work is supported by the European Research Council (ERC) under the European Union's Horizon 2020 Research and Innovation Programme under grant 866494 Project – MAESTRO. Also, this work is financially supported in part by German Research foundation (DFG) grant MA 5144/28-1 and via European Union in the frame of the project REGO (ID: 101070066).

*contributed equally to the work

Abstract

Advances in magnetoresponsive composites and (electro-)magnetic actuators have led to development of magnetic soft machines (MSMs) as building blocks for small-scale robotic devices. Near-field MSMs offer energy efficiency and compactness by bringing the field source and effectors in close proximity. Current challenges of near-field MSM are limited programmability of effector motion, dimensionality, ability to perform collaborative tasks, and structural flexibility. Herein, a new class of near-field MSMs is demonstrated that combines microscale thickness flexible planar coils with magnetoresponsive polymer effectors. We apply ultrathin manufacturing and magnetic programming of effectors to tailor their response to the non-homogeneous near-field distribution on the coil surface. The MSMs are demonstrated to lift, tilt, pull, or grasp in close proximity to each other. These ultrathin (90 μm) and lightweight (100 g/m^2) MSMs can operate at high frequency (25 Hz) and low energy consumption (0.5 W), required for the use of MSMs in portable electronics.

5.1 Introduction

The use of soft materials in mechatronics has opened up a vast design space permitting the development of new classes of machines [52], [159]–[162]. Related developments have shifted paradigms in a range of engineering disciplines, driving the transition from bulky, rigid constructions to flexible, lightweight integrated assemblies in areas such as biorobotics [163], haptics [164], [165], surgical technology [67], and microrobotics [166]. Magnetic fields have been extensively studied as one of the principal ways of actuating such soft machines.

Magnetic soft machines (MSMs) consist of soft elements with programmable magnetic properties, such as magnetoresponsive polymers[58] and small-scale electromagnetic coils[167]. The response of these elements to magnetic fields can mediate multitudinous mechanical behaviour of MSMs [168], [169], while allowing them to retain simple structure [55], [141], [170], [171], permitting laser machining [172], [173] and assembly [174], [175].

The magnetization profile of an MSM determines the response in a mag-

netic field. In particular, the actuation response of magnetoresoponsive polymers can be programmed by magnetizing in molds [54], [176], printing magnetic domains [140], [177], magnetic reprogramming [178]–[180], or programming of magnetic voxels [181]. Generally, MSMs are designed to operate in magnetic fields while taking advantage of surrounding field topology.

Far-field MSMs operate in magnetic fields generated by arrays of electromagnets or permanent magnets at distances up to a few tens of centimeters [40], [68], [182]. These MSMs can operate as untethered [183]–[185] or tethered devices [56], [127], [186], made of magnetoresponsive polymers or small electromagnetic coils [129]. Although far-field MSMs are highly mobile within their workspace, the workspace portability is tied to that of the magnetic field generation systems, which are generally bulky and heavy systems with limited portability. Consequently, far-field MSMs are often proposed for applications where workspace portability is less of a concern and miniaturization and untethered operation is advantageous, such as for biomedical applications [187], [188] as grippers [181], [189], muscles [190], stents [191], guidewires [155], and drug-delivery devices [175], [192].

Although proven to be challenging, there are active explorations aiming to realize independent and collaborative control of multiple far-field MSMs, including modulating phase or frequency response [106], [168], [181], [201], [202], geometry-based magnetic anisotropy [203], [204], stiffness variability [205], or manipulating the field topology [83], [206] at the cost of system complexity [207]. In the latter case, independent control of far-field MSMs, which are generally actuated with magnetic torques, requires 3 DOFs per effector when gradients are considered negligible [68]. Consequently, although large coils can have relatively low resistance [84], the increasing number of required coils and needed driving currents (scaling with distance) for independent control of far-field MSMs [206] result in high power consumption.

Alternatively, near-field MSMs bring field source and effector in direct vicinity. For example, permanent magnets are used for local magnetization and attraction of magnetorheological [208], [209] and ferrofluidic robots [210], or combined with liquid metal-based coil effectors to pro-

	Electromagnetic near-field source				Effector				Actuator	
Ref.	**Thickness (µm)**	**Field (mT)**	**Gradient (mT/mm)**	**Flexible**	**Type**	**Thickness (µm)**	**Magnetic profile**	**Motion**	**Sources (#)**	**Work Density ($kJ/(m^3 \cdot A)$)**
[193]	$30 \cdot 10^3$	6.7	-	no	fluid	-	adaptive	planar	25	-
[194]	$10 \cdot 10^3$	-	-	yes	perm.	$6 \cdot 10^3$	uniform	linear	1	0.056
[72]	$4 \cdot 10^3$	1.5	-	yes	perm.	700	uniform	linear	2	$2.5 \cdot 10^{-4}$
[195]	803	-	-	yes	perm.	500	uniform	planar	-	-
[196]	540	-	-	no	perm.	400	uniform	planar	48	-
[197]	470	0.1	-	no	perm.	500	uniform	planar	-	-
[198]	450	0.5	2	no	perm.	500	uniform	planar	128	-
[199]	378	0.5	2	no	perm.	790	uniform	planar	64	-
[200]	850	1	0.7	no	perm.	500	uniform	planar	64	-
[71]	376	0.8	-	no	polym.	170	uniform	linear	1	$8 \cdot 10^{-5}$
This	59	2	1	yes	polym.	30	nonunif.	progra.	1	0.3

Table 5.1: Comparison of near-field actuators comprising stationary electromagnetic sources with mobile effectors. For multi-layer printed circuit board-based sources [195]–[200] we have taken the distance between traces to be 0.2 mm for approximating thickness, unless reported otherwise. Effectors are reported in terms of type (Perm., permanent; Polym., polymer), thickness, magnetization profile (Nonunif., nonuniform), and motion (Progra., programmable). For the combined sources and effector the number of utilized sources per effector are shown. Also, work densities are listed, normalized with respect to currents. Values marked (-) are not reported in the respective works. Listed values are approximations where the indication "$\sim$" has been omitted for compactness.

duce soft fish-tail actuators [211], [212]. However, these permanent magnet sources are stiff, require mobility to modulate the field, or require electromagnetic effectors which are challenging to miniaturize. Alternatively, electromagnetic near-field sources generate time-varying fields. For example, copper solenoid arrays control planar motion of ferrofluidic robots [193], liquid metal-based solenoids exert linear forces on a permanent magnetic core for biomimicry [194] and push and pull permanent magnets as part of a soft gripper [72]. Also, printed circuit board-based coil arrays control diamagnetically levitating permanent magnets [195], [196], or direct sliding motion of disk-shaped permanent magnets [197]–[200]. Finally, planar copper coils deflect uniformly-magnetized membranes for microfluidic applications [71].

In this study we propose magnetoresponsive polymer effectors tailored to the nonhomogeneous axial and radial distribution of electromagnetic near-fields generated by ultrathin flexible coils. There are several advantages to this approach. First, the combination of electromagnetic near-field sources with magnetoresponsive polymer effectors combines the miniaturization ability and magnetic programmability of magnetoresponsive polymers with the temporal control of electromagnetic near-fields. Second, the flexibility of both effector and coil allows integration of the MSM onto flexible portable substrates. Third, the localized near-field permits independent actuation of MSMs in an array in close proximity. Additionally, model-based optimization of magnetoresponsive polymer effectors improves actuation response and allows utilization of the full functional surface area of the coils. A comparison between different electromagnetic near-field MSMs is presented in Table 5.1 to place this work in the context of the state of the art.

We report such near-field MSMs that combine single-layer planar coils with magnetoresponsive polymer effectors (henceforth called "effectors"). These flexible, ultrathin (30-300 μm), lightweight (100 g/m^2, including effector and coil), low power (down to 500 mW), and fast (25 Hz) machines operate with near-fields and gradients on the order of 2 mT and 1 T/m, respectively. We demonstrate near-field model-based computation of task-specific magnetization profiles on the basis of simulated exerted torques and forces. This methodology in combination with jig-based magnetiza-

tion and assembly-based fabrication produces effectors capable of lifting, tilting, pushing and pulling, and grasping. Further, we show operation of near-field MSMs in both air and aqueous environments, independent actuation in close proximity, synergistic operation, and integration on portable flexible curved surfaces to provide functionalization.

5.2 Results

The proposed near-field MSMs comprise two functional elements: A flexible planar spiral electromagnetic coil and a polymeric magnetic soft effector (Fig. 5.1.1). The magnetic soft effectors are considered parallel to the coil in its direct vicinity (< 1 mm). The function of each effector is mediated by deformation in response to the magnetic near-field ($\boldsymbol{B} \in \mathbb{R}^3$) generated by the current running through the coil (Fig. 5.1.2). We represent the near-field using a multipole expansion model fitted to field measurements within a volumetric sweep obtained above the coil surface. The magnetic field is provided with respect to the coil center reference frame ($\{\mathcal{C}\}$, Fig. 5.1.3) and depends on the geometry of a particular coil design. In this work, we use spiral copper coils with an outer radius of $R_\mathrm{o} = 6$ mm, inner radius of $R_\mathrm{i} = 1$ mm, Cu wire thickness of 9 µm, and resistance of 12 Ω, attached to a thin Mylar foil of thickness 50 µm (Fig. S5.1).

5.2.1 Magnetic near-field

The nonhomogeneous magnetic near-field ($\boldsymbol{B} \in \mathbb{R}^3$) generated by the coils at a unit current ($I = 1$ A) reaches magnitudes up to 2 mT, scaling linearly with operating current (Fig. 5.1.2). Gradients in the near-field are on the order of 1 T/m (Fig. S5.2). At steady operating currents of $I = 0.2$ A the magnetic near-field and gradient reaches 0.4 mT and 0.2 T/m, respectively, with a power consumption of 0.5 W. This power consumption is at least two orders of magnitude smaller than the wattage necessary for producing similar gradients with magnetic far-fields generated by large iron-cored electromagnets at conventional operating distances [84].

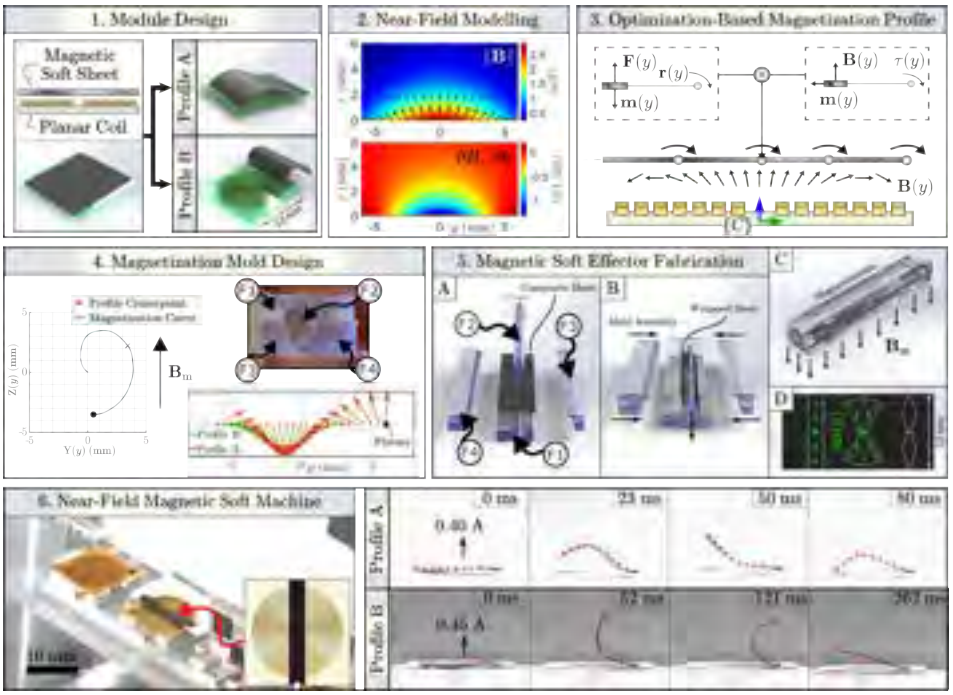

Figure 5.1: Design and fabrication of near-field magnetic soft machines (MSMs). (1) Near-field MSMs consist of magnetic soft elements as effectors located in proximity to a flexible planar coil substrate. Effectors can have different magnetization profiles that determine their deformation in response to the magnetic near-field of the coil. **(2)** Magnetic near-field profile ($\boldsymbol{B} \in \mathbb{R}^3$) and axial gradients ($\partial B_z/\partial z$) in the yz-plane above the coil surface produced by a current of 1 A. **(3)** Effectors lay flat on the coil in their reference configuration. The magnetization profile along the coil diameter ($\boldsymbol{m}(y) \in \mathbb{R}^3$) determines the experienced force ($\boldsymbol{F}(y) \in \mathbb{R}^3$) and torque ($\boldsymbol{\tau}(y) + \boldsymbol{r}(y) \times \boldsymbol{F}(y) \in \mathbb{R}^3$) due to the near-field ($\boldsymbol{B}(y)$), where $\boldsymbol{r}(y)$ represents a moment arm. **(4)** Two different desired effector magnetization profiles A and B, optimized for bending torque. Profile B constrains $\boldsymbol{\tau}(y)$ to be in the direction of bending. A 2D magnetization curve $(\mathrm{Y}(y), \mathrm{Z}(y))$ is computed from magnetization profiles (shown for profile A). Wrapping effectors around the curve in an external homogeneous field ($\boldsymbol{B}_\mathrm{m}$) results in the desired magnetization profile (also see Fig. S5.5). A 3D mold (F1-F4) is printed that represents the magnetization curve. **(5)** Unmagnetized sheets are wrapped inside the mold and magnetized (A-C). Post-magnetization the sheets have a non-uniform and uniform magnetization along their short and long axis, respectively (D). The sheets are laser-cut to form (parts of) effectors. **(6)** Coil and effector are assembled as a near-field MSM. Effector magnetization profile determines deflection response. High field gradients near the coil surface facilitate fast effector displacement (also see Fig. S5.7).

5.2.2 Magnetic soft effectors

Motion of magnetic effectors within the magnetic near-field generated by the coil results from exerted distributed forces ($\boldsymbol{F} \in \mathbb{R}^3$) and torques ($\boldsymbol{\tau} \in \mathbb{R}^3$), determined by the magnetization profile ($\boldsymbol{m} \in \mathbb{R}^3$) of the effector. For application-specific optimization of the magnetization profile we consider the effector as a parametric surface $\boldsymbol{r}(\alpha, z) = (r\cos\alpha, r\sin\alpha, z)$ parallel to the coil, where $\alpha \in [0, 2\pi]$, $r \in [0, R]$ spans the radius of the coil, and $z \in \mathbb{R}^+$ is the distance between the coil and effector.

Effectors are obtained by assembly of strips of pre-magnetized magnetic composite elements, which are laser-cut from magnetized sheets. The sheets are based on polydimethylsiloxane (PDMS) and hard magnetic microparticles with a volumetric ratio of 0.35 (Fig. S5.3). Here, we use a sheet thickness within the range of 30-400 µm depending on desired MSM functionality. This assembly method, as well as axially symmetric of the magnetic near-field, simplifies computation of magnetization profiles to one dimension, reducing the parametric surface to a straight curve ($\boldsymbol{r}(\alpha, z) \rightarrow (0, y, z)$) with $y \in [0, 2R]$ spanning the coil diameter. The magnetization profile of each element ($\boldsymbol{m}(y)$) is computed assuming their unactuated planar configuration (refer to Supplementary Text 1 and Fig. S5.4). The operation of each element is dictated by the acting distributed forces ($\boldsymbol{F}(y) = \nabla(\boldsymbol{B}(y) \cdot \boldsymbol{m}(y))$ and torques ($\boldsymbol{\tau}(y) = \boldsymbol{m}(y) \times \boldsymbol{B}(y)$) in the magnetic near-field of the coil (Fig. 5.1.3).

A homogeneous magnetic field ($\|\boldsymbol{B}_\mathrm{m}\| = 2$ T) is used for magnetization of magnetic composite sheets (Fig. 5.1.4). Combining the desired magnetization profile ($\boldsymbol{m}(y)$) of the sheets with the external field, a relative magnetizing angle ($\theta(y) = \angle(\boldsymbol{m}(y), \boldsymbol{B}_\mathrm{m})$) is computed. The relative magnetizing angles of the sheet across the coil diameter are used to compute a 2D magnetization curve, providing the desired magnetization profile of sheets when subjected to $\boldsymbol{B}_\mathrm{m}$ (Fig. S5.5). From the 2D curve, a 3D mold is fabricated for sheet magnetization (Fig. 5.1.4 F1-F4). The general structure of the mold (Fig. 5.1.5 A-C) facilitates folding of the composite sheets, permitting precise high-throughput and time-efficient magnetization, and providing a non-uniform and uniform magnetization along the short and long axis of the sheet, respectively (Fig. 5.1.5 D). The non-uniform magne-

tization profile along the short axis of the sheets are validated with stray field measurement-based reconstruction (see Supplementary Text 2 and Fig. S5.6).

The final magnetic effectors are assembled using kirigami-based techniques. Laser engraving is used to cut desired shapes from the magnetized sheets, constituting magnetic composite elements as building blocks for the effectors (Fig. 5.1.5 D). We demonstrate our framework using two elementary MSMs. The magnetic effectors constitute a continuous strip fixed to the coil substrate on one side (Fig. 5.1.6). Interaction between the near-field and magnetized material within the effectors produce bending moments cause C- and S-shaped deflection directly upon coil activation (movie S1). Using a high-speed camera in conjunction with an autonomous tracker the effectors are capable of moving with a maximum speed of 0.4 m/s and reach a steady state at 100-150 ms (Fig. S5.7). This dynamic response of the effector can be modified by activating the MSM with a different temporal profile of the magnetic near-field.

5.2.3 Individual magnetic soft machines

The current running through the electromagnetic coil of an MSM provides one degree of freedom to the magnetic effector. Effectors can be cut and assembled with varying structural complexity using kirigami-based techniques. These effectors can be designed to lift, tilt, grab, and pull/push by modifying the effector magnetization profile. We demonstrate this in a study employing effectors cut out of magnetic polymer sheets of thickness 30 µm with application-specific magnetic moment profiles (Fig. 5.2).

Lifting effectors employ a symmetric magnetization profile optimized for maximum vertical force at the coil center, as well as bending moments at the boundary. These MSMs are capable of vertical lifting of a payload (Fig. 5.2.1, movie S2). The lifting MSMs are assembled from two strips of magnetic composite soft elements placed perpendicular to one another and connected in the center. Flexures are laser cut in the effectors to enable stretching during vertical motion. The resulting MSM, constituting both coil and effector, has a weight of 15 mg and is able to lift payloads of 25 mg (Fig. 5.2.1 A1-A2) and 60 mg (Fig. 5.2.1 B1-B2) at coil currents of 0.2 A

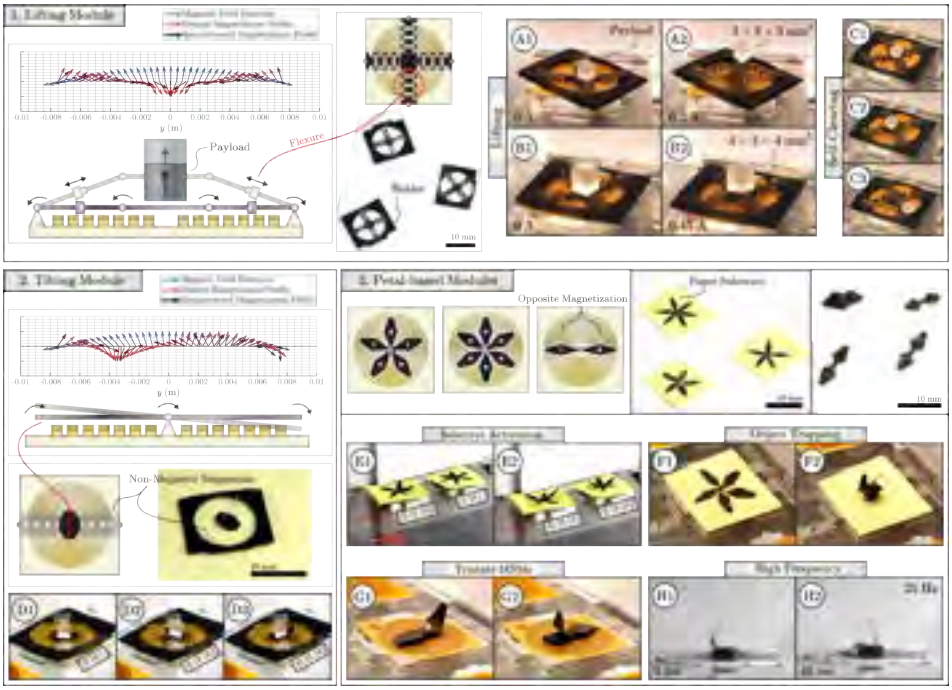

Figure 5.2: Examples of individual near-field magnetic soft machines (MSMs). **(1)** Lifting MSMs have magnetization profiles optimized for lifting forces at the center and bending moments on the connecting arms. Flexures are laser-cut on the arms to permit stretching. Payloads of 27 mg (A1-A2) and 64 mg (B1-B2) are lifted by the MSM weighing 15 mg, comprising coil and effector. High-bandwidth vibratory motion (> 10 Hz) facilitates shaking off payloads (C1-C3). **(2)** Tilting MSMs maximize torque about their transverse axis. The effectors are suspended above the coil by a non-magnetic polydimethylsiloxane (PDMS) strip containing flexures to enable stretch. These MSMs are able to tilt, e.g., a payload, here an 27 mg cube (D1-D3). **(3)** Petal-shaped elements are fixated on the coil center and have magnetization profiles that optimize bending moments at positive or negative coil current. Effectors can be activated selectively while being in close proximity, depending on current direction (E1-E2). Assemblies of identical petals show axisymmetric gripper-like deformation for object trapping (F1-F2). Oppositely-magnetized petals can be combined to make tristate MSMs, which have different configurations at positive, negative, and no current (G1-G2). Rapid phase shift in coil current allows effector motion at high frequency (H1-H2).

and 0.45 A, respectively. The payloads are 3D printed cubes with dimensions $3\times3\times3$ mm^3 and $4\times4\times4$ mm^3. Additionally, high-bandwidth motion of the lifting MSMs ($>$ 10 Hz) permits shaking off payloads (Fig. 5.2.1 C1-C3). The stroke length of the lifting effector is approximated at 2 mm for the 25 mg ($26.5 \cdot 10^{-5}$ N) cube in movie S2. Considering the approximate volume of the coil ($\varnothing 12 \times 0.06$ mm^3) and effector ($\varnothing 12 \times 0.03$ mm^3), the corresponding work density is on the order of 0.052 kJ/m^3. Similarly, considering the MSM weight of 15 mg the corresponding work capacity of the lifting MSM is on the order of $0.35 \cdot 10^{-4}$ kJ/kg. These values are for coil currents of 0.2 A. For currents of 1 A the work density and capacity scale linearly to 0.26 kJ/m^3 and $1.75 \cdot 10^{-4}$ kJ/kg, respectively.

Tilting effectors have a magnetization profile optimized for torque about their central axis (Fig. 5.2.2). These effectors are suspended over the coil center using a non-magnetic PDMS flexure-based segment. Such MSMs constitute a lightweight miniaturized tilt table to manipulate the orientation of cargo (Fig. 5.2.2 D1-D2, movie S3). Tilting effectors respond oppositely to positive and negative coil currents.

Gripper-like effectors are assembled from subcomponents referred to as petals, which can employ different magnetization profiles and be activated selectively (Fig. 5.2.3 E1-E2). These petals have a magnetization profile that maximizes the bending moment with respect to their point of attachment on the coil center (movie S4). Combining petals with similar magnetization profiles results in self-locking effectors suitable for object trapping (Fig. 5.2.3 F1-F2). The gripper does not reopen due to the combination of attractive forces in the locked state and the petals deflecting beyond the near-field. Finally, petals with dissimilar or opposite magnetization profiles may be combined to produce effectors with functional responses at different coil polarities, providing tristate MSMs (Fig. 5.2.3 G1-G2). Additionally, the petal-based MSMs are capable of periodic motion at frequencies reaching 25 Hz (Fig. 5.2.3 H1-H2).

5.2.4 Arrays of magnetic soft machines

Individual MSMs may be arranged as arrays with the possibility to be interconnected (Fig. 5.3). Due to the drop-off in the near-field magnitude

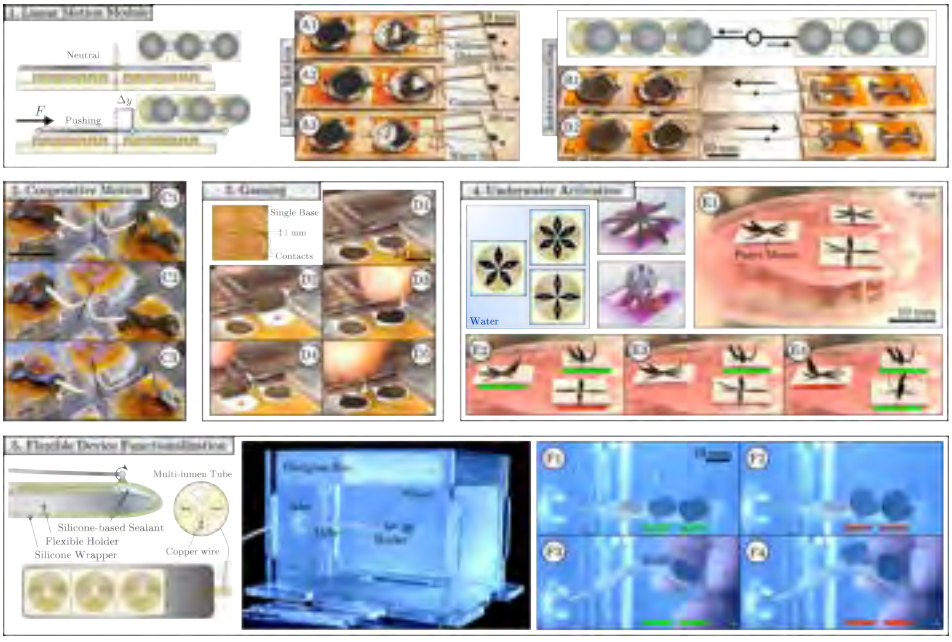

Figure 5.3: Magnetic soft machines (MSMs) as magnetic soft actuator array systems. **(1)** Interconnected effectors as soft muscles with planar linear force-optimized magnetization profiles. **(2)** Deflecting MSMs are interconnected to tilt a connecting element: a pre-bent paper strip. **(3)** Proximal positioning and independent actuation of effectors at non-equal time instants can be used for human interaction as a game. **(4)** Different effectors can be placed in proximity to each other and activated underwater, possibly permitting underwater applications. The bars underneath effectors indicate coils running positive (green), negative (red), or no (empty) current. **(5)** MSMs may be arranged on flexible or curved holders, suitable for medical applications. Coils and effectors are separated by a fluid-impermeable membrane, allowing effectors to operate while shielding the coil from direct contact with a surrounding fluid.

of the coil beyond its radial edge, the proximally positioned MSMs can be independently controlled.

Radial linear motion MSMs contain effectors that displace in the radial direction upon coil activation (Fig. 5.3.1, movie S5). The effectors carry magnetization profiles that are optimized to experience magnetic forces in the radial direction on the coil surface, with the achievable forces being quantified in simulation (Fig. S5.8). Notably, radial forces scale nonlinearly with effector thickness and displacement from the coil center, and linearly with magnetic volumetric ratio and coil current. The maximum stroke length of these effectors is approximately equal to the coil radius (R), that is a forward and backward stroke of $R/2$ constituting push/pull action. For a specific case of effectors with a thickness of $0.6p5 : f2$mm, magnetic volumetric ratio of 0.35, and coil current of $I = 1p5 : f2$A, the maximum work density and work capacity are on the order of $0.3p5 : f2\text{kJ/m}^3$ and $1 \cdot 10^{-4}p5 : f2$kJ/kg, respectively. Interconnection of these effectors for collaborative pulling and pushing action additively improves the achieable forces upon simultaneous activation. Alternatively, the linear motion MSMs can be positioned in an array and actuated independently for stand-alone or collaborative action (Fig. S5.9, movie S5).

Further, interconnected MSMs may also be selectively activated to achieve motion of an interconnecting structure, unable to be performed by individual MSMs (Fig. 5.3.2). Here, simultaneous antagonistic or agonistic activation of MSMs results in tilted or level orientation of the connecting element, respectively (movie S6). Interconnecting multiple similar or dissimilar MSMs can thus provide multi-DOF motion to connecting bodies.

Alternatively, arrays of individual MSMs and their independent activation can be used for human interaction (Fig. 5.3.3). Selective activation at non-equal time instants as well as their durability and safety, can be used for the realization, e.g., of interfaces intended for gaming, rehabilitation, and concentration practice (movie S6).

Finally, proximal MSMs can be activated within aqueous environments (Fig. 5.3.4). By contrast, selective activation of conventional far-field MSMs arranged in close proximity would require magnetic shielding or

multi-DOF electromagnetic systems. The flexibility of the coils permits integration and functionalization of flexible instruments (Fig. 5.3.5, movie S7). Coils are applied on a flexible 3D-printed holder. The MSMs can be operated when submerged underwater. A thin ($200p5 : f2\mu m$) rubber sheet around the holder shields coils from direct contact with water. Coils transition from a planar to curved surface without loss of functionality. Functionalization of a flexible probe tip is demonstrated with an array of grasping MSMs (Fig. 5.4). The effectors are able to press a payload between themselves and the coil surface (Fig. 5.4A). Payload transport and release is mediated by the direction of current through the coils (Fig. 5.4B). The flexible tip is designed to operate within a fluidic environment, shielding the coil from direct contact while allowing independent control of effectors (Fig. 5.4C). Deformation-independent functionality of the coils allows integration on passive and active flexible soft robots (Fig. 5.4D). The effectors are able to hold a payload (weight $20p5 : f2mg$) against the direction of gravity and release on demand (Fig. 5.4E). This demonstrates that the presented technology enables development of portable flexible devices with arrays of independently controlled actuators.

5.3 Discussion

This study reports operation of optimally-magnetized magnetoresponsive polymer effectors in the nonhomogeneous magnetic near-field generated by planar single-layer coils. By combining the microscale thickness manufacturing of coils and effectors, as well as utilizing a near-field localized to the surface area of the coils, selectively actuable and densely packed devices can be realized at scales that are currently infeasible for otherwise actuated structures, such as tendons or hydraulics. Based on the axial and radial distribution of the near-field and gradients, effector magnetization profiles are tailored to maximize torques or forces. We demonstrate the near-field MSMs as axial and radial linear actuators, tilting devices, grippers, gaming tools, and functional elements on flexible curved surfaces in air and aqueous environments.

The presented magnetic soft effectors expand the achievable motion of near-field MSMs seen in literature thus far. For example, looking at the existing tethered systems in this field, the arms of grippers are collectively actu-

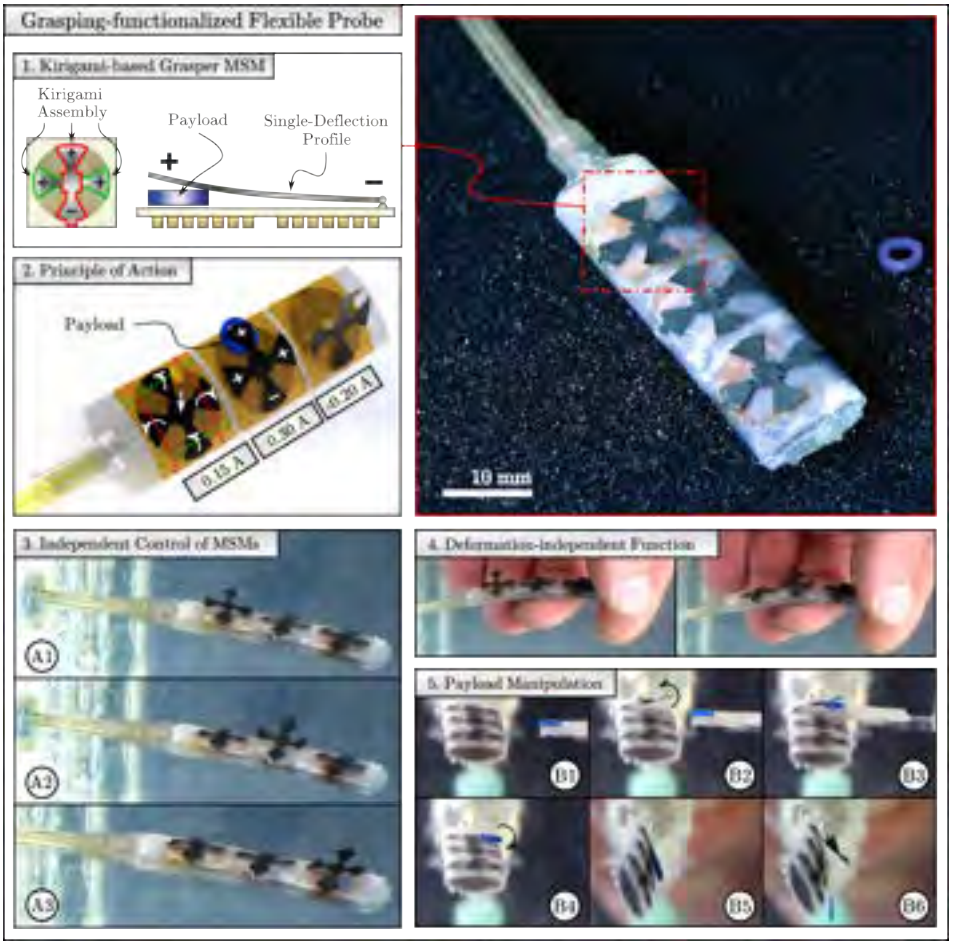

Figure 5.4: A flexible tip functionalized for payload grasping and release using near-field magnetic soft machines (MSMs). (1) The tip utilizes three independent grasping effectors, each assembled from single-deflection magnetic soft elements using kirigami-based technique. **(2)** Opening and closing of each effector is independently controlled by current within the respective planar coils. **(3)** Independent control of MSMs is demonstrated by actuating each effector using phase-shifted current inputs of 0.2 A. **(4)** The tip is fully flexible and the MSMs remain operational while subjected to external deformation. **(5)** The tip is used to grab and release a payload (20 mg).

ated on a thin single coil surface rather than requiring multiple adjacent coils [72]. Similarly, densely packed arrays of individually actuable grippers can be achieved, with tradeoff in mobility [189]. Tilting motion of planar polymer effectors is achieved instead of requiring electromagnetic fish-tail effectors [211]. Radial force-optimized effectors provide directional control by a single coil for sliding, rather than requiring multiple coils to direct sliding permanent magnets with uniform magnetization [200]. By utilizing the central and radial regions of the electromagnetic near-field, the number of sources to actuate an effector is reduced to one. Consequently, arrays of near-field MSMs with equal number of sources and effectors can be realized, scalable to the surface area of individual electromagnetic coils. Although coils with a diameter of 12 mm are used in this study, they can be scaled down to submillimeter scale [195]–[198]. Also, jig-based magnetization of effectors has been shown at sizes as small as 500 μm [174].

The fabrication of both coil and effectors at microscale thickness can be used to produce ultrathin muscle actuators, demonstrated as lifting and radial linear motion MSMs. Although the near-field MSMs have relatively low work capacity and work density compared to other types of artificial muscles [190], they are capable of high-bandwidth motion, push and pull action, large stroke compared to their thickness, as well as grid-like arrangement and independent actuation. Although our work reports MSM operation at frequencies up to 25 Hz, higher bandwidths can be achieved with different electronic equipment. A comparison between the presented MSMs (lifting and radial linear motion) and other types of artificial muscles and near-field magnetic actuators is shown in Table S5.1.

Muscle-like actuators are the lifting and radial linear motion MSM. For the lifting MSM, effector displacement is in the axial direction of the coil. Therefore, field magnitude changes but direction remains relatively constant, resulting in decreasing but invariably directed forces on the effector. Comparatively, for radial motion MSM, near-field direction changes but magnitude remains relatively constant, resulting in a shift from radial to axial forces with displacement relative to the coil center (Fig. S5.8). In both cases, forces (and torques) on effectors can be increased with coil current, or by increasing the volumetric ratio of magnetic microparticles and effector thickness, at the cost of bending stiffness and weight [56].

Near-field MSMs with effectors that deflect or displace in the axial direction of the coil benefit from impulse currents through the coils, whereas effectors operating in-plane can be operated with both impulse and step currents. This follows from the properties of the near-field, as field and gradient magnitudes approach zero at the radial edge of the coil and beyond a few millimeters above the surface. Increasing coil current scales power consumption quadratically, and power consumption of a near-field MSM array scales linearly with number of coils. The power consumption of single coils with resistance of 12 Ω and currents of 0.2-1 A used in this work ranges between 0.5-12 W. At constant operating currents at and below 0.2 A (0.5 W) we did not experience overheating of the coil, which is equivalent to providing impulse currents of 1 A for 40 ms per second, without active cooling.

We envision that near-field MSMs can find application in healthcare, electronics, fluidics, and optics. For example, radial linear actuators for needle biopsy [213], deflecting MSMs for concentration practice and hand movement during stroke rehabilitation [214], axial (lifting) linear actuators as electrical switches or programmable valves [71], and tilting surfaces for orienting mirrors or lenses [181]. Additionally, Joule-heating of coils can be utilized to fabricate magneto-thermal responsive effectors [215]. Finally, we envision that near-field MSMs can additionally be actuated with far-fields, i.e. synergistic near- and far-field actuation. In this case, the relatively high magnitude of fields and gradients in near- and far-fields, respectively, may be utilized. As an extension, due to the different near- and far-field properties the collaborative operation of near- and far-field MSMs can be investigated further. This gives even more freedom to the design of MSMs and enables further application in, e.g., minimally invasive surgical devices, independently-activated components in soft electronics, and small-scale local actuators in soft robotics.

5.4 Methods

5.4.1 Fabrication of flexible planar coils

The planar electromagnetic coils are prepared using polyimide laminate (DuPont™ Kapton®) substrate of 50 µm thickness with 9 µm thick copper coating (Fig. S5.1). Image-reversal optical lithography and wet etching is used to pattern the coil on the substrate. First, the copper surface is cleaned using O_2 oxygen plasma for 2 min. AZ5214e image reversal photoresist is spin coated at 1000 rpm for 30 s and baked at 110 °C for 2 min. The planar coil design is patterned using a UV laser writer (DWL66, Heidelberg Instruments, Germany) with a wavelength of 375 nm, post baked at 120 °C, flood exposed under UV light, and developed in AZ351b developer. Subsequently, the substrate is post baked at 120 °C for 5 min and laminate wet etched in 1:10 sodium persulfate solution in DI water (B327, AG TermoPasty, Grzegorz Gasowski, Poland) kept at 60 °C. Residual etching agent is removed with DI water. Photoresist is then removed with acetone, isopropanol, and DI water.

5.4.2 Modeling of magnetic near-field

The magnetic near-field generated by the coils at a constant operating current ($I = 0.15$ A) is measured with a Hall-effect sensor (MLX 90371, Melexis, Ypres, Belgium) attached to an Arduino Due microcontroller board (Fig. S5.2), assigned local frame ($\{E\}$). The sensor is moved in a volumetric sweep above the coil surface with a six-DOF Franka Emika robotic arm, assigned base frame $\{B\}$. Measurements are taken at different sensor positions (${}^B\boldsymbol{p} \in \mathbb{R}^3$) with constant orientation (${}^B_E\boldsymbol{R} \in \mathrm{SO}(3)$). Local measurements taken by the sensor (${}^E\boldsymbol{B}(I, {}^B\boldsymbol{p})$) are compensated for the earth magnetic field (${}^E\boldsymbol{B}_0$) and transformed to the base frame,

$$ {}^B\boldsymbol{B}(I, {}^G\boldsymbol{p}) = {}^B_E\boldsymbol{R}({}^E\boldsymbol{B}(I, {}^B\boldsymbol{p}) - {}^E\boldsymbol{B}_0). \tag{5.1} $$

The coil center position (${}^B\boldsymbol{p}_C$) is initially approximated from visual inspection of the measurements. Thereafter the field measurements are represented with respect to the coil center ($\{\boldsymbol{B}(I, \boldsymbol{p}) \,|\, \boldsymbol{p} = {}^B\boldsymbol{p} - {}^B\boldsymbol{p}_C\}$).

An N^{th}-order Cartesian multipole-expansion ($\Psi(\boldsymbol{p}) : \mathbb{R}^3 \to \mathbb{R}$) of the form

$$\Psi(\boldsymbol{p}) = \sum_{m=1}^{M} \sum_{n=1}^{N} b_n \cdot \frac{\partial^n}{\partial z^n} \frac{1}{\sqrt{x^2 + y^2 + (z + d_m)^2}}, \tag{5.2}$$

is implemented symbolically in Matlab R2022. The derived near-field model ($\tilde{\boldsymbol{B}} := \nabla\Psi(\boldsymbol{p}) \in \mathbb{R}^3$) is fit to the measurements, where $\nabla := \langle \frac{\partial}{\partial x}, \frac{\partial}{\partial y}, \frac{\partial}{\partial z} \rangle$ and $\langle \cdot \rangle$ represents a column vector. Field source displacement variables ($d_m \in \mathbb{R}^+$) are added along the coil axis to resolve unboundedness of Ψ in the near-field when $z \to 0$. Scalar coefficients ($b_n \in \mathbb{R}$), model order ($N \in \mathbb{Z}^+$), and number and values of displacement variables $\{M \in \mathbb{Z}^+, d_m\}$ are determined using a parametric sweep and convex optimization with Matlab's fmincon. The near-gradient field is obtained by symbolic differentiation of the near-field model ($\tilde{\boldsymbol{B}}_\nabla := \nabla^T \tilde{\boldsymbol{B}} \in \mathbb{R}^{3\times3}$). The field model is fit to measurements using linear least squares.

To improve the quality of fitting a near-field model ($\tilde{\boldsymbol{B}}(\boldsymbol{p}) : \mathbb{R}^3 \to \mathbb{R}^3$), the field measurements ($\boldsymbol{B}(I, \boldsymbol{p})$) are adjusted for uncertainties in the coil center position and Hall-effect sensor frame orientation. We consider an optimization vector ($\boldsymbol{o} = \langle \delta x, \delta y, \alpha, \beta, \gamma, \boldsymbol{d} \rangle,\ \boldsymbol{d} \in \mathbb{R}^M$) such that $\boldsymbol{p} := \boldsymbol{p} - \langle \delta x, \delta y, 0 \rangle$ and $\boldsymbol{B}(I, \boldsymbol{p}) := \boldsymbol{R}_x(\alpha)\boldsymbol{R}_y(\beta)\boldsymbol{R}_z(\gamma)\boldsymbol{B}(I, \boldsymbol{p})$. The combination $\{N, M\}$ minimizes

$$\begin{aligned} O(N, M) = \arg\min_{\boldsymbol{o}} \quad & \left\| \frac{\left(\tilde{\boldsymbol{B}}(\boldsymbol{p}) - \boldsymbol{B}(I, \boldsymbol{p})\right)}{\boldsymbol{B}(I, \boldsymbol{p})^T} \right\| \\ \text{s.t.} \quad & \boldsymbol{d} \geq \boldsymbol{0}, \quad \forall d_m. \end{aligned} \tag{5.3}$$

The objective function ($O(N, M)$) is chosen to equalize the influence of measurement-model errors in regions where the residual error is low but relative error may be high, i.e., the edges of the coil.

5.4.3 Materials and fabrication of magnetic soft effectors

Magnetic effectors are produced by from post-processing of vulcanized magnetic polymer composite (MPC) sheets. The MPC constitutes a suspension of polydimethylsiloxane (PDMS) and Pr-Fe-Co-Nb-B microparticles (MQP-16-7-11277-070, Magnequench GmbH, Germany) with a mean diameter of 5 µm. The MPC suspension is made by mixing PDMS at a

10:1 volume ratio of base-curing agent, followed by manual introduction of microparticles at a volumetric ratio of 0.35 (Fig. S5.3).

Molds for MPC sheets are made by laser engraving (Speedy 300, Trotec Laser, Marchtrenk, Austria) rectangular cavities with depth between 30-300 µm. The cavities are treated with a release agent (Ease Release 200, Smooth-On Inc., USA). MPC mixture is poured inside and uniformly distributed using a Stanley knife. Finally, the MPC-filled molds are vulcanized at 100 °C for 1 h to form sheets. The sheets are manually removed from the molds.

Magnetization of the sheets is determined based on desired magnetic torque and force distribution in the magnetic near-field of the coil (Fig. S5.4). Magnetization is performed using a uniform magnetic field ($\boldsymbol{B}_\mathrm{m}$) generated by a vibrating sample magnetometer (GMW 3474-140, GMW, Redwood City, California). Non-uniform magnetization profiles are achieved by wrapping sheets in 3D-printed molds (Fig. S5.5). The mold geometry is determined from a 2D magnetization curve. We compute this curve by considering a reference configuration of a planar MPC sheet perpendicular to the direction of $\boldsymbol{B}_\mathrm{m}$. In addition, the sheet has a desired magnetization profile $\boldsymbol{m}(y)$, where $y \in [0, 2R]$ spans the coil diameter. The magnetizing field and magnetization direction have an angular offset ($\theta(y) = \angle(\boldsymbol{B}_\mathrm{m}, \boldsymbol{m}(y))$). The magnetization curve is then computed with forward Euler integration,

$$\begin{bmatrix} \mathrm{Y}(y) \\ \mathrm{Z}(y) \end{bmatrix} = \int_0^y \begin{bmatrix} \cos\theta(\sigma) \\ -\sin\theta(\sigma) \end{bmatrix} \mathrm{d}\sigma. \tag{5.4}$$

Extruding the magnetization curve provides a mold around which sheets are wrapped for magnetization. At this point the sheets have non-uniform and uniform magnetization along their short and long axis, respectively. Finally, the sheets are laser-cut along the short axis to form one-dimensional non-uniformly magnetized elements which are subsequently assembled with a glue (Loctite 401) to form two-dimensional magnetic soft effectors.

5.4.4 Near-field MSM demonstrations

Demonstrations of near-field MSMs in water are performed within a laser-cut plexiglass box (Fig. 5.3). Coils are shielded from water by covering with

a plastic sheet (thickness 500 μm, Fig. 5.3.1). Also, silicone rubber (thickness 200 μm) is wrapped around the coils attached to a flexible 3D-printed holder (elastic resin, Formlabs Form 2). Current is supplied to the coils by copper wires running along a multi-lumen polyurethane tube, attached to the base of the flexible holder. Water is used to reduce friction between coil and effector during demonstrations of linear motion (Fig. 5.3.2). Interconnecting linear-motion MSMs is done by gluing (Loctite 401) a laser-cut silicone cover (thickness 200 μm) onto the effectors. Motion is constrained in a linear direction by a 3D-printed holder (elastic resin, Formlabs Form 2).

5.4.5 Control and power systems

Coils are powered by three dedicated iPOS3602 VX-CAT drives (Technosoft S.A., Neuchtel, Switzerland). The drives are connected to an external research laptop running Linux Ubuntu 18.04 through EtherCAT network. Selective current control is achieved via a custom-made interface implemented in C++. The current used during near-field MSM activation is limited to a maximum of 1 A.

5.5 Supplementary text

5.5.1 Magnetization of magnetic soft elements

Magnetic soft elements constitute elementary building blocks of effectors. They carry a one-dimensional non-uniform magnetization profile ($\boldsymbol{m}(y)$) along their longitudinal axis (y). Along this axis, the elements experience a force $\boldsymbol{F}(y)$ and torque $\boldsymbol{\tau}(y)$ due to the coil near-field ($\boldsymbol{B}(y)$), shown in Supplementary Figure S5.4.1. Fixating the soft element results in a bending moment due to both force and torque. Desired element magnetization profile ($\boldsymbol{m}(y)$) is computed based on cost-functions that optimize total bending moment, force, or torque. These cost-functions are used to compute $\boldsymbol{m}(y)$ that allows lifting, center deflection, and linear motion (Fig. S5.4.2).

Lifting elements are fixated on the radial edges of the coil (Fig. S5.4.2). For notation simplicity we define $y \in [0, 2R]$, where $R = 6$ mm is the radius of the coil. The magnetization profile optimizes vertical forces within the central region above the coil 4 mm ($4 \text{ mm} \leq y \leq 8$ mm), where axial gradients are strongest. At the coil extremities the magnetization profile optimizes bending moment for element deflection in the lifting direction. The associated cost function for lifting elements is thereafter defined as:

$$C_{\text{lift}}(\boldsymbol{m}(y)) = \begin{cases} \arg\max_{\boldsymbol{m}(y)} \hat{\boldsymbol{x}}^T \int_0^{y_1} \boldsymbol{m}(y) \times \boldsymbol{B}(y) + \langle 0, y, 0 \rangle \times \nabla(\boldsymbol{m}(y) \cdot \boldsymbol{B}(y))\, dy, \\ \qquad\qquad y_1 = 4 \text{ mm} \\ \arg\max_{\boldsymbol{m}(y)} \hat{\boldsymbol{z}}^T \int_{y_1}^{y_2} \nabla(\boldsymbol{m}(y) \cdot \boldsymbol{B}(y))\, dy, \\ \qquad\qquad y_2 = 8 \text{ mm} \\ \arg\min_{\boldsymbol{m}(y)} \hat{\boldsymbol{x}}^T \int_{y_2}^{y_3} \boldsymbol{m}(y) \times \boldsymbol{B}(y) + \langle 0, y - y_3, 0 \rangle \times \nabla(\boldsymbol{m}(y) \cdot \boldsymbol{B}(y))\, dy, \\ \qquad\qquad y_3 = 12 \text{ mm}, \end{cases} \tag{5.5}$$

where $\langle \cdot \rangle$ represents a column vector, $\hat{\boldsymbol{x}} = \langle 1, 0, 0 \rangle$, $\hat{\boldsymbol{z}} = \langle 0, 0, 1 \rangle$, and $\boldsymbol{m}(y) = \langle 0, m_y(y), m_z(y) \rangle$ computed numerically at discrete locations and given constant magnitude.

Similarly, center deflection and linear motion elements maximize bending moments relative to the coil center, and linear forces planar to the coil surface:

$$C_{\text{defl}}(\boldsymbol{m}(y)) = \underset{\boldsymbol{m}(y)}{\arg\max}\ \hat{\boldsymbol{x}}^T \int_0^{y_3} \boldsymbol{m}(y) \times \boldsymbol{B}(y) + \langle 0, y-R, 0\rangle \times \nabla(\boldsymbol{m}(y)\cdot\boldsymbol{B}(y))\ dy \tag{5.6}$$

$$C_{\text{lin}}(\boldsymbol{m}(y)) = \underset{\boldsymbol{m}(y)}{\arg\max}\ \hat{\boldsymbol{y}}^T \int_0^{y_3} \nabla(\boldsymbol{m}(y)\cdot\boldsymbol{B}(y))\ dy, \tag{5.7}$$

where $\langle 0, y-R, 0\rangle$ is the moment arm with respect to the coil center (since $y \in [0, 2R]$).

5.5.2 Validating effector magnetization

Magnetic soft effectors are assembled from one-dimensional pre-magnetized elements. The magnetization profile of the elements is reconstructed in terms of a magnetization angle ($\theta(y)$) at discrete locations along and with respect to their longitudinal axis (y). The discretized subvolumes are considered point dipoles.

The soft element is placed on a non-magnetic acrylic table (Fig. S5.6). A tri-axis Hall-effect sensor (MLX 90371, Melexis, Ypres, Belgium) is moved above the element by a Panda robotic arm (Franka Emika, Munich, Germany). The Hall-effect sensor is connected to an Arduino Due microcontroller transmitting field measurements to an external PC at 100 Hz. Field measurements are taken along the longitudinal direction of the element ($y \in [y_{\min}, y_{\max}]$) at different heights ($z \in \{1, 2, ..., 10\}$ mm). Sensor recording positions ($\boldsymbol{p}_{\text{r}} = \langle 0, y, z\rangle$) and corresponding field measurements ($\boldsymbol{B}_{\text{r}}(\boldsymbol{p}_r) \in \mathbb{R}^3$) are stored.

Reconstructed magnetization profiles of elements are defined by their unit dipole moment vectors ($\boldsymbol{m}_{\text{r}}(y)$). This profile is computed using a distributed point dipole model. We assume that each field measurement

($\boldsymbol{B}_{\mathrm{r}}(\boldsymbol{p}_{\mathrm{r}})$) is the sum of the field by each distributed point dipole:

$$\boldsymbol{B}_r(\boldsymbol{p}_r) = \int_{y_{\min}}^{y_{\max}} \boldsymbol{\beta}(\boldsymbol{p}_{\mathrm{r}}, y)\hat{\boldsymbol{m}}_{\mathrm{r}}(y)\, dy, \tag{5.8}$$

where $\boldsymbol{\beta}(\boldsymbol{p}_{\mathrm{r}}, y) \in \mathbb{R}^{3\times3}$ represents the external magnetic field magnitudes produced by a magnetic point dipole irrespective of its direction, and $\hat{\boldsymbol{m}}_{\mathrm{r}}(y)$ represents the direction of the point dipole:

$$\boldsymbol{\beta}(\boldsymbol{p}_{\mathrm{r}}, y) = \frac{\mu_0\mu_c}{4\pi\|\Delta\boldsymbol{p}\|^5}\left(3\Delta\boldsymbol{p}\Delta\boldsymbol{p}^T - \Delta\boldsymbol{p}^T\Delta\boldsymbol{p}\,\boldsymbol{I}_{3\times3}\right), \tag{5.9}$$

$$\Delta\boldsymbol{p} = \boldsymbol{p}_r - \langle 0, y, 0\rangle, \tag{5.10}$$

with μ_0 the vacuum magnetic permeability, μ_c is the subvolume dipole moment magnitude, and $\boldsymbol{I}_{3\times3}$ the identity matrix.

The distributed point dipole model (Eqn. (5.8)) is discretized as $D \in \mathbb{Z}^+$ unit point dipoles ($\hat{\boldsymbol{m}}_{\mathrm{r}}^i,\ i \in \{1, 2, ..., D\}$) distributed uniformly between $y_{\min}$ and $y_{\max}$. Thereafter, magnetization profile reconstruction from $M \in \mathbb{Z}^+$ field measurements ($\boldsymbol{B}_{\mathrm{r}}(\boldsymbol{p}_{\mathrm{r}}^j),\ j \in \{1, 2, ..., M\}$) becomes a linear least-squares problem,

$$\begin{bmatrix} \boldsymbol{B}_r(\boldsymbol{p}_r^1) \\ \vdots \\ \boldsymbol{B}_r(\boldsymbol{p}_r^M) \end{bmatrix} = \begin{bmatrix} \boldsymbol{\beta}(\boldsymbol{p}_r^1, y_{\min}) & \dots & \boldsymbol{\beta}(\boldsymbol{p}_r^1, y_{\max}) \\ & \vdots & \\ \boldsymbol{\beta}(\boldsymbol{p}_r^M, y_{\min}) & \dots & \boldsymbol{\beta}(\boldsymbol{p}_r^M, y_{\max}) \end{bmatrix} \begin{bmatrix} \hat{\boldsymbol{m}}_{\mathrm{r}}^1(y_{\min}) \\ \vdots \\ \hat{\boldsymbol{m}}_{\mathrm{r}}^D(y_{\max}) \end{bmatrix}. \tag{5.11}$$

For each sample we chose $D = 15$, $M \approx 25000$, $y_{\min}$ =-7.5 mm, and $y_{\max} = 7.5$ mm. The magnetization error of each element is quantified in terms of the reconstructed and desired angle ($\theta_{\mathrm{r}}(y), \theta_{\mathrm{d}}(y) \in \mathbb{S}$) between the longitudinal axis of the element (y) and the respective reconstructed and desired magnetization profile ($\boldsymbol{m}_{\mathrm{r}}(y), \boldsymbol{m}(y)$). The average angular error across all samples is 14.74^o.

5.6 Supplementary figures

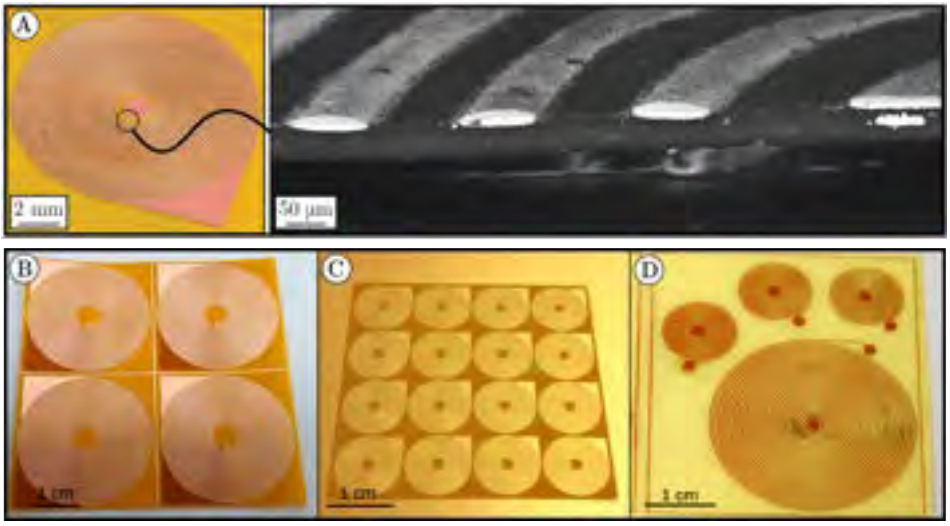

Figure S 5.1: Planar electromagnetic coil geometries. **(A)** Spiral planar copper coil with 24 revolutions used in this work. The coil has an inner and outer diameter of 2 mm and 12 mm, respectively. A copper coating with vertical thickness of 9 μm is attached to a polyimide laminate substrate of thickness 50 μm. Horizontal thickness and spacing of wires is 100 μm. **(B)** Coil diameters can be made arbitrarily bigger or **(C)** smaller, and prepared as individual units or as arrays of coils in a grid-like pattern on the same laminate substrate. **(D)** The symmetry of the array of coils can be freely chosen. Additionally, the array can consist of coils of different dimensions.

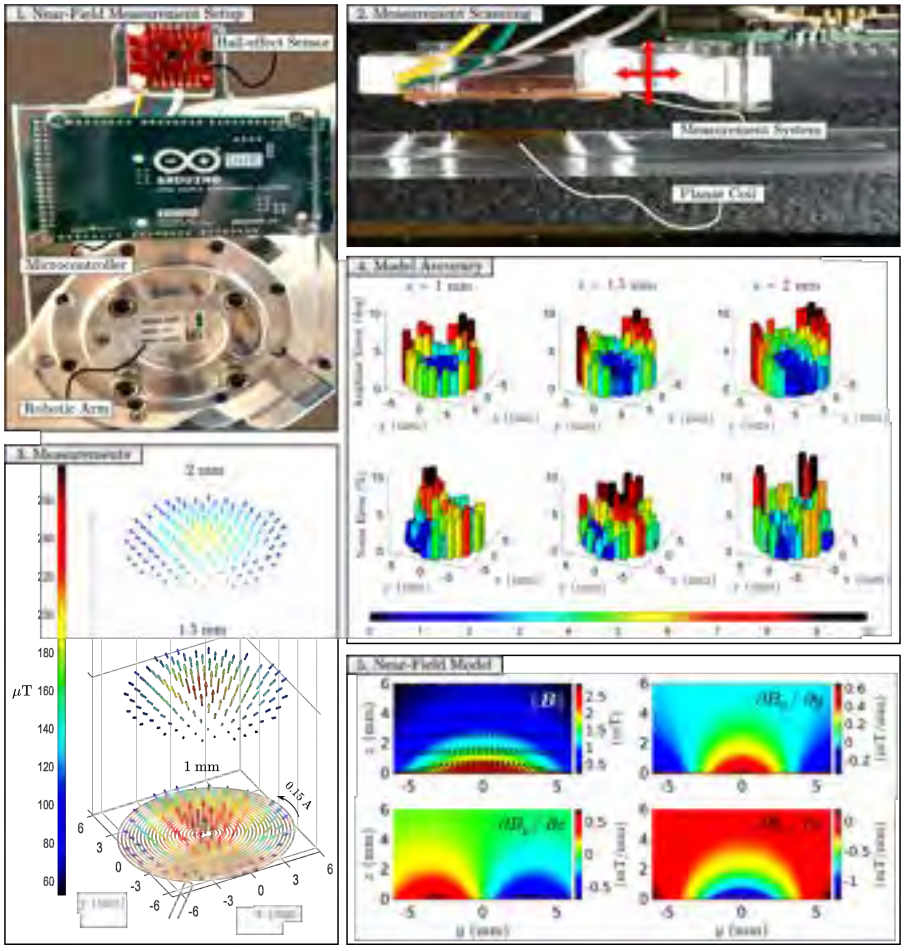

Figure S 5.2: Measurement and model results for magnetic near-field. **(1)** Measurement setup comprising a tri-axis Hall-effect sensor, Arduino Due microcontroller, and Franka Emika Panda robotic arm. **(2)** Field measurements are performed with a volumetric sweep above the coil surface at distances 1, 1.5, and 2 mm. **(3)** Measurements obtained at coil operating current of $I = 0.15$ A. The shown data are compensated for earth magnetic field. **(4)** Model accuracy. Angular discrepancy between measured and modeled field direction is within 1-3 ° in the central region of the coil and increases to 4-7 ° towards the edge. Norm discrepancy across the coil surface is in the range of 3-8%. **(5)** Modeled field magnitudes ($\|\boldsymbol{B}\| = \|\langle B_x, B_y, B_z \rangle\|$) and non-zero gradients in the yz-plane above the coil for a current $I = 1$ A.

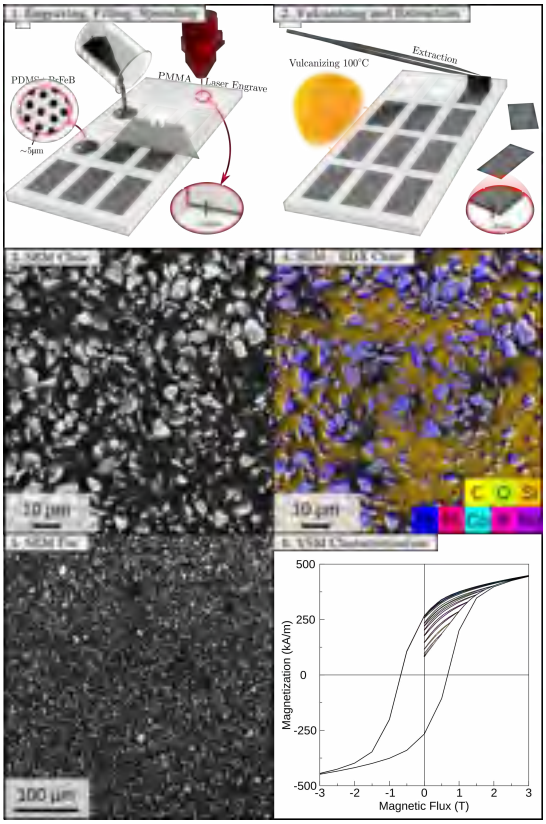

Figure S5.3: Fabrication and characterization of magnetic soft polymer composite (MPC) sheets. (1) Rectangular cavities of depth 30 μm are laser-engraved (Speedy 300, Trotec Laser, Marchtrenk, Austria) in an acrylic/PMMA plate. A suspension of polydimethylsiloxane (PDMS) and ferromagnetic microparticles (Pr-Fe-Co-Nb-B, MQP-16-7-11277-070, Magnequench GmbH, Germany) with mean diameter of 5 μm and volume fraction 0.35 is poured inside the cavities. The suspension is uniformly distributed in the molds and excess removed by sliding a Stanley knife. **(2)** Vulcanization of the suspension is performed at 100 °C for 1 h. The resulting magnetic soft composite sheets are thereafter extracted from the cavities. **(3)** Scanning electron microscopy (SEM) image of the top surface of a sheet. **(4)** EDX element analysis of the corresponding area. The element analysis identifies the chemical composition of the magnetic microparticles within the PDMS matrix. **(5)** Large field of view SEM image of the sheet. Magnetic microparticles are evenly distributed within the polymer matrix. **(6)** SQUID-VSM magnetic characterization of a uniformly magnetized sheet. Minor hysteresis loops reveal robustness of the pre-defined magnetic state of the sheets. The sheet retains its remanent magnetization of 25 kA/m even upon application of a magnetic field up to 0.5 T. The sheets have a coercivity of 0.7 T.

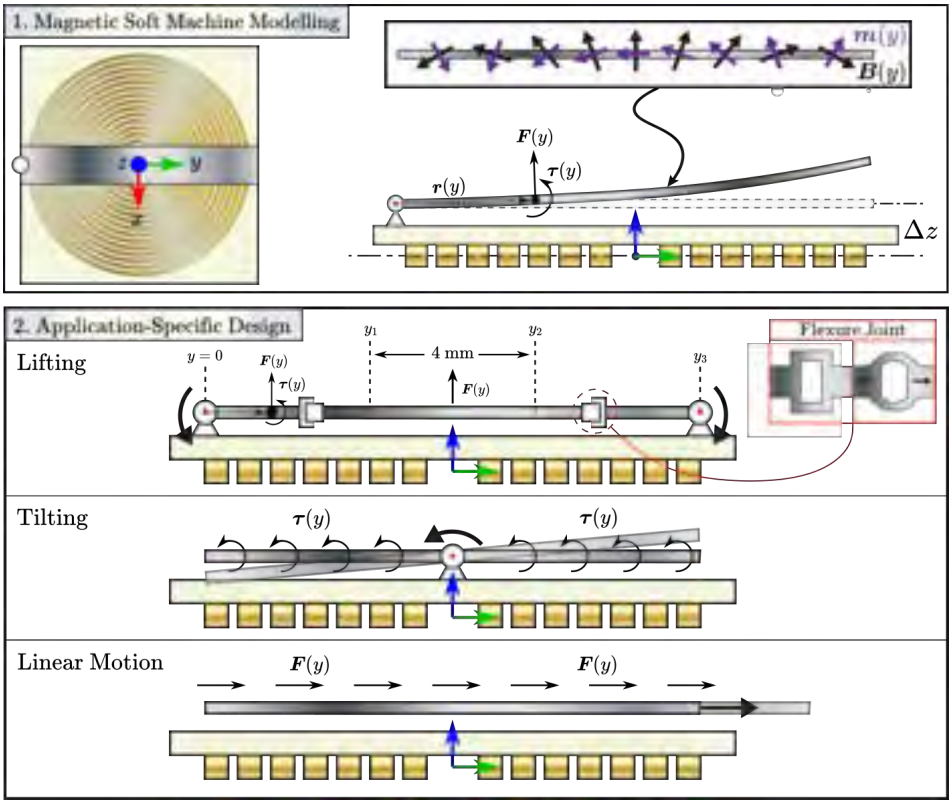

Figure S 5.4: modeling principles of magnetic soft machines (MSMs) as assemblies of magnetized soft elements. (1) Soft elements are considered one-dimensional strips on a coil, at non-zero height (Δz), with a magnetization profile ($\boldsymbol{m}(y)$) along their longitudinal axis (y). Interaction between $\boldsymbol{m}(y)$ and coil near-field ($\boldsymbol{B}(y)$) results in distributed forces ($\boldsymbol{F}(y) = \nabla(\boldsymbol{B}(y) \cdot \boldsymbol{m}(y))$) and torques ($\boldsymbol{\tau}(y) = \boldsymbol{m}(y) \times \boldsymbol{B}(y) + \boldsymbol{r}(y) \times \boldsymbol{F}(y)$), where $\boldsymbol{r}(y)$ represents a moment arm. **(2)** Application-specific magnetic force and torque distributions for lifting, tilting, and linear motion MSMs. Lifting elements are split in three sections: two extremities $\{(y_0\text{-}y_1), (y_2\text{-}y_3)\}$ and one center $(y_1\text{-}y_2)$. The left and right extremities are optimized for counter- and clockwise bending moments as a result of both forces and torques. The center is optimized for vertical forces. Flexure joints within the extremities allow extension during vertical displacement of the lifting element. Tilting elements are optimized for bending moments with respect to the central axis. Linear motion elements are optimized for planar forces.

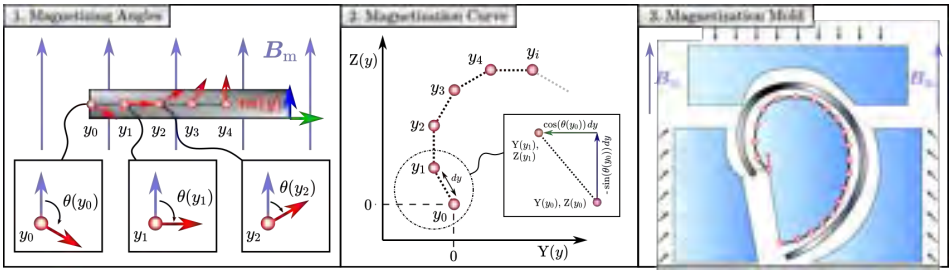

Figure S5.5: Computing magnetization curve and associated mold for a desired magnetic soft composite sheet magnetization profile ($\boldsymbol{m}(y)$) in an external homogeneous field ($\boldsymbol{B}_\mathrm{m}$). (1) Angular offset between desired magnetization profile and magnetizing field ($\theta(y) = \angle\boldsymbol{m}(y), \boldsymbol{B}_\mathrm{m}$) is computed along the longitudinal axis of the sheet (y). **(2)** A magnetization curve $(\mathrm{Y}(y), \mathrm{Z}(y))$ is computed using forward Euler integration: $\mathrm{Y}(y) = \int_0^y \cos(\theta(\sigma))d\sigma$ and $\mathrm{Z}(y) = \int_0^y -\sin(\theta(\sigma))d\sigma$. The magnetization curve represents a physical wrapping of the sheet which produces the desired magnetization profile when subjected to the magnetizing field. **(3)** The 2D magnetization curve is extruded to form a 3D mold. Wrapping the sheet inside the mold and subjecting to a uniform magnetizing field ($\boldsymbol{B}_\mathrm{m}$) produces the desired magnetization profile.

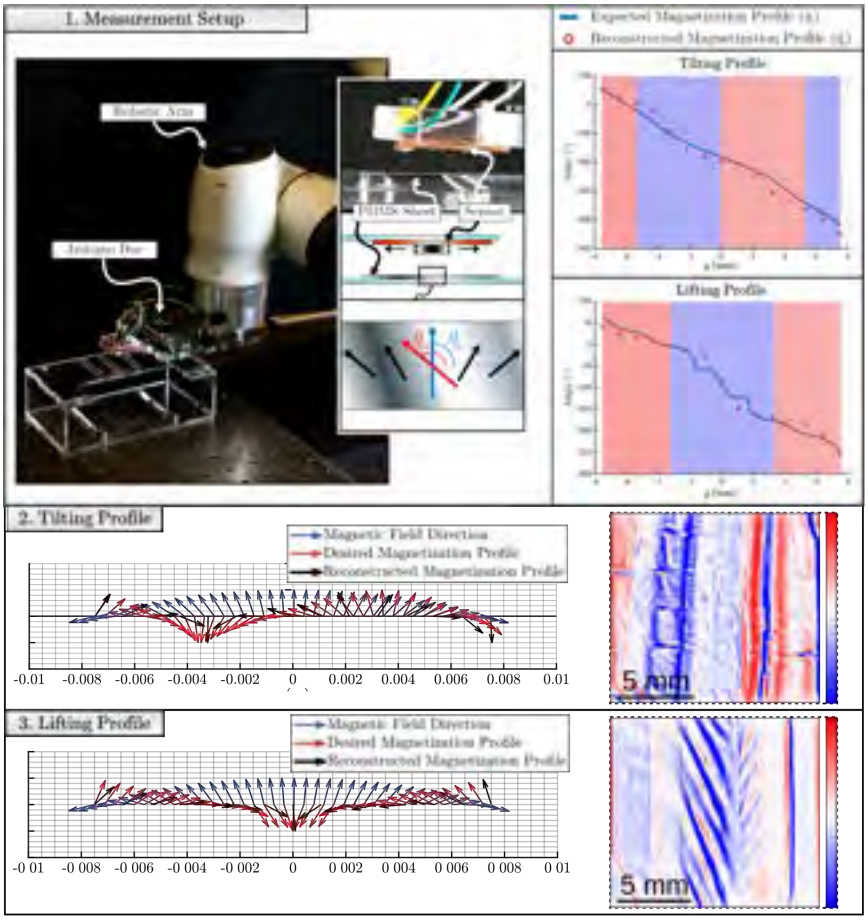

Figure S5.6: Validating magnetization of magnetic soft effectors. A Tri-axis Hall-effect sensor connected to an Arduino Due microcontroller and robotic arm is swept longitudinally over soft effectors. Magnetization direction is reconstructed in terms of a measured magnetization angle (θ_{m}) relative to the longitudinal element axis (y), and compared to the desired magnetization angle (θ_{d}). Validation is performed for soft effectors designed for tilting and lifting MSMs. Desired and reconstruction magnetization profiles are shown, as well as magnetic field directions on the planar coil surface. Stray fields measured directly on the element surface are shown, with red and blue colors indicating "out-of-page" and "into-page" magnetization.

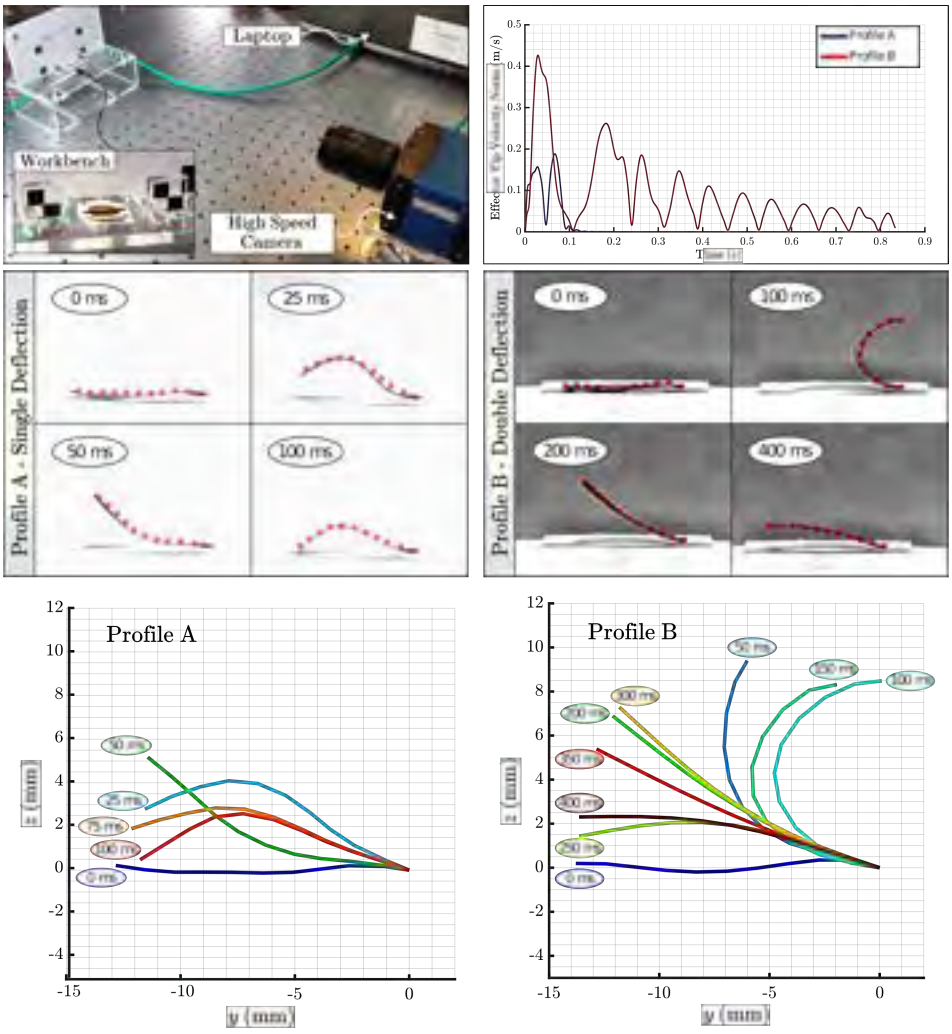

Figure S 5.7: Motion profile of magnetic soft effectors with different magnetization profiles (A and B) designed for single and double deflection. Coils are powered with a step current of 1 A. Effector motion is captured with a high speed camera, their longitudinal axis reconstructed, and tip velocity magnitude computed. Effector configurations are shown at different time constants.

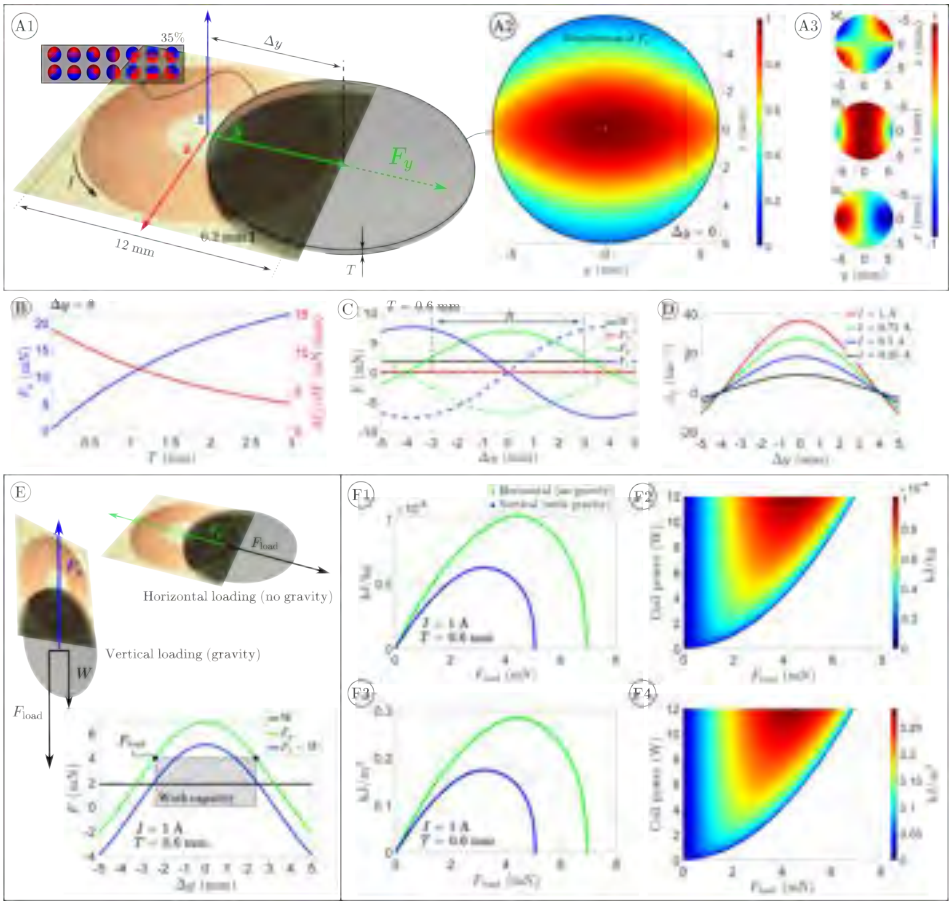

Figure S 5.8: Simulation analysis of radial linear actuators assuming no friction. **(A1)** Planar coil of diameter ($2R$ = 12 mm) running current (I) with a disk-shaped effector of thickness (T) positioned 0.2 mm above the surface. The effector has a magnetic volume fraction of 35 % and experiences a radial force ($F_y(\Delta y)$) depending on displacement (Δy) with respect to the coil center. **(A2)** Distribution of F_y across the effector surface when concentric with the coil for **(A3)** force-optimized magnetization ($\boldsymbol{M} = \langle M_x, M_y, M_z \rangle$) profiles. **(B)** Total F_y on the effector for varying thickness (T) at $\Delta y = 0$ and $I = 1$ A. **(C)** Weight (W) and magnetic forces on an effector of thickness $T = 0.6$ mm for displacements (Δy) at currents I =-1 A (dashed) and $I = 1$ A (solid), with **(D)** effector acceleration for different I. **(E)** Performable work by the effector on a load (F_{load}) with and without gravity. **(F1)** Work capacity of the effector for varying F_{load} at **(F2)** different coil power consumption (resistance 12 Ω). **(F3)** Energy density of the effector for varying F_{load} at **(F4)** different coil power consumption.

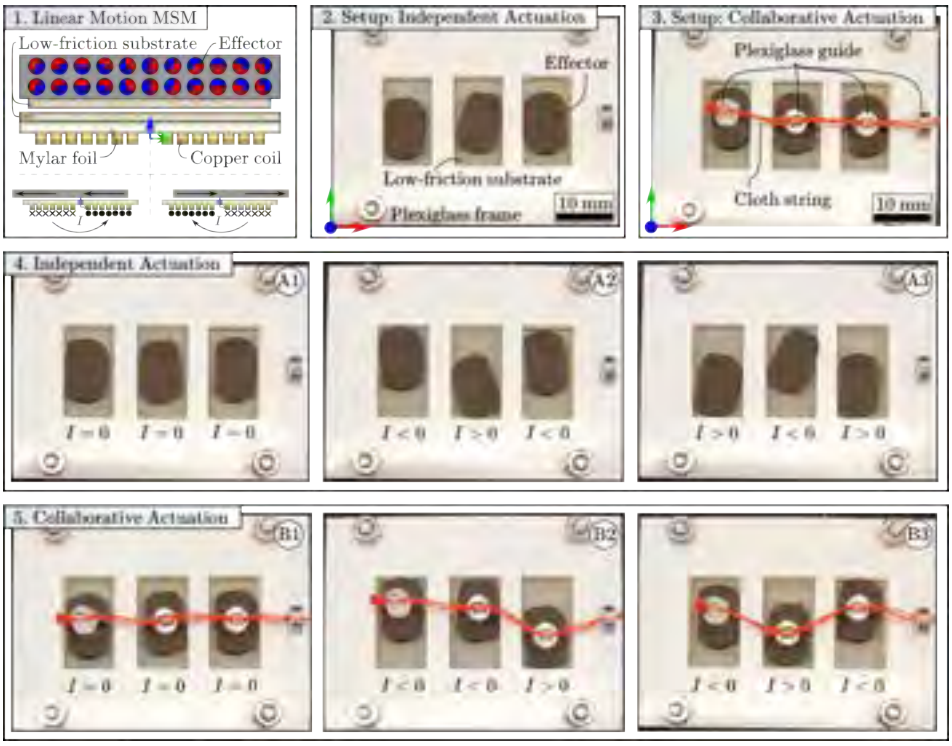

Figure S 5.9: Independent and collaborative actuation of adjacently positioned linear motion magnetic soft machines (MSMs). **(1)** Schematic representation of the linear motion MSM. A copper coil (thickness 9 µm) is attached to a mylar foil (50 µm), which is covered by a low-friction substrate comprising PTFE-coated fiberglass (100 µm). The magnetoresponsive effector (500 µm) has radial force-optimized magnetization profile and is also covered below by the low-friction substrate. The coil plane (yz-plane) is marked by the green and blue arrow. Depending on the direction of current (I) through the coil, the effector displaces along the positive or negative y-axis. **(2)** Setup to demonstrate independent actuation of three linear motion MSMs. Coils are not visible, but are positioned central below each rectangular channel. **(3)** Setup to demonstrate collaborative actuation of three linear motion MSMs. A cloth string is attached to each effector. **(4)** Demonstration of independent actuation. From the neutral configuration (A1), impulse currents ($I = 0.6$ A) are applied (A2) and subsequently reversed (A3). **(5)** Demonstration of collaborative actuation. From the neutral configuration (B1), impulse currents ($I = 0.6$ A) are applied to actuate effectors to form an S-shape (B2-B3). Also see movie S5.

Type	Size (mm)	Strain (%)	Work capacity (kJ/kg)	Work density (kJ/m^3)	Bandwidth (Hz)	Ref.
HSM	-	30	25	25	10	[216]
HFA	⌀3.2 × 130	115.7	0.15	-	25	[217]
TPA	⌀1 × 110	30.6	3.5	2000	0.4	[190]
MKA	⌀31 × 110	38	1.5	0.3	10	[218]
CAM	⌀4.6 × 100	50	0.38	-	4	[219]
HAS	⌀50 × 15	60	0.07	0.23	20	[220]
Type	**Size (mm)**	**Stroke (%)**	**Work capacity (kJ/(kg · A))**	**Work density (kJ/(m^3 · A))**	**Bandwidth (Hz)**	**Ref.**
MNF	⌀10 × 10	25	$6 \cdot 10^{-6}$	0.056	40	[64]
MNF	⌀9 × 4.7	25	-	$0.25 \cdot 10^{-3}$	45	[65]
MNF	⌀12 × 0.1	2000	$1.75 \cdot 10^{-4}$	0.26	25	This work (lifting)
MNF	⌀12 × 0.7	±25	$1 \cdot 10^{-4}$	0.3	25	This work (radial motion)

Table S 5.1: Comparison of different types of muscle actuators in terms of size, actuation strain or stroke, work capacity, work density, and bandwidth. HSM, human skeletal muscle; HFA, hydraulic filament actuator; TPA, twisted polymer actuator; CAM, cavatappi artificial muscle; HAS, HASEL: hydraulically amplied self-healing electrostatic; MNF, magnetic near-field. Note that for magnetic actuators stroke is reported instead of strain, because the working principle does not involve contraction or relaxation. Strain and stroke is defined with respect to the associated actuator dimension. Also, work capacity and work density are normalized with respect to driving currents. Although our work reports near-field MSM operation at frequencies up to 25 Hz, this is not the maximum achievable bandwidth. Listed values are approximations where the indication "∼" has been omitted for compactness.

III

Are you in there?

Preface

Previous chapters (Parts I and II) demonstrated in part computer- or human-controlled open- or closed-loop magnetic manipulation of MCRs in free space or with unobstructed visual feedback. However, in the clinical reality, MCRs inside the human body (intracorporeal) cannot be seen by the naked eye or external cameras, making it nontrivial to determine their location. Nevertheless, knowing the position and orientation of MCRs relative to the field sources of manipulation systems is essential for generating targeted actuation fields–a prerequisite for safe intracorporeal navigation.

A common claim in research articles is that spatial information about an MCR can be derived from medical imaging systems such as ultrasound or X-ray. Although this is true, reconstructing 3D spatial information from 2D images typically requires capturing multiple images from different angles. Furthermore, it is questionable whether manufacturers of medical imaging systems would share their necessary software for image analysis.

Therefore, **Part III** of this dissertation postulates that for magnetic robotic systems to succeed in clinical practice, they must function as closed systems. This means, they may be connected to other medical technology through a human in the loop, but must otherwise operate independently.

As a solution, **Chapter 6** explores the intracorporeal localization of MCRs by interpreting their extracorporeally measured magnetic fields using an eye-in-hand magnetometer mounted on a mobile manipulation system. The demonstrated localization method is based on the phenomenon that rotating magnetic dipoles generate dynamic, elliptically varying fields at any given position around them. We show that analyzing the properties of these ellipses enables estimation of the magnet's position and rotation axis relative to the measurement point. This information allows purposeful reconfiguration of the manipulation system to generate a desired actuating field. Thereby, a fully integrated magnetic surgical infrastructure is achieved, comprising the MCR, manipulation system, and eye-in-hand sensor, all functioning as a closed system.

6

Magnetic Localization and Manipulation of Locking Synchronous Motors

Note: *The following chapter is adapted from the article "Magnetic localization and manipulation of locking synchronous motors" by* ***M. Richter****, L. Masjosthusmann, P. Makushko, V. Kalpathy Venkiteswaran, D. Makarov, and S. Misra,* ***under review****. The chapter has been reformatted in terms of figures and tables to fit this doctoral thesis. No changes to the technical contents of this peer-reviewed manuscript have been made.*

Authors' Contributions: *M.R. conveived the project and managed the research. M.R. and L.M. fabricated the synchronous motors. M.R. developed the field model and localization algorithm, and performed characterization and tracking experiments. P.M. and D.M. designed and fabricated the planar electromagnetic coils. All co-authors participated in discussions. M.R. wrote the manuscript with contributions from all authors. V.K.V., D.M., and S.M. supervised this project.*

Funding Information: *This work was supported by the European Research Council (ERC) under the European Union's Horizon 2020 Research and Innovation Programme under grant 866494 Project–MAESTRO. Also, this work was financially supported in part by German Research Foundation (DFG) grant MA 5144/33-1, the European Union in the frame of project REGO (ID: 101070066), and ERC grant 3DmultiFerro (Project number: 101141331).*

Abstract

Collaboration between localization and manipulation systems is important for safe and efficient deployment of magnetic continuum robots [58], [60] during diagnostic and therapeutic interventions [221]. Recent clinical demonstrations have shown the potential of these robots to navigate tortuous environments under magnetic manipulation [155], [222]–[224]. Meanwhile, traditionally large stationary manipulation systems [40], [225] are being downsized for greater mobility and reduced floorspace, moving towards commercialization [45], [46], [226], [227]. These systems generate targeted magnetic fields towards manipulation of robots *in-vivo*, which is facilitated by localization systems that reconstruct relative three-dimensional (3D) position and orientation information essential for control [63], [228]. In this regard, localization connects manipulation systems to microsurgical devices.

Conventional medical localization methods use technologies like stereo vision [63], [91], biplane fluoroscopy [128], [229], angulated C-arm fluoroscopy [121], [230], ultrasound [231]–[234], or magnetic resonance imaging systems [129], [235], [236]. These methods are compatible with various types of microrobots and offer various spatial and temporal resolutions, penetration depths, and sizes of infrastructure [237]. However, closed-loop magnetic manipulation is a significant challenge due to often unknown coordinate transformations between physically disconnected reference frames of imaging and magnetic manipulation systems [73].

Alternatively, low-field localization methods (here defined in the nano- to milli-Tesla range), enable the development of magnetic tracking and manipulation systems that are independent of conventional medical imaging technologies [238]. These methods rely on detecting magnetic fields and reconstructing the relative pose of the field source [75]. They typically involve external magnetic field sources combined with internal sensorized devices [76], [239], [240] or magneto-mechanical resonators with external magnetometer arrays [241], [242].

Sensorized magnetic devices, often equipped with a single tri-axial magnetometer [243]–[246], can be localized relative to, and manipulated by, exter-

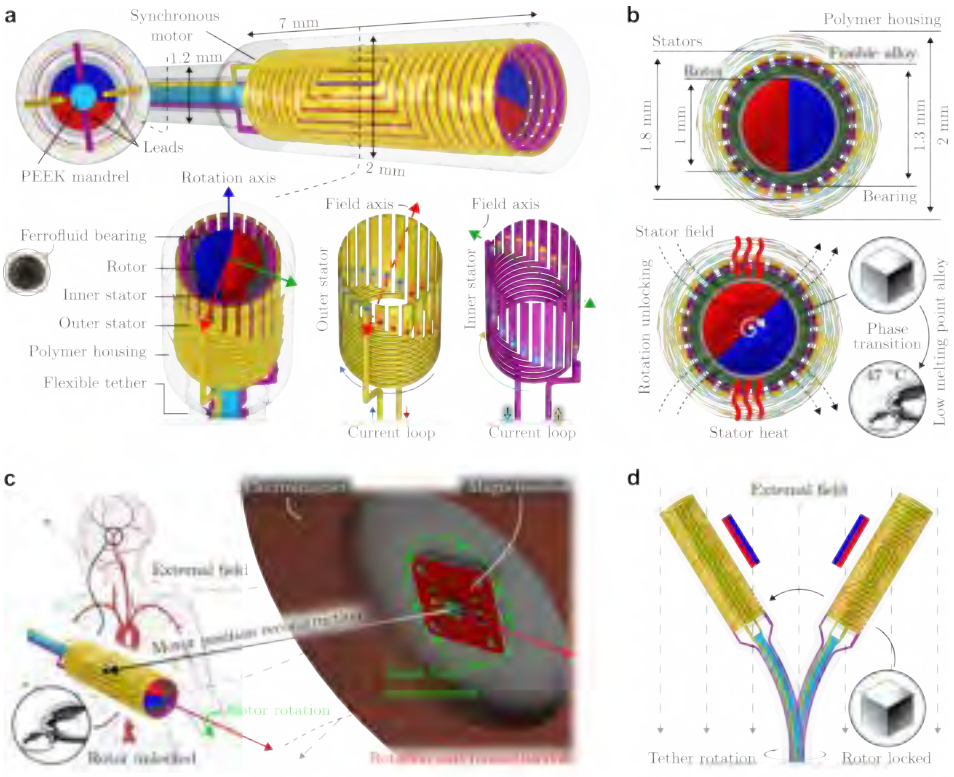

Figure 6.1: Schematic illustration of the permanent magnet synchronous motor (PMSM) for localization and manipulation. **a** Motor dimensions and components. The PMSM consists of two stators which are made up of two planar coils wrapped cylindrically around a permanent magnetic rotor with a ferrofluid bearing. **b** A fusible low melting point alloy (LMPA) fills the rotor cavity and functions as a rotor locking mechanism. The heat and field produced by the stators simultaneously induce LMPA liquefying and rotor rotation, respectively. **c** The rotor generates a rotating magnetic field which is detected by a single Hall effect sensor. These field measurements are used to determine the three-dimensional position and rotation axis of the motor. **d** When the LMPA solidifies, it locks the rotor in its orientation, enabling the motor to be steered in an external field by manually rotating the tether.

nal field generating hardware [238], [239]. However, device miniaturization is limited by the space required for the sensor and the need for a rigid magnet-sensor connection to prevent saturation and maintain a consistent local field [238]. Alternatively, resonators offer better miniaturization potential by using a single magnet for both localization and manipulation, but they require targeted excitation fields and external magnetometer arrays to measure oscillating fields [242]. Increasing numbers of stationary magnetometers are required to expand the localization workspace when physically decoupled from magnetic manipulation systems [247], [248]. This solution may have practical limitations in clinical settings. Alternatively, integration of external eye-in-hand magnetometers attached to mobile magnetic field generating systems provide connected mobile localization and manipulation workspaces [249].

In this work, we demonstrate a localization and manipulation approach that combines the benefits of sensorized devices, magneto-mechanical resonators, and eye-in-hand magnetometers. These include minimizing required number of magnetometers, generating alternating fields *in-vivo*, and integrating electromagnetic localization and manipulation workspaces. Our method is based on rotating magnetic dipoles, which produce fields with elliptically varying strength at any point in space [250]. These fields provide four possible solutions to the pose of a rotating field source, based on measurements from a single tri-axial magnetometer [76]. Herein, this ambiguity is resolved using a-priori knowledge of a rotating dipole position, obtained with closed-loop position feedback. The reconstructed dipole pose may be used to inform targeted generation of magnetic fields by a manipulation system.

As the rotating dipole, a milli-scale permanent magnet synchronous motor (PMSM) is developed (Fig. 6.1a). The motor includes planar-coil inspired [251] electromagnetic stators and a permanent magnet rotor. A ferrofluid bearing is used as an antifriction mechanism, and ensures concentricity of the rotor and stator (Supplementary Movie 1). This bearing is inspired from other small-scale linear [252] and rotary motors [253], [254], as low-cost and complexity alternatives to dry-film lubricants [255], jewel bearings [256], or micro-ball bearings [257].

In order to demonstrate localization and manipulation of PMSMs, we introduce a novel rotor locking mechanism to the PMSM (Fig. 6.1b). This mechanism is inspired from the thermal and reversible solid-liquid phase transition of low melting point alloys (LMPA) [66], [258]. Here, the stators of the PMSM act as heat and field sources [259] to induce LMPA liquefying and rotor rotation, respectively. The unlocked rotor (localization mode) allows reconstruction of the PMSM pose by an external magnetometer; the locked rotor (manipulation mode) allows the PMSM to act as a static permanent magnet able to be manipulated by external fields.

The external field source comprises an electromagnetic coil [232] equipped with an eye-in-hand tri-axial Hall effect sensor, for iterative magnetic manipulation and localization of the PMSM, respectively (Fig. 6.1c). Similar to the PMSM, the external system exhibits mode-switching. In localization mode, with the electromagnet deactivated and sensor/PMSM active, rotating fields from the PMSM are used to reconstruct its pose and reposition the coil. In manipulation mode, with the electromagnet activated and sensor/PMSM deactivated, the PMSM is mechanically rotated and displaced for steering (Fig. 6.1d).

The fabrication process of the PMSM, the characterization of its thermal and magnetic properties, as well as validation of the LMPA based locking mechanism are described. Governing equations are formulated for localization of rotating magnetic dipoles with perpendicular axes of magnetization and rotation. Quantitative experiments evaluate localization accuracy along 2D and 3D trajectories of the PMSM. Finally, a benchtop experiment demonstrates localization and manipulation of the PMSM in a tubular network, using an external integrated electromagnetic coil and eye-in-hand Hall effect sensor.

6.1 Results

6.1.1 Permanent magnet synchronous motor

Figure 6.2a illustrates the fabrication process and main components of the presented PMSM, comprising cylindrical stators made of two planar electromagnetic coils (Supplementary Fig. S6.1), a diametrically mag-

netized cylindrical rotor with ferrofluid bearing, an LMPA rotor lock, a polyvinylidene fluoride (PVDF) heat shrinkable tube stator holder, a polytetrafluoroethylene (PTFE) tether guiding power leads, and a resin shell/seal preventing LMPA leakage (cross-sectional views are provided in Supplementary Fig. S6.2).

Figure 6.2b shows the fabricated stator structure, including the PTFE tether, PVDF heat shrink, stators, and rotor cavity. A top view presents the cylindrical stator coils held by the PVDF tube, with the internal rotor cavity displaying the meandering copper strands of the coils. Figure 6.2c provides front and back side views of the stator. Meandering copper strands trace a cylindrical path and align at diametrically opposite positions, resulting in superposition of magnetic flux densities. Figure 6.2d depicts the rotor magnet inside the rotor cavity (north-pole marked in red), the fusible alloy contained in the rotor cavity, and an isometric view of PMSM with the outer resin shell.

6.1.2 Motor properties

Stator magnetic field

A finite element model (FEM) of the stator structure simulates the electromagnetic field within the PMSM's rotor. In the stator coils, longitudinal copper strands generate a magnetic field in the diametric direction, while radial strands produce a field in the longitudinal direction. The magnetic field strength of the inner stator within the rotor volume ranges from 3 mT A^{-1} to 6 mT A^{-1} (Fig. 6.3a), assuming linearity between the generated field and electric current. Further, with quadrature sinusoidal currents through the inner and outer stator, average field strengths of 3.9 mT A^{-1} and 3.6 mT A^{-1} are achieved in perpendicular directions (Fig. 6.3b). The difference is due to the different inner diameters of the stators.

Stator heating

Temperature changes due to resistive heating and passive cooling of the stators, were measured at room temperature (18 °C) and in a bath of stationary heated water ($\sim$ 37 °C) using a thermocouple positioned internally or on the external surface (Supplementary Fig. S6.3). During heating, quadra-

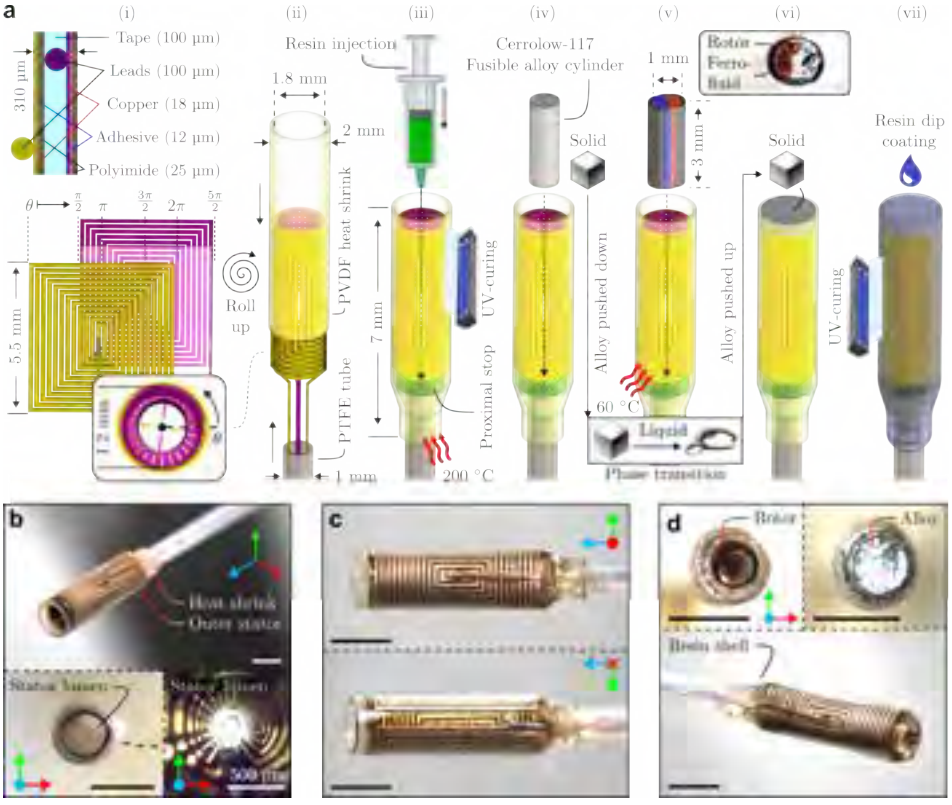

Figure 6.2: Permanent magnet synchronous motor (PMSM) components and assembly. a Fabrication of the PMSM. (i) Schematic of two stacked planar coils and a cross section with annotated dimensions. (ii) Planar coils are rolled into cylindrical stators with perpendicular angular orientation (θ). A PVDF tube maintains the shape and connects to a PTFE tube guiding power leads. (iii) An injected low-friction resin seals the proximal opening of the stator lumen. (iv) The stator lumen is filled with a solid cylinder of Cerrolow-117 alloy. (v) The cylinder is molten, followed by inserting a diametrically magnetized rotor with a ferrofluid bearing. (vi) The liquid alloy is pushed up by inserting the magnet, and cooled to solidify. (vii) The motor is sealed with a resin dip coating. **b** Photographs of the stator structure and lumen. **c** Front and back views showing coil edge alignment when wrapped. **d** Top-view and isometric photographs of the stator lumen with the rotor and fusible alloy, and finished PMSM. *Scale bar:* 2 mm.

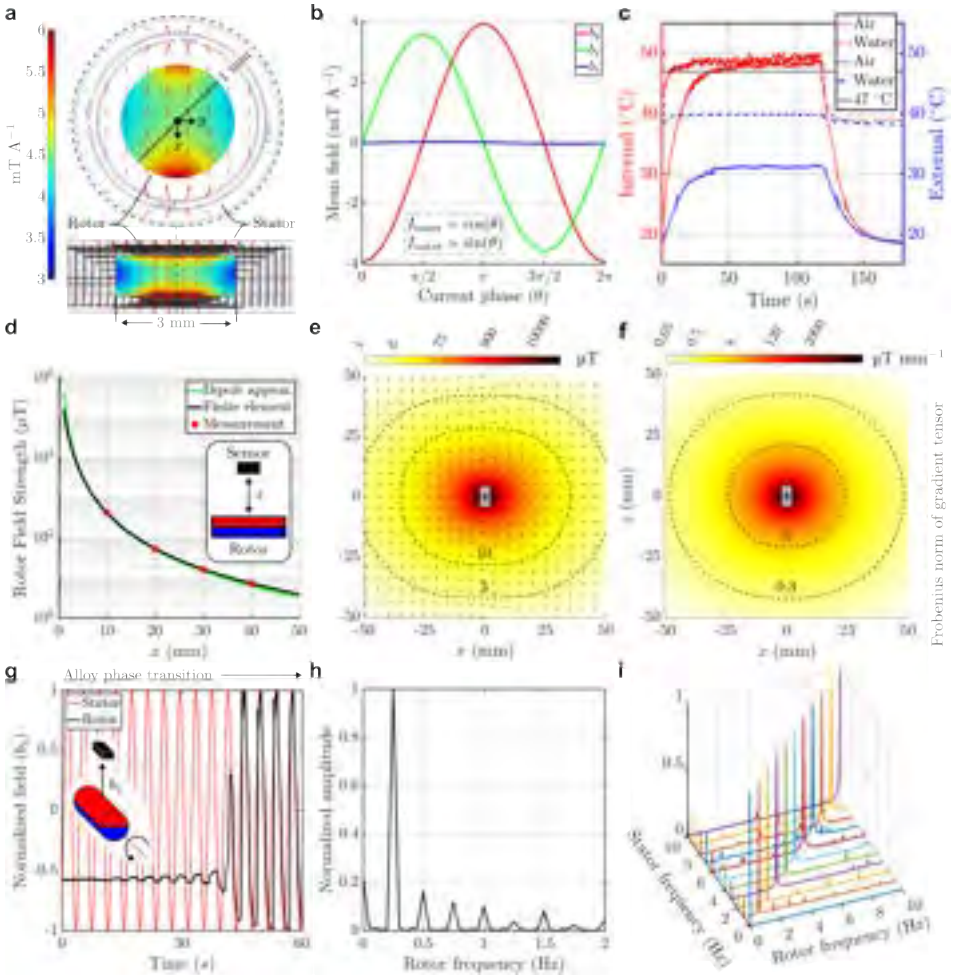

Figure 6.3: Characterization of magnetic, thermal, and frequency properties. **a-b** Simulated stator magnetic field ($\boldsymbol{b} = \langle b_x, b_y, b_z \rangle$) distribution in the rotor volume from quadrature unit-currents ($I_{\text{inner}}, I_{\text{outer}}$). **c** Measured internal and surface temperatures from 200 mA quadrature currents in room-temperature air (18 °C) and heated water (∼ 37 °C). **d** Rotor field strength along its magnetization axis. **e-f** Field and gradient norms in the magnetization plane (magnetization and rotation axes). **g** Unlocking rotor rotation by phase transition of fusible alloy during stator activation. **h** Frequency analysis of rotor field signal during unlocked state. **i** Frequency analysis for motor frequencies up to 10 Hz confirming synchronous rotation.

ture currents were applied to the inner ($I_{\text{inner}} = I\sin(2\pi f_{\text{m}}t)$) and outer stator coils ($I_{\text{outer}} = I\cos(2\pi f_{\text{m}}t)$) with current amplitude $I = 200$ mA and unit frequency ($f_{\text{m}} = 1$ Hz), over $t \in [0, 120]$ seconds. During cooling ($t \in (120, 180]$), currents were switched off. The quadrature current results in an electric power of $P = 0.165$ W, steady-state lumen temperatures of $T_{\text{internal}} \in \{49, 50\}$ °C, and PMSM surface temperatures of $T_{\text{external}} \in \{31, 40\}$ °C, in air and water, respectively (Fig. 6.3c).

Rotor magnetic field

The 3D magnetic field around the PMSM is modeled and scaled using field measurements from a Hall effect sensor (Fig. 6.3d-f). One-dimensional (1D) field measurements were taken by positioning the motor at varying distances ($x \in \{10, 20, 30, 40\}$ mm) above the sensor (Supplementary Fig. 4). The measured rotor field strengths ($b(x) \in \{411, 55, 18, 7\}$ µT) corresponds to the maximum field strength where the rotor's magnetization axis is coincident with the sensor. These measurements were taken during rotor rotation. Static background fields and noise were averaged out during signal processing (see Fig. 6.5b).

The 1D measurements are validated by comparison to a dipole approximation model, and thereafter used to scale a 3D finite element (FE) field model (Fig. 6.3d). This numerical FE model estimates magnetic fields around the rotor magnet. These estimates are used to fit an analytical 3D multipole expansion model (see Materials and Methods, $R^2 = 0.999$). Finally, this model and its spatial derivatives provide field strengths and gradients in the rotor's magnetization plane (Fig. 6.3e-f). We note that the general multipole expansion model may be interchanged for a simpler dipole approximation for modeling fields at sufficient distances from the rotor magnet [87].

Rotor locking alloy

The rotor locking mechanisms comprises a fusible alloy with a solid-liquid phase transition at 47 °C that melts due to resistive heating from the stators (Fig. 6.3g and Supplementary Movie 2).

Rotor unlocking is validated by positioning a Hall effect sensor above the motor, activating the stators with quadrature currents of $I = 175$ mA amplitude and $f_\mathrm{m} = 0.25$ Hz frequency, and measuring the magnetic field over 60 seconds. During the phase transition ($t \in [0, 45]$ s), the rotor field varies sinusoidally with temporal increasing amplitude. Once fully liquefied ($t > 45$ s), the rotor rotation is synchronous with the stator field. The duration until complete phase transition is consistent with the temperature elevation corresponding to the amplitude of quadrature current (Fig. 6.3c).

Motor rotation frequency

The rotor's synchronous rotation at the set motor frequency ($f_\mathrm{m} = 0.25$ Hz) is confirmed via frequency analysis of the field signal after liquefying of the alloy (Fig. 6.3h). Synchronous rotation is also validated across a range of frequencies ($f_\mathrm{m} \in \{1, 2, ..., 10\}$ Hz), with the upper limit imposed by the maximum sampling frequency ($f_\mathrm{s} = 20$ Hz) of the Hall effect sensor (Fig. 6.3i). In addition, a video recording shows rotor rotation up to a frequency of 10 Hz (Supplementary Movie 1).

6.1.3 Magnetic Localization

The proposed localization method matches measured to modeled rotating field properties of the rotor within its magnetization plane. This plane is defined by the rotor's rotation axis ($\hat{\boldsymbol{\omega}}_\mathrm{m}$) and magnetization axis ($\hat{\boldsymbol{\mu}}$), and contains 2D ellipse-shaped field isolines of uniform strength (Fig. 6.4a).

The 2D isolines are cross-sections of 3D tri-axial ellipsoids of constant field magnitude (b_iso), which rotate with the rotor by an angle (ϕ) about $\hat{\boldsymbol{\omega}}_\mathrm{m}$ (Fig. 6.4c). The field ($\boldsymbol{b}(\boldsymbol{p}, \phi)$) at any position ($\boldsymbol{p} \in \mathbb{R}^3$) changes in strength and direction synchronous to ϕ. Maximum field strength occurs when $\boldsymbol{p}$ coincides with the smallest isoline in the magnetization plane ($b_\mathrm{max} = \|\boldsymbol{b}(\boldsymbol{p}, \phi_\mathrm{max})\|$, where $\phi_\mathrm{max} \in \{0, \pi\}$. Minimum field strength occurs at quarter turn ($\phi_\mathrm{min} \in \{\pi/2, 3\pi/2\}$). The ratio of maximum to minimum field strength defines the field ratio ($b_\mathrm{ratio} = b_\mathrm{max}/b_\mathrm{min}$). Further, the field ($\boldsymbol{b}(\boldsymbol{p}, \phi)$) rotates within a plane around field rotation axis ($\hat{\boldsymbol{\omega}}_\mathrm{b}$) and forms an ellipse with principal axes $\{b_\mathrm{max}, b_\mathrm{min}\}$ (Supplementary Fig. S6.5).

These field properties apply to any position in space, which periodically coincides with an isoline in the magnetization plane. Therefore, field properties can be linked to isoline positions. Next, we formulate "rotor field isoline functions" to describe the relationship between rotating field properties and corresponding isoline positions.

Rotor field isoline functions

A 2D isoline in the rotor's magnetization plane is defined by field strength (b_{iso}) and position angle (β). We define an isoline position vector ($\boldsymbol{p}_{\text{e}}(b_{\text{iso}}, \beta)$) that traces the ellipse-shaped path, and that corresponds to a maximum field ($\boldsymbol{b}_{\max}(\boldsymbol{p}_{\text{e}})$), minimum field ($\boldsymbol{b}_{\min}(\boldsymbol{p}_{\text{e}})$), field rotation axis ($\hat{\boldsymbol{\omega}}_{\text{b}}(\boldsymbol{p}_{\text{e}})$), field ratio ($b_{\text{ratio}}(\boldsymbol{p}_{\text{e}}) = \|\boldsymbol{b}_{\max}(\boldsymbol{p}_{\text{e}})\|/\|\boldsymbol{b}_{\min}(\boldsymbol{p}_{\text{e}})\|$), and field rotation angle ($\alpha(\boldsymbol{p}_{\text{e}})$) between the field's rotation axis and the rotor's magnetization axis (Fig. 6.4d and Supplementary Fig. S6.5).

The rotor field isoline functions depend on (a subset of) isoline variables $\{b_{\text{iso}}, \beta\}$, and includes position ($\boldsymbol{p}_{\text{e}}(b_{\text{iso}}, \beta)$), field ratio ($b_{\text{ratio}}(\beta)$), and field angle ($\alpha(\beta)$). These three isoline functions are formulated based on simulated values from the magnetic field model of the rotor. The isoline functions show that the isoline position distance ($\|\boldsymbol{p}_{\text{e}}(b_{\text{iso}}, \beta)\|$) varies elliptically along along each isoline (Fig. 6.4e). Also, $b_{\text{ratio}} \in [1, 2]$ is cyclic and bounded along each isoline (also see Supplementary Text 1), with four possible solutions for $\beta \in \{\beta_1, \pi - \beta_1, \pi + \beta_1, -\beta_1\}$, $\beta_1 \in [0, \pi/2]$ (Fig. 6.4f). Similarly, $\alpha(\beta) \in [0, \pi]$ is cyclic and bounded. In this work, the ambiguity of β is resolved by using a-priori knowledge of rotor position through closed-loop feedback of previous localizations (eqn. (14) and Fig. 6.8d).

Notably, the magnetic field of the stators is ignored during formulation of the isoline functions. Upon synchronous rotation of the rotor's magnetization axis with the stator field, we assume that the stator only acts to amplify the PMSM's magnetic moment. In that case, although the PMSM's field strengths ($\{b_{\max}, b_{\min}\}$, $b_* := \|\boldsymbol{b}_*\|$) shift for some $\boldsymbol{p}_{\text{e}}$, its $\{b_{\text{ratio}}, \hat{\boldsymbol{b}}_{\min}, \hat{\boldsymbol{\omega}}_{\text{b}}\}$ does not. Since $\|\boldsymbol{p}_{\text{e}}\|$ depends on $b_{\text{iso}} \equiv b_{\max}$, this is the only theoretically affected isoline function (eqn. (9)). However, given the stator field's weakness compared to that of the rotor (Supplementary Fig. S6.6), its impact on $\{b_{\max}, b_{\min}\}$ is considered negligible.

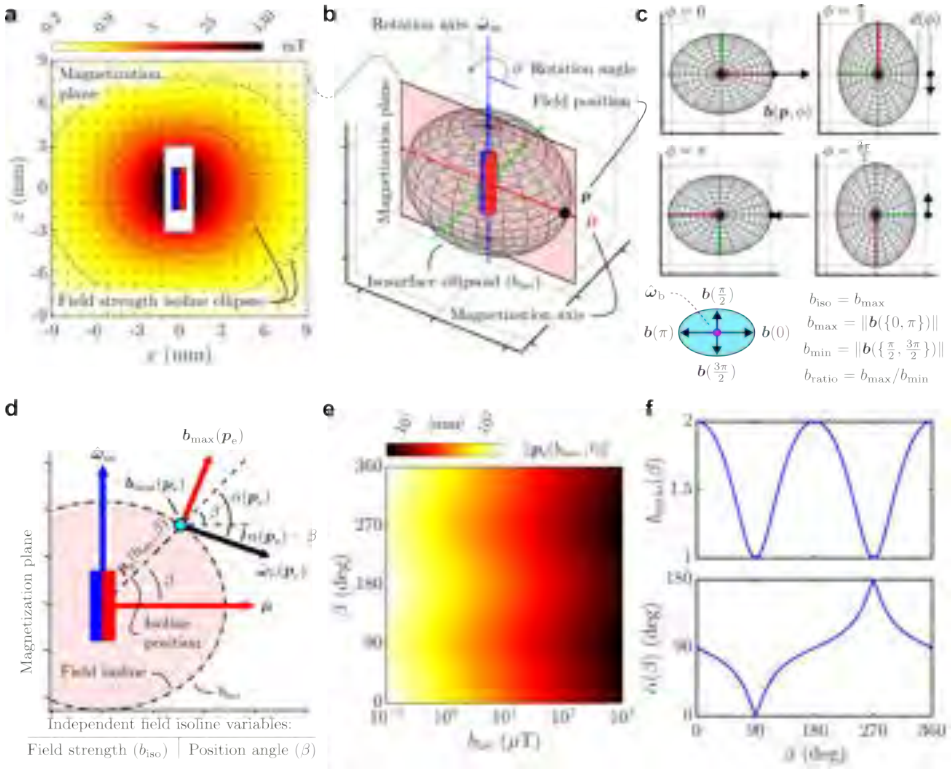

Figure 6.4: Formulation of rotor field isoline functions. **a** Magnetic field isolines and arrows in the rotor's magnetization plane (magnetization and rotation axes). **b** Field isolines are 2D cross-sections of tri-axial ellipsoidal field isosurfaces, which rotate about a motor rotation axis ($\hat{\boldsymbol{\omega}}_\mathrm{m}$) with an angle ($\phi$) during activation. **c** In situ rotation of field ellipsoidal isosurfaces generate rotating fields ($\boldsymbol{b}(\boldsymbol{p}, \phi)$) at any position ($\boldsymbol{p}$), which itself forms an ellipse with principal axes defined by the maximum and minimum field strengths ($b_\mathrm{max}, b_\mathrm{min}$). **d** Schematic representation of the magnetization plane, with an isoline ellipse traced by a position ($\boldsymbol{p}_\mathrm{e}(b_\mathrm{iso}, \beta)$) defined by the isoline field strength (b_iso) and position angle (β) from the magnetization axis ($\hat{\boldsymbol{\mu}}$). Any isoline position ($\boldsymbol{p}_\mathrm{e}$) is additionally associated with vectors of maximum field ($\boldsymbol{b}_\mathrm{max}$), minimum field ($\boldsymbol{b}_\mathrm{min}$), field rotation axis ($\hat{\boldsymbol{\omega}}_\mathrm{b}$), and scalars of field ratio ($b_\mathrm{ratio} = \|\boldsymbol{b}_\mathrm{max}\|/\|\boldsymbol{b}_\mathrm{min}\|$) and field angle ($\alpha := \angle\hat{\boldsymbol{\omega}}_\mathrm{b}, \boldsymbol{p}_\mathrm{e}$). A 3D representation is provided in Supplementary Figure S6.5. **e** Analytical function fit to isoline position vectors ($\boldsymbol{p}_\mathrm{e}(b_\mathrm{iso}, \beta) : \mathbb{R}^2 \to \mathbb{R}^2$), showing distances from rotor magnet to isolines positions. **f** Analytical function fit to field ratio ($b_\mathrm{ratio}(\beta) : \mathbb{R} \to \mathbb{R}$) and field angle ($\alpha(\beta) : \mathbb{R} \to \mathbb{R}$), considering that $\alpha(\beta) = \alpha(b_\mathrm{iso}, \beta) \equiv \alpha(\boldsymbol{p}_\mathrm{e})$.

Magnetic localization algorithm

Magnetic localization of the PMSM is informed by field measurements taken by a Hall effect sensor, at some position in space around the PMSM. These measurements are used in the rotor field isoline functions to compute the sensor's isoline position in the rotor's magnetization plane. Then, the position and rotation axis of the PMSM are determined using both the measured field components and the reconstructed isoline parameters (Supplementary Fig. S6.7). Figure 6.5a shows the localization setup, with a Hall effect sensor and PMSM. The goal is to reconstruct the motor's position (${}^{\mathrm{S}}\boldsymbol{p}_{\mathrm{m}}$) and rotation axis (${}^{\mathrm{S}}\boldsymbol{\omega}_{\mathrm{m}}$) relative to the sensor frame ({S}).

Figure 6.5b illustrates field measurement post-processing. Temporal field measurements (${}^{\mathrm{S}}\boldsymbol{b}(t)$) consist of the static earth's field, rotating PMSM field, and sensor noise. The earth's field is obtained through frequency analysis and subtracted from the measurement signal, giving the motor's field (${}^{\mathrm{S}}\boldsymbol{b}_{\mathrm{m}}(t)$). Then, a vector plot of ${}^{\mathrm{S}}\boldsymbol{b}_{\mathrm{m}}(t)$ shows formation of a 3D ellipse in the reference frame of the sensor (${}^{\mathrm{S}}\boldsymbol{R} = [{}^{\mathrm{S}}\hat{\boldsymbol{x}}, {}^{\mathrm{S}}\hat{\boldsymbol{y}}, {}^{\mathrm{S}}\hat{\boldsymbol{z}}]$), characterized by a normal vector equal to the field's rotation axis (${}^{\mathrm{S}}\boldsymbol{\omega}_{\mathrm{b}}$), and principal axes representing vectors of maximum (${}^{\mathrm{S}}\boldsymbol{b}_{\max}$) and minimum field strength (${}^{\mathrm{S}}\boldsymbol{b}_{\min}$). This additionally gives the field ratio (${}^{\mathrm{S}}b_{\mathrm{ratio}} = \|{}^{\mathrm{S}}\boldsymbol{b}_{\max}\|/\|{}^{\mathrm{S}}\boldsymbol{b}_{\min}\|$).

Figure 6.5c again visualizes ${}^{\mathrm{S}}\boldsymbol{b}_{\mathrm{m}}(t)$ in the sensor's reference frame, including the reconstructed ${}^{\mathrm{S}}\boldsymbol{b}_{\max}$, ${}^{\mathrm{S}}\boldsymbol{b}_{\min}$, and ${}^{\mathrm{S}}\hat{\boldsymbol{\omega}}_{\mathrm{b}}$. By definition, the rotor's magnetization plane is spanned by ${}^{\mathrm{S}}\hat{\boldsymbol{b}}_{\max}$ and ${}^{\mathrm{S}}\hat{\boldsymbol{\omega}}_{\mathrm{b}}$. Therefore, ${}^{\mathrm{S}}\hat{\boldsymbol{b}}_{\min}$ is perpendicular to the magnetization plane. The vector of maximum field strength is coincident and parallel to the magnetization plane, and identifies the isoline field strength ($b_{\mathrm{iso}} := \|{}^{\mathrm{S}}\boldsymbol{b}_{\max}\|$).

Figure 6.5d shows the method of matching field measurements to an isoline position in the magnetization plane, followed by reconstruction of the motor pose relative to the sensor. A non-unique isoline position angle (${}^{\mathrm{S}}\beta \in \{{}^{\mathrm{S}}\beta_1, {}^{\mathrm{S}}\beta_2, {}^{\mathrm{S}}\beta_3, {}^{\mathrm{S}}\beta_4\}$) is computed by minimizing the difference between measured and modeled field ratios. This leads to an associated isoline position (${}^{\mathrm{S}}\boldsymbol{p}_{\mathrm{e}}(b_{\mathrm{iso}}, {}^{\mathrm{S}}\beta)$) and field angle (${}^{\mathrm{S}}\alpha({}^{\mathrm{S}}\beta)$). Finally, the relative motor position (${}^{\mathrm{S}}\boldsymbol{p}_{\mathrm{m}}$) and rotation axis (${}^{\mathrm{S}}\hat{\boldsymbol{\omega}}_{\mathrm{m}}$) are found by rotating the

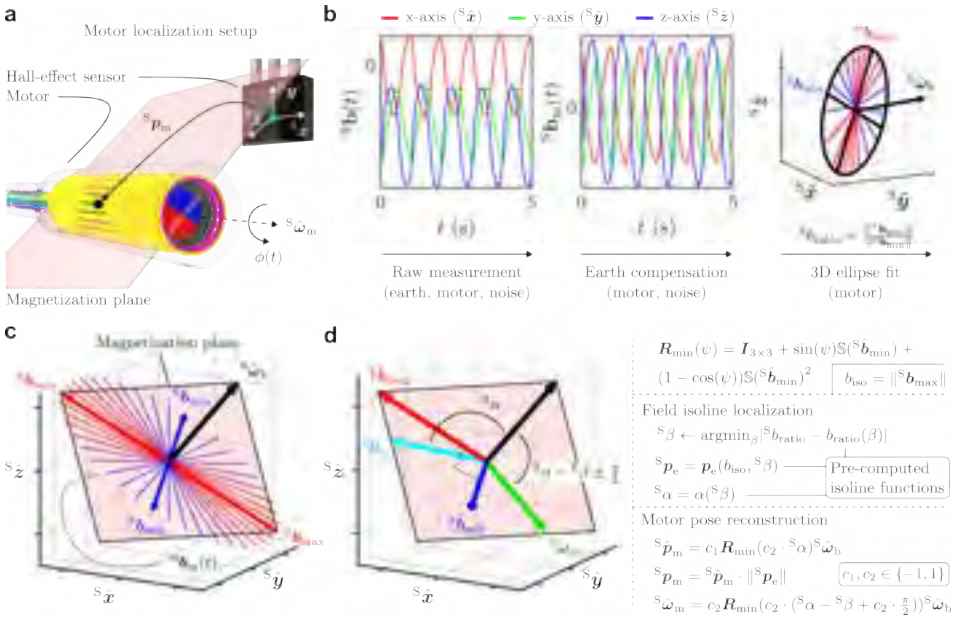

Figure 6.5: Schematic representation of the magnetic localization algorithm. **a** Setup with a Hall effect sensor and its local Cartesian axes ($\{{}^{\mathrm{S}}\hat{\boldsymbol{x}}, {}^{\mathrm{S}}\hat{\boldsymbol{y}}, {}^{\mathrm{S}}\hat{\boldsymbol{z}}\}$), and motor with position (${}^{\mathrm{S}}\boldsymbol{p}_{\mathrm{m}}$) and rotation axis (${}^{\mathrm{S}}\boldsymbol{\omega}_{\mathrm{m}}$) relative to the sensor. **b** Temporal field measurements (${}^{\mathrm{S}}\boldsymbol{b}(t)$) are compensated for the earth's field to obtain the motor field signal (${}^{\mathrm{S}}\boldsymbol{b}_{\mathrm{m}}(t)$). This signal forms an ellipse with principal axes equal to vectors of maximum (${}^{\mathrm{S}}\boldsymbol{b}_{\max}$) and minimum strength (${}^{\mathrm{S}}\boldsymbol{b}_{\min}$), and normal vector equal to the field's rotation axis (${}^{\mathrm{S}}\hat{\boldsymbol{\omega}}_{\mathrm{b}}$). **c** The rotor's magnetization plane is spanned by ${}^{\mathrm{S}}\hat{\boldsymbol{b}}_{\max}$ and ${}^{\mathrm{S}}\hat{\boldsymbol{\omega}}_{\mathrm{b}}$, with ${}^{\mathrm{S}}\hat{\boldsymbol{b}}_{\min}$ perpendicular. **d** A rotation matrix ($\boldsymbol{R}_{\min}(\psi)$) associated with the rotation vector (${}^{\mathrm{S}}\hat{\boldsymbol{b}}_{\min}\psi$) is defined, with $\mathbb{S}(*) : \mathbb{R}^3 \to \mathbb{R}^{3\times3}$ a skew-symmetric matrix. Isoline parameters are matched to the measured field ratio (${}^{\mathrm{S}}b_{\mathrm{ratio}}$), yielding solutions for the isoline position angle (${}^{\mathrm{S}}\beta$), position vector (${}^{\mathrm{S}}\boldsymbol{p}_{\mathrm{e}}$), and field angle (${}^{\mathrm{S}}\alpha$). These parameters are used to reconstruct the motor pose.

reconstructed field rotation axis (${}^{\mathrm{S}}\hat{\boldsymbol{\omega}}_{\mathrm{b}}$) around the perpendicular rotation vector (${}^{\mathrm{S}}\hat{\boldsymbol{b}}_{\mathrm{min}}\psi$) by a function of isoline angles ($\{{}^{\mathrm{S}}\beta, {}^{\mathrm{S}}\alpha\}$) scaled to coefficients ($c_1, c_2 \in \{-1, 1\}$). These combinations of coefficients represent the four possible solutions for ${}^{\mathrm{S}}\beta$ and can be obtained through optimization based on a-priori knowledge of motor position, or triangulation with an additional sensor.

Magnetic localization validation

Magnetic localization is validated by moving the PMSM relative to a fixed Hall effect sensor using a robotic arm (Supplementary Fig. S6.4 and Supplementary Movie 3). The PMSM is displaced such that the sensor traces field isoline positions ($\boldsymbol{p}_{\mathrm{e}}(b_{\mathrm{iso}}, \beta)$) of chosen isoline field strength (b_{iso}) and position angle (β) in the motor frame (Fig. 6.6a and Supplementary Movie 3). Known motor-robot-sensor transformations give the associated reference motor position ($\boldsymbol{p}_{\mathrm{m}}$) and rotation axis ($\hat{\boldsymbol{\omega}}_{\mathrm{m}}$) relative to the sensor. At each $\boldsymbol{p}_{\mathrm{e}}$, field measurement-based reconstruction of motor position (${}^{\mathrm{S}}\boldsymbol{p}_{\mathrm{m}}$) and rotation axis (${}^{\mathrm{S}}\hat{\boldsymbol{\omega}}_{\mathrm{m}}$) is performed (Fig. 6.6b). During localization, the PMSM is activated at a motor frequency of $f_{\mathrm{m}} = 1$ Hz for 30 s, with field measurements taken at the upper limit of our sensor sampling frequency ($f_{\mathrm{s}} = 20$ Hz).

Figure 6.6c shows localization results for isoline positions defined by various combinations of position angles ($\beta \in \{0, 7.5, 15, ..., 90\}$ °) and field strengths ($b_{\mathrm{iso}} \in \{6, 10, 20, 50, 100\}$ µT). The field strengths correspond to motor-sensor distances ($\|\boldsymbol{p}_{\mathrm{m}}\| \leq 43$ mm. The tracing of isolines by the sensor is validated through the maximum measured motor field strength (Fig. 6.6c(i)). The weakest isoline field strength ($b_{\mathrm{iso}} = 6$ µT) correspond to the lower boundary of signal-to-noise ratio (SNR ≥ 10 dB) for which we obtained consistent localization results (Fig. 6.6c(ii)).

Sensor noise, measured to be between 2-4 µT (Supplementary Fig. S6.6), determines whether the maximum and minimum field strength can be reliably differentiated (Fig. 6.6c(iii)). For those positions where $\|\boldsymbol{b}_{\mathrm{max}} - \boldsymbol{b}_{\mathrm{min}}\| \geq 2$ µT, errors in reconstructed field ratio are $|{}^{\mathrm{S}}b_{\mathrm{ratio}} - b_{\mathrm{ratio}}| \leq 0.12$ (Fig. 6.6c(iv)). The error in ${}^{\mathrm{S}}b_{\mathrm{ratio}}$ determines the error in isoline position angle (Fig. 6.5d and eqn. (8)) as $|{}^{\mathrm{S}}\beta - \beta| \leq 23$ ° (Fig. 6.6c(v)), and

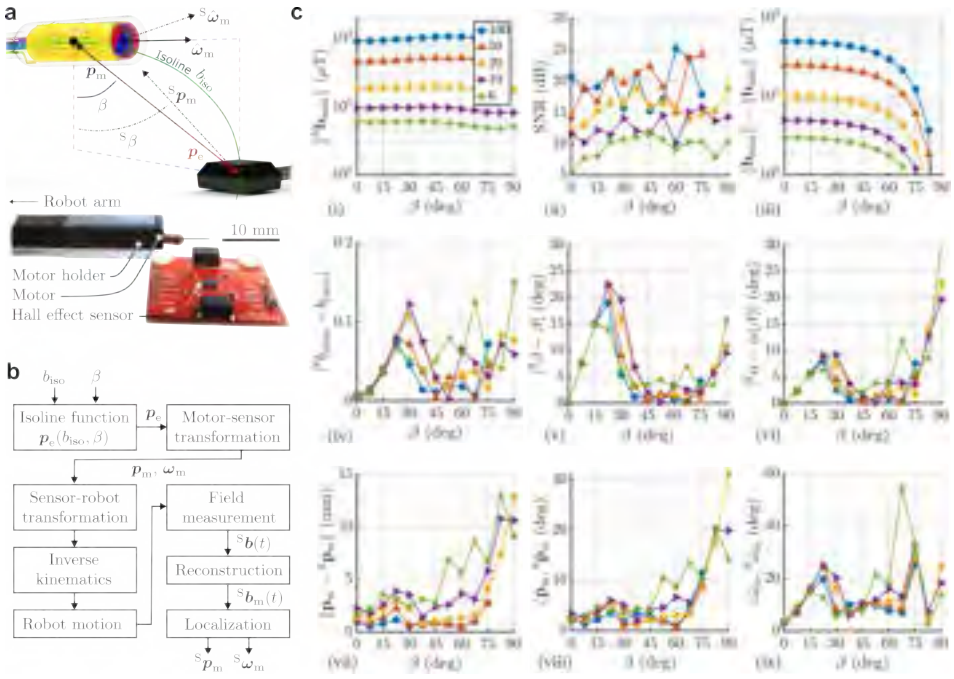

Figure 6.6: Magnetic localization of the permanent magnet synchronous motor (PMSM). a Experimental setup with a stationary Hall effect sensor and movable PMSM by a robotic arm. PMSM displacement moves the sensor along isoline positions ($\boldsymbol{p}_\mathrm{e}(b_\mathrm{iso}, \beta)$) of specific field strength (b_iso) and position angle (β). Real motor positions and rotation axis ($\boldsymbol{p}_\mathrm{m}$, $\hat{\boldsymbol{\omega}}_\mathrm{m}$) are known and compared to the measurement-based reconstructed motor pose. **b** Experimental procedure for magnetic localization. **c** Localization results for different isoline field strengths ($b_\mathrm{iso} \in \{6, 10, 20, 50, 100\}$ µT) and position angles ($\beta \in [0, 90]$ °), including (i) field strength, (ii) signal-to-noise ratio, (iii) theoretical difference in maximum and minimum field strengths, (iv) error between expected and reconstructed field ratio, (v) angular error in position angle, (vi) angular error in field angle, (vii) distance error in motor position, (viii) angular error in motor position vectors. (ix) angular error in motor rotation axis.

isoline field angle as $|^{\mathrm{S}}\alpha - \alpha(\beta)| \leq 10\ ^\circ$ (Fig. 6.6c(vi)). Finally, localization accuracy in distance offset is $\|\boldsymbol{p}_\mathrm{m} - {}^{\mathrm{S}}\boldsymbol{p}_\mathrm{m}\| \leq 7$ mm (Fig. 6.6c(vii)), and for directionality vectors of motor position $\angle\hat{\boldsymbol{p}}_\mathrm{m}, {}^{\mathrm{S}}\hat{\boldsymbol{p}}_\mathrm{m} \leq 11\ ^\circ$ (Fig. 6.6c(viii)) and rotation axis $\angle\hat{\boldsymbol{\omega}}_\mathrm{m}, {}^{\mathrm{S}}\hat{\boldsymbol{\omega}}_\mathrm{m} \leq 23\ ^\circ$ (Fig. 6.6c(ix)).

In order to analyze the angular errors in ${}^{\mathrm{S}}\hat{\boldsymbol{p}}_\mathrm{m}$ and ${}^{\mathrm{S}}\hat{\boldsymbol{\omega}}_\mathrm{m}$, consider that both equally depend on those in reconstructed field vectors ($\{{}^{\mathrm{S}}\hat{\boldsymbol{b}}_\mathrm{min}, {}^{\mathrm{S}}\hat{\boldsymbol{\omega}}_\mathrm{b}\}$), seen in the governing localization equations (Fig. 6.5d and eqns. (11)-(13)). Further, ${}^{\mathrm{S}}\hat{\boldsymbol{p}}_\mathrm{m}$ depends on ${}^{\mathrm{S}}\alpha$, whereas ${}^{\mathrm{S}}\hat{\boldsymbol{\omega}}_\mathrm{m}$ depends on $\{{}^{\mathrm{S}}\beta, {}^{\mathrm{S}}\alpha\}$. Also, ${}^{\mathrm{S}}\alpha$ depends on ${}^{\mathrm{S}}\beta$, that depends on ${}^{\mathrm{S}}b_\mathrm{ratio}$. From the partial derivatives of the isoline parameters, we observe that $|\partial\alpha(\beta \leq 60\ ^\circ)/\partial\beta| \leq 1$ and mitigates errors in ${}^{\mathrm{S}}\beta$, but amplifies above (Supplementary Fig. 8). This is seen from the peaks at $\beta = 23\ ^\circ$ and $\beta = 65\ ^\circ$ (Fig. 6.6c(v)-(vi)). Also, $|\partial\beta/\partial b_\mathrm{ratio}|$ and $|\partial\alpha/\partial b_\mathrm{ratio}|$ are most sensitive to errors at the boundary of $b_\mathrm{ratio}(\beta) \in \{1, 2\}$, and least sensitive when $b_\mathrm{ratio}(\beta) \in [1.1, 1.9]$. This corresponds to the relative motor-sensor configurations with isoline position angles of $\beta \in [25, 75]\ ^\circ$ (Fig. 6.4f).

Angular errors in $\{{}^{\mathrm{S}}\beta, {}^{\mathrm{S}}\alpha, {}^{\mathrm{S}}\hat{\boldsymbol{p}}_\mathrm{m}, {}^{\mathrm{S}}\hat{\boldsymbol{\omega}}_\mathrm{m}\}$ expectedly increase with β for which $\|\boldsymbol{b}_\mathrm{max} - \boldsymbol{b}_\mathrm{min}\|$ falls below the sensor noise and reconstructed components of the measured field become less accurate. Unexpectedly, however, the error $|^{\mathrm{S}}\beta - \beta|$ increases linearly with $\beta \leq 23\ ^\circ$ (Fig. 6.6c(v)). This error stems from an overestimation of ${}^{\mathrm{S}}b_\mathrm{ratio} \approx 2,\ \forall\beta \leq 23\ ^\circ$, which is observed for all field strengths and appears unrelated to the SNR (Fig. 6.6c(iv)). Therefore, it may be related to a problem with our sensor, such as a region of low accuracy and precision.

6.1.4 Three dimensional trajectory tracking

The three-dimensional tracking of motor pose is demonstrated along cubic (Fig. 6.7a), helical (Fig. 6.7b), and sinusoidal paths (Fig. 6.7c). Each trajectory consists of a series of predetermined positions ($\boldsymbol{p}_\mathrm{m} = \langle p_{\mathrm{m,x}}, p_{\mathrm{m,y}}, p_{\mathrm{m,z}}\rangle$) and rotation axes ($\hat{\boldsymbol{\omega}}_\mathrm{m}$) with respect to the sensor. These poses are iteratively traced by the PMSM using a robotic arm (Fig. 6.6a and Supplementary Movie 3). At each iteration, the motor's position (${}^{\mathrm{S}}\boldsymbol{p}_\mathrm{m}$) and rotation axis (${}^{\mathrm{S}}\hat{\boldsymbol{\omega}}_\mathrm{m}$) are reconstructed. At the first iteration, the known motor position ($\boldsymbol{p}_\mathrm{m}$) is used as the initial guess to compute ${}^{\mathrm{S}}\boldsymbol{p}_\mathrm{m}$. In subsequent

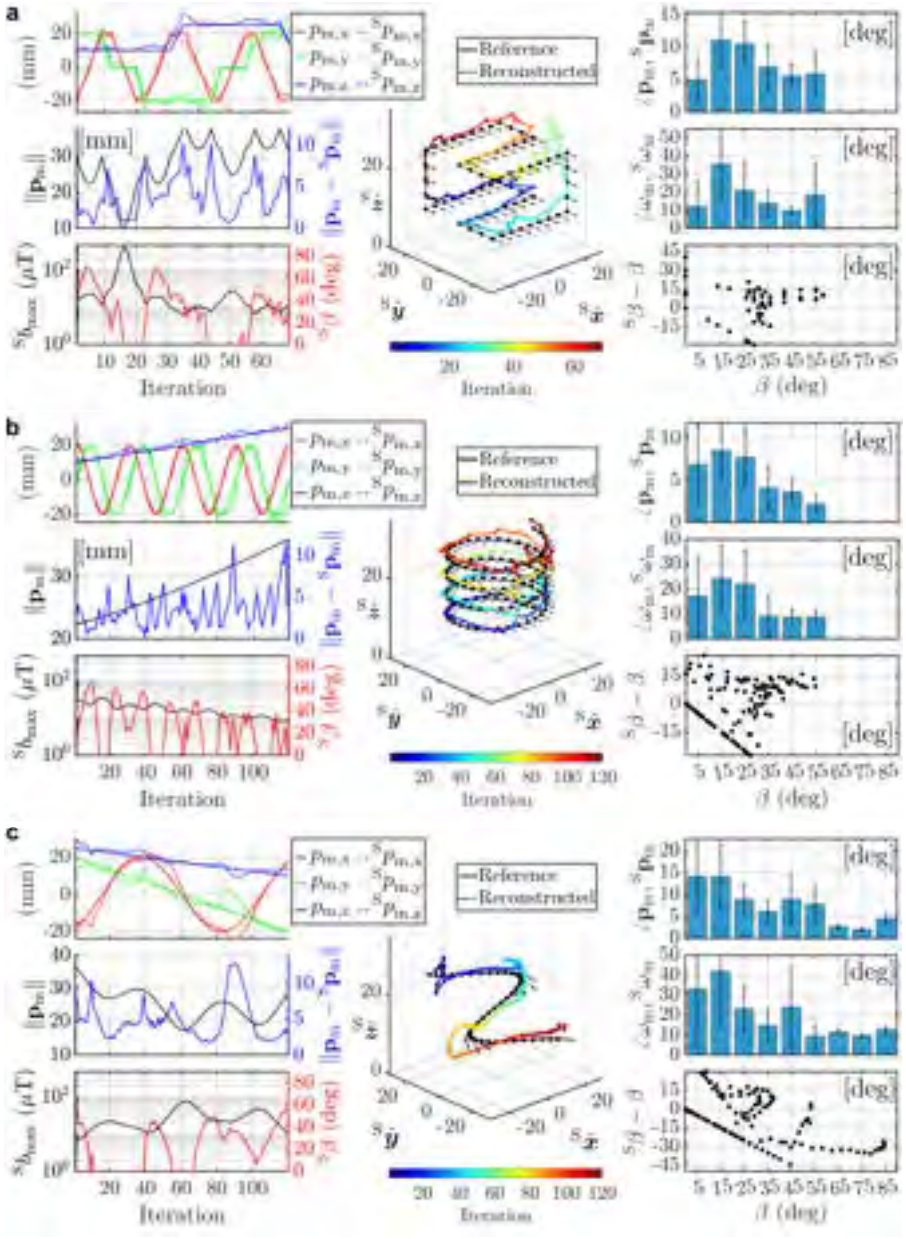

Figure 6.7: Tracking results of motor position ($\boldsymbol{p}_{\mathrm{m}}$, dots) and rotation axis ($\hat{\boldsymbol{\omega}}_{\mathrm{m}}$, arrows) with respect to the sensor frame, for **a** cubic, **b** spiral, and **c** sinusoidal trajectory.

iterations, the previously reconstructed ${}^{\mathrm{S}}\boldsymbol{p}_{\mathrm{m}}$ is used as feedback (Supplementary Fig. S6.7).

Figure 6.7 reports absolute sensor-to-motor distance ($\|\boldsymbol{p}_{\mathrm{m}}\|$) along each trajectory, localization distance error ($\|\boldsymbol{p}_{\mathrm{m}} - {}^{\mathrm{S}}\boldsymbol{p}_{\mathrm{m}}\|$), measured maximum field strength (${}^{\mathrm{S}}b_{\max} \equiv {}^{\mathrm{S}}b_{\mathrm{iso}}$), and reconstructed isoline position angle (${}^{\mathrm{S}}\beta$). Additionally, for all isoline position angles (β) along each trajectory, the angular errors in position angle (${}^{\mathrm{S}}\beta - \beta$), and PMSM directionality vectors for position ($\angle\boldsymbol{p}_{\mathrm{m}}, {}^{\mathrm{S}}\boldsymbol{p}_{\mathrm{m}}$) and rotation axes ($\angle\hat{\boldsymbol{\omega}}_{\mathrm{m}}, {}^{\mathrm{S}}\hat{\boldsymbol{\omega}}_{\mathrm{m}}$), are shown.

The tracking results support previous findings that localization is most accurate for $\beta \in [25, 75]$ ° (Fig. 6.6). Angular errors in position vectors are found to be within $\angle\boldsymbol{p}_{\mathrm{m}}, {}^{\mathrm{S}}\boldsymbol{p}_{\mathrm{m}} \in [5, 15]$ °, whereas for rotation axis within $\angle\hat{\boldsymbol{\omega}}_{\mathrm{m}}, {}^{\mathrm{S}}\hat{\boldsymbol{\omega}}_{\mathrm{m}} \in [10, 40]$ °. Localization errors increase for $\beta < 25$ °, possibly due to a region of low sensor accuracy and precision.

Significant errors and standard deviations in $\angle\hat{\boldsymbol{\omega}}_{\mathrm{m}}, {}^{\mathrm{S}}\hat{\boldsymbol{\omega}}_{\mathrm{m}}$ likely stem from incorrect optimization of the localization coefficients $\{c_1, c_2\}$ (eqn. (14)). Figure 6.7 (central panels) shows abrupt deviations in the reconstruct position, indicating a series of faulty localizations. These errors persist due to feedback to subsequent localization iterations (Supplementary Fig. 7). Since $\{c_1, c_2\}$ are optimized based on prior positions, the position angular error ($\angle\boldsymbol{p}_{\mathrm{m}}, {}^{\mathrm{S}}\boldsymbol{p}_{\mathrm{m}}$) changes less between iterations. However, an incorrect sign of $c_2 = \pm 1$ already introduces a 90 ° error in ${}^{\mathrm{S}}\hat{\boldsymbol{\omega}}_{\mathrm{m}}$ (eqn. (13)), with the potential for significant variation in angular errors ($\angle\hat{\boldsymbol{\omega}}_{\mathrm{m}}, {}^{\mathrm{S}}\hat{\boldsymbol{\omega}}_{\mathrm{m}}$) between iterations.

6.1.5 Magnetic localization and manipulation

Iterative magnetic localization and manipulation of the PMSM is demonstrated in a 2D tubular network (Supplementary Fig. S6.9 and Supplementary Movie 4). The experimental setup includes an integrated external localization-manipulation system comprising a Hall effect sensor mounted on the tip of an electromagnet, serving as the end-effector of a serial manipulator (Fig. 6.8a). The external system is vertically positioned above the PMSM and enclosing tubular network, using field measurements from the sensor to track and follow the PMSM's movement (Fig. 6.8b).

The system alternates between localization and manipulation modes (Fig. 6.8c). In localization mode, the active PMSM generates a rotating field, while the Hall effect sensor takes temporal field measurements. In this mode, the electromagnet is off to prevent sensor saturation and interference with the motor. In manipulation mode, the PMSM is locked and behaves as a passive, radially magnetized permanent magnet. The electromagnet is on to generate a stationary field for PMSM steering, allowing mechanical rotation to change its deflection plane (Fig. 6.8d).

Quantitative results show successful entrance into all tube bifurcations, as well as forward and backward tracking over a total distance of 40 cm in 300 s (Fig. 6.8e and Supplementary Fig. S6.10). In localization mode, the PMSM operates at 1 Hz, and the sensor records data at 20 Hz over 2 s. Post-processing for pose reconstruction averaged 1 second, achieving a trajectory-following frequency of about 0.3 Hz.

6.2 Discussion

This study reports a magnetic localization method for *in-vivo* rotable dipoles, which herein is a new type of locking permanent magnet synchronous motor (PMSM) based on solid-liquid phase changing low melting point alloy (LMPA). The rotating field generated by the PMSM allows for the reconstruction of its position and rotation axis by and relative to a single magnetometer, with four possible solutions. Additionally, we integrated the magnetometer with an electromagnet to create an eye-in-hand sensorized mobile electromagnetic manipulation system. By demonstrating iterative PMSM localization and manipulation, we aimed to show the potential of closed mobile magnetic navigation systems to operate independently of fluoroscopic imaging.

PMSM design. The PMSM demonstrated that 2D fabricated flexible electronics may be used as 3D stators with combined functionality as sources of magnetic field and heat. Using the heat generating property of stators has, to the authors' knowledge, for the first time been used to achieve reversible rotor locking. The ferrofluid bearing minimized friction,

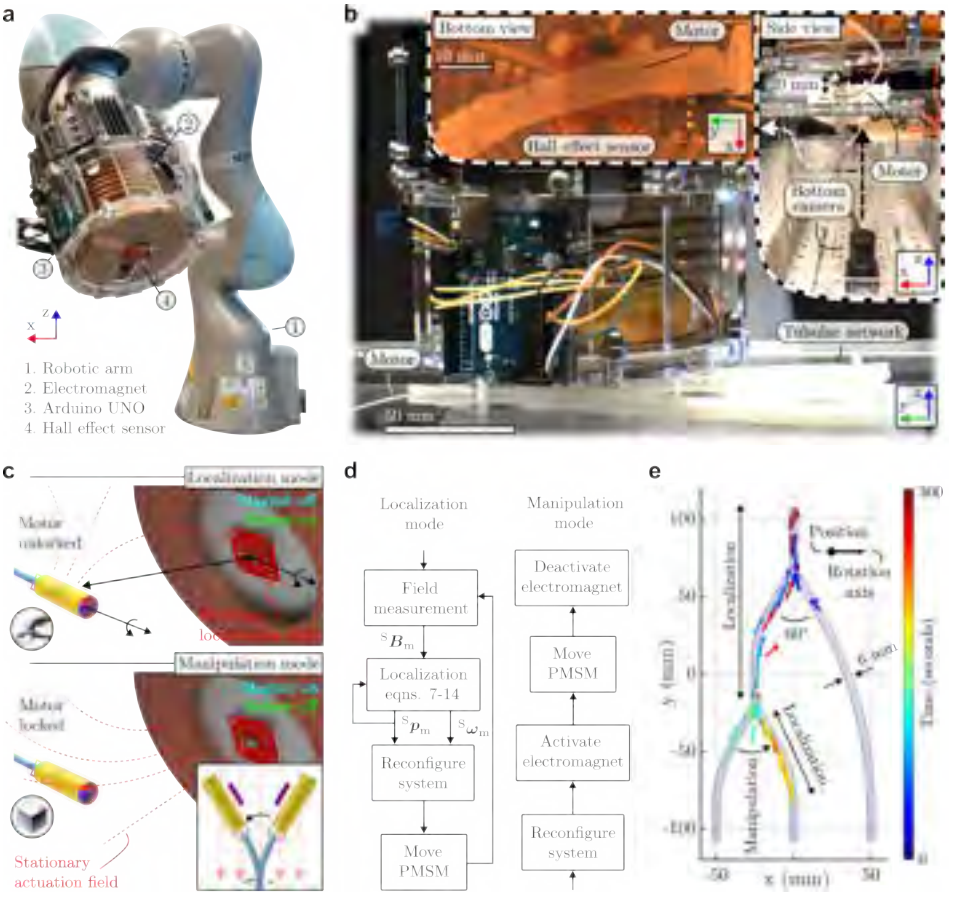

Figure 6.8: Magnetic localization and manipulation of the PMSM. a External system combining a robot arm, Hall effect magnetometer, and electromagnet. **b** Experimental setup including a tubular network enclosing the PMSM, vertically suspended electromagnet and magnetometer, and an upward facing camera. **c** Different operating modes for localization and manipulation, alternating between PMSM (un)locked states, combined with external magnet or magnetometer (in)activity. **d** Flow diagram for the localization and manipulation modes. **e** Navigation results.

opposed magnetic attraction between stators and rotor, and maintained concentricity during rotation (Supplementary Movie 1). However, manual fabrication (Fig. 6.2a) introduced functional inconsistencies. Alternatively, precise micro-fabricated parts should be considered for reliability and miniaturization [256]. Additionally, application of excess ferrofluid encapsulated the rotor, preventing locking by the LMPA.

Rotor locking mechanism. The selection of Cerrolow-117 as the LMPA for reversible rotor locking was based on its 47 °C phase transition temperature, which is close to physiologically safe [129] and below NdFeB demagnetization temperatures [260]. Also, atomically similar LMPAs have a viscosity close to water [261] and a magnetic permeability close to air [262]. However, due to its liquid state and toxic elements, encapsulation is required for medical applications [66].

Temperature measurements of the PMSM show that internal LMPA phase transition can be reached at surface temperatures ($\leq$ 44 °C) that prevent tissue injury (Fig. 6.3c) [129] Also, heating and cooling occur faster in water (37 °C) than in air (18 °C), with similar internal steady-state temperatures (49 °C). Surface temperature rises less in water (37-40 °C) than in air (18-31 °C). The system reaches steady-state in 20 s in water and 45 s in air, while passive cooling below the transition temperature takes just 2 s. This is indicative of the rate for switching between PMSM localization and manipulation modes. Therefore, mode-switching is limited by heating time but could be accelerated with increased stator currents and resistance-based temperature feedback [67].

Localization algorithm. The presented algorithm localizes a PMSM, modeled as a magnetic dipole with perpendicular rotation and magnetization axes. At its core, the algorithm uses precomputed rotor field isoline functions (eqns. (4)-(6)) that link rotating field properties to the rotating field source (Supplementary Fig. 7). By computing a ratio (b_{ratio}) of maximum and minimum field strengths ($\{b_{\max}, b_{\min}\}$) at a given position, the algorithm determines a set of isoline angles ($\{\beta, \alpha\}$) to rotate the measured field's rotation axis ($\hat{\boldsymbol{\omega}}_{\text{b}}$) into four possible combinations of dipole position

and rotation axis ($\{\hat{\boldsymbol{p}}_\mathrm{m}, \hat{\boldsymbol{\omega}}_\mathrm{m}\}$) (eqns. (8)-(10)).

This fourfold ambiguity is also reported in previous work [76]. Herein, this is resolved using prior knowledge of dipole position. However, this method risks forwarding of a previous faulty localization (Fig. 6.7). To prevent this, additional sensors may be mounted on the external manipulation system, enabling localization through triangulation.

Supporting the formulation of the isoline functions, we note that similar algorithms exist to localize a sensor based on the known temporal configuration of a rotating dipole [76], [263], [264]. However, in our reverse case, while similarly having access to field measurements, we have no information about the dipole rotation axis. This information is compensated for by formulating predetermined maps between rotating field components and the field source, i.e. the isoline functions.

Isoline function error sensitivity. The isoline functions exhibit different sensitivity to errors in field measurements depending on the relative configuration of the PMSM and sensor. Accordingly, regions of different localization error sensitivities may be distinguished around the rotor magnet [239], [265].

The error sensitivity describes how errors in measured field ratio (${}^\mathrm{S}b_\mathrm{ratio}$) affect errors in the isoline angles ($\{{}^\mathrm{S}\beta, {}^\mathrm{S}\alpha\}$). Partial derivatives indicate that $\partial\beta/\partial b_\mathrm{ratio}$ is least sensitive for $b_\mathrm{ratio} \in [1.1,\ 1.9]$, corresponding to $\beta \in [25, 75]\ ^\circ$ (Supplementary Fig. S6.8). Further, $|\partial\alpha/\partial\beta| \leq 1\ \forall\beta \in [0, 60]\ ^\circ$. This range corresponds to $b_\mathrm{ratio} \in [1.4, 2]$, for which errors in ${}^\mathrm{S}\beta$ are mitigated in ${}^\mathrm{S}\alpha$ but amplified above. Therefore, PMSM directionality vectors $\{{}^\mathrm{S}\hat{\boldsymbol{p}}_\mathrm{m}, {}^\mathrm{S}\hat{\boldsymbol{\omega}}_\mathrm{m}\}$ are least sensitive to reconstruction errors in ${}^\mathrm{S}b_\mathrm{ratio}$ for relative rotor-sensor positions at $\beta \in [25, 60]\ ^\circ$, for which $b_\mathrm{ratio} \in [1.4, 1.9]$. This region is supported by the localization experiments (Figs. 6.6 and 6.7).

Localization workspace. The localization workspace depends on the signal-to-noise ratio (SNR) of the rotor field measurement. The SNR is influenced by rotor size (magnetic moment) and sensor resolution and noise.

Here, the tri-axial Hall effect sensor has 5 mT measurement range, ~ 3 µT peak noise (Supplementary Fig. S6.6), and 0.1 µT resolution. A minimum SNR of 10 dB was identified for localization (Fig. 6.6c). Accordingly, the workspace was limited 40 mm distance from the sensor.

While this workspace is smaller than those using larger magnets [76], [244] or more precise sensors [241], [242], simulations suggest that reducing sensor noise could extend the workspace beyond 200 mm (Supplementary Fig. S6.11).

Localization accuracy. The localization accuracy, including angular errors in the PMSM's directionality vectors of position and rotation axis ($\{{}^{\mathrm{S}}\hat{\boldsymbol{p}}_{\mathrm{m}}, {}^{\mathrm{S}}\hat{\boldsymbol{\omega}}_{\mathrm{m}}\}$), depends on angular errors in the (direction of) measured minimum field strength and rotation axis ($\{{}^{\mathrm{S}}\boldsymbol{b}_{\mathrm{min}}, {}^{\mathrm{S}}\hat{\boldsymbol{\omega}}_{\mathrm{b}}\}$), as well as errors in the isoline angles ($\{{}^{\mathrm{S}}\beta, {}^{\mathrm{S}}\alpha\}$) (eqns. (11)-(13)). These are influenced by the sensor's SNR, accuracy, and precision. In this work, angular errors of 5-10 ° in ${}^{\mathrm{S}}\hat{\boldsymbol{p}}_{\mathrm{m}}$ and 10-30 ° error in ${}^{\mathrm{S}}\hat{\boldsymbol{\omega}}_{\mathrm{m}}$ were observed for a cylindrical rotor magnet (1 mm diameter, 3 mm length) along various 3D trajectories (Fig. 6.7).

Alternative sources of error, such as micrometer-range eccentricity during rotor rotation (Supplementary Movie 1) is considered negligible due to its near-zero field gradient (Fig. 6.3f). The stator field is similarly considered negligible, as its strength is one to two orders weaker than the rotor field (Supplementary Fig. S6.6). To improve localization accuracy, we hypothesize including localization methods for stationary magnets [75], as the rotor magnet's field (after filtering Earth's field) could be treated as stationary at each instant.

Localization frequency. The localization frequency (0.3 Hz) depends on rate of rotor rotation (1 Hz), sensor sampling frequency (20 Hz), the number of samples (40), and computation time. Higher localization frequencies can be achieved using faster sampling, reducing number of samples (speeding up measurement time and data processing). In combination, the rotor rotation rate could be increased, which was shown up to

10 Hz (Fig. 6.3i and Supplementary Movie 1). Faster rotor rotation rates may be achieved by increasing the current through the stators, at a cost of temperature elevation.

Magnetic manipulation. Magnetic manipulation was performed iteratively with localization, rather than simultaneously [238], [263]. This was necessary due to saturation of the eye-in-hand Hall effect sensor upon activation of the electromagnet. Additionally, the manipulation field, typically up to a few tens of milliTesla [225], is an order of magnitude stronger than the stator fields (Fig. 6.3b and Supplementary Fig. S6.6), which interferes with rotor rotation.

Rudimentary PMSM localization-informed system reconfiguration and manipulation was shown, limited to electromagnet displacement along the reconstructed motor rotation axis (Fig. 6.8c and Supplementary Movie 4). More advanced manipulation could be achieved by incorporating an electromagnet field model for model- and localization-informed reconfiguration [91].

Finally, due to the unknown radial orientation of the PMSM magnetic moment, initial application of a manipulation field causes deflection in an indeterminate plane. As a solution, we hypothesize that for synchronous motors, frequency analysis and sinusoidal fitting of field measurements can provide a time-dependent function to predict the direction of magnetic moment and, therefore, plane of deflection.

Future work. The efficacy of PMSM localization can be increased by improving sensor noise, resolution, and count. Integrating the presented algorithm with those for stationary magnets may further improve accuracy. For dipoles rotating at a constant frequency, sinusoidal fitting could be used to estimate rotor orientation and predict PMSM deflection. Multiple PMSMs with distinct frequencies could be simultaneously located via frequency analysis. The localization method may be applied to any structure incorporating or representing a rotating magnetic dipole with perpendicular magnetization and rotation axes, such as intravascular imaging

catheters [256], swimming robots [266], mechanically rotated continuum robots [224], and magnetically actuated untethered robots [267]. Beyond localization, local PMSM-generated rotating fields could be be used *in-vivo*, such as for actuation of microrobots [167], [268], wireless power transfer to implants [269], or aid in nerve regeneration [270] and cancer therapy [271], [272].

6.3 Materials and Methods

6.3.1 Fabrication of planar coils

Planar coils were fabricated from a 55 µm thick polyimide copper clad laminate (IM30-LM-000122, Goodfellow GmbH, Germany), comprising 25 µm thick polyimide, 12 µm epoxy adhesive, and 18 µm copper. The coils were prepared using optical lithography and wet etching processes. First, the copper surface was cleaned using O_2 plasma for 2 min. Then, the AZ5214 photoresist (MicroChemicals GmbH, Germany) was spin coated at 3000 rpm for 30 s and baked at 100 °C for 2 min. The coil structure was patterned using a direct UV-laser writer (DWL66, Heidelberg Instruments, Germany) with a 410 nm wavelength. The desired structure was revealed in 1:4 solution of AZ351b developer in deionized water. The laminate was subjected to post-baking at 100 °C for 2 min to ensure better adhesion of photoresist during wet etching. Thereafter, the laminate was wet etched at 60 °C in 1:10 sodium persulfate solution in DI water (B327, AG TermoPasty, Grzegorz Gasowski, Poland). Residual etching agent was removed with DI water, and the photoresist was cleaned off with acetone, isopropanol, and DI water.

Two versions of planar coil were made (inner and outer) (Supplementary Fig. S6.1a). Each coil has 12 windings. (1) The inner coil has a length of 5.5 mm and width of 4.35 mm. Copper strands have a width of 0.13 mm. Longitudinal strands are spaced 0.05 mm. Transverse strands are spaced 0.07 mm. The coil has a resistance of 0.9 Ω. (2) The outer coil has a length of 5.5 mm and width of 4.8 mm. Copper strands have a width of 0.15 mm. Longitudinal strands are spaced 0.05 mm. Transverse strands are spaced 0.05 mm. The coil has a resistance of 0.82 Ω.

6.3.2 Assembly of the PMSM

Enameled copper leads with a 50 µm diameter (TRU Components, Conrad Electronic SE) are soldered to the terminals of the planar coils (Supplementary Fig. 1b). The coils are aligned and adhered with a 1.2 mm transverse offset using 50 µm thick double-sided tape (tesa® 61250) placed around the leads (Fig. 6.2a(i)), then inserted into a polyvinylidene fluoride (PVDF) heat shrinkable tube (hellermanntyton 311-00169, Farnell) of 1.6 mm inner diameter, 1.9 mm outer diameter, and 7 mm length ((Fig. 6.2a(ii))). The coils' center-to-center offset displacement provides perpendicular angular orientation between the wrapped coils.

The copper leads are threaded through a polytetrafluoroethylene (PTFE) tube with a 0.66 mm inner and 0.96 mm outer diameter (ptfetubeshop, The Netherlands) (Fig. 6.2a(ii)), that serves as a protective tether and additionally houses a polyetheretherketone (PEEK) mandrel with 0.38 mm diameter (Zeus Industral Inc., USA). Heat is applied at 200 °C to shrink the PVDF tube, connecting it to the PTFE tether (Fig. 6.2a(iii)). Thereafter, low-friction resin (durable resin, Formlabs) is injected into the stator lumen, pushed down using a steel rod of 1.2 mm diameter, and UV-cured at 60 °C for 60 min (Form Cure, Formlabs), creating an airtight seal for the lumen and rigid connection to the PEEK mandrel.

A solid cylinder of fusible alloy (Cerrolow 117, Bolton Metal Products Co., Inc., USA) is placed in the rotor lumen (Fig. 6.2a(iv)). This cylinder is made by injecting liquefied alloy in a silicone tube of 1 mm inner diameter, followed by cooling and solidification, cutting to a 3 mm length with a stanley knife, and subsequent removal of the cylinder from the tube. Then, a constant current of 150 mA is applied to the inner stator, resulting in heating and liquefying the alloy. Thereafter, a diametrically magnetized rotor of 1 mm diameter and 3 mm length (SP0103DM-50, First4Magnets, UK), partially coated with ferrofluidic bearing (M-FER-10, Supermagnete, The Netherlands), is inserted and submerged in the liquefied alloy (Fig. 6.2a(v)). Consequently, the alloy fills the space around the rotor and is pushed upwards towards the distal exit of the stator lumen (Fig. 6.2a(vi)). Upon deactivation of the stator, the alloy solidifies. Finally, the assembled motor is dip-coated in UV-curable resin (durable resin,

Formlabs) and cured at at 40 °C to prevent intermediate phase transition of the alloy during curing, as well as leakage during activation (Fig. 6.2a(vii)).

6.3.3 PMSM thermal characterization

Thermal characterization was performed in air at room temperature (20 °C) with the permament magnet synchronous motor (PMSM) having an empty rotor cavity, i.e., without an internal rotor magnet or fusible alloy (see Fig. 6.2b). Quadrature currents were applied to the inner ($I_{\text{inner}} = I\cos(2\pi f_{\text{m}}t)$) and outer stator ($I_{\text{outer}} = I\sin(2\pi f_{\text{m}}t)$), with variable amplitude ($I \in \{150, 175, 200\}$ mA) and unit frequency ($f_{\text{m}} = 1$ Hz).

Temperature measurements over a duration of $t \in [0, 300]$ s were obtained using a 0.5 mm diameter K-type themocouple (RS PRO, 433-7917) attached to a thermocouple-to-digital converter module (Diligent Pmod TC1, RS PRO, 134-6476) and Arduino Nano. The thermocouple was positioned both on the outer surface of the PMSM and inside the rotor cavity to measure external and internal temperature increase, respectively (Supplementary Figure S5.2).

6.3.4 Rotor field model

We present an analytical model for accurately describing the magnetic field generated by cylindrical radially magnetized permanent rotors. The rotor volume is discretized into subvolumes, each modeled as field source using a multipole expansion model. Symmetry of the multipole expansion models among these subvolume field sources ensures axisymmetry of the magnetic field around the rotor's magnetization axis. This model is herein referred to as an finite element (FE)-inspired multipole/source expansion model.

Let ${}^{\text{R}}\boldsymbol{R} = [{}^{\text{R}}\hat{\boldsymbol{x}}, {}^{\text{R}}\hat{\boldsymbol{y}}, {}^{\text{R}}\hat{\boldsymbol{z}}] \in \text{SO}(3)$ be the rotor's local reference frame in its center of mass. Here, ${}^{\text{R}}\hat{\boldsymbol{z}}$ is the longitudinal axis, $\{{}^{\text{R}}\hat{\boldsymbol{x}}, {}^{\text{R}}\hat{\boldsymbol{y}}\}$ the radial axes, and ${}^{\text{R}}\boldsymbol{\mu} = {}^{\text{R}}\hat{\boldsymbol{x}}$ the magnetization axis. We also define a position vector ($\boldsymbol{p} := {}^{\text{R}}\boldsymbol{p} = \langle {}^{\text{R}}x, {}^{\text{R}}y, {}^{\text{R}}z\rangle$) expressed in ${}^{\text{R}}\boldsymbol{R}$.

Given a base harmonic scalar potential (${}^{\text{R}}\Psi_0(\boldsymbol{p} = 1/\|\boldsymbol{p}\|)$) that satisfies Laplace's equation, the corresponding field function (${}^{\text{R}}\boldsymbol{b}_0(\boldsymbol{p}) = \partial({}^{\text{R}}\Psi_0)/\partial\boldsymbol{p}$)

is divergence- and curl-free as required by Maxwell's equations in current-free space. This property extends to higher-order derivatives of the scalar potential with respect to the magnetization axis (${}^{\mathrm{R}}\Psi_u(\boldsymbol{p}) = \partial^u({}^{\mathrm{R}}\Psi_0)/\partial x^u$, $u \in \mathbb{N}$), and their associated fields (${}^{\mathrm{R}}\boldsymbol{b}_u(\boldsymbol{p}) = \partial({}^{\mathrm{R}}\Psi_u(\boldsymbol{p}))/\partial\boldsymbol{p}$), as well as those scaled by scalar coefficients ($a_u \in \mathbb{R}$). Scalar potentials with $u \in 2\mathbb{N}$ provide field functions ${}^{\mathrm{R}}\boldsymbol{b}_u(\boldsymbol{p})$ that contain (unpaired) monopole terms, such as tripole ($u = 2$) or pentapole ($u = 4$). Natural absence of monopoles therefore constrains $u \in 2\mathbb{N} + 1$ to be uneven.

Scalar potentials are assigned to subvolumes of the rotor, with displacement vectors ($\Delta\boldsymbol{p}_v,\ v \in \mathbb{N}$) relative to ${}^{\mathrm{R}}\boldsymbol{R}$. These vectors are part of a symmetric set ($\Delta\mathbb{P}_v$) with respect to the planes spanned by the principal axes in ${}^{\mathrm{R}}\boldsymbol{R}$:

$$\Delta\mathbb{P}_v = \{\Delta\boldsymbol{p}_v^{+++}, \Delta\boldsymbol{p}_v^{++-}, \Delta\boldsymbol{p}_v^{+-+}, \Delta\boldsymbol{p}_v^{-++}, \Delta\boldsymbol{p}_v^{+--}, \Delta\boldsymbol{p}_v^{-+-}, \Delta\boldsymbol{p}_v^{--+}, \Delta\boldsymbol{p}_v^{---}\},$$

where $\Delta\boldsymbol{p}_v^{\pm\pm\pm}$ has positive/negative xyz-components, and $\Delta\mathbb{P}_{v,i}$ is the $i^{\text{th}} \in \{1, 2, ..., 8\}$ displacement vector. Symmetry of the field model around the magnetization axis requires coefficients for pole-specific scalar potentials to be equal for all displacement vectors in a symmetric set. Accordingly, the base harmonic scalar potential is formulated:

$$ {}^{\mathrm{R}}\Psi_{0,v}(\boldsymbol{p}) = \sum_{i=1}^{8} \frac{1}{\|\boldsymbol{p} - \Delta\mathbb{P}_{v,i}\|}, \tag{6.1}$$

leading to the field expression for a symmetric set of source displacement vectors:

$$\begin{aligned} {}^{\mathrm{R}}\boldsymbol{b}_v(\boldsymbol{p}) &= \sum_{u=0} a_{2u+1,v} \cdot \frac{\partial}{\partial\boldsymbol{p}} \left(\frac{\partial^{2u+1}}{\partial x^{2u+1}} ({}^{\mathrm{R}}\Psi_{0,v}) \right) \\ &= a_{1,v}\,{}^{\mathrm{R}}\boldsymbol{b}_{1,v} + a_{3,v}\,{}^{\mathrm{R}}\boldsymbol{b}_{3,v} + a_{5,v}\,{}^{\mathrm{R}}\boldsymbol{b}_{5,v} + \ldots, \\ &= \underbrace{\begin{bmatrix} {}^{\mathrm{R}}\boldsymbol{b}_{1,v} & {}^{\mathrm{R}}\boldsymbol{b}_{3,v} & \ldots \end{bmatrix}}_{{}^{\mathrm{R}}\boldsymbol{B}_v(\boldsymbol{p})} \underbrace{\begin{bmatrix} a_{1,v} & a_{3,v} & \ldots \end{bmatrix}^T}_{\boldsymbol{a}_v}. \end{aligned} \tag{6.2}$$

Finally, the FE-inspired multipole/source expansion model is given by:

$$ {}^{\mathrm{R}}\boldsymbol{b}(\boldsymbol{p}) = \sum_{v=1} {}^{\mathrm{R}}\boldsymbol{B}_v(\boldsymbol{p})\boldsymbol{a}_v = \underbrace{\begin{bmatrix} {}^{\mathrm{R}}\boldsymbol{B}_1 & {}^{\mathrm{R}}\boldsymbol{B}_2 & \ldots \end{bmatrix}}_{{}^{\mathrm{R}}\boldsymbol{B}(\boldsymbol{p})} \underbrace{\begin{bmatrix} \boldsymbol{a}_1^T & \boldsymbol{a}_2^T & \ldots \end{bmatrix}^T}_{\boldsymbol{a}}. \tag{6.3}$$

This model was implemented using Matlab's symbolic toolbox (Matlab R2024, The Mathworks, Natick, Massachusetts, USA). The model coefficients were obtained by linear least squares regression with field estimates ${}^{\mathrm{R}}\tilde{\boldsymbol{b}}(\boldsymbol{p})$ obtained from a measurement-based scaled FEM of the rotor (COMSOL, Burlington, VT, USA), according to $\boldsymbol{a} = ({}^{\mathrm{R}}\boldsymbol{B}(\boldsymbol{p})^{\dagger}){}^{\mathrm{R}}\tilde{\boldsymbol{b}}(\boldsymbol{p})$, where $*^{\dagger}$ represents the pseudoinverse.

6.3.5 Rotor field isoline functions

Within the formulation of the following rotor field isoline functions, we again consider ${}^{\mathrm{R}}\boldsymbol{R} = [{}^{\mathrm{R}}\hat{\boldsymbol{x}}, {}^{\mathrm{R}}\hat{\boldsymbol{y}}, {}^{\mathrm{R}}\hat{\boldsymbol{z}}] \in \mathrm{SO}(3)$ as the rotor's local reference frame in its center of mass, ${}^{\mathrm{R}}\hat{\boldsymbol{x}}$ and ${}^{\mathrm{R}}\hat{\boldsymbol{z}}$ to span the rotor's magnetization plane, $\hat{\boldsymbol{\mu}} := {}^{\mathrm{R}}\hat{\boldsymbol{x}}$ as the rotor's magnetization axis, and $\hat{\boldsymbol{\omega}}_{\mathrm{m}} := {}^{\mathrm{R}}\hat{\boldsymbol{z}}$ as the rotor's rotation axis.

Isoline position

The isoline position vector function ($\boldsymbol{p}_{\mathrm{e}}(b_{\mathrm{iso}}, \beta) : \mathbb{R}^2 \rightarrow \mathbb{R}^2$) traces the circumference of two-dimensional, ellipse-shaped field isolines of uniform strength (b_{iso}) as a function of a position angle (β) relative to the rotor's magnetization axis (see Fig. 6.4). This function is formulated as:

$$\boldsymbol{p}_{\mathrm{e}}(b_{\mathrm{iso}}, \beta) = \langle c_{\mathrm{x}}(b_{\mathrm{iso}})\cos(\beta),\ c_{\mathrm{z}}(b_{\mathrm{iso}})\sin(\beta)\rangle, \tag{6.4}$$

with $c_{\mathrm{x}}(b_{\mathrm{iso}})$ and $c_{\mathrm{z}}(b_{\mathrm{iso}})$ coefficients dependent on the isoline field strength, modeled as second-order power functions: $c_{\mathrm{x}}(b_{\mathrm{iso}}) = c_{\mathrm{x},1} b_{\mathrm{iso}}^{c_{\mathrm{x},2}} + c_{\mathrm{x},3}$, with $c_{\mathrm{x},i}$ ($i \in \{1,2,3\}$) the power function parameters. The same model applies to $c_{\mathrm{z}}(b_{\mathrm{iso}})$.

To calculate the power function parameters, the rotor field function ${}^{\mathrm{R}}\boldsymbol{b}(\boldsymbol{p})$ is used to compute the magnetic field strength at various positions on a 2D grid within the magnetization plane. Matlab's *contour* function then generates matrices of 2D position vectors corresponding to different elliptical contour levels (b_{iso}). The ellipse coefficients ($c_{\mathrm{x}}(b_{\mathrm{iso}}), c_{\mathrm{z}}(b_{\mathrm{iso}})$) for each contour level are then obtained using the *fit_ellipse* function [273]. Finally, the independent parameters of the power functions ($c_{\mathrm{x},i}, c_{\mathrm{z},i}$) are determined using Matlab's *curve fitting* toolbox.

Isoline field ratio

The isoline field ratio scalar function ($b_{\text{ratio}}(\beta) : \mathbb{R} \to \mathbb{R}$) describes the ratio of maximum to minimum magnetic field strength at isoline position angles (β). This function is formulated as:

$$b_{\text{ratio}}(\beta) = a_0 + \sum_{k=1}^{8} \big(a_k \cos(k\beta w) + b_k \sin(k\beta w)\big), \tag{6.5}$$

where $a_k,\ b_k,\ w$ are Fourier coefficients.

To determine these coefficients, we select an isoline field strength ($b_{\text{iso}} = 100$ µT) and compute the field ratio over a range of position angles ($\beta \in \{1, 2, ..., 360\}^\circ$). The corresponding 2D isoline positions ($\boldsymbol{p}_{\text{e}}(b_{\text{iso}}, \beta) = \langle p_{\text{e,x}}, p_{\text{e,z}} \rangle$) are computed, and a 3D variant is defined as $\tilde{\boldsymbol{p}}_{\text{e}}(b_{\text{iso}}, \beta) = \langle p_{\text{e,x}},\ 0,\ p_{\text{e,z}} \rangle$.

Using the 3D rotor field function (${}^{\text{R}}\boldsymbol{b}(\boldsymbol{p})$), maximum field ($b_{\max}(\beta) = \|{}^{\text{R}}\boldsymbol{b}(\tilde{\boldsymbol{p}}_{\text{e}}(b_{\text{iso}}, \beta))\|$) and minimum field strength ($b_{\min}(\beta) = \|\boldsymbol{R}_{\text{z}}(\pi/2)^{\text{R}}\boldsymbol{b}(\boldsymbol{R}_{\text{z}}(\pi/2)^{\text{T}}\tilde{\boldsymbol{p}}_{\text{e}}(b_{\text{iso}}, \beta))\|$) are calculated for each angle β, where $\boldsymbol{R}_{\text{z}} \in \text{SO}(3)$ is a rotation matrix corresponding to the rotor's rotation axis ($\hat{\boldsymbol{\omega}}_{\text{m}} := {}^{\text{R}}\hat{\boldsymbol{z}}$). The field ratio is then determined as $b_{\text{ratio}}(\beta) = b_{\max}(\beta)/b_{\min}(\beta)$. Finally, the Fourier coefficients are obtained using Matlab's *curve fitting* toolbox, applying an 8-term Fourier series to fit $b_{\text{ratio}}(\beta)$ across the range of β.

Isoline field angle

The isoline field angle scalar function ($\alpha(\beta) : \mathbb{R} \to \mathbb{R}$) decribes the angle between the isoline position vector and field rotation axis. This function is formulated as:

$$\alpha(\beta) = a_0 + \sum_{k=1}^{20} a_k \cos(2\pi f_k \beta - b_k), \tag{6.6}$$

where $a_k,\ f_k,\ b_k$ are Fourier parameters.

To determine these parameters, we again select an isoline field strength ($b_{\text{iso}} = 100$ µT) and range of position angles ($\beta \in \{1, 2, ..., 360\}^\circ$), and compute 2D isoline positions ($\boldsymbol{p}_{\text{e}}(b_{\text{iso}}, \beta) = \langle p_{\text{e,x}},\ p_{\text{e,z}} \rangle$), a 3D variant $\tilde{\boldsymbol{p}}_{\text{e}}(b_{\text{iso}}, \beta) =$

$\langle p_{\mathrm{e,x}},\ 0,\ p_{\mathrm{e,z}}\rangle$, and maximum field strength ($\boldsymbol{b}_{\max}(\beta) = {}^{\mathrm{R}}\boldsymbol{b}(\tilde{\boldsymbol{p}}_{\mathrm{e}}(b_{\mathrm{iso}}, \beta))$) and minimum field strength ($\boldsymbol{b}_{\min}(\beta) = \boldsymbol{R}_{\mathrm{z}}(\pi/2)^{\mathrm{R}}\boldsymbol{b}(\boldsymbol{R}_{\mathrm{z}}(\pi/2)^{\mathrm{T}}\tilde{\boldsymbol{p}}_{\mathrm{e}}(b_{\mathrm{iso}}, \beta))$). The field rotation axis at each β is then computed as $\hat{\boldsymbol{\omega}}_{\mathrm{b}}(\beta) = \hat{\boldsymbol{b}}_{\max}(\beta) \times \hat{\boldsymbol{b}}_{\min}(\beta)$, where $\hat{*}$ denotes a unit-vector. The isoline field angle is then obtained as $\alpha(\beta) = \cos^{-1}(\hat{\tilde{\boldsymbol{p}}}_{\mathrm{e}} \cdot \boldsymbol{\omega}_{\mathrm{b}}(\beta))$. Finally, the Fourier parameters including amplitudes (a_k), frequencies (f_k), and phases (b_k) are obtained with the *ft_spect* function [274].

6.3.6 Motor field properties

A PMSM driven by quadrature currents in the inner ($I_{\mathrm{inner}} = I\sin(2\pi f_{\mathrm{m}}t)$) and outer ($I_{\mathrm{outer}} = I\cos(2\pi f_{\mathrm{m}}t)$) stators at a given motor frequency (f_{m}) generates a rotating magnetic field (${}^{\mathrm{S}}\boldsymbol{b}_{\mathrm{m}}(t)$). Field measurements are taken with a Hall effect sensor (MLX90371, Melexis, Ypres, Belgium) positioned around the PMSM, at a sampling frequency, $f_{\mathrm{s}} = 20$ Hz. The sensor samples the tri-axial magnetic field (${}^{\mathrm{S}}\boldsymbol{b}(t) = {}^{\mathrm{S}}\boldsymbol{b}_0 + {}^{\mathrm{S}}\boldsymbol{b}_{\mathrm{m}}(t) + \boldsymbol{n}_{\mathrm{s}}(t)$), which includes earth's static field (${}^{\mathrm{S}}\boldsymbol{b}_0$), the motor field ${}^{\mathrm{S}}\boldsymbol{b}_{\mathrm{m}}(t)$, and sensor noise ($\boldsymbol{n}_{\mathrm{s}}(t)$).

Tri-axial field measurements recorded at discrete time instants ($i\Delta t$), where $\Delta t = 1/f_s$, are stored in matrix form (${}^{\mathrm{S}}\boldsymbol{B} = [{}^{\mathrm{S}}\boldsymbol{b}(t_0), {}^{\mathrm{S}}\boldsymbol{b}(t_1), \ldots, {}^{\mathrm{S}}\boldsymbol{b}(t_M)]$). Fourier-derived frequency-specific amplitudes ($\boldsymbol{A}_{\mathrm{fft}}(f)$) are obtained with Matlab's *fft* function, giving the earth's field as ${}^{\mathrm{S}}\boldsymbol{b}_0 = \boldsymbol{A}_{\mathrm{fft}}(0)$. The motor field measurements matrix (${}^{\mathrm{S}}\boldsymbol{B}_{\mathrm{m}} = [{}^{\mathrm{S}}\boldsymbol{b}_{\mathrm{m}}(t_0), {}^{\mathrm{S}}\boldsymbol{b}_{\mathrm{m}}(t_1), \ldots, {}^{\mathrm{S}}\boldsymbol{b}_{\mathrm{m}}(t_M)]$) is then computed, with ${}^{\mathrm{S}}\boldsymbol{b}_{\mathrm{m}}(t_i) = {}^{\mathrm{S}}\boldsymbol{b}(t_i) - {}^{\mathrm{S}}\boldsymbol{b}_0$.

Considering zero noise, ${}^{\mathrm{S}}\boldsymbol{b}_{\mathrm{m}}(t)$ forms an ellipse and rotates in a plane with a normal vector equal to the field's rotation axis (${}^{\mathrm{S}}\hat{\boldsymbol{\omega}}_{\mathrm{b}}$), computed using the following minimization problem implemented with Matlab's *fmincon*:

$$\pm{}^{\mathrm{S}}\hat{\boldsymbol{\omega}}_{\mathrm{b}} = \arg\min_{\hat{\boldsymbol{\omega}}} \sum_{i=0}^{M} \sqrt{\left(\hat{\boldsymbol{\omega}} \cdot {}^{\mathrm{S}}\hat{\boldsymbol{b}}_{\mathrm{m}}(t_i)\right)^2}, \tag{6.7}$$

where $\hat{*}$ denotes a unit-vector. Further, we fit a 3D ellipse to ${}^{\mathrm{S}}\boldsymbol{B}_{\mathrm{m}}$, whose principal axes correspond to the vectors of maximum and minimum field strength. To this end, we define a rotation matrix (${}^{\mathrm{S}}_{\mathrm{E}}\boldsymbol{R} = [{}^{\mathrm{S}}\hat{\boldsymbol{x}}_{\mathrm{E}}, {}^{\mathrm{S}}\hat{\boldsymbol{y}}_{\mathrm{E}}, {}^{\mathrm{S}}\hat{\boldsymbol{z}}_{\mathrm{E}}]$) between the sensor and field ellipse frame where ${}^{\mathrm{S}}\hat{\boldsymbol{z}}_{\mathrm{E}} = {}^{\mathrm{S}}\hat{\boldsymbol{\omega}}_{\mathrm{b}}$, and ${}^{\mathrm{S}}\hat{\boldsymbol{x}}_{\mathrm{E}} \times {}^{\mathrm{S}}\hat{\boldsymbol{y}}_{\mathrm{E}} = {}^{\mathrm{S}}\hat{\boldsymbol{z}}_{\mathrm{E}}$ is arbitrary. The motor field measurements are projected

onto the 2D ellipse plane as ${}^{\mathrm{E}}\boldsymbol{B}_{\mathrm{m}} = \left({}^{\mathrm{S}}_{\mathrm{E}}\boldsymbol{R}^{\mathrm{T}}\right){}^{\mathrm{S}}\boldsymbol{B}_{\mathrm{m}}$. A 2D ellipse is then fit to the xy-components (${}^{\mathrm{E}}\boldsymbol{B}_{\mathrm{m,xy}}$) using the *fit_ellipse* function implemented in Matlab [273]. Given sufficient data points, it is assumed that sensor noise ($\boldsymbol{n}_{\mathrm{s}}(t)$) is averaged out during fitting of the ellipse. The principal axes of this ellipse represent the vectors of maximum (${}^{\mathrm{E}}\boldsymbol{b}_{\mathrm{max,xy}}$) and minimum (${}^{\mathrm{E}}\boldsymbol{b}_{\mathrm{min,xy}}$) field strength. Their respective 3D representations (${}^{\mathrm{E}}\boldsymbol{b} = \langle\, {}^{\mathrm{E}}\boldsymbol{b}_{\mathrm{xy}}, 0\rangle$) are then transformed back to the sensor's reference frame, yielding ${}^{\mathrm{S}}\boldsymbol{b}_{\mathrm{max}} = \left({}^{\mathrm{S}}_{\mathrm{E}}\boldsymbol{R}\right){}^{\mathrm{E}}\boldsymbol{b}_{\mathrm{max}}$ and ${}^{\mathrm{S}}\boldsymbol{b}_{\mathrm{min}} = \left({}^{\mathrm{S}}_{\mathrm{E}}\boldsymbol{R}\right){}^{\mathrm{E}}\boldsymbol{b}_{\mathrm{min}}$. Finally, the field ratio is obtained as ${}^{\mathrm{S}}b_{\mathrm{ratio}} = \|{}^{\mathrm{S}}\boldsymbol{b}_{\mathrm{max}}\|/\|{}^{\mathrm{S}}\boldsymbol{b}_{\mathrm{min}}\|$. Given the theoretical limits of field ratio ($b_{\mathrm{ratio}}(\beta) \in [1, 2]$), any measured ${}^{\mathrm{S}}b_{\mathrm{ratio}}$ that falls outside this range is adjusted to the nearest boundary value.

6.3.7 Reconstruction of motor pose

The motor pose relative to and expressed in the sensor frame $\{S\}$ is defined by the motor's position (${}^{\mathrm{S}}\boldsymbol{p}_{\mathrm{m}}$) and rotation axis (${}^{\mathrm{S}}\boldsymbol{\omega}_{\mathrm{m}}$). These vectors are computed using the measured motor field properties ($\{{}^{\mathrm{S}}\hat{\boldsymbol{\omega}}_{\mathrm{b}}, {}^{\mathrm{S}}\boldsymbol{b}_{\mathrm{max}}, {}^{\mathrm{S}}\boldsymbol{b}_{\mathrm{min}}, {}^{\mathrm{S}}b_{\mathrm{ratio}}\}$) and rotor field isoline functions, including isoline position ($\boldsymbol{p}_{\mathrm{e}}(b_{\mathrm{iso}}, \beta)$), field ratio ($b_{\mathrm{ratio}}(\beta)$), and field angle ($\alpha(\beta)$).

An isoline position in the rotor's magnetization plane is matched to the sensor's motor field measurements by according to:

$$ {}^{\mathrm{S}}\beta = \underset{\beta\in[0,\pi/2]}{\arg\min} |{}^{\mathrm{S}}b_{\mathrm{ratio}} - b_{\mathrm{ratio}}(\beta)|, \tag{6.8} $$

$$ {}^{\mathrm{S}}\boldsymbol{p}_{\mathrm{e}} = \boldsymbol{p}_{\mathrm{e}}({}^{\mathrm{S}}b_{\mathrm{iso}}, {}^{\mathrm{S}}\beta), \tag{6.9} $$

$$ {}^{\mathrm{S}}\alpha = \alpha({}^{\mathrm{S}}\beta), \tag{6.10} $$

where ${}^{\mathrm{S}}b_{\mathrm{iso}} = \|{}^{\mathrm{S}}\boldsymbol{b}_{\mathrm{max}}\|$ is the measured isoline field strength. Because the vectors ${}^{\mathrm{S}}\boldsymbol{b}_{\mathrm{max}}$ and ${}^{\mathrm{S}}\hat{\boldsymbol{\omega}}_{\mathrm{b}}$ span the reconstructed magnetization plane, with ${}^{\mathrm{S}}\boldsymbol{b}_{\mathrm{min}}$ being perpendicular to this plane, a rotation matrix $\boldsymbol{R}_{\mathrm{min}}(\psi) \in \mathrm{SO}(3)$ is defined based on the rotation vector ${}^{\mathrm{S}}\hat{\boldsymbol{b}}_{\mathrm{min}}\psi$, and the motor pose computed as:

$$ {}^{\mathrm{S}}\hat{\boldsymbol{p}}_{\mathrm{m}} = c_1\boldsymbol{R}_{\mathrm{min}}(c_2{}^{\mathrm{S}}\alpha){}^{\mathrm{S}}\hat{\boldsymbol{\omega}}_{\mathrm{b}}, \tag{6.11} $$

$$ {}^{\mathrm{S}}\boldsymbol{p}_{\mathrm{m}} = {}^{\mathrm{S}}\hat{\boldsymbol{p}}_{\mathrm{m}} \cdot \|{}^{\mathrm{S}}\boldsymbol{p}_{\mathrm{e}}\|, \tag{6.12} $$

$$ {}^{\mathrm{S}}\hat{\boldsymbol{\omega}}_{\mathrm{m}} = c_2\boldsymbol{R}_{\mathrm{min}}\big(c_2 \cdot ({}^{\mathrm{S}}\alpha - {}^{\mathrm{S}}\beta + c_2\pi/2)\big){}^{\mathrm{S}}\hat{\boldsymbol{\omega}}_{\mathrm{b}}, \tag{6.13} $$

where $c_j \in \{-1, 1\}$ ($j \in \{1, 2\}$) are coefficients that represent rotation direction. Herein, the coefficients are determined based on a previously known or reconstructed motor position vector (${}^{\mathrm{S}}\hat{\boldsymbol{p}}_{\mathrm{m}}(t_{i-1})$) according to:

$$\{c_1, c_2\} = \underset{c_1, c_2 \in \{-1,1\}}{\arg\min} \cos^{-1}\left({}^{\mathrm{S}}\hat{\boldsymbol{p}}_{\mathrm{m}}(t_{i-1}) \cdot {}^{\mathrm{S}}\hat{\boldsymbol{p}}_{\mathrm{m}}(t_i)\right), \tag{6.14}$$

6.3.8 Magnetic localization and manipulation

The magnetic localization and manipulation hardware includes an external integrated Hall effect sensor (MLX90371, Melexis, Belgium), a custom electromagnetic coil, and robotic arm (Kuka LBR Iiwa-14 R821, Augsburg, Germany), as well as an internal PMSM. The PMSM navigates a custom tubular network of opaque silicone tubes and Y-shaped connectors, each with a 6 mm inner diameter, demonstrating 2D localization and manipulation thereof in the horizontal xy-plane.

For localization, the external system provides the sensor's temporal orientation (${}^{\mathrm{B}}_{\mathrm{S}}\boldsymbol{R}$ and position (${}^{\mathrm{B}}\boldsymbol{p}_{\mathrm{S}}$ relative to base of the robot. When the PMSM is active and near the sensor, the pose reconstruction using the measured motor field matrix (${}^{\mathrm{S}}\boldsymbol{B}_{\mathrm{m}}$) leads to the motor position (${}^{\mathrm{S}}\boldsymbol{p}_{\mathrm{m}}$) and rotation axis (${}^{\mathrm{S}}\hat{\boldsymbol{\omega}}_{\mathrm{m}}$) relative to both the sensor and robot base, calculated as ${}^{\mathrm{B}}\boldsymbol{p}_{\mathrm{m}} = {}^{\mathrm{B}}\boldsymbol{p}_{\mathrm{S}} + {}^{\mathrm{B}}_{\mathrm{S}}\boldsymbol{R}{}^{\mathrm{S}}\boldsymbol{p}_{\mathrm{m}}$ and ${}^{\mathrm{B}}\hat{\boldsymbol{\omega}}_{\mathrm{m}} = {}^{\mathrm{B}}_{\mathrm{S}}\boldsymbol{R}{}^{\mathrm{S}}\hat{\boldsymbol{\omega}}_{\mathrm{m}}$. The robot then repositions the sensor horizontally above the calculated motor position.

For manipulation, when the PMSM is inactive, the electromagnet is displaced 20 mm along the xy-projection of the last reconstructed ${}^{\mathrm{B}}\hat{\boldsymbol{\omega}}_{\mathrm{m}}$. The electromagnet generates a static magnetic field across the PMSM, which is manually rotated to alter its magnetization direction and deflection plane. The electromagnet is then turned off and reset to its initial position.

6.3.9 Motor Power System

The motor power system comprises a custom-designed coil driver connected to the stator leads of the permanent magnet synchronous motor (Supplementary Fig. S6.12). The coil driver includes a bidirectional DC triple motor controller shield (Motoron M3S256, Pololu Robotics) connected to an Arduino UNO. Each output of the shield is connected in series to a

custom inductor (∼50 µH), made of 6 mm diameter ferrite core (RSPro, Fair-Rite, 172-9993) and manually wound 0.5 mm diameter copper wire, and a current sensor (ACS712 5A, AZDelivery).

The output signal of the current sensor is smoothened by a 10 nF ceramic capacitor placed between its ground and output pins. This current sensor is used in closed-loop current regulation, managed by a custom-designed PID controller. The Arduino board is powered via a PC with a serial communication to command the current amplitudes and frequencies for stator activation. Finally, the motor shield is powered through a socket connected to a 240 V AC to 24 V DC transformer, which is then stepped down to 8 V using a DC-DC converter (LM2596S, AZDelivery).

6.4 Supplementary Text – Field ratio of rotating dipoles

Given the magnetic point dipole approximation, defined as

$$\boldsymbol{b}(\boldsymbol{p}) = \frac{\mu_0}{4\pi}\left(\frac{3\boldsymbol{p}(\boldsymbol{\mu}\cdot\boldsymbol{p})}{\|\boldsymbol{p}\|^5} - \frac{\boldsymbol{\mu}}{\|\boldsymbol{p}\|^3}\right), \tag{6.15}$$

where $\boldsymbol{b}(\boldsymbol{p}) \in \mathbb{R}^3$ is the magnetic field at some position ($\boldsymbol{p} \in \mathbb{R}$), and $\boldsymbol{\mu} \in \mathbb{R}^3$ is the dipole moment. Consider that the dipole is rotating, and that $\boldsymbol{\mu}$ is perpendicular to the rotation axis ($\hat{\boldsymbol{\omega}}$). We define an angle of rotation ($\phi \in [0, 2\pi)$), let the dipole's rotation axis be its local z-axis ($\boldsymbol{\omega} = \hat{\boldsymbol{z}}$), and define the rotated dipole moment as $\boldsymbol{\mu}_\phi = \boldsymbol{R}_z(\phi)(\mu\hat{\boldsymbol{x}})$.

The field is maximum when $\boldsymbol{\mu}$ and $\boldsymbol{p}$ are parallel, i.e. for $\boldsymbol{\mu}_0 = \mu\hat{\boldsymbol{x}}$ and $\boldsymbol{p} = p\hat{\boldsymbol{x}}$,

$$\begin{aligned}
\boldsymbol{b}_{\max}(\boldsymbol{p}) &= \frac{\mu_0}{4\pi}\left(\frac{3p\hat{\boldsymbol{x}}(\mu\hat{\boldsymbol{x}}\cdot p\hat{\boldsymbol{x}})}{p^5} - \frac{\mu\hat{\boldsymbol{x}}}{p^3}\right) \\
&= \frac{\mu_0}{4\pi}\left(\frac{3p^2\mu\hat{\boldsymbol{x}}(\hat{\boldsymbol{x}}\cdot\hat{\boldsymbol{x}})}{p^5} - \frac{\mu\hat{\boldsymbol{x}}}{p^3}\right) \\
&= \frac{\mu_0}{4\pi}\left(\frac{2\mu}{p^3}\right)\hat{\boldsymbol{x}}.
\end{aligned}$$

Conversely, the field is minimum when $\boldsymbol{\mu}$ and $\boldsymbol{p}$ are perpendicular, i.e. for $\boldsymbol{\mu}_{\pi/2} = \mu\hat{\boldsymbol{y}}$ and $\boldsymbol{p} = p\hat{\boldsymbol{x}}$,

$$\boldsymbol{b}_{\min}(\boldsymbol{p}) = \frac{\mu_0}{4\pi}\left(-\frac{\mu}{p^3}\right)\hat{\boldsymbol{y}}.$$

Therefore, the ratio between the maximum and minimum field strength, for a rotating dipole, is at most two,

$$b_{\text{ratio}} = \frac{\|\boldsymbol{b}_{\max}(\boldsymbol{p})\|}{\|\boldsymbol{b}_{\min}(\boldsymbol{p})\|} = 2.$$

6.5 Supplementary Figures

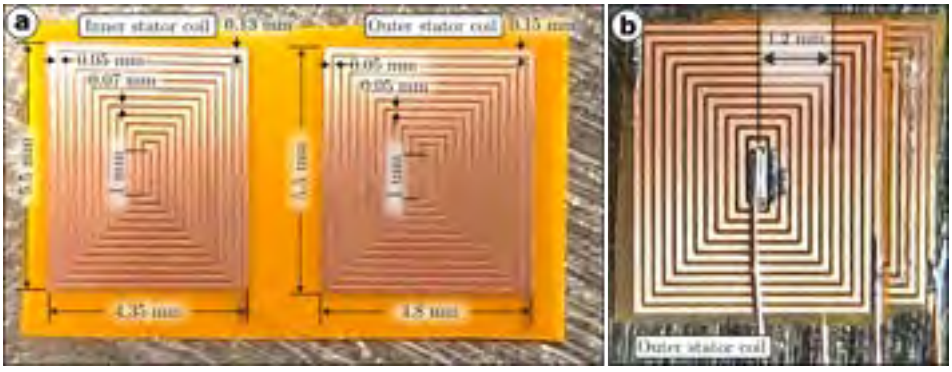

Figure S6.1: Planar coils design. **a** Rectangular planar coils with annotated dimensions. **b** Stacked inner and outer stator coils with a center-to-center offset displacement. Soldered copper power leads are visible. Photograph taken prior to cylindrical deformation to form stator coils.

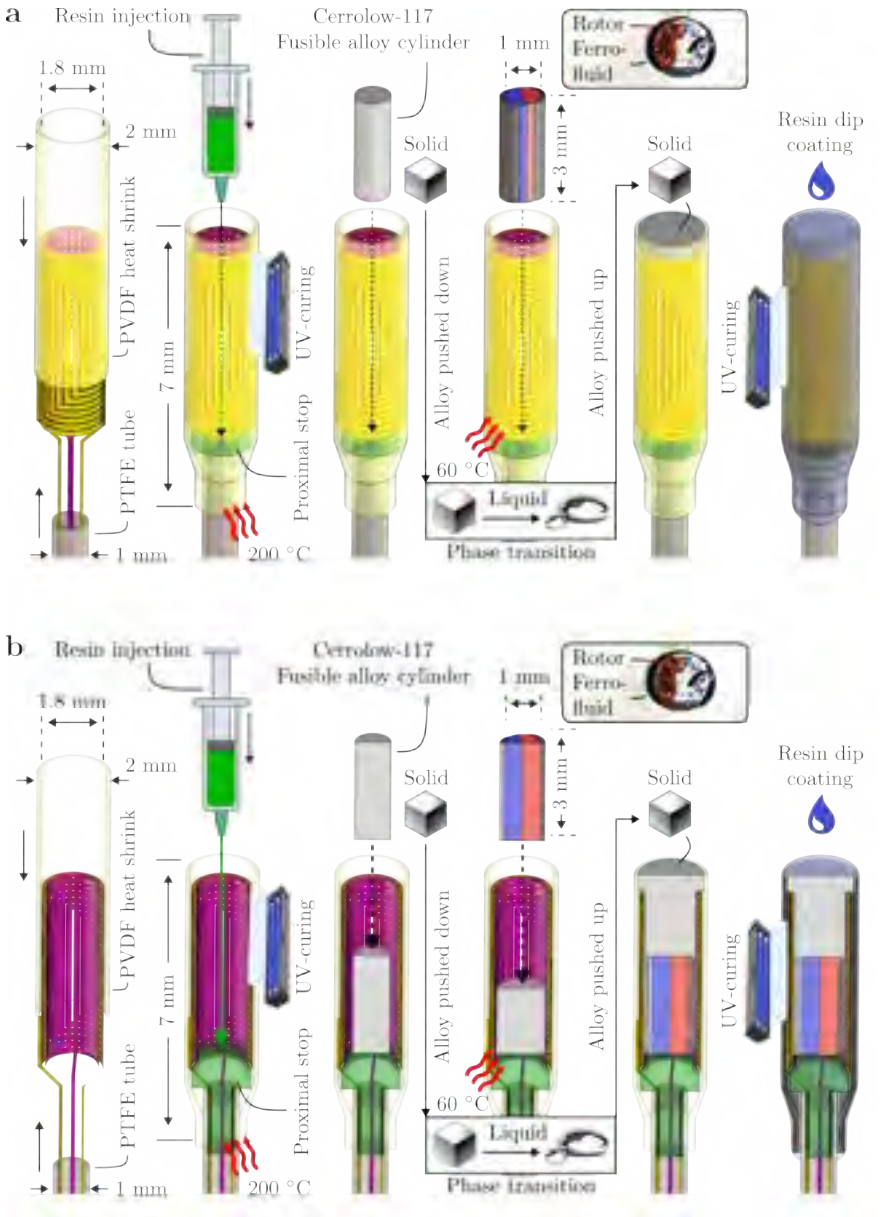

Figure S 6.2: Fabrication process of the permanent magnet synchronous motor. a Non-cross-sectional view of fabrication steps. **b** Cross-section view showing internal arrangements of components.

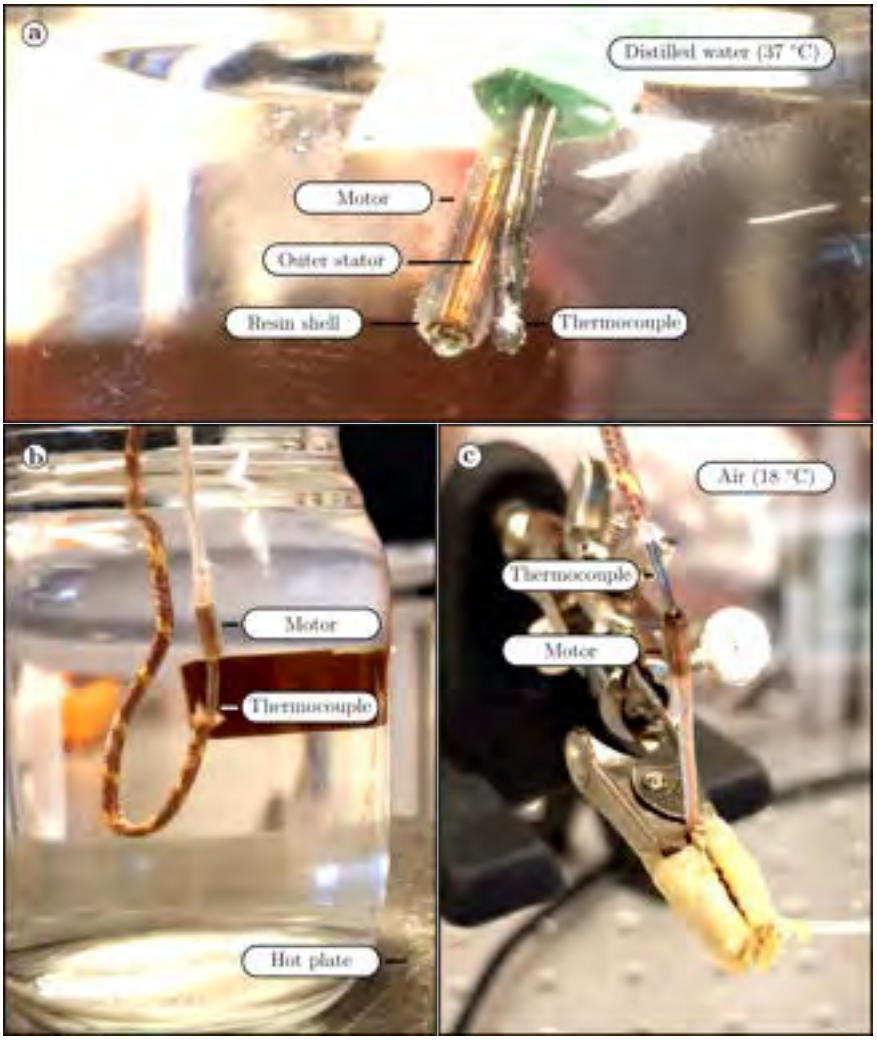

Figure S 6.3: Temperature measurements. **a** External temperature measurement inside a bath of distilled water at 37 °C. Visible are the motor with outer stator and resin shell, but without the permanent magnet rotor, and a thermocouple placed along its outer surface. **b** Internal temperature measurement inside a bath (glass jar) of distilled water at 37 °C. The thermocouple is placed inside the motor's rotor cavity. The water is heated with a hot plate. **c** Internal temperature measurement inside air at 18 °C.

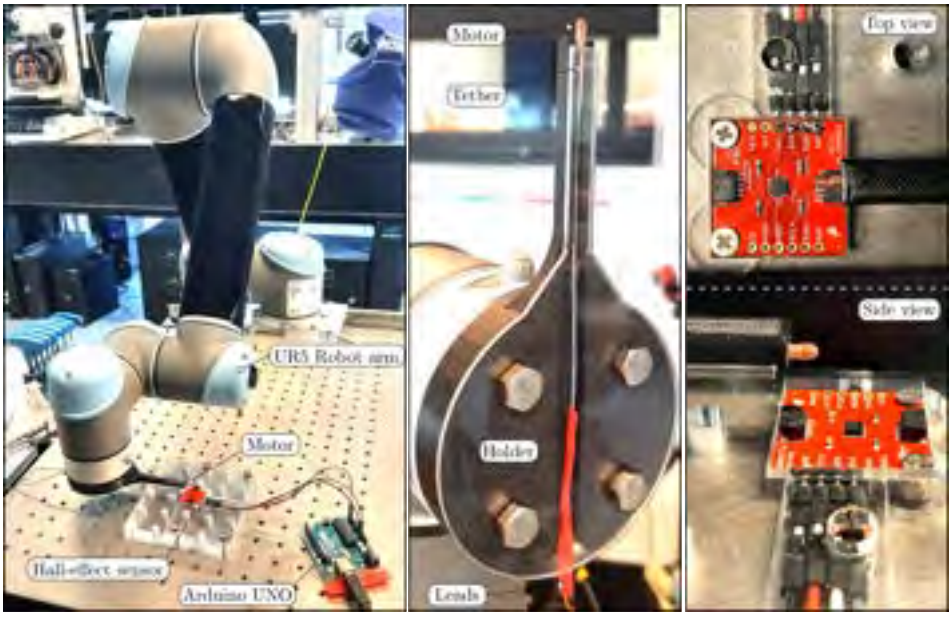

Figure S 6.4: Experimental setup for rotor field characterization and validation of the localization algorithm. The setup consists of a UR5 serial robotic arm, connected to a 3D-printed holder that positions the motor horizontally above a Hall effect sensor. The sensor is connected to an Arduino UNO, which is itself connected to a PC.

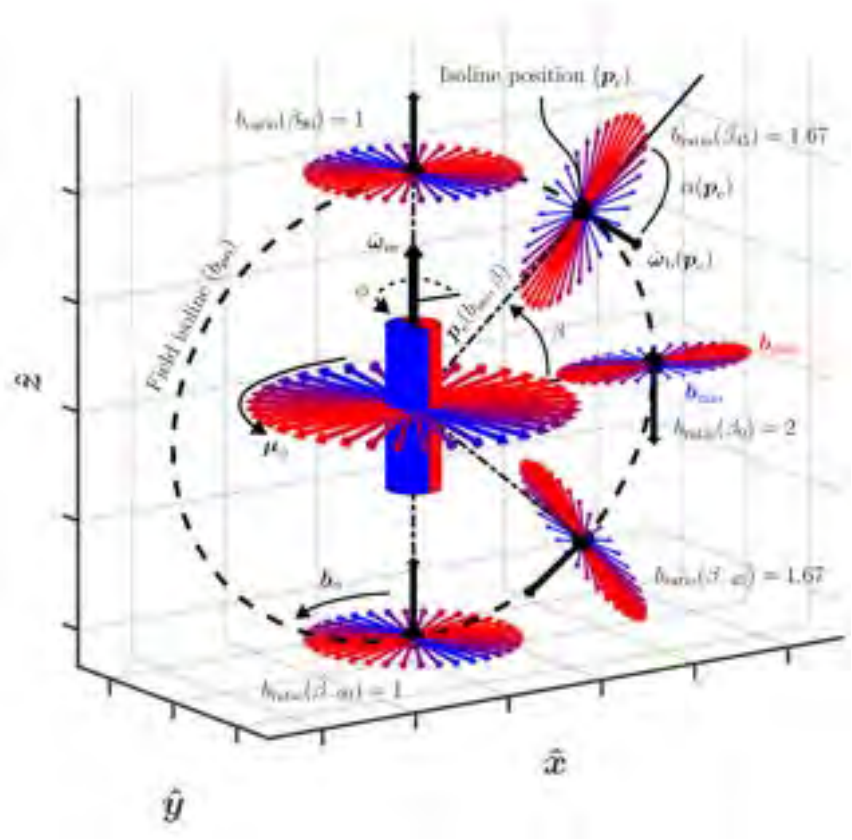

Figure S6.5: A 3D representation of a rotating magnetic dipole (rotor magnet) with perpendicular magnetization and rotation axes. The magnet has rotation axis ($\hat{\boldsymbol{\omega}}_\mathrm{m}$) and rotation angle ($\phi$), that orient the rotating dipole moment ($\boldsymbol{\mu}_\phi$). During magnet rotation, at any position in space, the field ($\boldsymbol{b}_\phi$) rotates in-plane with a field rotation axis ($\hat{\boldsymbol{\omega}}_\mathrm{b}$). The field has an elliptically varying field strength between maximum ($\boldsymbol{b}_\mathrm{max}$) and minimum ($\boldsymbol{b}_\mathrm{min}$) values, with an associated field ratio ($b_\mathrm{ratio} = \|\boldsymbol{b}_\mathrm{max}\|/\|\boldsymbol{b}_\mathrm{min}\|$). Within the magnetization plane of the magnet, spanned by $\hat{\boldsymbol{\omega}}_\mathrm{m}$ and $\hat{\boldsymbol{\mu}}_{\phi=0}$, a field isoline ellipse (dashed line) is defined of constant field strength (b_iso). Each position on the ellipse, termed the isoline position ($\boldsymbol{p}_\mathrm{e}(b_\mathrm{iso}, \beta)$), depends on b_iso and an isoline position angle ($\beta = \angle \boldsymbol{p}_\mathrm{e}, \boldsymbol{\mu}_0$). Then, each $\boldsymbol{p}_\mathrm{e}(b_\mathrm{iso}, \beta)$ is associated with field vectors of maximum strength ($\boldsymbol{b}_\mathrm{max}(\boldsymbol{p}_\mathrm{e})$), minimum strength ($\boldsymbol{b}_\mathrm{min}(\boldsymbol{p}_\mathrm{e})$), and rotation ($\hat{\boldsymbol{\omega}}_\mathrm{b}(\boldsymbol{p}_\mathrm{e})$), as well as scalars of field ratio ($b_\mathrm{ratio}(\boldsymbol{p}_\mathrm{e})$) and field angle ($\alpha(\boldsymbol{p}_\mathrm{e}) = \angle \boldsymbol{p}_\mathrm{e}, \hat{\boldsymbol{\omega}}_\mathrm{b}(\boldsymbol{p}_\mathrm{e})$).

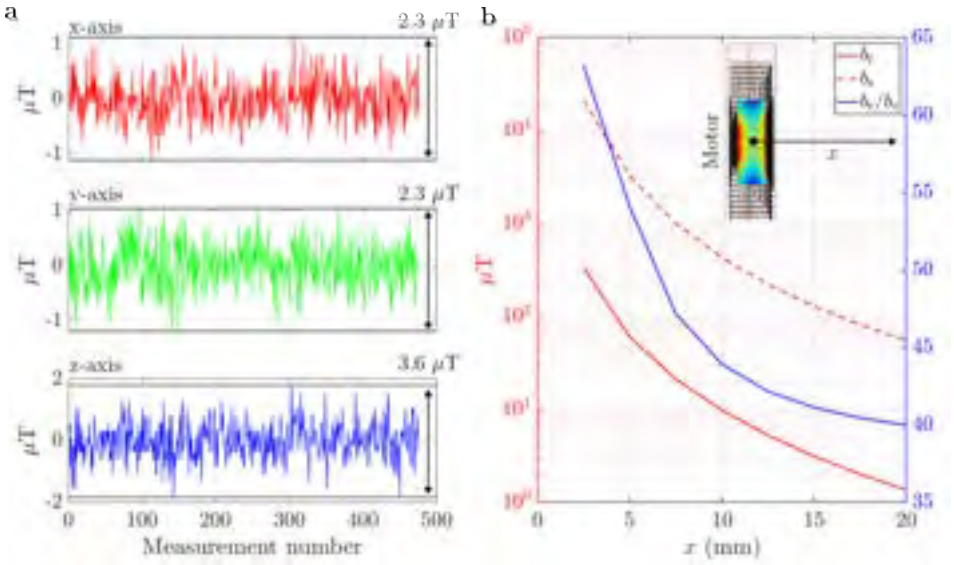

Figure S6.6: Hall effect sensor noise and comparison between magnetic fields of the rotor and stator. **a** Noise signal of the Hall effect sensor obtained from a mean-correction of static background field measurements. **b** Finite element simulated magnetic fields of the permanent magnet rotor (b_r) and electromagnet stator (b_s), corrected for driving current (200 mA). In addition, the ratio between rotor and stator fields ($b_\mathrm{r}/b_\mathrm{s}$) is shown.

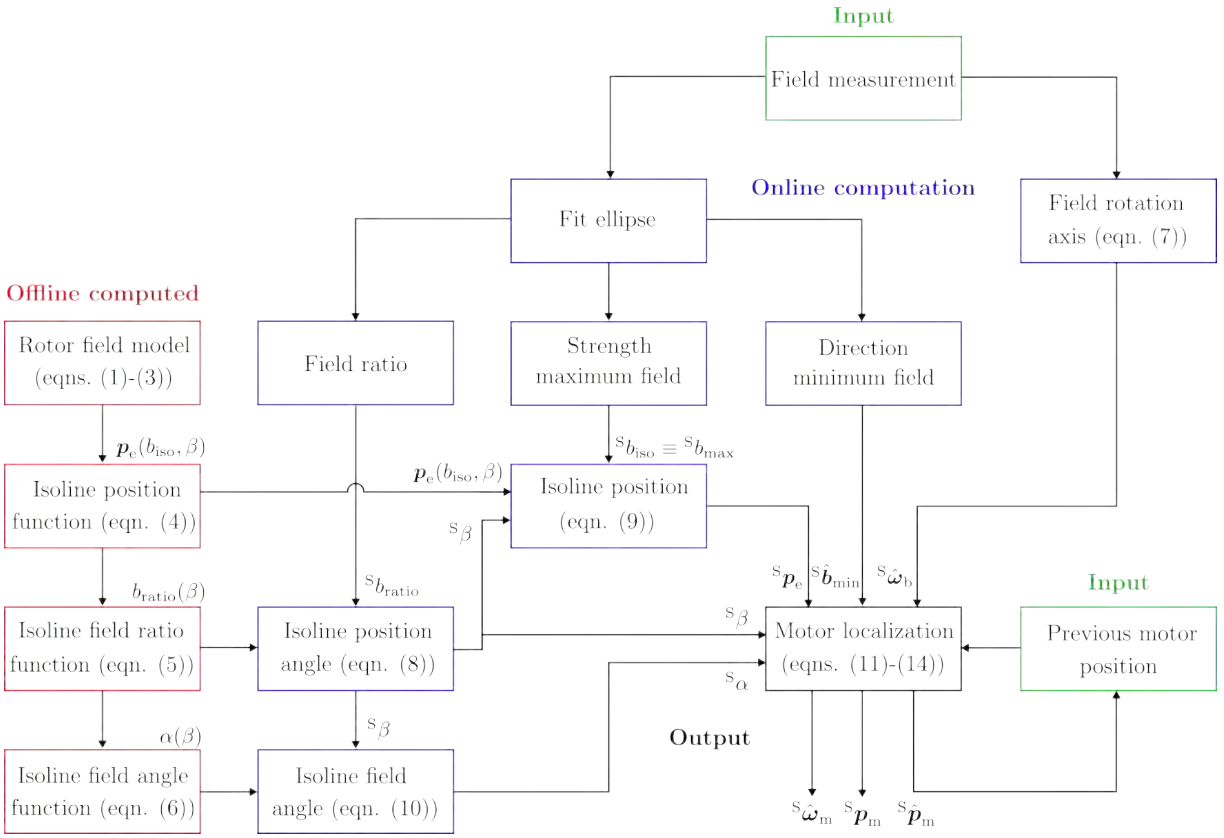

Figure S6.7: Flow diagram of the localization algorithm. Offline computed rotor field isoline functions are used in conjunction with field measurements to provide online estimations of the motor's position and rotation axis.

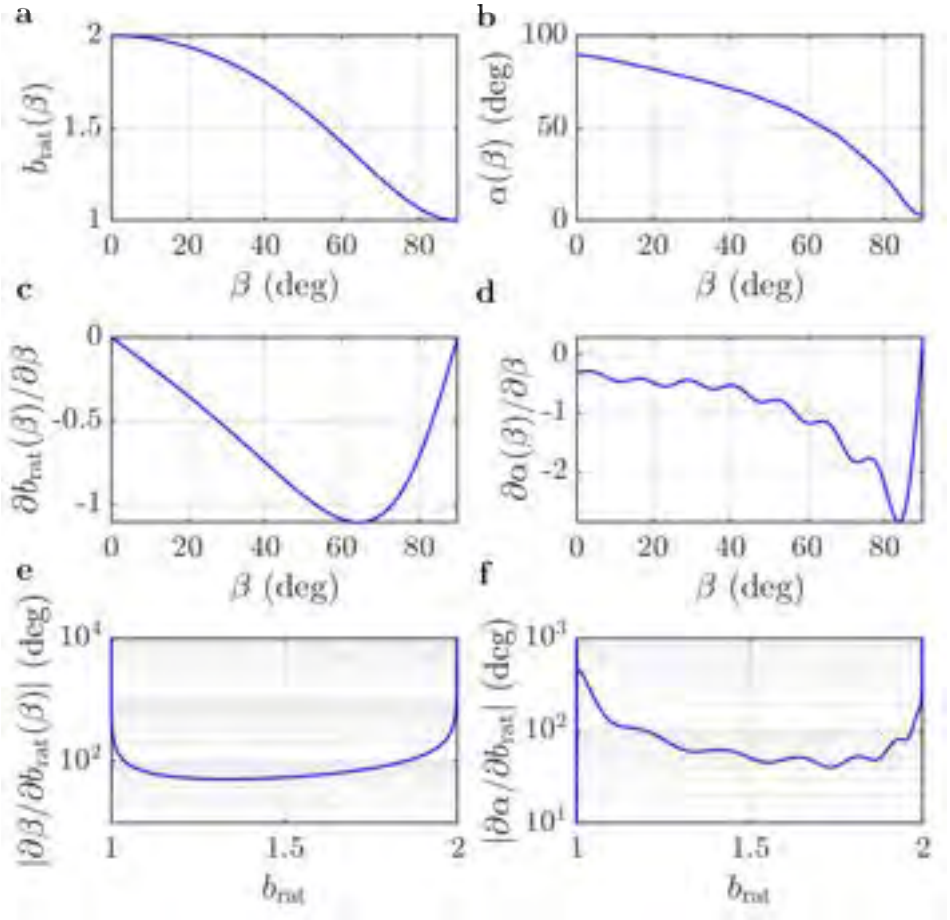

Figure S6.8: Error sensitivity of the (angular) rotor isoline functions. **a** Output of the rotor isoline function for field ratio ($b_{\mathrm{rat}}(\beta) := b_{\mathrm{ratio}}(\beta)$) at isoline position angles (β). **b** Output of the rotor isoline function for field angle ($\alpha(\beta)$) at isoline position angles (β). **c** Gradient of $b_{\mathrm{ratio}}(\beta)$ with respect to β. **d** Gradient of $\alpha(\beta)$ with respect to β. The oscillatory profile is due to the sinusoidal function (eqn. (6) of main text) that is fit to $\alpha(\beta)$. **e** Error sensitivity of β with respect to field ratio: $\partial\beta/\partial b_{\mathrm{rat}} = 1/(\partial b_{\mathrm{rat}}/\partial\beta)$. **f** Error sensitivity of α with respect to field ratio: $\partial\alpha/\partial b_{\mathrm{rat}} = (\partial\alpha/\partial\beta)\cdot(\partial\beta/\partial b_{\mathrm{rat}})$.

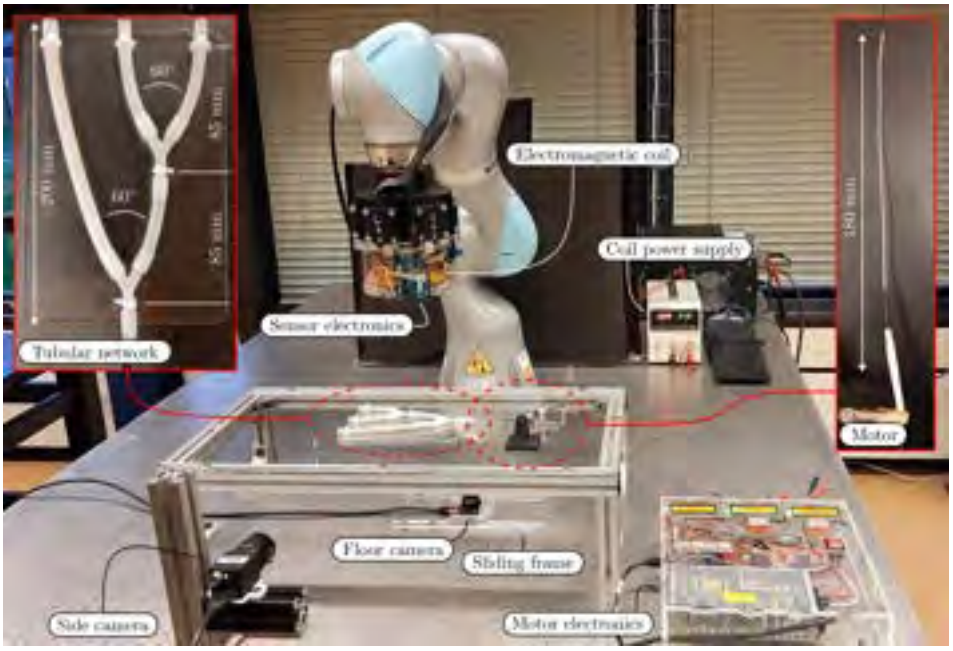

Figure S6.9: Overview of the experimental setup for demonstration of magnetic localization and manipulation. A permanent magnet synchronous motor (PMSM) is navigated through a tubular network using an external electromagnetic coil. Localization is performed by a tri-axial eye-in-hand magnetometer attached to the tip of the coil.

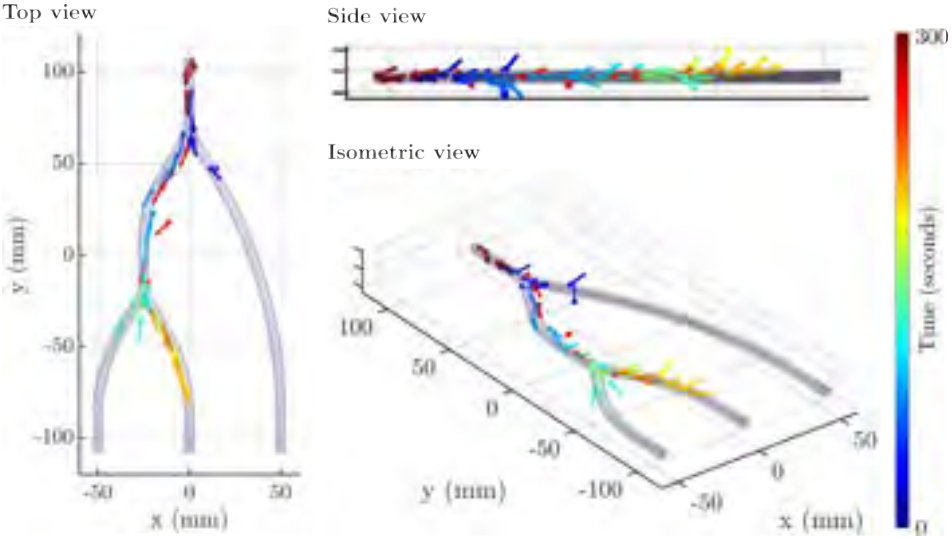

Figure S6.10: Experiment results of magnetic localization and manipulation. Tracked positions (dots) and rotation axes (arrows) of the permanent magnet synchronous motor (PMSM) in the tubular network over time, for different viewpoints.

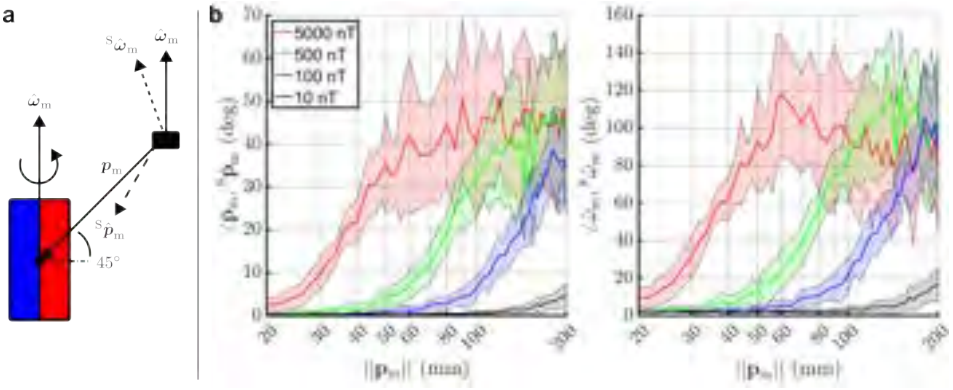

Figure S 6.11: Simulated angular errors of reconstructed position and rotation axis vectors for different sensor noise levels. **a** Configuration of the rotor magnet and magnetometer considered in simulation. The rotor magnet is associated with a position vector ($\boldsymbol{p}_\mathrm{m}$) and rotation axis ($\hat{\boldsymbol{\omega}}_\mathrm{m}$), as well as a reconstructed position vector ($^\mathrm{S}\boldsymbol{p}_\mathrm{m}$) and rotation axis ($^\mathrm{S}\hat{\boldsymbol{\omega}}_\mathrm{m}$) from simulated sensor field measurements. **b** Simulated angular discrepancies between known and reconstructed position vectors and rotation axes over a range of motor-sensor distances and for different magnitudes of sensor noise. Mean values (solid line) and standard deviations (shaded area) are obtained from twenty simulations using uniformly distributed random noise values of shown maximum magnitudes ($\{10, 100, 500, 5000\}$ nT). For reference, our Hall effect magnetometer showed noise magnitudes of 4000 nT.

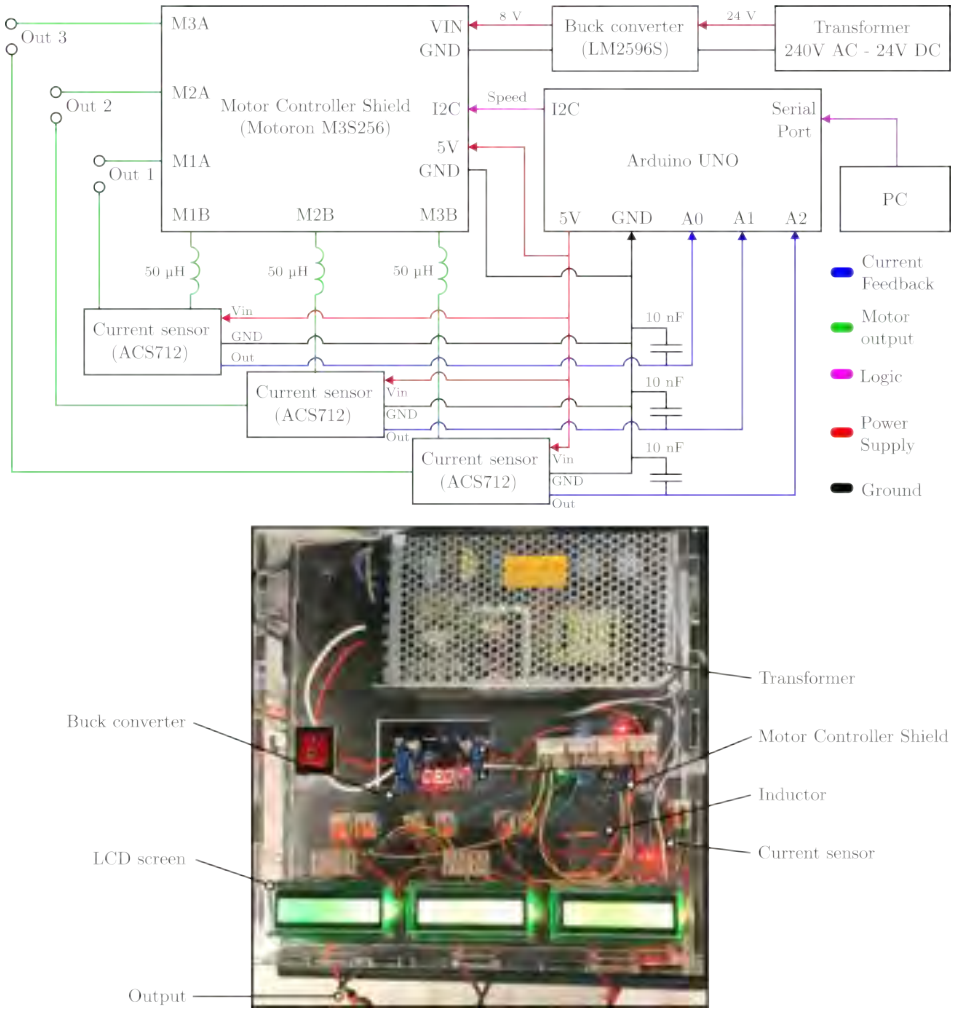

Figure S6.12: Electronic circuit diagram of the custom coil diver. Desired stator current, frequency, and phase commands are sent from a PC to an Arduino UNO. These commands are converted to a motor speed (integer in range of -800 to +800), with the sign denoting the direction of current flow and the magnitude representing the PWM duty cycle. Closed-loop current regulation via current sensors is used to iteratively update the motor speed value to match the commanded quadrature current magnitudes and direction through the motor's stator coils (out 1-2).

IV

Concluding Remarks

6

7

Conclusions and Future Work

In this dissertation, important challenges related to modeling of magnetic field sources and continuum robots are addressed. These challenges included application of model-based robot design and control, as well as design considerations for magnetic continuum robots regarding practical and relevant intracorporeal localization. The broad range of topics, designs, models, fabrication methods, and algorithms can be used as inspiration for new studies. Also, they provide valuable practical teaching relevant for future system implementation and functionality considerations. This chapter summarizes the relevant findings of the presented works, formulates answers to the proposed research questions, and provides research recommendations for future studies.

7.1 Conclusions

7.1.1 Part I: Shaping Fields, Bending Robots

Part I of this dissertation includes Chapters 2 and 3, which address challenges related to modeling the mechanical response of magnetic continuum robots (MCRs) within external fields, as well as model-based magnetic shape control of MCRs. These chapters propose a clinically relevant millimeter-scale magnetic continuum robotics approach for pose control and guiding instruments that is synonymous to the functionality of larger industrial serial robotic arms. The envisioned clinical application is such that magnetic continuum robots move through tubular anatomy (e.g., vessels, esophagus)

and can function as "robotic arms" at their destination (e.g., insufflated stomach or colon, or the heart).

Chapter 2 (RQ.1*) proposes a general approach to achieve independent orientation control of multiple hard magnets (points of actuation), positioned at discrete positions along the length of an MCR, by shaping the applied field generated with a magnetic manipulation system. This approach included (1) a continuum mechanics model of the MCR, (2) a digital twin of a magnetic manipulation system, and (3) an orientation control loop utilizing these models' estimations to construct a Jacobian matrix that relates changes in MCR magnets' orientation to quasi-static changes in the manipulation system's configuration. Although closed-loop orientation control of a two-magnet MCR was physically demonstrated in 2D, and in 3D in simulation with an extended manipulation system, this research provides practical considerations for multi-point orientation control of MCRs, related to hardware and software implementation.

First, passive hard magnets, with fixed magnetic moments, rely on shaping of external fields for actuation. As the number of hard magnets in an MCR increases, the manipulation system must generate increasingly nonuniform fields to actuate each magnet, placing a significant burden on the manipulation system for additional degrees of freedom (DOFs). To achieve multi-point orientation control, each magnetic actuation point should ideally contribute the necessary DOFs, akin to actuators in serial robotic arms. A potential practical solution involves orthogonal saddle coils, capable of independently generating axial or radial magnetic moments [129], allowing actuation within uniform fields. Although such coils generate weaker magnetic moments than hard magnets and require stronger fields for actuation, such fields from a magnetic resonance imaging system have successfully been used to actuate coil-based MCRs [275].

Second, while the continuum mechanics-based model accurately predicts MCR shape deformation in magnetic fields, solving the necessary boundary value problem is computationally expensive. In our setup, the manipula-

*RQ.1: How to model multi-magnet continuum robots, as well as formulate a general control method for achieving higher-order shapes of these robots in the workspace of manipulation systems?

tion system with 8 DOFs (electromagnet currents and positions) required solving a boundary value problem for each actuation parameter to estimate changes in MCR magnets' orientation. These computations were performed sequentially, limiting the control loop frequency to 2 Hz, which would further decrease with additional actuation parameters. Future implementations should use parallel computation to solve the (independent) boundary value problems to improve efficiency.

Chapter 3 (RQ.2[†]) extended MCR shape deformation with tool guidance. This was achieved by replacing the previously inert flexible body of the MCR with a temperature-controlled polymer that transitions between minimum and maximum stiffness (elastic modulus) at specific temperature thresholds. The MCR was treated as either locked (maximum stiffness) or unlocked (minimum stiffness). Tool guidance involved deforming the unlocked MCR with magnetic fields, locking its shape to resist further deformation, passing a stainless steel needle through its lumen (transferring elastic potential energy from the MCR to the tool), and reaching a combined shape as a result of an elastic equilibrium between the MCR and the tool.

Therefore, in response to RQ.2[†] and considering some target destination for a guided instrument, the necessary shape of the locked MCR must be computationally determined, followed by calculating the magnetic field needed to deform the unlocked MCR accordingly. Chapter 3 demonstrated this using a continuum mechanics-based model for concentric tube robots. The process relied on five computational steps: (1) estimate magnetic torque on the undeformed unlocked MCR, (2) compute the deformed unlocked MCR shape's curvature vector, (3) assign the curvature vector of the deformed unlocked MCR to the pre-curvature vector of the undeformed locked MCR, (4) calculate the combined shape of the locked MCR and tool; deformed locked MCR, and (5) iterate until the desired shape of the deformed locked MCR is achieved.

However, each iteration required numerically solving four computation-

[†]RQ.2: How to extend geometrically exact models of magnetic continuum robots to include variable stiffness and guidance of nested tools, as well as formulate a control method for tool guidance?

ally expensive boundary value problems, making the method infeasible for real-time control. While the model supports MCR design, simulations with surgical instruments, and open-loop control, further practical model assumptions–such as a constant-curvature–could enable real-time closed-loop control. In the future, the concepts from Chapters 2 and 3, along with the suggestions outlined here, could be integrated towards closed-loop multi-point orientation control of a variable stiffness MCR for tool guidance, using stereo vision-based shape feedback. Instead of camera images, biplane X-ray could be used as clinical substitute [128].

7.1.2 Part II: It's by Design

Part II of this dissertation, comprising Chapters 4 and 5, explores the concept of local magnetic interactions. While Part I focused solely on conventional magnetic interactions, where a globally generated field from an external manipulation system acted on an MCR, Part II addresses internally generated fields that are both produced by and act upon the MCR itself. These local interactions can be passive, resulting from permanent magnetization, or active, from electromagnetic components integrated into the MCR.

Chapter 4 (RQ.3[‡]) proposes a novel geometric design for MCRs intended to utilize passive locally generated magnetic fields. This design utilizes a magnetic polymer composite, consisting of magnetic powder suspended in silicone, shaped into a single helix. The helix is magnetized along its central axis, giving each subvolume a magnetic polarity and producing a local field parallel to the axis. The magnetic field generated by each winding interacts with adjacent windings, where (1) fields exert torques that oppose helix deflection, and (2) field gradients exert a torque through a force and moment arm that promote helix deflection.

It is concluded that local dipole interactions within hard magnetic soft helices can either oppose or promote deflection, depending on whether local field strength or field gradients dominate in exerting bending torques, respectively. Since field gradients increase more rapidly than field strength

[‡]RQ.3: How can magnetic continuum robots be designed to beneficially utilize local dipole interactions?

near the field source, the effect of these interactions in improving flexibility becomes more pronounced as the distance between windings decreases and as the winding width (moment arm for magnetic forces) increases.

The design of our helices featured a monolithic structure comprising a single helix (resembling a die spring) wound around an open cylindrical core. Simulations showed that during bending, most material strain occurred in the cylinder. Future designs should remove/replace this cylinder, as its additional stiffness partially offsets the benefits of increasing magnetic powder concentration, which strengthen local dipole interactions. Instead, the cylinder could be replaced with a magnetically inert silicone tube, leaving only the helix as the magnetic structure. Future research should explore the effects of magnetic particle concentration, pitch, and winding geometry on structural bending rigidity. The hypothesis is that increasing magnetic particle concentration will consistently improve both the overall magnetic moment and the effectiveness of local magnetic interactions. This approach intends to create greater magnetic moment and flexibility for increasing concentration of magnetic powder, unlike conventional cylindrical geometries that exhibit a tradeoff between these properties above a concentration of 20% [56].

Chapter 5 (RQ.4[§]) focused on active local magnetic interactions. Unlike the passive magnetic interactions previously discussed, which were designed to influence the mechanical properties of MCRs, these interactions involve a locally generated magnetic field interacting with an adjacent magnetic effector to actively induce a mechanical response. As an answer to RQ.4[§], MCRs are proposed consisting of two main components: (1) flexible electromagnetic coils capable of actively generating a local field, and (2) surface-mounted hard magnetic effectors that move in response to the generated field.

It is concluded that flexible electromagnetic coils and hard magnetic effectors can be combined to create machines capable of performing preprogrammed tasks, such as functioning as linear actuators or grippers, and that can also be mounted on continuum robots as functionalized elements.

[§]RQ.4: How to shape magnetization profiles of continuum robots to achieve preprogrammed shape deformation in locally generated nonuniform fields?

These magnetic machines rely on the local field generated by their respective coils, allowing multiple machines to operate independently in close proximity. The primary design parameters for these machines include: the coil geometry (determines the field it generates), the effector geometry (affects mechanical properties), and the effector magnetization (influences the torques and forces exerted on the effectors by the coil field).

Our work focused on shaping the magnetization profiles of hard magnetic effectors with two-dimensional geometries (e.g., disk or flower petals), specifically tailored to the fields generated by single-layer circular coils. To the best of our knowledge, this study presents the first examples of such machines. However, this exploration of magnetic soft machines is far from exhaustive, and several avenues for further research remain.

The magnetization profiles were optimized for torques or forces in the machine's deactivated configuration, but effector deformation during activation alters the alignment of the magnetization direction and magnetic field. Incorporating these deformations into improved simulations could enhance the model-based design of magnetization profiles. Additionally, alternative coil geometries, such as flower-shaped coils designed to mimic flower-shaped effector grippers, could strengthen the match between the field and magnetization profile, improving the mechanical response and overall functionality of the effectors. Further, investigating passive magnetic interactions between effector segments could also enhance their mechanical response to active magnetic interactions. Finally, stacking multiple independently operable coils with varying geometries could produce dynamic local fields, expanding the DOFs of magnetic machines.

7.1.3 Part III: Are you in there?

Part III of this dissertation, comprising Chapter 6, addresses the challenge of intracorporeal localization of MCRs. While Parts I and II focused on continuum mechanics-based design and control of MCRs in open laboratory settings, clinical application of MCRs presents an important challenge. In the human body, visual obstruction prevents camera-based tracking of MCR positions, and available medical imaging systems typically provide only two-dimensional images, making three-dimensional pose reconstruc-

tion of MCRs difficult. Nevertheless, this information is required for the targeted generation of magnetic fields by manipulation systems, a prerequisite for safe intracorporeal actuation and control of MCRs.

In **Chapter 6** (RQ.5[¶]) it is postulated that any practical clinical application of MCRs requires a magnetic surgical robotic infrastructure–robot, localization system, manipulation system–to function as a closed system. A closed system is independent of other operating room technologies, though potentially reliant on clinician input. To this end, the reconstruction of position and orientation information of MCRs based on their magnetic fields and external measurements of these fields is demonstrated. This method is compatible with in-place rotating magnetic dipoles that have perpendicular rotation and magnetization axes.

It was shown that the three-dimensional position and rotational axis of a magnet measuring 1 mm in diameter and 3 mm in length can be reconstructed up to a distance of 40 mm using a single tri-axial Hall effect magnetometer. Also, simulations indicate that this reconstruction range can be extended to a clinically relevant distance beyond 200 mm by using magnetometers with improved sensitivity down to the nanoTesla range.

Our implementation included the development of a novel milli-scale synchronous motor to achieve magnet rotation. However, simpler approaches should be explored in practice, such as manually rotating a tip magnet mechanically via a torqueable guidewire–a method already standard for reorienting and navigating magnetically inert vascular wires. Future research could investigate the use of additional magnetometers, along with the computation of covariance matrices for position estimates based on known measurement noise, or measured signal-to-noise ratios. This would enable statistical pose reconstruction by integrating data from multiple sensors.

[¶]RQ.5: How to achieve intracorporeal localization of magnetic continuum robots by interpreting their inherent field externally?

7.2 Future Prospects

This doctoral dissertation "***Shaping Magnetics in Surgical Robotics***" contributes to the research domain that investigates possible magnetic and geometric design choices for magnetic robots and manipulation systems. Design choices shape how mangnetically reponsive devices interact with magnetic field sources. In this context, Chapters 2–6 illustrate how magnetic model-based device design and control can enhance the steerability, functionality, and practical implementation of magneto-surgical robots.

Future advancements in this field are expected to build upon current trends. This includes continuing development of novel magnetic and geometric designs for (un)tethered devices and manipulation systems. In addition, further exploration of applications in areas such as endovascular, pulmonary, gastrointestinal, and laparoscopic interventions. Also, practical considerations for clinical implementation of magneto-surgical robots will continue to be formulated and addressed. Based on the herein obtained learning, potential directions of these advancements are hypothesized.

7.2.1 Advanced designs of magnetic continuum robots

Research on design of magnetic continuum robots (MCRs) has explored various aspects, including possible fabrication methods, material compositions, geometric shapes, magnetization profiles, types of manipulation fields for control, and their intended movement. As a result, MCRs have been made that roll, jump, swim, wiggle, and bend [58]. Regardless of design, the fundamental physical principles that govern material properties (mechanical and magnetic) and magnetic interactions remain the same. An understanding of these principles enables model-based design of MCRs and optimization towards some objective value.

Advanced designs of MCRs may aim to achieve multiple objectives, possibly divided into primary (e.g., bending) and secondary (e.g., required field for that bending). By considering multiple objectives, MCRs improve their functionality with potentially expanded application potential. This doctoral dissertation already presents several examples, including:

- Incorporating variable stiffness materials to enable switching between

operation modes: manipulation and instrument guiding (Chapter 3).

- Enhancing responsiveness to magnetic fields through local dipole interactions, reducing the need for stronger external fields from manipulation systems (Chapter 4).
- Physically combining electromagnetic actuators and hard magnetic soft effectors as small-scale machines (Chapter 5).
- Utilizing dynamic magnetic properties to allow localization in environments where visual tracking is obstructed (Chapter 6).

The intended application and desired behavior of MCRs should determine their design requirements, guiding the development of more advanced designs. Traditionally, aspects such as device design, localization, and manipulation have been treated separately, even though they are fundamentally interconnected. To create more advanced MCRs, future designs should simultaneously account for the available manipulation system and its magnetic field capabilities, explore additional complementary actuation principles to enhance control (e.g., tendon), have an intended localization method (e.g., vision-based tracking, magnetic sensing, or embedded sensors), and consider other application-specific factors such as stiffness (tissue interaction), surface coating, or drug-carrying capacity.

7.2.2 Multi-modal localization and autonomous navigation

Localization of MCRs is essential for their navigation, as it informs targeted generation of magnetic fields for manipulation. The safety of MCR manipulation during medical procedures relies on both accurate localization and the clinician's ability to visualize anatomy in three dimensions. Traditional medical imaging technologies, such as ultrasound and X-ray, typically provide 2D images, requiring clinicians to rely on their expertise in 3D human anatomy to interpret the images and make informed decisions.

To achieve 3D localization of MCRs and inform magnetic field generation, bi-plane imaging combined with MCR segmentation – demonstrated using cameras in Chapter 2 – can be utilized. Recent studies have also shown the feasibility of this approach using X-rays in a clinical setting [128], [276].

Although bi-plane images can be captured simultaneously using two single-plane imaging systems, this setup limits the available space around the patient. Alternatively, repositioning or angulating a single-plane system sequentially can achieve bi-plane imaging [35], [277], but is time-consuming and not suitable for real-time localization.

Nevertheless, medical imaging technologies remain invaluable in providing visual feedback to clinicians. However, relying solely on them for 3D localization of MCRs presents aforementioned practical challenges. Instead – or in combination – magnetic localization methods are uniquely compatible with MCRs. One such approach is demonstrated in Chapter 6, alongside other algorithms that depend on MCRs' magnetic field properties and relative position to a field sensor [75], [76], [238], [241]–[243], [246], [247], [249], [278]–[280].

An advantage of magnetic localization is its focus on tracking the device. This allows traditional single-plane 2D imaging systems to retain their primary function without needing to be repurposed for real-time localization. A multi-modal approach that combines 3D magnetic localization (specific to MCRs), single plane 2D medical imaging, and 3D pre-operative scans could offer several advantages:

1. The recorded trajectory of an MCR through magnetic localization could be used to align a pre-operative scan with the base frame of the manipulation system, potentially enabling (semi-)autonomous navigation in the future.

2. Processing 2D medical images can serve as a validation tool to enhance the accuracy of magnetic localization, improving intra-operative safety during MCR manipulation.

3. Integrating 3D localization data with pre-operative scans can provide clinicians with a real-time, 3D visualization of the MCR within the patient's anatomy.

7.2.3 Expanding applications of magnetic continuum robots

Traditional MCRs – flexible structures embedded with magnetic elements – are designed to move upon application of external magnetic fields. In

this setup, the manipulation system acts as the actuator, while the MCR functions as the effector. This approach has been primarily used for navigation, enabling controlled movement of wires, catheters, or capsules through anatomical pathways such as blood vessels, airways, or the gastrointestinal tract.

The research presented in Chapter 5 and Chapter 6 extends the role of MCRs beyond their traditional function as passive navigational tools. There, the MCRs themselves incorporate electromagnetic sources to generate dynamic magnetic fields. Expanding MCR functionality in this way opens up new possibilities for medical applications.

Expanding the application of MCRs towards, e.g., generators of dynamic field inside the body offers unique advantages over external systems. In particular, these fields are localized and non-uniform, characterized by high gradients. These fields are could be particularly useful for targeted therapy and regenerative medicine. Some potential applications include:

1. Local physical manipulation (Chapter 5): Integrating magnetic soft machines in MCRs could enable localized physical manipulation in anatomical cavities, such as tissue manipulation.
2. Wireless power transfer: Dynamic fields from MCRs could potentially be used to locally recharge, e.g., pacemakers [269].
3. Nerve regeneration: The local generated fields by MCRs could be used to stimulate nerve cells and guide their growth [270], [281].
4. Guiding magnetotactic bacteria: Local delivery and steering of magnetically-responsive microorganisms could be applied in targeted drug delivery and uptake [282].
5. Attracting circulating nanoparticles: The high gradients from locally generated fields could be applied to attracting anti-tumor magnetic nanoparticles (MNPs) toward tumor vasculature [283], [284].
6. MNP-based cancer therapy: Local dynamic fields can act on nanoparticle-loaded cancer cells to apply mechanical stress and induce cell death [271], or aid in breaking nanoparticle chains to improve their cellular uptake for hyperthermia treatment [272].

7.2.4 Collaborating with clinicians

Ongoing research in magnetics for surgical robotics shows how design choices in magneto-surgical robotics determine feasible control methods and clinical applications. As the number of publications on magnetic (soft) robots increases, research appears to diverge into two main directions: design sophistication and clinical relevance.

As designs grow more complex, the practical application in surgery may be overlooked. To bridge the gap between technological advancements and clinical needs, close collaboration with clinicians is essential. As our understanding of magnetic design, control, and localization improves – with contributions in this doctoral dissertation – clinicians' expertise is required to guide this knowledge toward meaningful medical applications.

Bibliography

[1] N. L. Erb-Satullo, "The innovation and adoption of iron in the ancient near east," *Journal of Archaeological Research*, vol. 27, pp. 557–607, 2019.

[2] D. C. Mattis and D. C. Mattis, "History of magnetism," *The Theory of Magnetism I: Statics and Dynamics*, pp. 1–38, 1981.

[3] D. C. Giancoli, *Physics for scientists and engineers with modern physics*. Pearson Education, 2008, vol. 2.

[4] M. R. Mourino, "From thales to lauterbur, or from the lodestone to mr imaging: magnetism and medicine." *Radiology*, vol. 180, no. 3, pp. 593–612, 1991.

[5] B. Arnold *et al.*, *The letter of Petrus Peregrinus on the magnet, AD 1269*. Good Press, 2023.

[6] J. Hirschberg, *Ueber die Magnet-Extraction von Eisensplittern aus dem Augeninnern:(nach einem am 4. Januar 1883 in der Gesellschaft der Charité-Aerzte gehaltenen Vortrag)*. Hirschwald, 1883.

[7] "Powerful electromagnet for the use of oculists," *Scientific American Magazine*, vol. 105, no. 26, 1911.

[8] U. Häfeli, "The history of magnetism in medicine," *Magnetism in medicine*, vol. 2, pp. 3–25, 1998.

[9] H. C. Oersted, "On electro-magnetism," *Annals of Philosophy*, vol. 2, pp. 321–337, 1821.

[10] W. Sturgeon, "Xxv. on electro-magnets," *The Philosophical Magazine*, vol. 11, no. 63, pp. 194–205, 1832.

[11] O. Haab, "Die verwendung sehr starker magnete zur entfernung von eisensplittern aus dem auge," *Ber. dtsch. ophthal. Ges*, vol. 22, pp. 163–172, 1892.

[12] C. A. Coulomb, *Essai sur une application des regles de maximis et minimis quelques problemes de statique, relatits a l'architecture.* Memoires de Mathematique de l'Academie Royale de Science, 1776.

[13] A.-M. Ampère, *Memoires de l'Academie Royale des Sciences.* Académie royale des sciences (France), 1823.

[14] M. Faraday, "Lviii. on the physical character of the lines of magnetic force," *The London, Edinburgh, and Dublin Philosophical Magazine and Journal of Science*, vol. 3, no. 20, pp. 401–428, 1852.

[15] C. F. Gauss, *Werke.* Cambridge University Press, 2011, vol. 6.

[16] G. Cavalleri, G. Spavieri, and G. Spinelli, "The ampere and biot-savart force laws," *european Journal of Physics*, vol. 17, no. 4, p. 205, 1996.

[17] J. C. Maxwell, "A treatise on electricity and magnetism," *Clarendon Press google schola*, vol. 2, pp. 3408–3425, 1873.

[18] D. J. Griffiths, *Introduction to electrodynamics.* Cambridge University Press, 2023.

[19] S. Hilal, W. Michelsen, and J. Driller, "Pod catheter: a means for small vessel exploration," *Journal of Applied Physics*, vol. 40, no. 3, pp. 1046–1046, 1969.

[20] M. Sagawa, S. Fujimura, N. Togawa, H. Yamamoto, and Y. Matsuura, "New material for permanent magnets on a base of nd and fe," *Journal of Applied Physics*, vol. 55, no. 6, pp. 2083–2087, 1984.

[21] J. Driller, S. Hilal, W. Michelsen, B. Sollish, B. Katz, and W. Konig Jr, "Development and use of the pod catheter in the cerebral vascular system," *Medical research engineering*, vol. 8, no. 4, pp. 11–16, 1969.

[22] R. Ritter, M. Grady, M. Howard, and G. Gillies, "Magnetic stereotaxis: computer-assisted, image-guided remote movement of implants in the brain," *Innovation et technologie en biologie et médecine*, vol. 13, no. 4, pp. 437–449, 1992.

[23] D. Montgomery, R. Weggel, M. Leupold, S. Yodh, and R. Wright, "Superconducting magnet system for intravascular navigation," *Journal of Applied Physics*, vol. 40, no. 5, pp. 2129–2132, 1969.

[24] S. K. Hilal, W. Michelsen, J. Driller, and E. Leonard, "Magnetically guided devices for vascular exploration and treatment," *Radiology*, vol. 113, no. 3, pp. 529–540, 1974.

[25] J. Kunzler and M. Tanenbaum, "Superconducting magnets," *Scientific American*, vol. 206, no. 6, pp. 60–67, 1962.

[26] P. A. Abetti and P. Haldar, "One hundred years of superconductivity: science, technology, products, profits and industry structure," *International Journal of Technology Management*, vol. 48, no. 4, pp. 423–447, 2009.

[27] K. Strnat, G. Hoffer, J. Olson, W. Ostertag, and J. Becker, "A family of new cobalt-base permanent magnet materials," *Journal of Applied Physics*, vol. 38, no. 3, pp. 1001–1002, 1967.

[28] J. Alksne, "Magnetically controlled intravascular catheter." *Surgery*, vol. 64, no. 1, pp. 339–345, 1968.

[29] R. G. McNeil, R. C. Ritter, B. Wang, M. A. Lawson, G. T. Gillies, K. Wika, E. G. Quate, M. Howard, and M. S. Grady, "Functional design features and initial performance characteristics of a magnetic-implant guidance system for stereotactic neurosurgery," *IEEE transactions on biomedical engineering*, vol. 42, no. 8, pp. 793–801, 1995.

[30] D. C. Meeker, E. H. Maslen, R. C. Ritter, and F. M. Creighton, "Optimal realization of arbitrary forces in a magnetic stereotaxis system," *IEEE transactions on magnetics*, vol. 32, no. 2, pp. 320–328, 1996.

[31] M. S. Grady, M. A. Howard, R. G. Dacey, W. Blume, M. Lawson, P. Werp, and R. C. Ritter, "Experimental study of the magnetic stereotaxis system for catheter manipulation within the brain," *Journal of neurosurgery*, vol. 93, no. 2, pp. 282–288, 2000.

[32] M. N. Faddis, W. Blume, J. Finney, A. Hall, J. Rauch, J. Sell, K. T. Bae, M. Talcott, and B. Lindsay, "Novel, magnetically guided

catheter for endocardial mapping and radiofrequency catheter ablation," *Circulation*, vol. 106, no. 23, pp. 2980–2985, 2002.

[33] G. Gillies, R. Ritter, W. Broaddus, M. Grady, M. Howard III, and R. McNeil, "Magnetic manipulation instrumentation for medical physics research," *Review of Scientific Instruments*, vol. 65, no. 3, pp. 533–562, 1994.

[34] K. Hertting, S. Ernst, F. Stahl, S. Mathew, H. Meulenbrug, J. Reimers, K.-H. Kuck, and K. Krause, "Use of the novel magnetic navigation system niobe in percutaneous coronary interventions; the hamburg experience." *Eurointervention: Journal of Europcr in Collaboration with the Working Group on Interventional Cardiology of the European Society of Cardiology*, vol. 1, no. 3, pp. 336–339, 2005.

[35] T. Krings, J. Finney, P. Niggemann, P. Reinacher, N. Lück, A. Drexler, J. Lovell, A. Meyer, R. Sehra, P. Schauerte *et al.*, "Magnetic versus manual guidewire manipulation in neuroradiology: in vitro results," *Neuroradiology*, vol. 48, pp. 394–401, 2006.

[36] M. P. Armacost, J. Adair, T. Munger, R. R. Viswanathan, F. M. Creighton, D. T. Curd, and R. Sehra, "Accurate and reproducible target navigation with the stereotaxis niobe® magnetic navigation system," *Journal of Cardiovascular Electrophysiology*, vol. 18, pp. S26–S31, 2007.

[37] F. Kiemeneij, M. S. Patterson, G. Amoroso, G. Laarman, and T. Slagboom, "Use of the stereotaxis niobe® magnetic navigation system for percutaneous coronary intervention: Results from 350 consecutive patients," *Catheterization and Cardiovascular Interventions*, vol. 71, no. 4, pp. 510–516, 2008.

[38] M. P. Kummer, J. J. Abbott, B. E. Kratochvil, R. Borer, A. Sengul, and B. J. Nelson, "Octomag: An electromagnetic system for 5-dof wireless micromanipulation," *IEEE Transactions on Robotics*, vol. 26, no. 6, pp. 1006–1017, 2010.

[39] S. Erni, S. Schürle, A. Fakhraee, B. E. Kratochvil, and B. J. Nelson, "Comparison, optimization, and limitations of magnetic manipula-

tion systems," *Journal of Micro-Bio Robotics*, vol. 8, pp. 107–120, 2013.

[40] Z. Yang and L. Zhang, "Magnetic actuation systems for miniature robots: A review," *Advanced Intelligent Systems*, vol. 2, no. 9, p. 2000082, 2020.

[41] P. Valdastri, G. Ciuti, A. Verbeni, A. Menciassi, P. Dario, A. Arezzo, and M. Morino, "Magnetic air capsule robotic system: proof of concept of a novel approach for painless colonoscopy," *Surgical endoscopy*, vol. 26, pp. 1238–1246, 2012.

[42] V. N. Le, N. H. Nguyen, K. Alameh, R. Weerasooriya, and P. Pratten, "Accurate modeling and positioning of a magnetically controlled catheter tip," *Medical Physics*, vol. 43, no. 2, pp. 650–663, 2016.

[43] P. E. Dupont, N. Simaan, H. Choset, and C. Rucker, "Continuum robots for medical interventions," *Proceedings of the IEEE*, vol. 110, no. 7, pp. 847–870, 2022.

[44] C. M. Heunis, B. Silva, G. Sereni, M. C. Lam, B. Belakhal, A. Gaborit, B. Wermelink, B. R. Geelkerken, and S. Misra, "The flux one magnetic navigation system: A preliminary assessment for stent implantation," *IEEE Robotics and Automation Letters*, vol. 8, no. 9, pp. 5640–5647, 2023.

[45] S. Gervasoni, N. Pedrini, T. Rifai, C. Fischer, F. C. Landers, M. Mattmann, R. Dreyfus, S. Viviani, A. Veciana, E. Masina *et al.*, "A human-scale clinically ready electromagnetic navigation system for magnetically responsive biomaterials and medical devices," *Advanced Materials*, vol. 36, no. 31, p. 2310701, 2024.

[46] K. Obstein, C. Landewee, J. Norton, J. Martin, S. Caló, J. W. Kow, B. Scaglioni, and P. Valdastri, "The magnetic flexible endoscope: Phase 1 first-in-human trial," *Gastrointestinal Endoscopy*, vol. 99, no. 6, p. AB581, 2024.

[47] "Stereotaxis inc., genesisx," https://www.stereotaxis.com/products/#!/genesis, accessed: 2025-1-7.

[48] "Flux robotics b.v., flux one." https://www.fluxrobotics.nl/#product, accessed: 2025-1-7.

[49] "Stereotaxis inc., map-it catheters," https://www.stereotaxis.com/products/#!/apt, accessed: 2025-1-7.

[50] "Magnebotix, navion," https://www.magnebotix.com/navion, accessed: 2025-1-7.

[51] "Nanoflex robotics," https://nanoflexrobotics.com/our-technology/, accessed: 2025-1-7.

[52] D. Rus and M. T. Tolley, "Design, fabrication and control of soft robots," *Nature*, vol. 521, no. 7553, pp. 467–475, 2015.

[53] E. Diller, J. Zhuang, G. Zhan Lum, M. R. Edwards, and M. Sitti, "Continuously distributed magnetization profile for millimeter-scale elastomeric undulatory swimming," *Applied Physics Letters*, vol. 104, no. 17, 2014.

[54] G. Z. Lum, Z. Ye, X. Dong, H. Marvi, O. Erin, W. Hu, and M. Sitti, "Shape-programmable magnetic soft matter," *Proceedings of the National Academy of Sciences*, vol. 113, no. 41, pp. E6007–E6015, 2016.

[55] W. Hu, G. Z. Lum, M. Mastrangeli, and M. Sitti, "Small-scale soft-bodied robot with multimodal locomotion," *Nature*, vol. 554, no. 7690, pp. 81–85, 2018.

[56] Y. Kim, G. A. Parada, S. Liu, and X. Zhao, "Ferromagnetic soft continuum robots," *Sci. Robot*, vol. 4, no. 33, p. 7329, 2019.

[57] G. Mao, D. Schiller, D. Danninger, B. Hailegnaw, F. Hartmann, T. Stockinger, M. Drack, N. Arnold, and M. Kaltenbrunner, "Ultrafast small-scale soft electromagnetic robots," *Nature communications*, vol. 13, no. 1, p. 4456, 2022.

[58] Y. Kim and X. Zhao, "Magnetic soft materials and robots," *Chemical reviews*, vol. 122, no. 5, pp. 5317–5364, 2022.

[59] J. Burgner-Kahrs, D. C. Rucker, and H. Choset, "Continuum robots for medical applications: A survey," *IEEE Transactions on Robotics*, vol. 31, no. 6, pp. 1261–1280, 2015.

[60] Z. Yang, H. Yang, Y. Cao, Y. Cui, and L. Zhang, "Magnetically actuated continuum medical robots: A review," *Advanced intelligent systems*, vol. 5, no. 6, p. 2200416, 2023.

[61] C. Alessi, C. Agabiti, D. Caradonna, C. Laschi, F. Renda, and E. Falotico, "Rod models in continuum and soft robot control: a review," *arXiv preprint arXiv:2407.05886*, 2024.

[62] J. Sikorski, C. M. Heunis, F. Franco, and S. Misra, "The armm system: An optimized mobile electromagnetic coil for non-linear actuation of flexible surgical instruments," *IEEE Transactions on Magnetics*, vol. 55, no. 9, pp. 1–9, 2019.

[63] J. Edelmann, A. J. Petruska, and B. J. Nelson, "Magnetic control of continuum devices," *The International Journal of Robotics Research*, vol. 36, no. 1, pp. 68–85, 2017.

[64] P. E. Dupont, J. Lock, B. Itkowitz, and E. Butler, "Design and control of concentric-tube robots," *IEEE Transactions on Robotics*, vol. 26, no. 2, pp. 209–225, 2009.

[65] C. Chautems, A. Tonazzini, D. Floreano, and B. J. Nelson, "A variable stiffness catheter controlled with an external magnetic field," in *2017 IEEE/RSJ International Conference on Intelligent Robots and Systems (IROS)*. IEEE, 2017, pp. 181–186.

[66] C. Chautems, A. Tonazzini, Q. Boehler, S. H. Jeong, D. Floreano, and B. J. Nelson, "Magnetic continuum device with variable stiffness for minimally invasive surgery," *Advanced Intelligent Systems*, vol. 2, no. 6, p. 1900086, 2020.

[67] M. Mattmann, C. De Marco, F. Briatico, S. Tagliabue, A. Colusso, X.-Z. Chen, J. Lussi, C. Chautems, S. Pané, and B. Nelson, "Thermoset shape memory polymer variable stiffness 4d robotic catheters," *Advanced Science*, p. 2103277, 2022.

[68] J. J. Abbott, E. Diller, and A. J. Petruska, "Magnetic methods in robotics," *Annual Review of Control, Robotics, and Autonomous Systems*, vol. 3, pp. 57–90, 2020.

[69] F. P. Gosselin, V. Lalande, and S. Martel, "Characterization of the deflections of a catheter steered using a magnetic resonance imaging system," *Medical physics*, vol. 38, no. 9, pp. 4994–5002, 2011.

[70] L. Wang, D. Zheng, P. Harker, A. B. Patel, C. F. Guo, and X. Zhao, "Evolutionary design of magnetic soft continuum robots," *Proceedings of the National Academy of Sciences*, vol. 118, no. 21, p. e2021922118, 2021.

[71] M. M. Said, J. Yunas, R. E. Pawinanto, B. Y. Majlis, and B. Bais, "Pdms based electromagnetic actuator membrane with embedded magnetic particles in polymer composite," *Sensors and Actuators A: Physical*, vol. 245, pp. 85–96, 2016.

[72] T. N. Do, H. Phan, T.-Q. Nguyen, and Y. Visell, "Miniature soft electromagnetic actuators for robotic applications," *Advanced Functional Materials*, vol. 28, no. 18, p. 1800244, 2018.

[73] F. Carpi and C. Pappone, "Stereotaxis niobe® magnetic navigation system for endocardial catheter ablation and gastrointestinal capsule endoscopy," *Expert review of medical devices*, vol. 6, no. 5, pp. 487–498, 2009.

[74] C. Shi, X. Luo, P. Qi, T. Li, S. Song, Z. Najdovski, T. Fukuda, and H. Ren, "Shape sensing techniques for continuum robots in minimally invasive surgery: A survey," *IEEE Transactions on Biomedical Engineering*, vol. 64, no. 8, pp. 1665–1678, 2016.

[75] D. Son, S. Yim, and M. Sitti, "A 5-d localization method for a magnetically manipulated untethered robot using a 2-d array of hall-effect sensors," *IEEE Transactions on Mechatronics*, vol. 21, no. 2, pp. 708–716, 2015.

[76] K. M. Popek, A. W. Mahoney, and J. J. Abbott, "Localization method for a magnetic capsule endoscope propelled by a rotating magnetic dipole field," in *2013 IEEE International Conference on Robotics and Automation*. IEEE, 2013, pp. 5348–5353.

[77] T. da Veiga, J. H. Chandler, P. Lloyd, G. Pittiglio, N. J. Wilkinson, A. K. Hoshiar, R. A. Harris, and P. Valdastri, "Challenges of con-

tinuum robots in clinical context: a review." *Progress in Biomedical Engineering*, 2020.

[78] T. L. Thomas, V. K. Venkiteswaran, G. Ananthasuresh, and S. Misra, "A monolithic compliant continuum manipulator: A proof-of-concept study," *Journal of Mechanisms and Robotics*, vol. 12, no. 6, 2020.

[79] J. Sikorski, S. Mohanty, and S. Misra, "Milimac: Flexible catheter with miniaturized electromagnets as a small-footprint system for microrobotic tasks," *IEEE Robotics and Automation Letters*, vol. 5, no. 4, pp. 5260–5267, 2020.

[80] G. Pittiglio, L. Barducci, J. W. Martin, J. C. Norton, C. A. Avizzano, K. L. Obstein, and P. Valdastri, "Magnetic levitation for soft-tethered capsule colonoscopy actuated with a single permanent magnet: a dynamic control approach," *IEEE Robotics and Automation Letters*, vol. 4, no. 2, pp. 1224–1231, 2019.

[81] P. Lloyd, A. K. Hoshiar, T. da Veiga, A. Attanasio, N. Marahrens, J. H. Chandler, and P. Valdastri, "A learnt approach for the design of magnetically actuated shape forming soft tentacle robots," *IEEE Robotics and Automation Letters*, vol. 5, no. 3, pp. 3937–3944, 2020.

[82] A. J. Petruska and B. J. Nelson, "Minimum bounds on the number of electromagnets required for remote magnetic manipulation," *IEEE Transactions on Robotics*, vol. 31, no. 3, pp. 714–722, 2015.

[83] S. Salmanipour and E. Diller, "Eight-degrees-of-freedom remote actuation of small magnetic mechanisms," *IEEE International Conference on Robotics and Automation (ICRA)*, 2018.

[84] J. Sikorski, I. Dawson, A. Denasi, E. E. Hekman, and S. Misra, "Introducing bigmag—a novel system for 3d magnetic actuation of flexible surgical manipulators," in *2017 IEEE International Conference on Robotics and Automation (ICRA)*. IEEE, 2017, pp. 3594–3599.

[85] C. M. Heunis, J. Sikorski, and S. Misra, "Flexible instruments for endovascular interventions: Improved magnetic steering, actuation, and image-guided surgical instruments," *IEEE Robotics & Automation Magazine*, vol. 25, no. 3, pp. 71–82, 2018.

[86] F. Ongaro, C. M. Heunis, and S. Misra, "Precise model-free spline-based approach for magnetic field mapping," *IEEE Magnetics Letters*, vol. 10, pp. 1–5, 2018.

[87] A. J. Petruska and J. J. Abbott, "Optimal permanent-magnet geometries for dipole field approximation," *IEEE Transactions on Magnetics*, vol. 49, no. 2, pp. 811–819, 2012.

[88] A. J. Petruska, J. Edelmann, and B. J. Nelson, "Model-based calibration for magnetic manipulation," *IEEE Transactions on Magnetics*, vol. 53, no. 7, pp. 1–6, 2017.

[89] V. K. Venkiteswaran, J. Sikorski, and S. Misra, "Shape and contact force estimation of continuum manipulators using pseudo rigid body models," *Mechanism and Machine theory*, vol. 139, pp. 34–45, 2019.

[90] D. C. Rucker and R. J. Webster III, "Statics and dynamics of continuum robots with general tendon routing and external loading," *IEEE Transactions on Robotics*, vol. 27, no. 6, pp. 1033–1044, 2011.

[91] J. Sikorski, A. Denasi, G. Bucchi, S. Scheggi, and S. Misra, "Vision-based 3-d control of magnetically actuated catheter using bigmag—an array of mobile electromagnetic coils," *IEEE/ASME Transactions on Mechatronics*, vol. 24, no. 2, pp. 505–516, 2019.

[92] S. Jeon, A. K. Hoshiar, K. Kim, S. Lee, E. Kim, S. Lee, J.-y. Kim, B. J. Nelson, H.-J. Cha, B.-J. Yi *et al.*, "A magnetically controlled soft microrobot steering a guidewire in a three-dimensional phantom vascular network," *Soft Robotics*, vol. 6, no. 1, pp. 54–68, 2019.

[93] B. Siciliano, L. Sciavicco, L. Villani, and G. Oriolo, *Robotics: modelling, planning and control*. Springer Science & Business Media, 2010.

[94] S. Antman, *Nonlinear Problems of Elasticity*. Springer-Verlag, 1995.

[95] J. Till, V. Aloi, and C. Rucker, "Real-time dynamics of soft and continuum robots based on cosserat rod models," *The International Journal of Robotics Research*, vol. 38, no. 6, pp. 723–746, 2019.

[96] F. Khan, A. Donder, S. Galvan, F. R. y Baena, and S. Misra, "Pose measurement of flexible medical instruments using fiber bragg gratings in multi-core fiber," *IEEE Sensors Journal*, vol. 20, no. 18, pp. 10 955–10 962, 2020.

[97] Y. Fu, H. Liu, W. Huang, S. Wang, and Z. Liang, "Steerable catheters in minimally invasive vascular surgery," *The International Journal of Medical Robotics and Computer Assisted Surgery*, vol. 5, no. 4, pp. 381–391, 2009.

[98] V. Ojha, S. N. Raju, A. Deshpande, K. P. Ganga, and S. Kumar, "Catheters in vascular interventional radiology: an illustrated review," *Diagnostic and Interventional Radiology*, vol. 29, no. 1, p. 138, 2023.

[99] A. Dohan, Y. Guerrache, M. Boudiaf, J.-P. Gavini, R. Kaci, and P. Soyer, "Transjugular liver biopsy: indications, technique and results," *Diagnostic and Interventional Imaging*, vol. 95, no. 1, pp. 11–15, 2014.

[100] P. J. Swaney, A. W. Mahoney, B. I. Hartley, A. A. Remirez, E. Lamers, R. H. Feins, R. Alterovitz, and R. J. Webster III, "Toward transoral peripheral lung access: Combining continuum robots and steerable needles," *Journal of Medical Robotics Research*, vol. 2, no. 01, p. 1750001, 2017.

[101] H. B. Gilbert, J. Neimat, and R. J. Webster, "Concentric tube robots as steerable needles: Achieving follow-the-leader deployment," *IEEE Transactions on Robotics*, vol. 31, no. 2, pp. 246–258, 2015.

[102] C. Bergeles, A. H. Gosline, N. V. Vasilyev, P. J. Codd, J. Pedro, and P. E. Dupont, "Concentric tube robot design and optimization based on task and anatomical constraints," *IEEE Transactions on Robotics*, vol. 31, no. 1, pp. 67–84, 2015.

[103] T. L. Thomas, J. Bos, J. J. Huaroto, V. Kalpathy Venkiteswaran, and S. Misra, "A magnetically actuated variable stiffness manipulator based on deployable shape memory polymer springs," *Advanced Intelligent Systems*, p. 2200465, 2023.

[104] N. J. Van De Berg, D. J. Van Gerwen, J. Dankelman, and J. J. Van Den Dobbelsteen, "Design choices in needle steering—a review," *IEEE/ASME Transactions on Mechatronics*, vol. 20, no. 5, pp. 2172–2183, 2014.

[105] D. C. Rucker, B. A. Jones, and R. J. Webster III, "A geometrically exact model for externally loaded concentric-tube continuum robots," *IEEE Transactions on Robotics*, vol. 26, no. 5, pp. 769–780, 2010.

[106] H. Gu, Q. Boehler, H. Cui, E. Secchi, G. Savorana, C. De Marco, S. Gervasoni, Q. Peyron, T.-Y. Huang, S. Pane *et al.*, "Magnetic cilia carpets with programmable metachronal waves," *Nature Communications*, vol. 11, no. 1, pp. 1–10, 2020.

[107] M. Mattmann, Q. Boehler, X.-Z. Chen, S. Pané, and B. J. Nelson, "Shape memory polymer variable stiffness magnetic catheters with hybrid stiffness control," in *2022 IEEE/RSJ International Conference on Intelligent Robots and Systems (IROS)*. IEEE, 2022, pp. 9589–9595.

[108] J. Lussi, M. Mattmann, S. Sevim, F. Grigis, C. De Marco, C. Chautems, S. Pané, J. Puigmartí-Luis, Q. Boehler, and B. J. Nelson, "A submillimeter continuous variable stiffness catheter for compliance control," *Advanced Science*, vol. 8, no. 18, p. 2101290, 2021.

[109] S. S. Antman, "Problems in nonlinear elasticity," *Nonlinear Problems of Elasticity*, pp. 513–584, 2005.

[110] J. Till, V. Aloi, K. E. Riojas, P. L. Anderson, R. J. Webster III, and C. Rucker, "A dynamic model for concentric tube robots," *IEEE Transactions on Robotics*, vol. 36, no. 6, pp. 1704–1718, 2020.

[111] M. Richter, V. K. Venkiteswaran, and S. Misra, "Multi-point orientation control of discretely-magnetized continuum manipulators," *IEEE Robotics and Automation Letters*, vol. 6, no. 2, pp. 3607–3614, 2021.

[112] R. T. Farouki, "Rational rotation-minimizing frames—recent advances and open problems," *Applied Mathematics and Computation*, vol. 272, pp. 80–91, 2016.

[113] R. M. Murray, Z. Li, and S. S. Sastry, *A Mathematical Introduction to Robotic Manipulation*. CRC press, 2017.

[114] J. M. Gere and B. J. Goodno, *Mechanics of materials*, 8th ed. Cengage learning, 2013, ch. G, pp. 1045–1047.

[115] R. J. Webster III and B. A. Jones, "Design and kinematic modeling of constant curvature continuum robots: A review," *The International Journal of Robotics Research*, vol. 29, no. 13, pp. 1661–1683, 2010.

[116] G. Pittiglio, A. L. Orekhov, T. da Veiga, S. Calò, J. H. Chandler, N. Simaan, and P. Valdastri, "Closed loop static control of multi-magnet soft continuum robots," *IEEE Robotics and Automation Letters*, 2023.

[117] A. Ramadani, M. Bui, T. Wendler, H. Schunkert, P. Ewert, and N. Navab, "A survey of catheter tracking concepts and methodologies," *Medical Image Analysis*, p. 102584, 2022.

[118] A. Hong, A. J. Petruska, and B. J. Nelson, "Tracking a magnetically guided catheter with a single rotating c-arm," in *2015 IEEE International Conference on Robotics and Automation (ICRA)*. IEEE, 2015, pp. 618–623.

[119] M. Ourak, S. De Buck, X. T. Ha, O. Al-Ahmad, K. Bamps, J. Ector, and E. Vander Poorten, "Fusion of biplane fluoroscopy with fiber bragg grating for 3d catheter shape reconstruction," *IEEE Robotics and Automation Letters*, vol. 6, no. 4, pp. 6505–6512, 2021.

[120] P. J. Swaney, J. Burgner, H. B. Gilbert, and R. J. Webster, "A flexure-based steerable needle: high curvature with reduced tissue damage," *IEEE Transactions on Biomedical Engineering*, vol. 60, no. 4, pp. 906–909, 2012.

[121] A. Hong, A. J. Petruska, A. Zemmar, and B. J. Nelson, "Magnetic control of a flexible needle in neurosurgery," *IEEE Transactions on Biomedical Engineering*, vol. 68, no. 2, pp. 616–627, 2020.

[122] T. L. Bruns, A. A. Remirez, M. A. Emerson, R. A. Lathrop, A. W. Mahoney, H. B. Gilbert, C. L. Liu, P. T. Russell, R. F. Labadie,

K. D. Weaver *et al.*, "A modular, multi-arm concentric tube robot system with application to transnasal surgery for orbital tumors," *The International Journal of Robotics Research*, vol. 40, no. 2-3, pp. 521–533, 2021.

[123] A. Ataollahi, R. Karim, A. S. Fallah, K. Rhode, R. Razavi, L. D. Seneviratne, T. Schaeffter, and K. Althoefer, "Three-degree-of-freedom mr-compatible multisegment cardiac catheter steering mechanism," *IEEE Transactions on Biomedical Engineering*, vol. 63, no. 11, pp. 2425–2435, 2013.

[124] A. Ali, A. Sakes, E. A. Arkenbout, P. Henselmans, R. van Starkenburg, T. Szili-Torok, and P. Breedveld, "Catheter steering in interventional cardiology: Mechanical analysis and novel solution," *Proceedings of the Institution of Mechanical Engineers, Part H: Journal of Engineering in Medicine*, vol. 233, no. 12, pp. 1207–1218, 2019.

[125] F. Campisano, S. Caló, A. A. Remirez, J. H. Chandler, K. L. Obstein, R. J. Webster III, and P. Valdastri, "Closed-loop control of soft continuum manipulators under tip follower actuation," *The International journal of robotics research*, vol. 40, no. 6-7, pp. 923–938, 2021.

[126] N. Garbin, L. Wang, J. H. Chandler, K. L. Obstein, N. Simaan, and P. Valdastri, "A disposable continuum endoscope using piston-driven parallel bellow actuator," in *2018 International Symposium on Medical Robotics (ISMR)*. IEEE, 2018, pp. 1–6.

[127] L. Pancaldi, P. Dirix, A. Fanelli, A. M. Lima, N. Stergiopulos, P. J. Mosimann, D. Ghezzi, and M. S. Sakar, "Flow driven robotic navigation of microengineered endovascular probes," *Nature communications*, vol. 11, no. 1, p. 6356, 2020.

[128] J. Hwang, S. Jeon, B. Kim, J.-y. Kim, C. Jin, A. Yeon, B.-J. Yi, C.-H. Yoon, H.-J. Park, S. Pané *et al.*, "An electromagnetically controllable microrobotic interventional system for targeted, real-time cardiovascular intervention," *Advanced healthcare materials*, vol. 11, no. 11, p. 2102529, 2022.

[129] M. F. Phelan III, M. E. Tiryaki, J. Lazovic, H. Gilbert, and M. Sitti, "Heat-mitigated design and lorentz force-based steering of an mri-driven microcatheter toward minimally invasive surgery," *Advanced Science*, vol. 9, no. 10, p. 2105352, 2022.

[130] A. Azizi, C. C. Tremblay, K. Gagné, and S. Martel, "Using the fringe field of a clinical mri scanner enables robotic navigation of tethered instruments in deeper vascular regions," *Science Robotics*, vol. 4, no. 36, p. eaax7342, 2019.

[131] S. L. Charreyron, Q. Boehler, A. N. Danun, A. Mesot, M. Becker, and B. J. Nelson, "A magnetically navigated microcannula for subretinal injections," *IEEE transactions on biomedical engineering*, vol. 68, no. 1, pp. 119–129, 2020.

[132] C. M. Heunis, K. J. Behrendt, E. E. Hekman, C. Moers, J.-P. P. de Vries, and S. Misra, "Design and evaluation of a magnetic rotablation catheter for arterial stenosis," *IEEE/ASME transactions on mechatronics*, vol. 27, no. 3, pp. 1761–1772, 2021.

[133] J. Sikorski, C. M. Heunis, R. Obeid *et al.*, "A flexible catheter system for ultrasound-guided magnetic projectile delivery," *IEEE Transactions on Robotics*, vol. 38, no. 3, 2021.

[134] L. Barducci, G. Pittiglio, J. C. Norton, K. L. Obstein, and P. Valdastri, "Adaptive dynamic control for magnetically actuated medical robots," *IEEE robotics and automation letters*, vol. 4, no. 4, pp. 3633–3640, 2019.

[135] J. W. Martin, B. Scaglioni, J. C. Norton, V. Subramanian, A. Arezzo, K. L. Obstein, and P. Valdastri, "Enabling the future of colonoscopy with intelligent and autonomous magnetic manipulation," *Nature machine intelligence*, vol. 2, no. 10, pp. 595–606, 2020.

[136] Y. Li, C. Guo, W. Xin, T. Pan, W. Li, P. W. Y. Chiu, and Z. Li, "Design and preliminary evaluation of an electromagnetically actuated soft-tethered colonoscope," *IEEE Transactions on Medical Robotics and Bionics*, vol. 3, no. 2, pp. 402–413, 2021.

[137] J. Hwang, J.-y. Kim, and H. Choi, "A review of magnetic actuation systems and magnetically actuated guidewire-and catheter-based microrobots for vascular interventions," *Intelligent Service Robotics*, vol. 13, pp. 1–14, 2020.

[138] Z. Yang, L. Yang, M. Zhang, Q. Wang, S. C. H. Yu, and L. Zhang, "Magnetic control of a steerable guidewire under ultrasound guidance using mobile electromagnets," *IEEE Robotics and Automation Letters*, vol. 6, no. 2, pp. 1280–1287, 2021.

[139] T. Zhang, L. Yang, X. Yang, R. Tan, H. Lu, and Y. Shen, "Millimeter-scale soft continuum robots for large-angle and high-precision manipulation by hybrid actuation," *Advanced Intelligent Systems*, vol. 3, no. 2, p. 2000189, 2021.

[140] Y. Kim, H. Yuk, R. Zhao, S. A. Chester, and X. Zhao, "Printing ferromagnetic domains for untethered fast-transforming soft materials," *Nature*, vol. 558, no. 7709, pp. 274–279, 2018.

[141] S. Wu, W. Hu, Q. Ze, M. Sitti, and R. Zhao, "Multifunctional magnetic soft composites: A review," *Multifunctional materials*, vol. 3, no. 4, p. 042003, 2020.

[142] A. N. Gent, "On the relation between indentation hardness and young's modulus," *Rubber Chemistry and Technology*, vol. 31, no. 4, pp. 896–906, 1958.

[143] M. Mooney, "The viscosity of a concentrated suspension of spherical particles," *Journal of colloid science*, vol. 6, no. 2, pp. 162–170, 1951.

[144] A. Deswal, B. K. Tamang, and A. Bala, "Study of aortic-common iliac bifurcation and its clinical significance," *Journal of clinical and diagnostic research: JCDR*, vol. 8, no. 7, p. AC06, 2014.

[145] R. P. Dyches, K. J. Eaton, and H. F. Smith, "The roles of celiac trunk angle and vertebral origin in median arcuate ligament syndrome," *Diagnostics*, vol. 10, no. 2, p. 76, 2020.

[146] A. Ekingen, E. S. Hatipoğlu, and C. Hamidi, "Distance measurements and origin levels of the coeliac trunk, superior mesenteric

artery, and inferior mesenteric artery by multiple-detector computed tomography angiography," *Anatomical Science International*, vol. 96, no. 1, pp. 132–141, 2021.

[147] A. B. Desai, D. S. Shah, C. J. Bhatt *et al.*, "Measurement of the distance and angle between the aorta and superior mesenteric artery on ct scan: values in indian population in different bmi categories," *Indian Journal of Surgery*, vol. 77, no. 2, pp. 614–617, 2015.

[148] P. Reymond, F. Merenda, F. Perren, D. Rufenacht, and N. Stergiopulos, "Validation of a one-dimensional model of the systemic arterial tree," *American Journal of Physiology-Heart and Circulatory Physiology*, vol. 297, no. 1, pp. H208–H222, 2009.

[149] G.-Y. Suh, G. Choi, R. J. Herfkens, R. L. Dalman, and C. P. Cheng, "Three-dimensional modeling analysis of visceral arteries and kidneys during respiration," *Annals of vascular surgery*, vol. 34, pp. 250–260, 2016.

[150] R. Richardson Jr, J. Miller, and W. M. Reichert, "Polyimides as biomaterials: preliminary biocompatibility testing," *Biomaterials*, vol. 14, no. 8, pp. 627–635, 1993.

[151] B. Venzac, S. Deng, Z. Mahmoud, A. Lenferink, A. Costa, F. Bray, C. Otto, C. Rolando, and S. Le Gac, "Pdms curing inhibition on 3d-printed molds: why? also, how to avoid it?" *Analytical chemistry*, vol. 93, no. 19, pp. 7180–7187, 2021.

[152] V. Saggiomo and A. H. Velders, "Simple 3d printed scaffold-removal method for the fabrication of intricate microfluidic devices," *Advanced Science*, vol. 2, no. 9, p. 1500125, 2015.

[153] C. A. Taylor, C. P. Cheng, L. A. Espinosa, B. T. Tang, D. Parker, and R. J. Herfkens, "In vivo quantification of blood flow and wall shear stress in the human abdominal aorta during lower limb exercise," *Annals of biomedical engineering*, vol. 30, pp. 402–408, 2002.

[154] E. S. Gang, B. L. Nguyen, Y. Shachar, L. Farkas, L. Farkas, B. Marx, D. Johnson, M. C. Fishbein, C. Gaudio, and S. J. Kim, "Dynamically

shaped magnetic fields: initial animal validation of a new remote electrophysiology catheter guidance and control system," *Circulation: Arrhythmia and Electrophysiology*, vol. 4, no. 5, pp. 770–777, 2011.

[155] Y. Kim, E. Genevriere, P. Harker, J. Choe, M. Balicki, R. W. Regenhardt, J. E. Vranic, A. A. Dmytriw, A. B. Patel, and X. Zhao, "Telerobotic neurovascular interventions with magnetic manipulation," *Science Robotics*, vol. 7, no. 65, p. eabg9907, 2022.

[156] I. Penskiy, A. Gerratt, and S. Bergbreiter, "Friction, adhesion and wear properties of pdms films on silicon sidewalls," *Journal of Micromechanics and Microengineering*, vol. 21, no. 10, p. 105013, 2011.

[157] C. Lin, H. J. Kaper, W. Li, R. Splinter, and P. K. Sharma, "Role of endothelial glycocalyx in sliding friction at the catheter-blood vessel interface," *Scientific Reports*, vol. 10, no. 1, p. 11855, 2020.

[158] P. Connes, T. Alexy, J. Detterich, M. Romana, M.-D. Hardy-Dessources, and S. K. Ballas, "The role of blood rheology in sickle cell disease," *Blood reviews*, vol. 30, no. 2, pp. 111–118, 2016.

[159] S. Kim, C. Laschi, and B. Trimmer, "Soft robotics: a bioinspired evolution in robotics," *Trends in biotechnology*, vol. 31, no. 5, pp. 287–294, 2013.

[160] P. Calvert, "Hydrogels for soft machines," *Advanced materials*, vol. 21, no. 7, pp. 743–756, 2009.

[161] S. Li, H. Bai, R. F. Shepherd, and H. Zhao, "Bio-inspired design and additive manufacturing of soft materials, machines, robots, and haptic interfaces," *Angewandte Chemie International Edition*, vol. 58, no. 33, pp. 11 182–11 204, 2019.

[162] X. Huang, M. Ford, Z. J. Patterson, M. Zarepoor, C. Pan, and C. Majidi, "Shape memory materials for electrically-powered soft machines," *Journal of Materials Chemistry B*, vol. 8, no. 21, pp. 4539–4551, 2020.

[163] T. Bützer, O. Lambercy, J. Arata, and R. Gassert, "Fully wearable actuated soft exoskeleton for grasping assistance in everyday activities," *Soft robotics*, vol. 8, no. 2, pp. 128–143, 2021.

[164] J. Yin, R. Hinchet, H. Shea, and C. Majidi, "Wearable soft technologies for haptic sensing and feedback," *Advanced Functional Materials*, vol. 31, no. 39, p. 2007428, 2021.

[165] S. Biswas and Y. Visell, "Emerging material technologies for haptics," *Advanced Materials Technologies*, vol. 4, no. 4, p. 1900042, 2019.

[166] M. Medina-Sánchez, V. Magdanz, M. Guix, V. M. Fomin, and O. G. Schmidt, "Swimming microrobots: Soft, reconfigurable, and smart," *Advanced Functional Materials*, vol. 28, no. 25, p. 1707228, 2018.

[167] N. Ebrahimi, C. Bi, D. J. Cappelleri, G. Ciuti, A. T. Conn, D. Faivre, N. Habibi, A. Hošovskỳ, V. Iacovacci, I. S. Khalil *et al.*, "Magnetic actuation methods in bio/soft robotics," *Advanced Functional Materials*, vol. 31, no. 11, p. 2005137, 2021.

[168] V. K. Venkiteswaran, L. F. P. Samaniego, J. Sikorski, and S. Misra, "Bio-inspired terrestrial motion of magnetic soft millirobots," *IEEE Robotics and automation letters*, vol. 4, no. 2, pp. 1753–1759, 2019.

[169] H. Zhu, Y. Wang, Y. Ge, Y. Zhao, and C. Jiang, "Kirigami-inspired programmable soft magnetoresponsive actuators with versatile morphing modes," *Advanced Science*, vol. 9, no. 32, p. 2203711, 2022.

[170] J. A.-C. Liu, J. H. Gillen, S. R. Mishra, E. E. Evans, and J. B. Tracy, "Photothermally and magnetically controlled reconfiguration of polymer composites for soft robotics," *Science advances*, vol. 5, no. 8, p. eaaw2897, 2019.

[171] J. Cui, T.-Y. Huang, Z. Luo, P. Testa, H. Gu, X.-Z. Chen, B. J. Nelson, and L. J. Heyderman, "Nanomagnetic encoding of shape-morphing micromachines," *Nature*, vol. 575, no. 7781, pp. 164–168, 2019.

[172] G. Kravanja, I. A. Belyaeva, L. Hribar, I. Drevenšek-Olenik, M. Shamonin, and M. Jezeršek, "Laser micromachining of magnetoactive elastomers as enabling technology for magnetoresponsive surfaces," *Advanced Materials Technologies*, vol. 7, no. 5, p. 2101045, 2022.

[173] X. Wang, G. Mao, J. Ge, M. Drack, G. S. Cañón Bermúdez, D. Wirthl, R. Illing, T. Kosub, L. Bischoff, C. Wang *et al.*, "Untethered and ultrafast soft-bodied robots," *Communications Materials*, vol. 1, no. 1, p. 67, 2020.

[174] J. Zhang, Z. Ren, W. Hu, R. H. Soon, I. C. Yasa, Z. Liu, and M. Sitti, "Voxelated three-dimensional miniature magnetic soft machines via multimaterial heterogeneous assembly," *Science robotics*, vol. 6, no. 53, p. eabf0112, 2021.

[175] Y. Dong, L. Wang, N. Xia, Z. Yang, C. Zhang, C. Pan, D. Jin, J. Zhang, C. Majidi, and L. Zhang, "Untethered small-scale magnetic soft robot with programmable magnetization and integrated multifunctional modules," *Science advances*, vol. 8, no. 25, p. eabn8932, 2022.

[176] Z. Chen, Y. Lin, G. Zheng, Y. Yang, Y. Zhang, S. Zheng, J. Li, J. Li, L. Ren, and L. Jiang, "Programmable transformation and controllable locomotion of magnetoactive soft materials with 3d-patterned magnetization," *ACS Applied Materials & Interfaces*, vol. 12, no. 52, pp. 58 179–58 190, 2020.

[177] M. H. D. Ansari, V. Iacovacci, S. Pane, M. Ourak, G. Borghesan, I. Tamadon, E. Vander Poorten, and A. Menciassi, "3d printing of small-scale soft robots with programmable magnetization," *Advanced Functional Materials*, p. 2211918, 2023.

[178] Y. Alapan, A. C. Karacakol, S. N. Guzelhan, I. Isik, and M. Sitti, "Reprogrammable shape morphing of magnetic soft machines," *Science advances*, vol. 6, no. 38, p. eabc6414, 2020.

[179] H. Deng, K. Sattari, Y. Xie, P. Liao, Z. Yan, and J. Lin, "Laser reprogramming magnetic anisotropy in soft composites for reconfigurable 3d shaping," *Nature communications*, vol. 11, no. 1, p. 6325, 2020.

[180] H. Song, H. Lee, J. Lee, J. K. Choe, S. Lee, J. Y. Yi, S. Park, J.-W. Yoo, M. S. Kwon, and J. Kim, "Reprogrammable ferromagnetic domains for reconfigurable soft magnetic actuators," *Nano Letters*, vol. 20, no. 7, pp. 5185–5192, 2020.

[181] T. Xu, J. Zhang, M. Salehizadeh, O. Onaizah, and E. Diller, "Millimeter-scale flexible robots with programmable three-dimensional magnetization and motions," *Science Robotics*, vol. 4, no. 29, p. eaav4494, 2019.

[182] M. Eshaghi, M. Ghasemi, and K. Khorshidi, "Design, manufacturing and applications of small-scale magnetic soft robots," *Extreme Mechanics Letters*, vol. 44, p. 101268, 2021.

[183] T. Wang, H. Ugurlu, Y. Yan, M. Li, M. Li, A.-M. Wild, E. Yildiz, M. Schneider, D. Sheehan, W. Hu *et al.*, "Adaptive wireless millirobotic locomotion into distal vasculature," *Nature Communications*, vol. 13, no. 1, p. 4465, 2022.

[184] Y. Ju, R. Hu, Y. Xie, J. Yao, X. Li, Y. Lv, X. Han, Q. Cao, and L. Li, "Reconfigurable magnetic soft robots with multimodal locomotion," *Nano Energy*, vol. 87, p. 106169, 2021.

[185] Z. Ren, R. Zhang, R. H. Soon, Z. Liu, W. Hu, P. R. Onck, and M. Sitti, "Soft-bodied adaptive multimodal locomotion strategies in fluid-filled confined spaces," *Science Advances*, vol. 7, no. 27, p. eabh2022, 2021.

[186] L. Pancaldi, L. Noseda, A. Dolev, A. Fanelli, D. Ghezzi, A. J. Petruska, and M. S. Sakar, "Locomotion of sensor-integrated soft robotic devices inside sub-millimeter arteries with impaired flow conditions," *Advanced Intelligent Systems*, vol. 4, no. 5, p. 2100247, 2022.

[187] M. Sitti, "Miniature soft robots—road to the clinic," *Nature Reviews Materials*, vol. 3, no. 6, pp. 74–75, 2018.

[188] B. Wang, K. F. Chan, K. Yuan, Q. Wang, X. Xia, L. Yang, H. Ko, Y.-X. J. Wang, J. J. Y. Sung, P. W. Y. Chiu *et al.*, "Endoscopy-assisted magnetic navigation of biohybrid soft microrobots with rapid endoluminal delivery and imaging," *Science Robotics*, vol. 6, no. 52, p. eabd2813, 2021.

[189] J. Zhang, O. Onaizah, K. Middleton, L. You, and E. Diller, "Reliable grasping of three-dimensional untethered mobile magnetic microgripper for autonomous pick-and-place," *IEEE Robotics and Automation Letters*, vol. 2, no. 2, pp. 835–840, 2017.

[190] M. Li, Y. Tang, R. H. Soon, B. Dong, W. Hu, and M. Sitti, "Miniature coiled artificial muscle for wireless soft medical devices," *Science Advances*, vol. 8, no. 10, p. eabm5616, 2022.

[191] Y. Tang, M. Li, T. Wang, X. Dong, W. Hu, and M. Sitti, "Wireless miniature magnetic phase-change soft actuators," *Advanced Materials*, vol. 34, no. 40, p. 2204185, 2022.

[192] Q. Ze, S. Wu, J. Dai, S. Leanza, G. Ikeda, P. C. Yang, G. Iaccarino, and R. R. Zhao, "Spinning-enabled wireless amphibious origami millirobot," *Nature Communications*, vol. 13, no. 1, p. 3118, 2022.

[193] X. Fan, X. Dong, A. C. Karacakol, H. Xie, and M. Sitti, "Reconfigurable multifunctional ferrofluid droplet robots," *Proceedings of the National Academy of Sciences*, vol. 117, no. 45, pp. 27 916–27 926, 2020.

[194] W. R. Johnson, S. J. Woodman, and R. Kramer-Bottiglio, "An electromagnetic soft robot that carries its own magnet," *IEEE 5th International Conference on Soft Robotics (RoboSoft)*, pp. 761–766, 2022.

[195] R. Pelrine, A. Wong-Foy, A. Hsu, and B. McCoy, "Self-assembly of milli-scale robotic manipulators: A path to highly adaptive, robust automation systems," *2016 International Conference on Manipulation, Automation and Robotics at Small Scales (MARSS)*, pp. 1–6, 2016.

[196] K. Vikrant and G. Jayanth, "Diamagnetically levitated nanopositioners with large-range and multiple degrees of freedom," *Nature Communications*, vol. 13, no. 1, p. 3334, 2022.

[197] S. Chowdhury, B. V. Johnson, W. Jing, and D. J. Cappelleri, "Designing local magnetic fields and path planning for independent actuation of multiple mobile microrobots," *Journal of Micro-Bio Robotics*, vol. 12, pp. 21–31, 2017.

[198] B. V. Johnson, S. Chowdhury, and D. J. Cappelleri, "Local magnetic field design and characterization for independent closed-loop control of multiple mobile microrobots," *IEEE/ASME Transactions on Mechatronics*, vol. 25, no. 2, pp. 526–534, 2020.

[199] Y. Kantaros, B. V. Johnson, S. Chowdhury, D. J. Cappelleri, and M. M. Zavlanos, "Control of magnetic microrobot teams for temporal micromanipulation tasks," *IEEE Transactions on Robotics*, vol. 34, no. 6, pp. 1472–1489, 2018.

[200] G. Cui, P. Zhang, X. Liu, L. Xie, W. Huang, P. Pan, J. Qu, and Q. Fan, "Novel coil array design and modeling for independent control of multiple magnetic microrobots," *IEEE Transactions on Industrial Electronics*, 2022.

[201] S. Zhang, R. Zhang, Y. Wang, P. R. Onck, and J. M. Den Toonder, "Controlled multidirectional particle transportation by magnetic artificial cilia," *ACS nano*, vol. 14, no. 8, pp. 10 313–10 323, 2020.

[202] X. Dong, G. Z. Lum, W. Hu, R. Zhang, Z. Ren, P. R. Onck, and M. Sitti, "Bioinspired cilia arrays with programmable nonreciprocal motion and metachronal coordination," *Science Advances*, vol. 6, no. 45, p. eabc9323, 2020.

[203] S. Tottori, N. Sugita, R. Kometani, S. Ishihara, and M. Mitsuishi, "Selective control method for multiple magnetic helical microrobots," *Journal of Micro-Nano Mechatronics*, vol. 6, pp. 89–95, 2011.

[204] K. E. Peyer, L. Zhang, and B. J. Nelson, "Bio-inspired magnetic swimming microrobots for biomedical applications," *Nanoscale*, vol. 5, no. 4, pp. 1259–1272, 2013.

[205] B. Aksoy and H. Shea, "Multistable shape programming of variable-stiffness electromagnetic devices," *Science Advances*, vol. 8, no. 21, p. eabk0543, 2022.

[206] J. Rahmer, C. Stehning, and B. Gleich, "Spatially selective remote magnetic actuation of identical helical micromachines," *Science Robotics*, vol. 2, no. 3, p. eaal2845, 2017.

[207] Q. Boehler, S. Gervasoni, S. L. Charreyron, C. Chautems, and B. J. Nelson, "On the workspace of electromagnetic navigation systems," *IEEE Transactions on Robotics*, 2022.

[208] M. Sun, C. Tian, L. Mao, X. Meng, X. Shen, B. Hao, X. Wang, H. Xie, and L. Zhang, "Reconfigurable magnetic slime robot: deformation, adaptability, and multifunction," *Advanced Functional Materials*, vol. 32, no. 26, p. 2112508, 2022.

[209] Z. Chen, W. Lu, Y. Li, P. Liu, Y. Yang, and L. Jiang, "Solid–liquid state transformable magnetorheological millirobot," *ACS Applied Materials & Interfaces*, vol. 14, no. 26, pp. 30 007–30 020, 2022.

[210] X. Fan, Y. Jiang, M. Li, Y. Zhang, C. Tian, L. Mao, H. Xie, L. Sun, Z. Yang, and M. Sitti, "Scale-reconfigurable miniature ferrofluidic robots for negotiating sharply variable spaces," *Science Advances*, vol. 8, no. 37, p. eabq1677, 2022.

[211] G. Mao, M. Drack, M. Karami-Mosammam, D. Wirthl, T. Stockinger, R. Schwödiauer, and M. Kaltenbrunner, "Soft electromagnetic actuators," *Science Advances*, vol. 6, no. 26, p. eabc0251, 2020.

[212] R. Guo, L. Sheng, H. Gong, and J. Liu, "Liquid metal spiral coil enabled soft electromagnetic actuator," *Science China Technological Sciences*, vol. 61, pp. 516–521, 2018.

[213] D. Ye, J. Xue, S. Yuan, F. Zhang, S. Song, J. Wang, and M. Q.-H. Meng, "Design and control of a magnetically-actuated capsule robot with biopsy function," *IEEE Transactions on Biomedical Engineering*, vol. 69, no. 9, pp. 2905–2915, 2022.

[214] N. Friedman, V. Chan, D. Zondervan, M. Bachman, and D. J. Reinkensmeyer, "Musicglove: Motivating and quantifying hand movement rehabilitation by using functional grips to play music," *2011 Annual International Conference of the IEEE Engineering in Medicine and Biology Society*, pp. 2359–2363, 2011.

[215] M. Ha, G. S. Cañón Bermúdez, J. A.-C. Liu, E. S. Oliveros Mata, E. E. Evans, J. B. Tracy, and D. Makarov, "Reconfigurable magnetic origami actuators with on-board sensing for guided assembly," *Advanced Materials*, vol. 33, no. 25, p. 2008751, 2021.

[216] M. Li, A. Pal, A. Aghakhani, A. Pena-Francesch, and M. Sitti, "Soft actuators for real-world applications," *Nature Reviews Materials*, vol. 7, no. 3, pp. 235–249, 2022.

[217] P. T. Phan, T. T. Hoang, M. T. Thai, H. Low, N. H. Lovell, and T. N. Do, "Twisting and braiding fluid-driven soft artificial muscle fibers for robotic applications," *Soft Robotics*, vol. 9, no. 4, pp. 820–836, 2022.

[218] D. Villegas, M. Van Damme, B. Vanderborght, P. Beyl, and D. Lefeber, "Third–generation pleated pneumatic artificial muscles for robotic applications: development and comparison with mckibben muscle," *Advanced Robotics*, vol. 26, no. 11-12, pp. 1205–1227, 2012.

[219] D. R. Higueras-Ruiz, M. W. Shafer, and H. P. Feigenbaum, "Cavatappi artificial muscles from drawing, twisting, and coiling polymer tubes," *Science Robotics*, vol. 6, no. 53, p. eabd5383, 2021.

[220] E. Acome, S. K. Mitchell, T. Morrissey, M. Emmett, C. Benjamin, M. King, M. Radakovitz, and C. Keplinger, "Hydraulically amplified self-healing electrostatic actuators with muscle-like performance," *Science*, vol. 359, no. 6371, pp. 61–65, 2018.

[221] X. Du and J. Yu, "Image-integrated magnetic actuation systems for localization and remote actuation of medical miniature robots: A survey," *IEEE Transactions on Robotics*, vol. 39, no. 4, pp. 2549–2568, 2023.

[222] G. Pittiglio, P. Lloyd, T. da Veiga, O. Onaizah, C. Pompili, J. H. Chandler, and P. Valdastri, "Patient-specific magnetic catheters for atraumatic autonomous endoscopy," *Soft Robotics*, vol. 9, no. 6, pp. 1120–1133, 2022.

[223] M. Richter, M. Kaya, J. Sikorski, L. Abelmann, V. Kalpathy Venkiteswaran, and S. Misra, "Magnetic soft helical manipulators with local dipole interactions for flexibility and forces," *Soft Robotics*, 2023.

[224] R. Dreyfus, Q. Boehler, S. Lyttle, P. Gruber, J. Lussi, C. Chautems, S. Gervasoni, J. Berberat, D. Seibold, N. Ochsenbein-Kölble *et al.*,

"Dexterous helical magnetic robot for improved endovascular access," *Science Robotics*, vol. 9, no. 87, p. eadh0298, 2024.

[225] D. V. Kladko and V. V. Vinogradov, "Magnetosurgery: Principles, design, and applications," *Smart Materials in Medicine*, vol. 5, no. 1, pp. 24–35, 2024.

[226] B. J. Nelson, "An electromagnetic robot for navigating medical devices," *Nature Reviews Bioengineering*, vol. 2, no. 5, pp. 370–371, 2024.

[227] M. Richter, V. K. Venkiteswaran, J.-P. de Vries, and S. Misra, "Apollo: advanced magnetic probes for minimally invasive endovascular interventions," *European Heart Journal*, vol. 45, no. 29, pp. 2589–2591, 2024.

[228] J. Lussi, S. Gervasoni, M. Mattille, R. Dreyfus, Q. Boehler, M. Reinehr, N. Ochsenbein, B. J. Nelson, and U. Moehrlen, "Magnetically guided laser surgery for the treatment of twin-to-twin transfusion syndrome," *Advanced Intelligent Systems*, vol. 4, no. 11, p. 2200182, 2022.

[229] B. Laulicht, N. J. Gidmark, A. Tripathi, and E. Mathiowitz, "Localization of magnetic pills," *Proceedings of the National Academy of Sciences*, vol. 108, no. 6, pp. 2252–2257, 2011.

[230] R. Dreyfus, Q. Boehler, C. Chautems, and B. Nelson, "A navigation console to steer magnetic instruments under radiological guidance for neuro-vascular interventions," in *Proceedings of the 14th Hamlyn Symposium on Medical Robotics 2022*. The Hamlyn Centre, Imperial College London, 2022, pp. 79–80.

[231] S. Tognarelli, V. Castelli, G. Ciuti, C. Di Natali, E. Sinibaldi, P. Dario, and A. Menciassi, "Magnetic propulsion and ultrasound tracking of endovascular devices," *Journal of Robotic Surgery*, vol. 6, pp. 5–12, 2012.

[232] C. M. Heunis, Y. P. Wotte, J. Sikorski, G. P. Furtado, and S. Misra, "The armm system-autonomous steering of magnetically-actuated catheters: Towards endovascular applications," *IEEE Robotics and automation letters*, vol. 5, no. 2, pp. 705–712, 2020.

[233] F. Suligoj, C. M. Heunis, J. Sikorski, and S. Misra, "Robust–an autonomous robotic ultrasound system for medical imaging," *IEEE Access*, vol. 9, pp. 67 456–67 465, 2021.

[234] Z. Li, J. Li, Z. Wu, Y. Chen, M. Yeerbulati, and Q. Xu, "Design and hierarchical control of a homocentric variable stiffness magnetic catheter for multi-arm robotic ultrasound-assisted coronary intervention," *IEEE Transactions on Robotics*, 2024.

[235] O. Erin, M. Boyvat, M. E. Tiryaki, M. Phelan, and M. Sitti, "Magnetic resonance imaging system–driven medical robotics," *Advanced Intelligent Systems*, vol. 2, no. 2, p. 1900110, 2020.

[236] S. Mutlu, O. Yasa, O. Erin, and M. Sitti, "Magnetic resonance imaging-compatible optically powered miniature wireless modular lorentz force actuators," *Advanced Science*, vol. 8, no. 2, p. 2002948, 2021.

[237] A. Aziz, S. Pane, V. Iacovacci, N. Koukourakis, J. Czarske, A. Menciassi, M. Medina-Sánchez, and O. G. Schmidt, "Medical imaging of microrobots: Toward in vivo applications," *ACS Nano*, vol. 14, no. 9, pp. 10 865–10 893, 2020.

[238] D. von Arx, C. Fischer, H. Torlakcik, S. Pané, B. J. Nelson, and Q. Boehler, "Simultaneous localization and actuation using electromagnetic navigation systems," *IEEE Transactions on Robotics*, 2023.

[239] A. Z. Taddese, P. R. Slawinski, M. Pirotta, E. De Momi, K. L. Obstein, and P. Valdastri, "Enhanced real-time pose estimation for closed-loop robotic manipulation of magnetically actuated capsule endoscopes," *The International Journal of Robotics Research*, vol. 37, no. 8, pp. 890–911, 2018.

[240] B. Rivkin, C. Becker, B. Singh, A. Aziz, F. Akbar, A. Egunov, D. D. Karnaushenko, R. Naumann, R. Schäfer, M. Medina-Sánchez, D. Karnaushenko, and O. G. Schmidt, "Electronically integrated microcatheters based on self-assembling polymer films," *Science Advances*, vol. 7, no. 51, p. eabl5408, 2021.

[241] B. Gleich, I. Schmale, T. Nielsen, and J. Rahmer, "Miniature magneto-mechanical resonators for wireless tracking and sensing," *Science*, vol. 380, no. 6648, pp. 966–971, 2023.

[242] F. Fischer, C. Gletter, M. Jeong, and T. Qiu, "Magneto-oscillatory localization for small-scale robots," *npj Robotics*, vol. 2, no. 1, p. 1, 2024.

[243] S. Yim and M. Sitti, "3-d localization method for a magnetically actuated soft capsule endoscope and its applications," *IEEE Transactions on Robotics*, vol. 29, no. 5, pp. 1139–1151, 2013.

[244] K. M. Popek, T. Schmid, and J. J. Abbott, "Six-degree-of-freedom localization of an untethered magnetic capsule using a single rotating magnetic dipole," *IEEE Robotics and Automation Letters*, vol. 2, no. 1, pp. 305–312, 2016.

[245] J. C. Norton, P. R. Slawinski, H. S. Lay, J. W. Martin, B. F. Cox, G. Cummins, M. P. Desmulliez, R. E. Clutton, K. L. Obstein, S. Cochran *et al.*, "Intelligent magnetic manipulation for gastrointestinal ultrasound," *Science Robotics*, vol. 4, no. 31, p. eaav7725, 2019.

[246] S. Sharma, A. Telikicherla, G. Ding, F. Aghlmand, A. H. Talkhooncheh, M. G. Shapiro, and A. Emami, "Wireless 3d surgical navigation and tracking system with 100μm accuracy using magnetic-field gradient-based localization," *IEEE Transactions on Medical Imaging*, vol. 40, no. 8, pp. 2066–2079, 2021.

[247] Y. Xu, K. Li, Z. Zhao, and M. Q.-H. Meng, "A novel system for closed-loop simultaneous magnetic actuation and localization of wce based on external sensors and rotating actuation," *IEEE Transactions on Automation Science and Engineering*, vol. 18, no. 4, pp. 1640–1652, 2020.

[248] ——, "Adaptive simultaneous magnetic actuation and localization for wce in a tubular environment," *IEEE Transactions on Robotics*, vol. 38, no. 5, pp. 2812–2826, 2022.

[249] M. Zhang, L. Yang, C. Zhang, Z. Yang, and L. Zhang, "Simultaneous actuation and localization of magnetic robots using mobile coils and eye-in-hand hall-effect sensors," in *2021 IEEE/RSJ International Conference on Intelligent Robots and Systems (IROS)*. IEEE, 2021, pp. 8515–8521.

[250] E. Paperno, I. Sasada, and E. Leonovich, "A new method for magnetic position and orientation tracking," *IEEE Transactions on Magnetics*, vol. 37, no. 4, pp. 1938–1940, 2001.

[251] D. Makarov, M. Melzer, D. Karnaushenko, and O. G. Schmidt, "Shapeable magnetoelectronics," *Applied Physics Letters*, vol. 3, no. 1, 2016.

[252] B. Assadsangabi, M. Tee, and K. Takahata, "Ferrofluid-assisted levitation mechanism for micromotor applications," in *2013 Transducers & Eurosensors XXVII: The 17th International Conference on Solid-State Sensors, Actuators and Microsystems (TRANSDUCERS & EUROSENSORS XXVII)*. IEEE, 2013, pp. 2720–2723.

[253] B. Assadsangabi, M. H. Tee, S. Wu, and K. Takahata, "Catheter-based microrotary motor enabled by ferrofluid for microendoscope applications," *Journal of Microelectromechanical Systems*, vol. 25, no. 3, pp. 542–548, 2016.

[254] S. M. H. Jayhooni, B. Assadsangabi, and K. Takahata, "A stepping micromotor based on ferrofluid bearing for side-viewing microendoscope applications," *Sensors and Actuators A: Physical*, vol. 269, pp. 258–268, 2018.

[255] R. Bandorf, H. Lüthje, C. Henke, J. Wiebe, J.-H. Sick, and R. Küster, "Different carbon based thin films and their microtribological behaviour in mems applications," *Surface and coatings technology*, vol. 200, no. 5-6, pp. 1777–1782, 2005.

[256] T. Wang, C. Lancée, R. Beurskens, J. Meijer, B. Knapen, A. F. van der Steen, and G. van Soest, "Development of a high-speed synchronous micro motor and its application in intravascular imaging," *Sensors and Actuators A: Physical*, vol. 218, pp. 60–68, 2014.

[257] N. Ghalichechian, A. Modafe, M. I. Beyaz, and R. Ghodssi, "Design, fabrication, and characterization of a rotary micromotor supported on microball bearings," *Journal of Microelectromechanical Systems*, vol. 17, no. 3, pp. 632–642, 2008.

[258] C. Chautems and B. J. Nelson, "The tethered magnet: Force and 5-dof pose control for cardiac ablation," in *2017 IEEE international conference on robotics and automation (ICRA)*. IEEE, 2017, pp. 4837–4842.

[259] M. Richter, J. Sikorski, P. Makushko, Y. Zabila, V. K. Venkiteswaran, D. Makarov, and S. Misra, "Locally addressable energy efficient actuation of magnetic soft actuator array systems," *Advanced Science*, p. 2302077, 2023.

[260] M.-D. Calin and E. Helerea, "Temperature influence on magnetic characteristics of ndfeb permanent magnets," in *2011 7th international symposium on advanced topics in electrical engineering (ATEE)*. IEEE, 2011, pp. 1–6.

[261] H. Kuhn, W. Hughes, and E. Gaylord, "Measurements of the viscosity of liquid wood's metal," *British Journal of Applied Physics*, vol. 13, no. 10, p. 527, 1962.

[262] X. Zhang, J. Liu, and Z. Deng, "Bismuth-based liquid metals: advances, applications, and prospects," *Materials Horizons*, vol. 11, no. 6, pp. 1369–1394, 2024.

[263] K. M. Popek, T. Hermans, and J. J. Abbott, "First demonstration of simultaneous localization and propulsion of a magnetic capsule in a lumen using a single rotating magnet," in *2017 IEEE International Conference on Robotics and Automation (ICRA)*. IEEE, 2017, pp. 1154–1160.

[264] A. J. Sperry, J. J. Christensen, and J. J. Abbott, "Six-degree-of-freedom localization with a 3-axis accelerometer and a 2-axis magnetometer for magnetic capsule endoscopy," *IEEE Robotics and Automation Letters*, vol. 7, no. 2, pp. 2110–2115, 2022.

[265] Y. Shen, S. Dong, D. Liu, K. Zhang, and H. Wang, "Active 6-dof electromagnetic pose tracking using orientation control of the magnetic source," in *2023 IEEE International Conference on Robotics and Biomimetics (ROBIO)*. IEEE, 2023, pp. 1–7.

[266] P. Valdastri, E. Sinibaldi, S. Caccavaro, G. Tortora, A. Menciassi, and P. Dario, "A novel magnetic actuation system for miniature swimming robots," *IEEE Transactions on Robotics*, vol. 27, no. 4, pp. 769–779, 2011.

[267] L.-J. W. Ligtenberg, N. C. Rabou, C. Goulas, W. C. Duinmeijer, F. R. Halfwerk, J. Arens, R. Lomme, V. Magdanz, A. Klingner, E. A. Klein Rot *et al.*, "Ex vivo validation of magnetically actuated intravascular untethered robots in a clinical setting," *Communications Engineering*, vol. 3, no. 1, p. 68, 2024.

[268] Y. Hou, H. Wang, R. Fu, X. Wang, J. Yu, S. Zhang, Q. Huang, Y. Sun, and T. Fukuda, "A review on microrobots driven by optical and magnetic fields," *Lab on a Chip*, vol. 23, no. 5, pp. 848–868, 2023.

[269] S. R. Khan, S. K. Pavuluri, G. Cummins, and M. P. Desmulliez, "Wireless power transfer techniques for implantable medical devices: A review," *Sensors*, vol. 20, no. 12, p. 3487, 2020.

[270] Y. Qian, Y. Cheng, J. Cai, X. Zhao, Y. Ouyang, W.-E. Yuan, and C. Fan, "Advances in electrical and magnetic stimulation on nerve regeneration," *Regenerative Medicine*, vol. 14, no. 10, pp. 969–979, 2019.

[271] E. Zhang, M. F. Kircher, M. Koch, L. Eliasson, S. N. Goldberg, and E. Renstrom, "Dynamic magnetic fields remote-control apoptosis via nanoparticle rotation," *ACS Nano*, vol. 8, no. 4, pp. 3192–3201, 2014.

[272] J. Choi, D.-i. Kim, J.-y. Kim, S. Pané, B. J. Nelson, Y.-T. Chang, and H. Choi, "Magnetically enhanced intracellular uptake of superparamagnetic iron oxide nanoparticles for antitumor therapy," *ACS Nano*, vol. 17, no. 16, pp. 15 857–15 870, 2023.

[273] A. Aghayan, "fit_ellipse," https://www.mathworks.com/matlabcentral/fileexchange/3215-fit_ellipse, MATLAB Central File Exchange, 2003, retrieved June 20, 2024.

[274] ——, "Amplitude and phase spectra of a signal (Fourier transform)," https://www.mathworks.com/matlabcentral/fileexchange/63965-amplitude-and-phase-spectra-of-a-signal-fourier-transform, MATLAB Central File Exchange, 2020, retrieved May 16, 2024.

[275] A. D. Losey, P. Lillaney, A. J. Martin, D. L. Cooke, M. W. Wilson, B. R. Thorne, R. S. Sincic, R. L. Arenson, M. Saeed, and S. W. Hetts, "Magnetically assisted remote-controlled endovascular catheter for interventional mr imaging: in vitro navigation at 1.5 t versus x-ray fluoroscopy," *Radiology*, vol. 271, no. 3, pp. 862–869, 2014.

[276] P. B. Nguyen, B. Kang, D. Bappy, E. Choi, S. Park, S. Y. Ko, J.-O. Park, and C.-S. Kim, "Real-time microrobot posture recognition via biplane x-ray imaging system for external electromagnetic actuation," *International journal of computer assisted radiology and surgery*, vol. 13, pp. 1843–1852, 2018.

[277] Y. Chen, N. Y. Shah, S. S. Goswami, A. Lange, F. Von Haxthausen, M. M. Sieren, J. Hagenah, F. Ernst, and V. García-Vázquez, "Localization of endovascular tools in x-ray images using a motorized c-arm: visualization on hololens," in *Current Directions in Biomedical Engineering*, vol. 6, no. 1. De Gruyter, 2020, p. 20200029.

[278] T. da Veiga, G. Pittiglio, M. Brockdorff, J. H. Chandler, and P. Valdastri, "Six-degree-of-freedom localization under multiple permanent magnets actuation," *IEEE Robotics and Automation Letters*, 2023.

[279] C. Fischer, T. Quirin, C. Chautems, Q. Boehler, J. Pascal, and B. J. Nelson, "Gradiometer-based magnetic localization for medical tools," *IEEE Transactions on Magnetics*, vol. 59, no. 2, pp. 1–5, 2022.

[280] I. S. Khalil, A. Adel, D. Mahdy, M. M. Micheal, M. Mansour, N. Hamdi, and S. Misra, "Magnetic localization and control of helical robots for clearing superficial blood clots," *APL bioengineering*, vol. 3, no. 2, 2019.

[281] Z. Fan, X. Wen, X. Ding, Q. Wang, S. Wang, and W. Yu, "Advances in biotechnology and clinical therapy in the field of peripheral nerve regeneration based on magnetism," *Frontiers in Neurology*, vol. 14, p. 1079757, 2023.

[282] I. S. Khalil, M. P. Pichel, L. Abelmann, and S. Misra, "Closed-loop control of magnetotactic bacteria," *The International Journal of Robotics Research*, vol. 32, no. 6, pp. 637–649, 2013.

[283] J. B. Tracy and T. M. Crawford, "Magnetic field-directed self-assembly of magnetic nanoparticles," *MRS bulletin*, vol. 38, no. 11, pp. 915–920, 2013.

[284] J. J. Huaroto, M. Richter, M. Malafaia, J. Kim, C.-S. Kim, J.-O. Park, J. Sikorski, and S. Misra, "Magneed–needle-shaped electromagnets for localized actuation within compact workspaces," *IEEE Robotics and Automation Letters*, vol. 8, no. 6, pp. 3908–3915, 2023.

Acknowledgements

In preparation to writing this part, I am making a list of names of those I want to thank. It is an interesting moment of retrospection that leads to a realization about how many incredible people were involved in shaping the past 5 years of my academic journey–master's and doctoral.

I'm deeply grateful to my promoter, **Sarthak**. I still remember reaching out in 2019 as a master's student, looking for an internship to prepare for my thesis at SRL. You directed me to a great lab in Leeds, where I first got into magnetics. Later, you were there during my graduation at SRL and shortly welcomed me as the first PhD researcher under your ERC grant, MAESTRO. Thank you for your guidance in those early years, for pushing me to explore new directions, and for your all your support. Thank you for involving me in grant writing and journal invitations. Your expertise, combined with the freedom to explore my ideas, shaped me into the researcher I am today.

As my daily supervisor, **Venkat**, you've guided me through both my master's and PhD journeys at SRL. I still remember us working tirelessly over the Christmas holiday in 2020, revising our first RaL paper over Teams. You were there for my graduation and even recommended me as a PhD candidate. I couldn't have asked for a better daily supervisor. Your insights into scientific writing, technical content, and magnetic robots have been invaluable along the way.

I also want to thank everyone else at SRL. **Yu-Hsiang**, we share a similar sense of humor and are at almost the same stage in life, which made our (short but not really) coffee break conversations so much fun. Thanks for helping Tra make spring rolls, inviting Jessica and me for dinner, and joining our board game nights. You (both) are awesome! **Tra**, you're such a lovely person. Thanks for showing us around the Düsseldorf Christmas market. I am curious about where life takes you both. **Juan**, from learning to cycle when starting out, teaching me French after a night out, to sharing experiences in manually assembling micro-scale things, what a time it's

been. **Lukas** & **Simon**, you proved that Germans have a great sense of humor! It has been fantastic to see what you were building in the lab. I wish you all the best in finishing your PhDs. **Antonio**, you brought light actuation to SRL. I hope you go on to build great things. **Yuxin**, the way you overcame early PhD struggles was truly impressive. Seeing you collaborate early on with experienced researchers and teach yourself AI was inspiring. **Nick**, you came all the way from the US for your postdoc – SRL is lucky to have you. Wishing you and your wife an exciting future ahead! And to the Groningen crew–**Chen**, **Zihan**, **Zhuoyue**, and **Kaixuan**–thanks for the great laughs during your visits to Twente and good luck during your PhDs and post-docs!

Also, a hymn to all of SRL Twente's great alumni who I got to know along the way. **Christoff**, it feels like we've known each other forever—dinners, board games, braais, your bachelor party, wedding, meeting your family, even your dad helping jumpstart our stalled car (rent a cheapie!) on a mountain campsite. These few words can't possibly capture all the memories. **Henrike**, you are a big part of Christoff's journey here. Thanks for being a great friend to Jessica, inviting her to your bachelorette party, and welcoming both of us to your wedding. **Jakub**, you were my first in many things. First to introduce me to BigMag, first as a novice to show me uncommented C++ code with "I write so it's obvious what's happening," and first as a worried first-year PhD to tell me that "the research field is already pretty saturated." You let me collaborate on your planar coil project and eventually let me take over when you moved to industry. For so long, you were everywhere in SRL, and your code still is. **Theodosia**, I hope you find plenty of occasions to use the engraved Japanese steak knives I got you for your PhD farewell, despite being vegetarian (oops me). **Mert**, thanks for the great conversations and for sharing baklava from your special drawer. **Sumit**, the father of acoustic microrobots at SRL. You were the last of the Yos Trinity (Jakub, Christoff, and you) to leave. Wishing you the best in your academic career. **Amin**, from printed flexures to foldable sheet metal, it was always exciting to see what you were working on. Best of luck in Maastricht and beyond. **Frank**, walking away from a PhD took real courage, especially after coming all the way from Greece. Wishing you strength and happiness ahead with Renya. **Franco**, you created a miniature sun (inside joke) and stole the show during a BNR interview.

You revived Batmag, and it can't be understated how impressive that is.

A huge thank you to the support staff in the Department of Biomechanical Engineering. Funny enough, you all gave me the chance to speak Dutch at work. **Jeanine**, you've always been "my rots in de branding" at SRL. Your magic with calendars and scheduling kept everything running, and in my final months, you regularly checked in on me and everyone else. You're amazing. **Lianne**, you also always looked out for us, and I'll always happily look back on our chats about vacations and so much more. **Yolanda**, thanks for patiently arranging a substitute access card every time I forgot mine. Also, I probably saw your last name more than any other, cycling past the Assinkhof daily. **Rob**, you might have brought the biggest change to SRL. Like a superhero, you swooped in–installing safety buttons, optimizing setups, organizing equipment, and even helping me sort out the KUKA software mess. And now, as I type this, you're swooping off again to new responsibilities. Finally, a big thank you to the rest of the technical staff–**Gert Jan**, **Martijn**, **Quint**, **Michiel**, and **Roger**–for everything you do!

I also want to thank the great scientists in Dresden–**Denys** and **Pasha**–whose expertise in flexible electronics made Chapters 5 and 6 possible. Also, to **Giovanni**, my internship supervisor in Leeds, who first introduced me to magnetics in surgical robotics. To my past and present office mates–**Shahriar**, **Fay**, **Alex**, **Wietze**, **Hellebore**, **Alaa**, and **Mina**–thanks for all the laughs and great conversations over the years. And to the students I had the pleasure of supervising, as well as those I met during my own time at SRL–**Kasper**, **Ritwik**, **Jessie**, **Sarah**, and **Dion**–your technical creativity led to new ideas and discussions, which I hope taught you as much as it did me.

Finally, to my parents, **Pap** en **Mam**, and my sweet **Jessica** who have been with me and supported me throughout. As I am thinking about what to write here, I conclude that I can only say this: thank you for *everything*.

About the Author

Michiel Richter was born on April 27, 1994, in Hardenberg, The Netherlands. He earned an International Baccalaureate Diploma from the International School Eerde in Ommen, The Netherlands, and completed a Bachelor's degree in Clinical Technology in 2017, followed by a Master's degree in Biomedical Engineering in 2020, at the University of Twente in Enschede, The Netherlands. During his studies, he completed two research internships: one at Medisch Spectrum Twente hospital in Enschede and the other at the Science and Technologies of Robotics in Medicine (STORM) Lab in Leeds, United Kingdom. For his Master's research, he focused on control of magnetic flexible robots at the Surgical Robotics Laboratory (SRL), under the supervision of Prof. Dr. Sarthak Misra and Dr. Venkatasubramanian Kalpathy Venkiteswaran in the Department of Biomechanical Engineering at the University of Twente. Motivated by his interest in magnetics for surgical robotics, he joined the SRL as a doctoral researcher in February 2021, continuing his work on the design, modeling, and control of magnetic continuum robots under the supervision of Prof. Dr. Sarthak Misra.